UNIVERSITÁ DEGLI STUDI DI MODENA E REGGIO-EMILIA

Dipartimento di Scienze Fisiche, Informatiche e Matematiche
School of Graduate Studies in Physics and Nanosciences

Tesi per il conseguimento del titolo di Dottore di Ricerca in Fisica

---

Computational investigation of noble metals on reducible metal-oxide surfaces for catalytic applications

---

Candidata:
Giulia Righi

Relatore:
Prof.ssa Rita Magri

Coordinatore della Scuola di Dottorato:
Prof. Marco Affronte

XXXII ciclo

Abstract

Catalysis is fundamental to many industrial processes, and, in the last years, much research has been devoted to find new catalysts. In the most common heterogenous catalysis reactions occur at the surface of a solid catalysts, and among catalysts metal oxides play an important role. Very often metals, and in particular, noble metals nanoparticles are adsorbed on the surface to increase the rates of the reactions. Noble metals are, indeed, excellent catalysts for the reactions involved in the energy production and conversion, however, due to their high cost it is fundamental to reduce the amount of noble metals maintaining the same performances. The most promising way is to pass from nanoparticles to single atoms, where the single atoms are the catalytic centers of the reactions.
In this thesis, using an $ab-initio$ approach based on the density functional theory, we have investigated the catalytic activity of noble metal atoms, where single atoms are adsorbed on top or are substitutional to other atoms on the cerium dioxide CeO_2 and maghemite γ-Fe_2O_3 surfaces. In the first part of this work, we have investigated the dissociation of the H_2 molecule on single Ag, Cu, and Au atoms adsorbed on the pristine CeO_2 (111) surface, or substituting a surface Ce atom on a reduced, or partially hydrogenated surface. In each one of these configurations the noble metal has a different oxidation state, and in this way, we have the possibility to understand how the charge transfers between the noble metal atom, the metal oxide, and the hydrogen atoms influence the reactivity of the surface. The oxidation of H_2 is a crucial reaction since it is the reaction which occurs at the anode of the proton exchange membrane fuel cells ($PEMFC_s$). In general, we have found that the presence of noble metals decreases the activation energy, and, among the noble metals, Ag seems the best candidate as single atom catalyst for this reaction.
The performance of Ag as a single atom catalyst has been investigated also towards methane activation. We have considered a single Ag atom substituting one surface Ce atom on the (111) and (100) ceria surfaces. The presence of single Ag atoms lowers significantly the energy required to break the first C-H bond, which is usually considered the rate limiting step of the reaction. Ag allows also for the direct conversion of methane into methanol, and for the (111) surface the energy of this reaction is lower than the energy required to dissociate CH_4 into CH_3 + H.
In the second part of the thesis we have studied the catalytic activity of the (001) maghemite surfaces, one of the less studied iron oxides. Maghemite differs from the most stable and studied magnetite only for the presence of Fe vacancies, and for the absence of reduced Fe^{2+} cations. For the first time we have considered explicitly the iron vacancies, beyond the mean field approach. We have found that the Fe vacancies increase the reducibility and the oxidation activity of the surfaces. This is due to the presence of less charged surface oxygens due to the Fe vacancies. The removal of a surface oxygen leads to a surface reconstruction, firstly proposal in this thesis, which is the most stable surface termination among those investigated.
We have studied, moreover, the most favorable sites for adsorption or cation/anion substitution of Cu, Ag, and Au atoms on the most stable (001) maghemite surface. We have investigated different configurations, and found that at room temperature

and pressure the surfaces where the noble metal atoms substitute Fe cations can be formed with a larger energy gain. We have also studied how single noble metals atoms dispersed on the surface affect the reducibility of the surfaces, and the adsorption of the carbon monoxide molecules. The obtained results have been compared with similar results on the pristine maghemite surface.
The results of this thesis suggest that noble metal modified reducible oxide surfaces may provide a viable answer in the search of new less expensive and better performing catalysts.

Sommario

La catalisi é fondamentale nella maggior parte dei processi industriali, e negli ultimi anni molte ricerche si sono indirizzate verso la scoperta di nuovi catalizzatori. Nella catalisi eterogenea, la piú diffusa tra i diversi tipi di catalisi, le reazioni avvengono alla superficie di catalizzatori solidi, e tra i piú impiegati ci sono gli ossidi metallici. Frequentemente, nanoparticelle metalliche, in particolare costituite da metalli nobili, sono assorbite sulla superficie Per aumentare le velocitá di reazione. I metalli nobili sono infatti ottimi catalizzatori per le reazioni che riguardano la conversione di energia. Tuttavia, a causa dell'elevato costo dei metalli nobili, sarebbe cruciale riuscire a diminuire la quantitá di metalli utilizzati mantenendo peró la stessa efficenza catalitica. Per fare ció la via piú promettente é di ridurre le dimensioni delle nanopartcelle a singoli atomi sulla superficie, e proprio i singoli atomi sono i centri catalizzatori.
In questa tesi, utilizzando un approccio a primi principi, basato sulla teoria del funzionale densitá, si é investigato il ruolo nelle proprietá catalitiche di metalli nobili assorbiti o dopanti nelle superficie di ossido di cerio CeO_2 e maghemite γ-Fe_2O_3. Nella prima parte della tesi, abbiamo investigato la dissociazione della molecola di idrogeno su un singolo atomo di Ag, Cu, e Au assorbiti sulla superficie (111) dell'ossido di cerio, o in sostituzione di un atomo di cerio su una superficie ridotta o parzialmente idrogenata. In ogni configurazione gli stati di ossidazione dei metalli nobili sono differenti, e in questo modo abbiamo la possibilitá come i trasferimenti di carica tra i metalli nobili, gli ossidi metallici e l'idrogeno influenzano la reattivitá della superficie. L'ossidazione dell'idrogeno é una reazione cruciale che avviene all'anodo delle pile a combustione a scambio protonico (PEMFCs). In generale, abbiamo trovato che la presenza dei metalli nobili abbassa l'energia richiesta per attivare H_2, e tra i metalli nobili Ag sembra essere il migliore candidato come. singolo atomo catalizzatore per questo tipo di reazione. Si é investigato anche l'efficienza dell'argento come singolo atomo catalizzatore per l'attivazione di una molecola di metano. Abbiamo considerato un singolo atomo di Ag che sostituiva un atomo di Ce nelle superfici (111) e (100). La presenza dell'atomo di Ag abbassa in modo significativo l'energia richiesta per rompere il. primo legame C-H, che é considerato di solito lo stadio cineticamente limitante della reazione. Inoltre, la presenza dell'atomo di Ag permette la formazione di una molecola di metanolo direttamente dal metano, e in particolare, per la superficie (111), l'energia per ottenere ció é inferiore alla barriera energetica della reazione $CH_4 \rightarrow CH_3 + H$.
Nella seconda parte della tesi abbiamo studiato le proprietá catalitiche della superficie (001) della maghemite. Per la prima volta abbiamo considerato esplicitamente le vacanze di ferro andando oltre l'approccio a campo medio. La maghemite differisce dalla piú stabile e piú studiata magnetite, solo per la presenza delle vacanze di Fe e per l'assenza di ridotti Fe^{2+}, ma le proprietá di riduzione sono diverse. Le vacanze di Fe aumentano la riducibilitá e l'ossidazione delle superfici. Questo effetto é dovuto alla presenza di ossigeni superficiali meno carichi. A seguito della rimozione di un ossigeno superficiale abbiamo trovato una nuova ricostruzione superficiale, che é la piú stabile tra quelle investigate.

Si é studiato, inoltre, l'interazione tra singoli atomi di Cu, Ag, e Au e la piú stabile (001) superficie di maghemite. Abbiamo considerato tre diverse configurazioni: metallo assorbito sulla superficie pura, e metallo in sostituzione di un catione o anione, e le superfici dopate sembrano essere le piú stabili a temperatura e pressione ambiente. Abbiamo studiato anche l'effetto dei singoli metalli nobili dispersi sulla superficie sulla riducibilitá della superficie, e sull'assorbimento del monossido di carbonio. I risultati ottenuti sono stati comparati con quelli ottenuti per la superficie originaria.

Contents

To my parents

Chapter 1

Introduction

1.1 Catalysis

Catalysis plays a key role in the physical, biological, and chemical sciences [1]. More than 85% of industrial processes make use of catalysts to speed up chemical reactions, as shown in Fig. 1.1a, and, consequently, improvement of the efficiency and selectivity of catalysts is a very important goal.
The word "*catalysis*" was used for the first time by Berzelius in 1836 to try to explain several experimental observations as wine fermentation, or decomposition of hydrogen peroxide in the presence of metals [2].
Catalysis was defined by Ostwald [3] in 1895 as the process by means of which the rates of reactions are increased significantly by the presence of small quantities of different substances, the catalysts. In the presence of catalysts, as shown in Fig. 1.2, the energy required to pass from the reactants to the products, the so-called activation energy E_a, decreases.

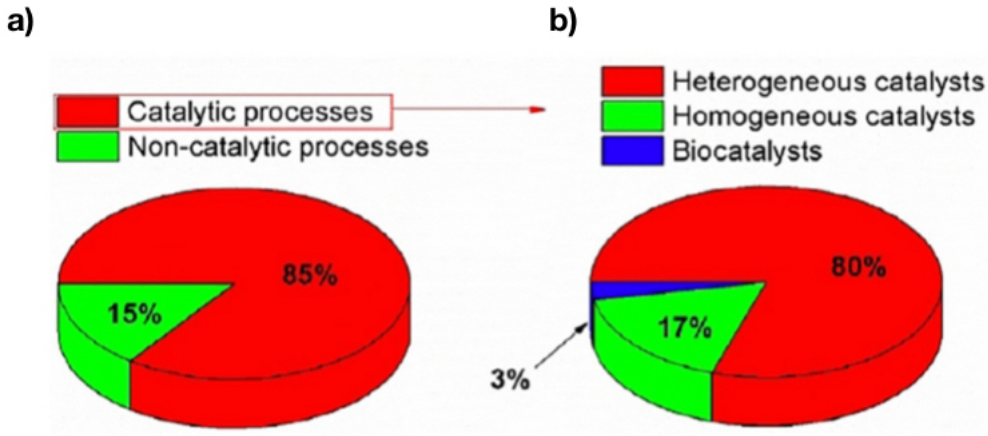

FIGURE 1.1: a) Use of catalysts in the industrial processes; b) use of different kinds of catalysts. Adapted from Ref. [1].

Catalysis, and consequently catalysts, as shown in Fig. 1.1b, are classified as homogenous, biological, and heterogenous. In the homogenous catalysis the reactants and the catalysts are in the same physical phase, with a defined geometry and environment, for example metal salts in organic acids. The main drawback of this kind of catalysts is the difficulty to separate the products. In the biological catalytic processes, the active sites are at the center of the enzymes, which show an high activity but they are not very resistant [4]. In the most common heterogenous catalysis, the reactants and the catalysts are in different phases, and, consequently, the separation of the products is easy. Usually, heterogenous reactions occur at the surface of solid

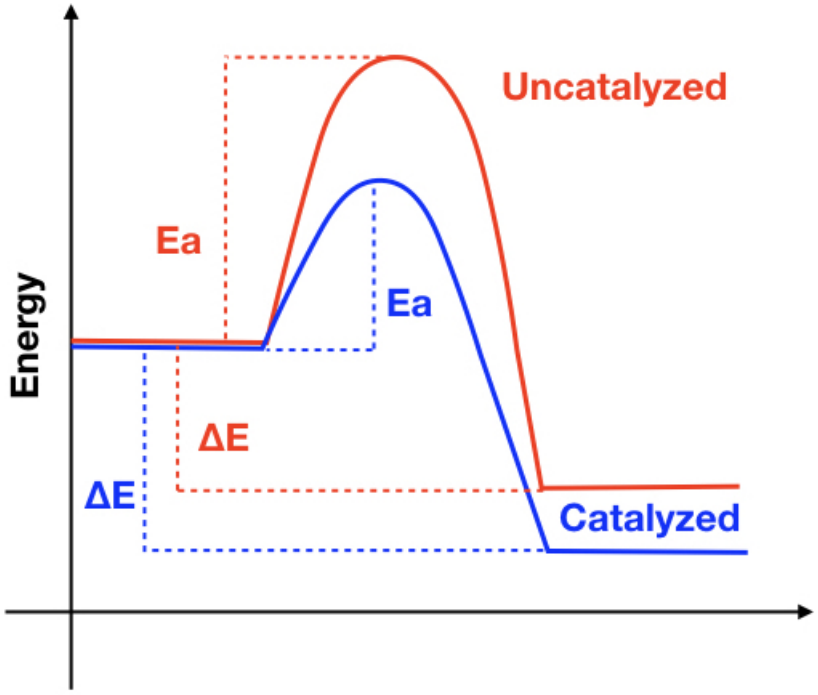

FIGURE 1.2: Energy profile of a chemical reaction in absence (red line) or in presence (blue line) of a catalyst.

catalysts, such as metals, solid acids or basis, zeolites, or metal oxides.

1.1.1 Metal oxides in catalisys

Since the '50s, metal oxides, compounds of oxygen and metals, have become notable because it was found that they were able to catalyze several reactions such as hydrotreating, oxidation, and acid-base reactions [1]. Metal oxides show different structural and electronic properties, and consequently several catalytic properties can be found. On the basis of their general chemical behavior oxides are classified as nonreducible or reducible [5]. In nonreducible oxides the removal of oxygen atoms is difficult, due to the inability of the metal atoms of changing their oxidation state. These oxides usually have a large band gap, and the excess of charge, due to the creation of oxygen vacancies, determines the appearance of new states in the gap, since the cation states are too high in energy to host the electrons. On the other hand, in the reducible oxides, the energy cost of removal an oxygen is significantly lower: the excess of charge, in this case, is acquired by the cation states, which do not lie too much high in energy. This charge transfer determines a variation of the metal oxidation state [5].
In this thesis only reducible oxides have been considered.
In a catalytic reaction metal oxides can be inert supports for catalysts or can be catalysts themselves. These two different situations are schematized in Fig. 1.3. In Fig. 1.3a, the oxide material supports the catalysts, which usually consist in metal nanoparticles, and it does not interact directly with the environment: only the metal particles participate actively during the reaction. In other situations, as shown in Figs. 1.3b and 1.3c, instead, metal oxides play an active role during the reaction,

becoming catalysts themselves. In these cases it is possible to observe, for example, the formation of oxygen vacancies, or the adsorption of different species on the oxide surface caused by the dissociation of molecules. In some cases (see Fig. 1.3c) the oxide material is both a catalyst itself, and also a support for catalytic metal nanoparticles. Both the metal oxide and the nanoparticles participate actively to promote the chemical reactions.

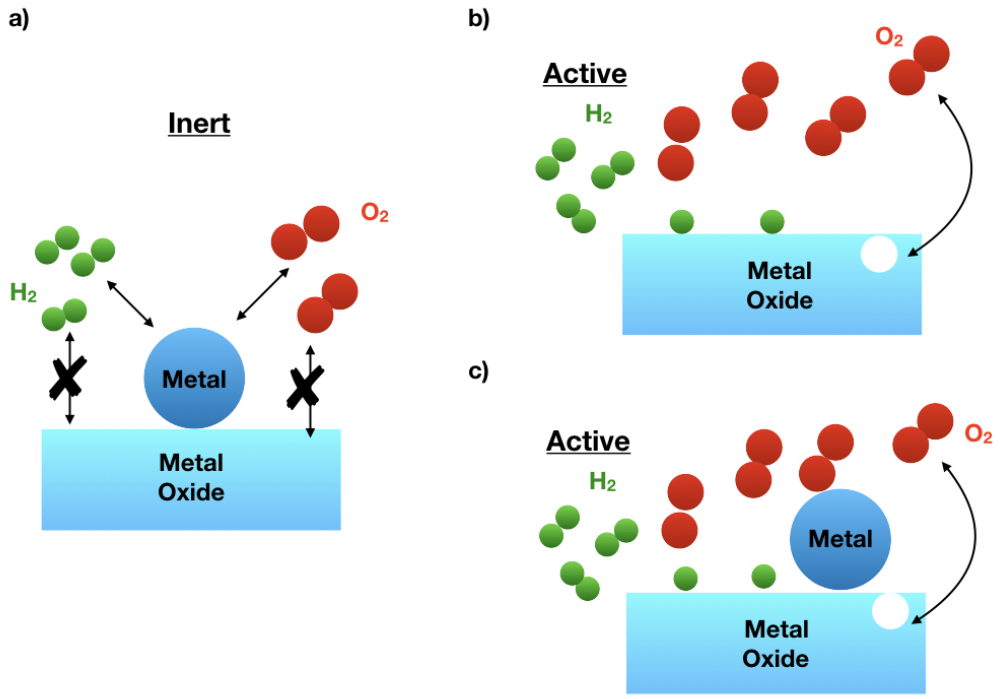

FIGURE 1.3: a) Metal oxide used as a inert support of catalysts; b) metal oxide used as a catalyst; and c) metal used as a catalyst and as a support of metal nanoparticles.

Metal nanoparticles, and in particular noble metal nanoparticles are often adsorbed on the surfaces to increase the rate of reactions as shown in Fig. 1.4 (this situation is indicated as 3D in figure). Metals are, indeed, important catalysts on their own applied to energy production and transformation and process [6]. However, only the metal atoms, which are located on the surface of the nanoparticles, participate in the reaction. Consequently, due to the high cost of noble metals, much research has been devoted to find a way to increase the efficiency of the catalytic system reducing simultaneously the amount of metal. A most promising way to reach this goal is to reduce the dimensions of the nanoparticles to obtain single isolated atoms that need to be anchored to the oxide surface as shown as Monomer in Fig. 1.4. In the single atom catalysis (SAC), the catalytic centers are these single metal atoms. Only recently, the words "Single atom catalysts" have attracted attention [7] as shown in Fig. 1.5, and studies on their possible application to catalysis have flourished. The spread of SAC studies has occurred in parallel to the development of experimental techniques apt to synthesize, and characterize dispersed single atoms on the surface [4].

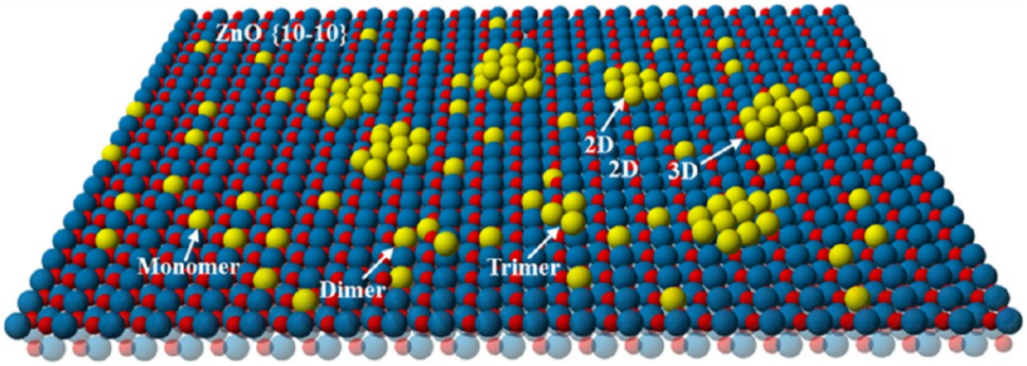

FIGURE 1.4: Single atoms, dimer, trimer, and nanoparticles supported on metal oxide, from Ref. [6].

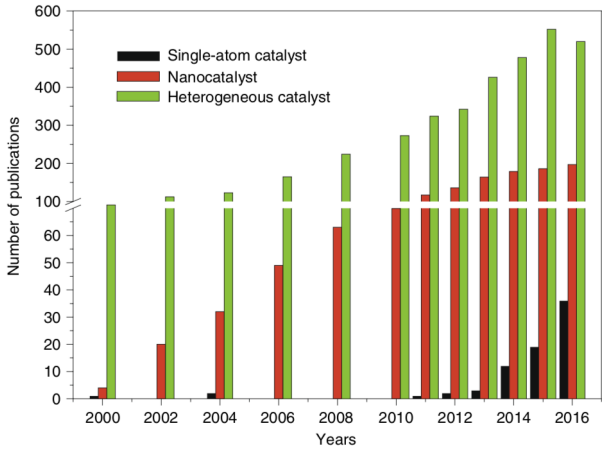

FIGURE 1.5: Number of publications which report the terms single atom catalyst, nanocatalyst, and heterogenous catalysts, from Ref. [7].

1.1.2 Metal atoms dispersed on the surface

One of the first observations related to the catalytic activity of atoms dispersed on a surface was reported by Asakura et al. [8]. They found that the reaction rates of propane combustion on MgO were similar for single platinum cations as for Pt nanoparticles. However, the turning point is the article of Fu et al. [9] concerning the efficiency of non metallic Au and Pt species dispersed on ceria surfaces in the gas-shift reaction ($CO+H_2O \rightleftharpoons CO_2+H_2$). Later, in 2005, Zhang et al. [10] found that Au^{3+} ions on ZrO_2 were able to hydrogenate 1,3-butadiene to butane, and in the 2007 Hackett et al. [11] have observed an high activity of Pd sites on mesoporous Al_2O_3 in the selective aerobic oxidation of allylic alcohols . Only in the 2011 the term *Single Atom Catalyst* was proposed by Qiao et al. [12] to describe the activity of single Pt atoms on FeO_x towards CO oxidation.
Several techniques have been proposed to synthesize single atoms anchored to the surface: physical methods as atomic layer deposition (ALD), which has been used to build model catalysts [6], [7], or chemical methods as the wet chemistry method [7], which is used to synthesize supported heterogenous catalysts and to anchor single atoms. Other approaches proposed in the literature to obtain single atoms are the

pyrolysis method, which is used for single atoms supported on carbon-based materials, the mass-selected soft-landing method, which allows for synthesizing single atoms on any flat supports, and the metal leaching method, which has been used by Fu et al. to produce single Au and Pt cations on ceria [9].
Different reactions can be catalyzed by single atoms. Single atoms show, for example, great performances in CO [13], methane [14], and formaldehyde [15] oxidation reactions. Other important reactions are hydrogenation of nitroarenes [16] and acetylene [17], water-gas-shift reactions [18], and methanol steam reforming [19], [20]. Recently, the application of SAC in electrocatalysis and photocatalysis has become an area of research interest [21], [22].
Cui et al. [7] have highlighted the role of the support since the single atom catalyst doesn't exist without it. The single atom is, indeed, stabilized by the interaction with the surface. Thus, varying the kind of support, the stability, and the catalytic activity of the atoms can be different. Metal oxides are largely used as supports for SAC. The presence of metal and oxygen vacancies, and of hydroxy groups on the surface, helps to stabilize the single atoms. At low level of metal loading the single atoms tend to occupy the positions of the cations of the oxide as shown in Fig. 1.6 [6], where aberration-corrected HAADF-STEM images of Au_1/ZnO, Pt_1/FeO_x, and Pt_1/NiO are reported. It is evident by the schematic pictures in Figs. 1.6c and 1.6d, that the noble metals atoms are in the positions where the oxide metal atoms should be. It is important to note that the presence of defects, as cation vacancies, can modify the sites of the noble metals. They tend to occupy in general the empty sites. When the metal atoms are in substitutional sites, a doped surface is formed, and the presence of the dopant atom modifies strongly the chemical properties of the oxide [5]. The surface oxygen atoms near the dopant are often more reactive due to the modification of the original metal-oxygen bond. For example, the replacement of the oxide cation with a lower valence dopant decreases the energy required to create an oxygen vacancy as found, for example, for Au on TiO_2 [23]. The decrease of the oxygen binding energy affects significantly the catalytic activity of the system. Oxidation and oxidative dehydrogenation reactions are, indeed, a remarkable part of industrial processes [5], and these reactions follow the Mars and van Krevelen mechanism [24]. In this mechanism the oxides, and, in particular, the most reactive oxygen atoms are active players in the catalytic reactions. For example, the reactants can bind to these oxygen atoms to oxygenate themselves, leading to the formation of oxygen vacancies on the surface. Clearly, in order to close the catalytic processes it is necessary to dissociate oxygen molecules present in the atmosphere to refill the vacancies. Thus, the creation of surface oxygen vacancies is an important step of the reaction, and its description is fundamental to understand the reduction/ oxidation processes, and to design better catalytic materials. However, experimentally, the characterization of one vacancy is not easy, although in the last years, steps forward have been done using atomic force microscopy (AFM) and scanning tunneling microscopy (STM).
The density functional theory (DFT) is a useful tool to investigate the reaction mechanisms of heterogenous catalysis from an atomistic point of view, and to study SAC in particular. In this regard is of fundamental support to experimental investigations.
The reduction of the nanoparticles sizes determines a variation of the electronic properties, and a modification of the metal-surface and metal-adsorbates interactions. All these aspects can affect the catalytic activity. Thus, to determine the role of the single metal atom during the catalytic reaction is crucial for assessing the viability of this route to improve efficiency and reduce costs.

In this thesis we have considered cerium and iron oxides which are promising materials as catalysts in the energy processes [25], [26]. These oxides are reducible oxides, a property which could make of them good supports for single metal atoms. Single noble metal atoms on both the oxides have, indeed, been recently synthesized, and observed experimentally. Qiao et al. [27], for example, have realized single Au atoms on ceria, whereas Xie et al. [28] have synthesized single Pt atoms on CeO_2. As shown in Fig. 1.7a for Au, the noble metal atoms tend to occupy the cation vacancies present on the surface. In both cases, the authors have found an high catalytic activity. The presence of other defects, such as surface steps on the (111) ceria surface, increases the stability of the single atoms as found for Pt [29]. However, an high stability of single metal atoms on the surface could affect negatively their catalytic activity, as found by Tran et al. [30] for methanol dissociation since this would affect the catalyst self-healing capability. Thus, an equilibrium between stability and reactivity is necessary to guarantee single metal atoms anchored to the surface, which are also active.
Single Cu, Ag, Au atoms have been synthesized also on magnetite Fe_3O_4 [31], [32], the most stable iron oxide. As shown in Fig. 1.7b for the Ag case, atoms are adsorbed on the surface at the positions of Fe atoms below the outermost layer. Also Qiao et al. [12] have observed that single Pt atoms on hematite (0001) occupy the positions of the Fe atoms, and these atoms exhibit high activity for CO oxidation, and preferential oxidation of CO in hydrogen atmosphere (PROX).
To understand the noble metal-support interactions, the effect of the environment, and the role of the noble metals during the reactions is, indeed, a fundamental task in order to design better catalysts.

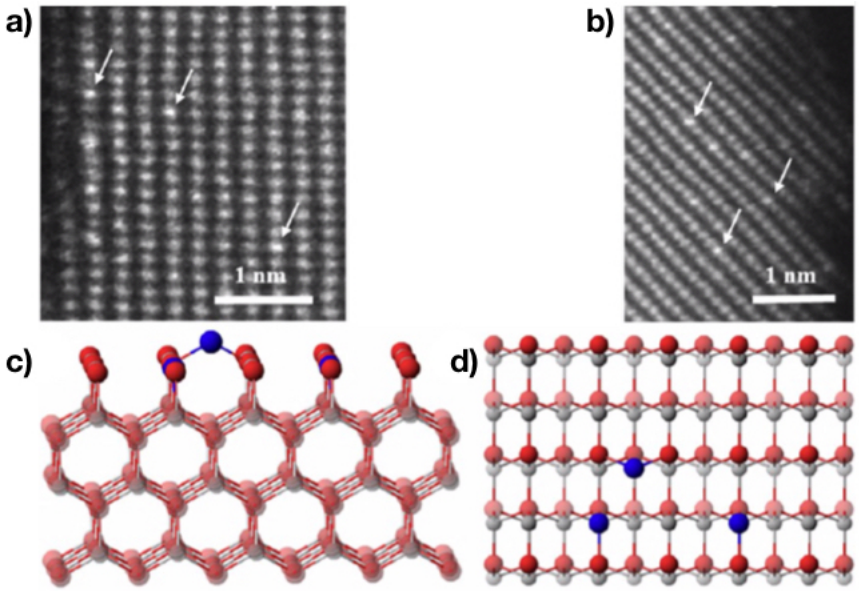

FIGURE 1.6: Aberration-corrected HAADF-STEM of a) Au on ZnO nanowires; b) Pt/NiO nanocrystals. c) Schematic picture of the side and top view of the location of metal (blue ball) on ZnO {10-10} surfaces. Red and gray balls are oxygen and Zn atoms, respectively. Adapted from Ref. [6].

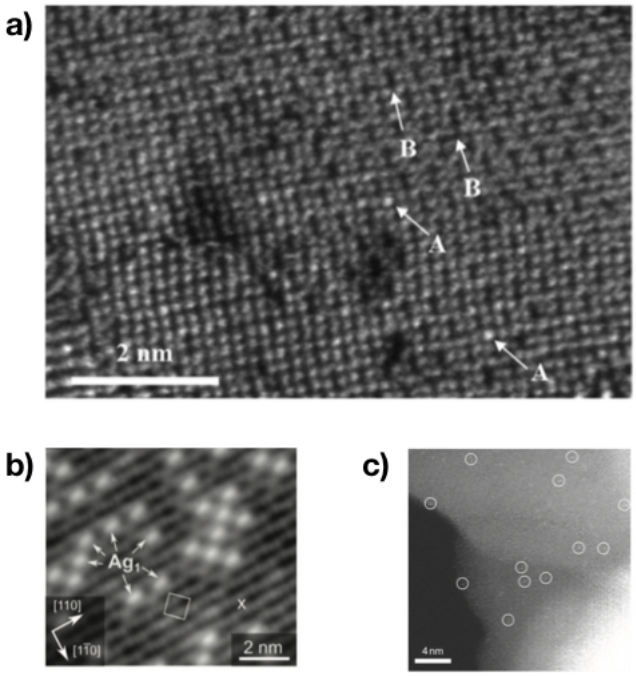

FIGURE 1.7: a) Aberration corrected HAADF-STEM image of Au_1/CeO_2. The label A indicates the Au atoms, whereas B are cluster of Ce vacancies, from Ref. [6]. b) STM image of Ag on magnetite (Fe_3O_4) adapted from Ref. [31]. c) HAADF-STEM image of Pt single atoms (white circles) dispersed on FeO_x, from Ref. [12].

1.2 Goals and outline of the thesis

As mentioned above, catalysis plays a key role in industry, and the identification of new effective catalysts is crucial. This is the main goal of this work. We have tried to understand how the presence of single metal atoms dispersed on the surface, and of surface defects such as cation and anion vacancies, affects the catalytic activity.
In the first part of the thesis, see chapters 3 and 4, we have investigated the role of single noble metal atoms dispersed on cerium oxide surfaces towards two important catalytic reactions: the H_2 oxidation and the CH_4 dissociation. Nowadays, to increase the rates of these two reactions is crucial. The first reaction is indeed the reaction which occurs at the anode of fuel cells, important devices to produce clean energy, whereas the second is the reaction to activate methane, the main component of natural gas. The high cost to activate the CH bond is the main drawback for its utilization, and thus, a very important goal is to find a catalyst capable to lower the activation energy.
The second part of the thesis concerns the study of the (001) maghemite surfaces. Maghemite is one of the less studied iron oxides. The goal of Chapter 5 is to understand the role of the iron vacancies, which characterize maghemite from magnetite, in the surface redox activity. In this thesis, for the first time, the iron vacancies will be described without the use of the mean field approach. In Chapter 6 the interaction between noble metal atoms and the maghemite surface is studied. Moreover, we have investigated how the atoms modify the reduction of the surface, and the adsorption of carbon monoxide. In this thesis we have focused mainly on single Ag atoms, since silver is the less studied among the noble metal atoms.

The thesis is organized as follows: in Chapter 2 the computational methods used in this work are introduced, then in Chapter 3, the role of the different noble metal atoms, Cu, Ag, and Au on CeO_2 (111) on H_2 dissociation is investigated. Also the diffusion of the hydrogen atom, after H_2 dissociation, and water formation on the pristine and Ag doped CeO_2 surfaces has been investigated to interpret experimental findings. In Chapter 4 the dissociation of methane on the pristine and Ag doped CeO_2 surfaces is studied. In this case two different ceria surface orientations, the (100) versus the (111) are compared to determine which would be more effective in CH_4 activation. In Chapter 5 the reduction and oxidation properties of the (001) maghemite surfaces have been investigated, and compared to those calculated for the (001) magnetite surfaces. Different surface terminations have been taken into account. In Chapter 6 the structural and electronic properties of single Cu, Ag, and Au atoms dispersed on the most stable (001) maghemite surface are studied. In Appendix A we report the work performed in order to optimize the parameters for the calculation of this thesis. The calculation parameters, the pseudopotentials, and the value of the Hubbard parameter U have been chosen so as to obtain a correct description of the structural and electronic properties of of CeO_2 and Ce_2O_3. The results obtained have been also compared to the experimental results. In Appendix B the reduced cerium configurations for thin layers of CeO_2 and CeO_{2-x} deposited on Ag (inverse catalysis) have been investigated.

Chapter 2

Theoretical Background

In this chapter we will briefly present the theories on which the calculations of this thesis are based. In Sec. 2.1 the main concepts underlying the density functional theory (DFT) which has been used to determine the equilibrium configurations are presented. In Sec. 2.2 I will discuss the Hubbard correction to the standard density functional theory which has been employed to describe the electronic properties of the oxides. Then, we will present in Sec. 2.3, the nudge elastic method (NEB) used to determine the minimum energy path (MEP) of the reactions. At the end of this chapter, in Sec. 2.4, we will describe the slab method used to describe the surfaces by recovering a 3D spatial periodicity.

2.1 The density functional theory

The density functional theory (DFT) is a ground-state theory by means of which it is possible to determine the quantum states of molecules and solids. In the last years DFT calculations have increased significantly: in the year 2000 the word "*DFT*" appeared in the abstracts or in the titles of scientific papers more than 2000 times. The basis of the theory was proposed in the sixties in order to describe chemical or biological systems and use only a physical quantity, the electron density, as basic variable. It made possible to substitute the electron wavefunction which depends on the $3N$ coordinates of the N electrons with a scalar function of the position. This simplification opened the way to the computation of the ground state of solids with a large number of atoms.

2.1.1 Density Functional Theory

The density functional theory was formulated by Hohenberg and Kohn [33] and Kohn and Sham [34]. In the DFT the main point is the mapping of the interacting electronic systems onto a not interacting one. The Hohenberg-Kohn (HK) theorem is the key point of the theory. It establishes that: i) the external potential v_{ext} is a unique functional of the electron density n, and ii) the energy functional assumes its minimum value for the ground state density of the system. The energy functional of the interacting electron system is:

$$E_v[n] = T_s[n] + \int v_{ext}(\mathbf{r})n(\mathbf{r})d^3\mathbf{r} + \frac{1}{2}\int \frac{n(\mathbf{r})n(\mathbf{r}')}{|\mathbf{r}-\mathbf{r}'|}d^3\mathbf{r}d^3\mathbf{r}' + E_{xc}[n], \qquad (2.1)$$

where $n(\mathbf{r})$ is the charge density of the not interacting electronic system with the same ground state charge density of the interacting one, $T_s[n]$ the kinetic energy functional of the not interacting system, and $v_{ext}(\mathbf{r})n(\mathbf{r})$ is the external potential acting on the electrons.The third term of Eq. 2.1 is the Hartree energy, which is the

Coulomb interaction between electrons, and the latter term is the exchange correlation energy which describes the interactions between the electrons not already considered in the Hartree term.
The ground state density of the interacting system can be obtained solving the one particle equations:

$$\begin{aligned} &\left\{-\nabla^2 + v_{eff}[n]\right\}\varphi_i(\mathbf{r}) = \epsilon_i\varphi_i(\mathbf{r}), \\ &i = 1, 2..., N, \end{aligned} \tag{2.2}$$

where N is the number of particles in the system, and φ_i the solution of the Kohn-Sham equations. The effective potential $v_{eff}[n]$ can be written as:

$$v_{eff}[n] = v_{ext}(\mathbf{r}) + \int \frac{n(\mathbf{r'})}{|\mathbf{r} - \mathbf{r'}|} d^3\mathbf{r'} + \frac{\delta E_{xc}[N]}{\delta n(\mathbf{r})}. \tag{2.3}$$

Solved the Kohn-Sham equations, the electron density n can be calculated as the sum over the occupied one electron orbitals:

$$n(\mathbf{r}) = \sum_{i=1}^{N} |\varphi_i(\mathbf{r})|^2. \tag{2.4}$$

The kinetic energy $T_s[n]$ can be written explicitly as:

$$T_s[n] = \sum_{i=1}^{N} \int \varphi_i^*(\mathbf{r})[-\nabla^2]\varphi_i(\mathbf{r}) d^3\mathbf{r}. \tag{2.5}$$

Since the energy functional $\mathrm{E}_v[n]$ depends on the charge density, to determine the ground state energy an iterative procedure is required. To do this, an initial guess for the charge density is done, for example the superposition of the atomic charge densities, and then the equations are solved. A new set of wavefunctions is obtained, and using the new φ_i, the new charge density is calculated. By mixing the new charge density with the previous one, a new charge density is obtained which will be the input of the new iteration. The iterative procedure will go on until the difference between the input and output charge densities is smaller than a threshold value. Clearly, to solve Eq. 2.2, it is necessary to write explicitly the exchange correlation functional. The first approximation was proposed by Kohn and Sham in the 1965: they wrote the functional as a function of the charge density $n(\mathbf{r})$:

$$E_{xc}[n] = \int \epsilon_{xc}[n(\mathbf{r})] n(\mathbf{r}) d^3\mathbf{r}, \tag{2.6}$$

where ϵ_{xc} is the exchange and correlation energy per electron of an homogenous electron gas. This approximation is known as Local Density Approximation (LDA). Another important approximation is the Generalized Gradient Correction (GGA), where the functional is a function of the local density and of the local gradient of the density. Usually the gradient term is expressed as a multiplicative factor for which different expressions have been proposed:

$$E_{xc}[n] = \int \epsilon_{xc}[n(\mathbf{r})] F_{xc}[n(\mathbf{r}), \nabla n(\mathbf{r})] n(\mathbf{r}) d^3\mathbf{r}. \tag{2.7}$$

In this thesis we have used this second approximation for the exchange and correlation functional, the one proposed by Perdew, Burke, and Ernzerhof [35].

2.1.2 Pseudopotential Theory

To reduce the computational time the use of pseudopotentials has been proposed. The properties of the solids are investigated considering only the valence electrons, which only determine their electronic and chemical properties, without considering explicitly the core electrons, which are localized near the atomic nuclei. Philipps and Kleimann [36] proposed the first theory using the orthogonalized plane-waves method of Herring [36]. They suggested to write the valence-electron states as a smooth pseudo wavefunction which can be expresses as a plane wave φ, which must satisfy the equation:

$$T|\varphi> + V^{ps}|\varphi> = E|\varphi>, \tag{2.8}$$

where V^{ps} is the pseudopotential obtained from the true potential. Different pseudopotentials can be chosen but they have to produce a pseudo-wavefunction, which is the same as the true wavefunction outside the core region. Several pseudopotentials have been proposed, such as norm-conserving, PAW (projected augmented wave), ultrasoft pseudopotentials (US). In this thesis we have used US pseudopotentials [37].

2.1.3 Total Energy in a Crystal

We want to write explicitly the expression of the total ground state energy of a crystal calculated using the DFT. For a crystal we can write the Kohn-Sham equations as:

$$\left\{-\nabla^2 + V_{eff}(\mathbf{r}) - E_n(\mathbf{k})\right\} \varphi_{n,k}(\mathbf{r}) = 0, \tag{2.9}$$

where the effective potential V_{eff} is

$$V_{eff}(\mathbf{r}) = \sum_{R,j} V_j^{ps,ion}(\mathbf{r} - \mathbf{R} - \mathbf{t}^{(j)}, \mathbf{r}' - \mathbf{R} - \mathbf{t}^{(j)}) + \int_\Omega \frac{n(\mathbf{r}')}{|\mathbf{r} - \mathbf{r}'|} d^3\mathbf{r}' + V_{xc}(\mathbf{r}). \tag{2.10}$$

$\mathbf{t}^{(j)}$ are the atomic positions, Ω is the volume of the crystal, $\mathbf{R}$ the lattice vector, and $E_n(\mathbf{k})$ the energy of the state in band n and with crystal wave-vector k. V_{eff} is the sum of three terms: i) the non local pseudopotential $V_j^{ps,ion}$ for each atom j at the position $\mathbf{R} + \mathbf{t}^{(j)}$, ii) the Hartree potential, and iii) the exchange correlation potential. The total energy is:

$$E_{Total}[V_{eff}] = E_{kin} + E_H + E_{xc} + E_{ec} + E_{cc}, \tag{2.11}$$

where E_{kin} is the kinetic energy, E_H the Hartree energy, E_{xc} the exchange and correlation energy, E_{ec} the electron-ion energy, and E_{cc} the ion-ion energy.

2.2 The LDA+U approach

In this work we have investigated the cerium and iron oxides. The cations Ce and Fe which have in their valence strong correlated d and f electrons. The traditional LDA and GGA approximations to the exchange and correlation functional fail to describe the insulator character of these oxides. This is probably due to the over-delocalization of the valence electrons, or to the stabilization of the metallic ground state. Also the not complete cancellation of the self interaction of the electrons in these states may determine a delocalization of the electrons. One of the models

proposed to address this problem is the Hubbard model. We can write the Hubbard Hamiltonian as:

$$H_{Hub} = t \sum_{<i,j>,\sigma} (c^{\dagger}_{i,\sigma} c_{j,\sigma} + h.c.) + U \sum_{i} n_{i,\uparrow} n_{i,\downarrow}, \tag{2.12}$$

where $< i, j >$ are first neighbor atomic sites, $c^{\dagger}_{i,\sigma}$ and $c_{j,\sigma}$ are the electronic creation and annihilation operators for electrons localized on site i with spin σ, and $n_{i,\sigma}$ is the number operator. The factor t is the amplitude of the hopping beteween two neighbors atomic sites, whereas U, the Hubbard term, is the strength of the Coulomb interaction between electrons localized on the same site. The Coulomb interaction is considered by means of a term proportional to the product of the occupation numbers of atomic states for electrons on the same site.
The LDA+U approach is a correction to the DFT to describe the correlated system. The Hubbard correction is, indeed, applied only to the correlated d and f electrons, whereas the other electrons are treated in the traditional way. In this approach the total energy can be written as proposed by Anisimov et al. [38],[39],[40] :

$$E_{LDA+U}[n(\mathbf{r})] = E_{LDA}[n(\mathbf{r})] + E_{Hub}[\left\{n^{I\sigma}_{m}\right\}] - E_{dc}[\left\{n^{I\sigma}\right\}], \tag{2.13}$$

where E_{LDA} is the energy calculated with the energy functional, E_{Hub} is the energy of the electron-electron interaction in the localized states obtained using the Hubbard Hamiltonian, and E_{dc} is the energy of the electron-electron interaction already present in E_{LDA} which has to be subtracted to avoid a double counting. The latter term is evaluated as a mean field approximation to E_{Hub}. $n^{I\sigma}_{m}$ are the atomic orbital occupations of the atom I, where the Hubbard correction is applied. In the last term $n^{I\sigma} = \sum_{m} n^{I\sigma}_{m}$. The Hubbard term H_{Hub} is a functional of the occupation numbers. We can write the energy functional specialized to on-site interactions as:

$$E = E_{LDA} + \sum_{I} [\frac{U^I}{2} \sum_{m,\sigma \neq m',\sigma'} n^{I\sigma}_{m} n^{I\sigma'}_{m'} - \frac{U^I}{2} n^I (n^I - 1)], \tag{2.14}$$

where m is the localized state, I the atomic site, and $n^{I\sigma}_{m} = n^{I\sigma}_{mm}$. The Hubbard and the double counting terms of Eq. 2.13 are the second and third terms of Eq. 2.14, respectively. It is easy to derive the Hubbard potential applied on the Kohn-Sham wave functions:

$$V|\varphi^{\sigma}_{n,k}> = V_{LDA}|\varphi^{\sigma}_{n,k}> + \sum_{I,m} U^I (\frac{1}{2} - n^{I\sigma}_{m}) |\phi^{I}_{m}><\phi^{I}_{m}|\varphi^{\sigma}_{n,k}> . \tag{2.15}$$

It is important to note that if the occupation number $n^{I\sigma}_{m}$ is less than $1/2$, the Hubbard potential is repulsive, whereas it is attractive in the other case. In this way the fractional occupations are less favored. In the calculations, the final output does not depend on the initial configurations since, during the iterations, the occupation changes, and also the sign of the Hubbard potential can change.
However, this formulation is not invariant under rotation of the atomic basis set chosen to determine the occupations $n^{I\sigma}_{m}$. Liechtenstein et al. [41] and Anisimov et al.

[42] proposed a rotationally invariant formulation:

$$E_{Hub}[\{n^I_{mm'}\}] = \frac{1}{2}\sum_{\{m\},\sigma,I}\Big\{< m,m''|V_{ee}|m',m''' > n^{I\sigma}_{mm'}, n^{I-\sigma}_{m''m'''} + (< m,m''|V_{ee}|m',m''' > - < m,m''|V_{ee}|m''',m' >) n^{I\sigma}_{mm'} n^{I\sigma}_{m''m'''}\Big\}, \tag{2.16}$$

where

$$< m,m''|V_{ee}|m',m''' >= \sum_{k=0}^{2l} a_k(m,m',m'',m''')F^k, \tag{2.17}$$

with

$$a_k(m,m',m'',m''') = \frac{4\pi}{2k+1}\sum_{q=-k}^{k} < lm|Y_{kq}|lm' >< lm''|Y^*_{kq}|lm''' >, \tag{2.18}$$

and 0<k<2l. In Eqs. 2.17 and 2.18 l is the angular moment of the d or f electrons, and $n^{I\sigma}_{mm'}$ are the atomic orbital occupations. V_{ee} describes the interaction between electrons located on the same site, and F^k are parameters, which, in the Hartree Fock approximation, are the radial Slater integrals. Usually F^k are expressed in terms of the on site Coulomb interaction, U, and of the exchange interaction, J as:

$$\begin{aligned} U &= \frac{1}{(2l+1)^2}\sum_{m,m'} < m,m'|V_{ee}|m,m' >= F^0, \\ J &= \frac{1}{2l(2l+1)}\sum_{m\neq m'} < m,m'|V_{ee}|m',m >= \frac{F^2+F^4}{14}. \end{aligned} \tag{2.19}$$

m and m' are the atomic orbitals with the same l. For the d electrons only F^0, F^2, and F^4 are required, whereas for the f electrons also the F^6 term is required. The ratio F^4/F^2 and F^6/F^4 are obtained by assuming that they have the same value as isolated atoms.
In this thesis we have used the Hubbard correction as implemented in the Quantum Espresso code by Cococcioni et. al. [43]. The authors focus their attention on the on-site Coulomb interaction, setting to zero the J term which describes the higher multipolar terms. In this way we can write the Hubbard correction energy as:

$$\begin{aligned} E_U[\{n^{I\sigma}_{mm'}\}] &= E_{Hub}[\{n^I_{mm'}\}] - E_{DC}[\{n^I\}] = \frac{U}{2}\sum_l\sum_{m,\sigma}\left\{n^{I\sigma}_{mm} - \sum_{m'} n^{I\sigma}_{mm'} n^{I\sigma}_{m'm}\right\} \\ &= \frac{U}{2}\sum_{I,\sigma} Tr[\mathbf{n}^{I\sigma}(1-\mathbf{n}^{I\sigma})]. \end{aligned} \tag{2.20}$$

If we choose the representation which diagonalizes the occupation matrix ($\mathbf{n}^{I\sigma}\mathbf{v}^{I\sigma}_i = \lambda^{I\sigma}_i\mathbf{v}^{I\sigma}_i$), where $\lambda^{I\sigma}_i = \sum_{k,\nu} f_{k\nu} < \varphi^\sigma_{k\nu}|\phi^I_m >< \phi^I_m|\varphi^\sigma_{k\nu} >$, with 0<$\lambda^{I\sigma}_i$<1 the energy becomes:

$$E_U[\{n_{mm'}\}] = \frac{U}{2}\sum_{I,\sigma}\sum_i \lambda^{I\sigma}_i(1-\lambda^{I\sigma}_i). \tag{2.21}$$

The value of U determines a penalty to apply to the energy favoring the full or empty occupations. It is interesting to note that the occupation matrix $n^{I\sigma}_{mm'}$ is not uniquely

defined. For example, the Mulliken population or the projections on normalized atomic orbitals can be chosen to calculate $n^{I\sigma}_{mm'}$.
Important references for this section are the Camellone's Phd thesis, the Lecture of Camelllone at the "Correlated Electrons: From Models to Materials" school, and Cococcioni and De Gironcoli paper, Physical Review B, 71, 035105, 2005.

2.3 The reaction path

In a chemical reaction the reactants are transformed into the products, which represent another, usually more, stable configuration of the system as shown in Fig. 2.1. The reactants have to overcome a barrier energy, which is named activation energy E_a, to reach the other minimum of energy. The state, corresponding to this maximum of energy, is named transition state, see Fig. 2.1.
The system oscillates around the minima, and the time scale of this process is approximated as $\tau_{vibr} = \sqrt{\frac{m}{V''(q_{min})}}$, where V'' is the curvature of the potential energy surface, q_{min} are the coordinates of the atoms of the system at the minima, and m is the mass of the particles of the system. The time requested to jump from the reactants to the products (τ_{jump}), overcoming the transition state, depends on temperature, and it can be approximated as $\tau_{jump} \sim \tau_{vibr} e^{\frac{E_a}{K_B T}}$, as proposed by Van't-Hoff Arrhenius. Thus, at very low temperature, the rate of the process is very low. The overcome of the activation energy is a rare event. These processes are called *thermally activated processes*. It is important to note that the activation energy is related to the transition state, and its determination is not easy. The Nudge Elastic Method (NEB) is a method to individuate the minimum energy path between an initial (reactants) and final (products) states of a reaction.

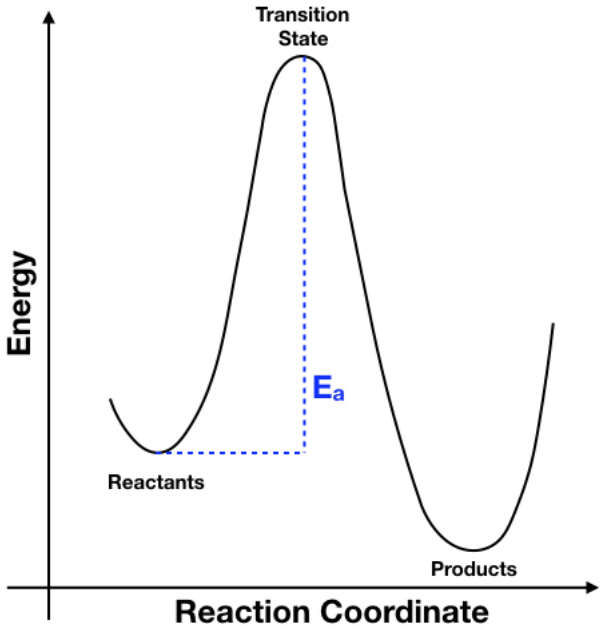

FIGURE 2.1: Schematic picture of the reaction path of a chemical reaction through a transition state.

2.3.1 Nudge Elastic Method

The minimum energy path (MEP) is the reaction path which passes through the saddle (transition) points, and in the limit of the low temperatures, is the most likely one. Along the MEP, the components of the force perpendicular to the path are zero:

$$\nabla V(\mathbf{r}(s)) - \boldsymbol{\tau}(s)(\boldsymbol{\tau}(s) \cdot \nabla V(\mathbf{r}(s))) = 0 \tag{2.22}$$

where $\boldsymbol{\tau}(s)$ is the normalized tangent vector and s is the reaction coordinate by means of which the MEP is parametrized, $s \in [0, 1]$. Solving numerically the equations allows one to determine the MEP, and the transition states. To do this it is necessary to discretize the reaction coordinate and the path:

$$\begin{aligned} & s \rightarrow i \cdot \delta s \\ & \mathbf{r}(s) \rightarrow \mathbf{r}_i \\ & \boldsymbol{\tau}(s) \rightarrow \boldsymbol{\tau_i} = \frac{\mathbf{r}_{i+1} - \mathbf{r}_{i-1}}{|\mathbf{r}_{i+1} - \mathbf{r}_{i-1}|}. \end{aligned} \tag{2.23}$$

We can rewrite Eq. 2.22 as:

$$\nabla V(\mathbf{r}_i) - \boldsymbol{\tau}_i(\boldsymbol{\tau}_i \cdot \nabla V(\mathbf{r}_i) = 0. \tag{2.24}$$

The equations, one for each image, are solved when the energy is minimized on the hyperplane orthogonal to the path.The minimization of the energy can be done iteratively using different algorithms: first, a path with equispaced images $\mathbf{r}_i$ is build, and then each image evolves using a fictitious dynamics obtained by the projected force:

$$F(\mathbf{r}_i)_{perp} = -[\nabla V(\mathbf{r}_i) - \boldsymbol{\tau}_i(\boldsymbol{\tau}_i \cdot \nabla V(\mathbf{r}_i))]. \tag{2.25}$$

Only when for all the images $\mathbf{r}_i$ the perpendicular forces are zero, the path is converged.
The main drawback is that the distance between the images is not conserved. To solve this problem, in the Nudge Elastic Method, each image is connected to the nearest ones by springs of zero rest-lengths [44], [45], [46]. Each image is subjected to the external forces $(\mathbf{F}(\mathbf{r}_i)_{perp})$, which are projected orthogonally to the path, and to the forces of the springs $\mathbf{F}(\mathbf{r}_i)_{elastic}$, which are projected along the path. The sum of the forces is:

$$\mathbf{F}(\mathbf{r}_i) = -(\nabla V(\mathbf{r}_i) - \nabla V(\mathbf{r}_i) \cdot \boldsymbol{\tau}_i) - \boldsymbol{\tau}_i(\boldsymbol{\tau}_i \cdot \nabla \frac{K_i}{2}(\mathbf{r}_{i+1} - \mathbf{r}_i)^2). \tag{2.26}$$

The images that satisfy Eq. 2.24 evolve with an algorithm such as the steepest-descent or the Broyden one. The initial guess is a linear interpolation between the final and initial points (configuartions of reactants and products).

Recently, it has been proposed an improvement of the NEB method, the so-called climbing image (CI-NEB). This method allows for the determination of the saddle point once the minimum energy path has been individuated. The image with the highest energy, after some iterations, is individuated, and the component of the force parallel to the MEP, which acts on it, is inverted:

$$\mathbf{F}(\mathbf{r}_{i_{max}}) = -\nabla V(\mathbf{r}_{i_{max}}) + 2\boldsymbol{\tau}_{i_{max}}(\boldsymbol{\tau}_{i_{max}} \cdot \nabla V(\mathbf{r}_{i_{max}})). \tag{2.27}$$

In this way the image with the highest energy can climb along the minimum energy path.

Two important references for this section are the lectures of Simone Piccinin Rare events and Nudged Elastic Band method, and the Phd thesis of Carlo Sbraccia [47].

2.4 The slab method

In the heterogenous catalysis, as shown in Chapter 1, the reactions occur at the surface of solid catalysts, and the reactivity depends on the structure of the surface. Thus, a correct description of the surfaces in crucial to describe and understand the catalytic reactions. Surfaces break the three dimensional periodicity. However, the computational algorithms, such as the Fast Fourier Transforms (FFT), of the Quantum Espresso Package require a 3D periodicity. In order to reintroduce the 3D periodicity, taking advantage of the periodic boundary conditions, the slab method is used to describe surfaces. In this method 2D portions of materials (slabs) are separated by regions of vacuum along the direction orthogonal to the surface. The width of the vacuum region must be chosen carefully in order to avoid undesired interactions between the surfaces. Moreover, the electron density must be zero in the vacuum region. The slabs can be asymmetric or symmetric. In the asymmetric slabs the atomic positions of the last layers are fixed to their bulk positions, and only the atoms of the top layers are allowed to relax. In many cases to eliminate unphysical electronic states which may appear in the electronic gap it is necessary to passivate one side of the slab [48]. Due to the asymmetry of the slab a dipole can be generated, and consequently an artificial contribution due to the dipole interaction will be present in the total energy. Thus, a dipole correction must be employed: to do this, usually a dipole, opposite to the previous one, in the vacuum region is added. On the other hand, in a symmetric slab only a central plane (a mirror plane) is fixed, whereas all the others are allowed to relax. In this way the dipole disappears but the main drawback is that a greater number of layers is required. In this thesis we have used both these approaches: the asymmetric slabs are used to investigate the ceria surfaces, whereas the maghemite surfaces are described by means of symmetric slabs.

Chapter 3

H_2 Dissociation on ceria

In this chapter we will briefly introduce cerium oxides (Sec 3.1), and then, in Sec. 3.2, we will report a study of the reactivity of single noble metal atoms supported on $CeO_2(111)$ surfaces towards the H_2 molecule. In Sec. 3.3, the effects of the interaction between the hydrogen gas and the pristine and Ag doped CeO_2 surfaces has been investigated to interpret the experimental results obtained at the SESAMO Laboratory of the University of Modena and Reggio-Emilia.

3.1 Cerium Oxide

Cerium is the first of the rare-earth elements, and among them it is the most abundant one on the Earth as shown in Fig. 3.1.

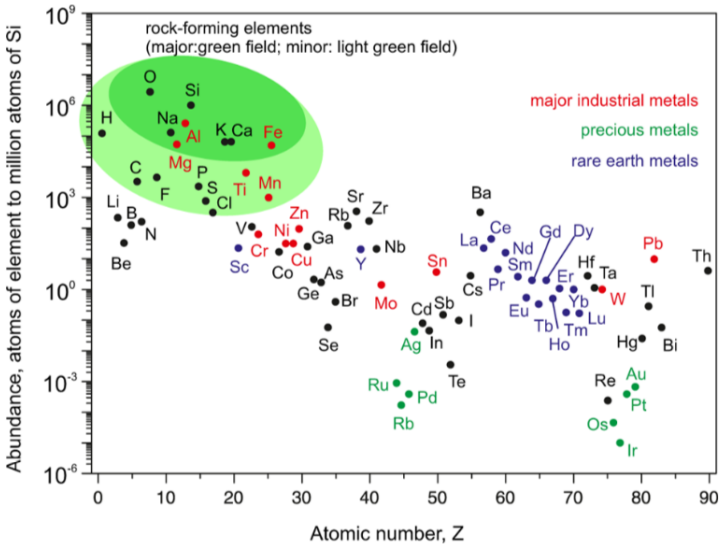

FIGURE 3.1: Abundance of the elements in the Earth's upper continental crust in function of the atomic number [25].

The cerium electronic configuration, $4f^2 5d^0 6s^2$, is characterized by the partial occupation of the f states. In Figs. 3.2a and 3.2b unit cells of the two main stoichiometric cerium-oxygen compounds, cerium dioxide and cerium trioxide, are shown. Cerium dioxide (CeO_2) is the most stable one: it is a white/yellow powder, which crystallizes with a fluorite structure. The CeO_2 unit cell is face-centered with space group $Fm\bar{3}m$, and each Ce atom is bonded to eight oxygen atoms. All the valence electrons belong to the oxygen atoms, the Ce f states are, consequently, empty. The

cerium oxidation state is +4. From an electronic point of view, CeO_2 is an insulator with an energy gap of ~ 3 eV. Cerium trioxide (Ce_2O_3), instead, is an hexagonal sesquoxide A-type, space group $P\bar{3}m1$, see Fig. 3.2b, and all the cerium atoms are in a +3 oxidation state. Thus, the f states of each Ce are occupied by one electron. In this thesis we have investigated only the catalytic activity of cerium dioxide, but the geometrical, magnetic, and electronic properties of both cerium oxides have been studied in Appendix A to determine the value of the Hubbard correction parameter U to apply in these calculations.
CeO_2 is a reducible oxide, and it is characterized by the ability of losing, storing, and transporting oxygen. This is one of the most important properties of cerium oxide, and it is known as *Oxygen Store Capacity* (OSC) [25]. This property is related to the ability of cerium to pass very easily from the 4+ to the 3+ oxidation state, and vice versa.
Since the late 70's CeO_2 has been considered for applications, and in 2015 more than 26000 scientific articles have been published about ceria [25], many of them related to catalysis in the field of energy conversion. However, ceria can be employed also in other fields as medicine and biology. It has been shown, for example, that ceria can be used for making drug delivery devices [49].
We have focused our investigation on catalytic applications of ceria. The three way catalyst (TWC_s) is the most known and successful application of cerium based materials: it facilitates the oxidation of CO and hydrocarbons, and the reduction of NO produced by the combustion of fuel [50]. Catalysts based on ceria are largely used also for water-gas shift reactions [51], [51], [52], [53], CO oxidation reactions, [54], [55], soot combustion for the diesel engines [56], [57], and hydrocarbon reforming
In a catalytic reaction ceria is used as a catalyst or as an active support for other catalysts [25]. It has been shown indeed, that the presence of single noble metals on the surface can increase the reactivity of the system towards some reactions: for example a single Au atom on ceria increases the CO oxidation rate [27], or a single Ni atom favors the water gas shift reaction [58].
Recently, ceria has been proposed as catalyst for electrodes in the fuel cells, electrochemical devices which convert chemical energy into electricity through chemical reactions. Indeed, ceria has been used in solid fuel cells ($SOFC_s$) [59], [60] or in proton exchange membrane fuel cells ($PEMFC_s$) [61], [62]. In the first kind of cells, ceria con be used at the cathodes, or at the anodes and, if doped, also as an electrolyte, whereas, in the PEMFC cerium oxide is usually used only as anode material. The main reaction which occurs at the anode is, indeed, H_2 dissociation and, it is known that ceria facilitates H_2 dissociation [63]. Does the presence of Cu, Ag, or Au atoms increase the reaction rates of H_2 oxidation?
The hydrogen gas is, usually, the fuel of the cells, but its transportation is difficult due to its high flammability. A possible solution is to obtain hydrogen from methanol, which is a stable and safe fuel. Hydrocarbon reforming is indeed one of the main applications for ceria catalytic activity [64], [65], [66]. It is known indeed that CeO_2 favors the C-H bond breaking [67].
Moreover, currently, much research is devoted to find new catalytic systems to increase the rates of reaction of methane (CH_4) activation in order to exploit the new large reserves of natural gas which are recently discovered. Does the presence of Ag atoms doping the ceria surfaces leads to an increase of the C-H bond activation? Can a methane molecule be converted directly into a methanol molecule, in the presence of an Ag atom? In Chapter 4 we have answered these questions.

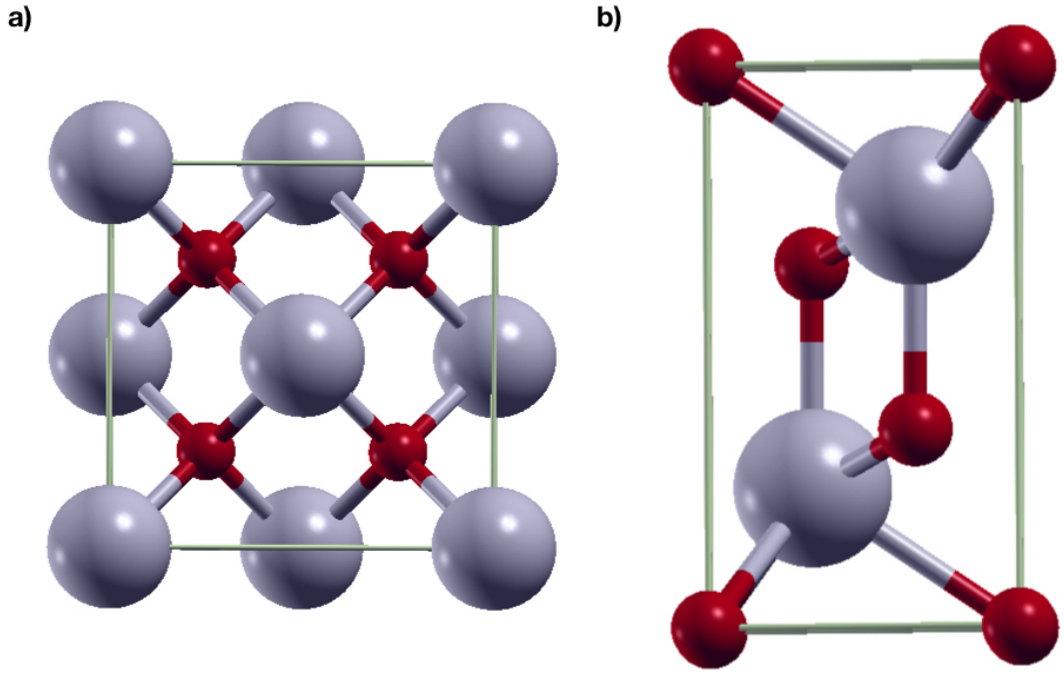

FIGURE 3.2: a) CeO_2, b) Ce_2O_3 bulk unit cell. Gray and balls are the cerium and oxygen atoms, respectively.

3.2 H_2 Dissociation on Noble Metal Single Atom Catalysts Adsorbed on and Doped into CeO_2 (111)

The text of this section is copied by the article "H_2 Dissociation on Noble Metal Single Atom Catalysts Adsorbed on and Doped into CeO_2 (111)", The Journal of Physical Chemistry C, 123, 9875-9883, 2019, G.Righi, R. Magri, and A. Selloni, https://doi.org/10.1021/acs.jpcc.9b00609. Adapted with permission from The Journal of Physical Chemistry C. Copyright 2019 American Chemical Society.

3.2.1 Introduction

Catalysts are essential in many industrial and energy conversion processes. Noble metals have shown excellent catalytic properties for energy production and conversion [6], but their use on the large scale is limited by the high cost. An important goal is thus to reduce the amount of noble metal while maintaining or possibly increasing the performance. It was recently proposed that this goal could be achieved by single noble metal atoms on a supporting surface [68]. In this so-called single atom catalysis (SAC), the main catalytic center is an isolated supported metal atom. SAC has received increasing attention over the last years, and new techniques to prepare and characterize single atom catalysts have been developed, including wet chemistry, mass selected soft landing, and atomic layer deposition1. While such single atom catalysts are expected to exhibit novel properties in comparison to those of nanoparticle catalysts, understanding of their activity is still limited [69]. In this work, we investigate the reactivity of single noble metal atoms focusing on the dissociation and oxidation of H_2 on Ag, Au and Cu atoms supported on CeO_2 (111), the most stable [70], [71], [72], [73] and frequently exposed surface of CeO_2 nanocrystals. As

the reaction occurring at the anodes of proton exchange membrane fuel cells (PEMFCs), the oxidation of H_2 is of both scientific and technological interest. Currently, platinum is the metal of choice for the anode catalyst in PEMFCs but its high cost and scarcity limits its use in industrial applications [74]. Replacing platinum with a cheaper material is crucial for increasing the competitive advantage of fuel cells. A good candidate is cerium oxide, a strongly reducible oxide catalyst [75], [25], [76] that is also known to be a good electrode material for electrochemical devices. [77] and to facilitate the oxidation of H_2, especially in the presence of noble or transition metals [63]. As shown by recent experiments, metal atoms on CeO_2 often occupy Ce substitutional sites at low levels of loading [6], and surface cation (Ce) vacancies have been reported to be essential for stabilizing single atom catalysts . Qiao et al. [27] synthesized single Au atom catalysts supported on CeO_2, and observed that the Au atoms were indeed accommodated in the Ce vacancies. Based on the classification of McFarland et al. [78], Ag, Au, and Cu atoms belong to the class of low valence dopants (LVDs) for CeO_2. The main effect of LVDs is to determine an increase of the oxidative power of the oxygen atoms near the dopant [78]. Consequently, these dopant metal atoms should be good candidates for decreasing the activation energy for H_2 dissociation. Motivated by the above findings and predictions [6], [27], in this work we use first principles calculations to investigate the mechanism of H_2 oxidation on single noble metal atoms either adsorbed on or doped into CeO_2 (111). We mainly focus on single Ag atom catalysts, and compare the adsorption and reactivity of Ag to those of Cu and Au, for which several SAC studies are already available [27], [79]. Three different configurations of the single metal atom (M) catalyst are examined: a) M adsorbed on the pristine CeO_2 (111) surface; b) M substituting a Ce atom in the presence of an excess electron supplied by an adsorbed H atom; c) M substituting a Ce atom in the presence of a nearby oxygen vacancy. These configurations correspond to three different initial oxidation states of the noble metal atom, +1 for case a), +3 for case b), and +2 for case c), which allows us to obtain insight into the influence of the metal oxidation state on the activation of H_2. Oxidation states are here evaluated through established procedures based on analysis of geometries, atomic charges and partial densities of states (see Sec. 3.2.2). Although approximate, this approach is widely used and found to provide meaningful trends for a wide range of systems. While more accurate methods for determining oxidation states are now available [80], [81], they are typically quite demanding and outside the scope of the present investigation.

3.2.2 Computational Methods

Calculations were performed using spin-polarized density functional theory (DFT) with the gradient-corrected Perdew- Burke-Ernezhof (PBE) [35] exchange and correlation functional as implemented in the Quantum Espresso Package [82], [83]. The interaction between electrons and ions was described by ultra-soft pseudopotentials. The wave function and charge density energy cutoffs were set to 30 Ry and 320 Ry, respectively. To account for electron correlations in CeO_2, we applied the Hubbard correction (DFT+U) on the f orbitals of the cerium atoms using the implementation of Cococcioni et al. [43]. The U parameter was set to 4 eV, a value that reproduces experimental and theoretical results of previous studies. CeO_2 crystallizes in the fluorite structure. The bulk primitive cell was optimized using a $7 \times 7 \times 7$ Monkhorst-Pack (MP) mesh grid [84]; the resulting lattice parameter is a=5.52 Å in good agreement with the experimental value a_{exp}= 5.41 Å [85]. The CeO_2 (111) surface was modeled using slabs with three O-Ce-O trilayers and 15 Å of vacuum to

avoid interactions between the repeated images. A (3×3) surface supercell was used, and the irreducible part of the surface Brillouin zone was sampled using a (2×2×1) MP mesh grid [84]. A (4×4) surface supercell was used to study H_2 dissociation on an Ag_2 dimer. Atomic positions were relaxed with convergence thresholds of 10^{-5} eV and 1×10^{-2} eV/Å for the total energy and ionic forces, respectively. Atoms of the last trilayer were kept fixed in their bulk positions. The formation energy of an oxygen vacancy was calculated as:

$$E_{form} = E_{def} + \frac{1}{2}E_{O_2} - E_{pristine}, \tag{3.1}$$

where E_{def} is the energy of the surface with the oxygen vacancy, $E_{pristine}$ is the energy of the slab without the oxygen vacancy, and E_{O_2} is the energy of the O_2 molecule. The adsorption energy of a noble metal atom on the CeO_2 surface was calculated as:

$$E^M_{ads} = E_{M/CeO_2} - E_M - E_{CeO_2}, \tag{3.2}$$

where E_{M/CeO_2} is the energy of the surface with the metal absorbed, E_M is the energy of the metal in the gas phase, and E_{CeO_2} is the energy of the pristine surface.The H_2 adsorption energy was calculated as:

$$E_{ads}(H_2) = E_{H_2/M@CeO_2} - E_{H_2} - E_{M@CeO_2}, \tag{3.3}$$

where $E_{H_2/M@CeO_2}$ is the energy of the slab with the supported metal atom (M) and the H_2 molecule, $E_{M@CeO_2}$ is the energy of the slab with the supported metal atom but without H_2, and E_{H_2}) is the energy of the H_2 molecule. E_{H_2} was determined using a cubic box with a 20 Å edge; the computed bond length is 0.75 Å , in good agreement with the experimental value (0.740 Å) and other DFT calculations (0.743 Å [79]). H_2 dissociation pathways were determined using the climbing image nudged method (CI-NEB) [86] with seven images. Charge transfers along the pathways were estimated by analyzing Bader charges [87] and projected density of states (PDOS).

3.2.3 Results and Discussion

Geometries and Electronic Properties of Single Noble Metal Atom Catalysts on CeO_2(111)

For each single noble metal atom (M), we have studied three different configurations on the CeO_2(111) surface: an adsorbed M (M/CeO_2); M substituting a Ce atom in the presence of an excess electron supplied by an adsorbed H atom (M:H-CeO_2); and M substituting a Ce atom in the presence of a surface oxygen vacancy (M:CeO_{2-x}). Fig. 3.3 and Fig. 3.4 show side and top views, respectively, of the three configurations while Fig. 3.5 reports the corresponding orbital projected density of states (PDOS). For each case, we first discuss the results for Ag and next compare the behavior of Ag to the other noble metals (Cu and Au).

M/CeO_2

Fig. 3.3d shows the structure of an adsorbed Ag atom on CeO_2(111). Ag binds on top of an oxygen atom of the third layer and is coordinated to three surface oxygen atoms, with adsorption energy of -1.31 eV, less than the cohesive energy [88] . The adsorption causes a charge transfer from Ag to the oxide, which results in the formation of a cation Ag^+, and the reduction of one second neighbor cerium atom from

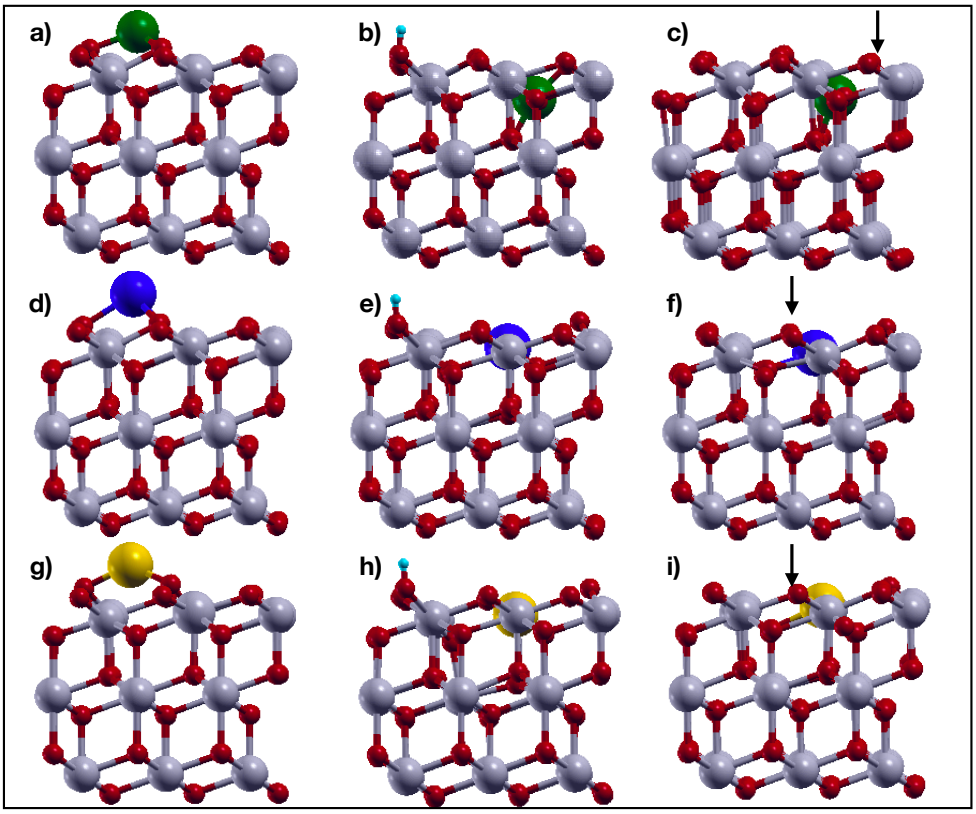

FIGURE 3.3: Models (side views) of a supported noble metal atom M (M = Cu, Ag, Au) on CeO_2(111) investigated in this work: a), d), g) M adsorbed on CeO_2 (M/CeO_2); b), e), h) M substituting a Ce atom in the presence of an adsorbed H (M:H-CeO_2); c), f), i) M substituting a Ce atom in the presence of an Oxygen vacancy (M:CeO_{2-x}). Green (first row), blue (2nd row), and yellow (third row) spheres indicate the Cu, Ag, and Au atoms, respectively. Gray and red balls represent Cerium and Oxygen atoms. Arrows indicate the positions of the Oxygen atoms that were removed. Top views of these models are shown in Figure 3.4.

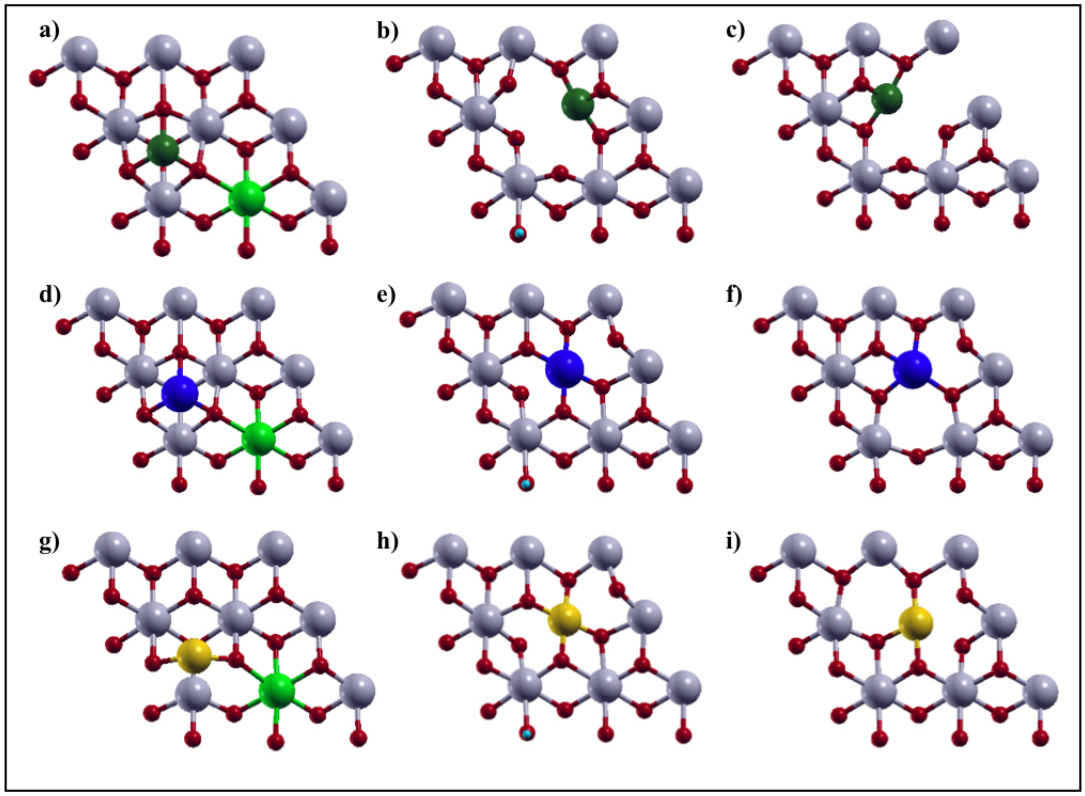

FIGURE 3.4: Top view of the model of a supported noble metal atom M (M = Cu, Ag, Au) on CeO_2(111) investigated in this work: a), d), g) M adsorbed on CeO_2 (M/CeO_2); b), e), h) M substituting a Ce atom in the presence of an adsorbed H (M:H-CeO_2); c), f), i) M substituting a Ce atom in the presence of an oxygen vacancy (M:CeO_{2-x}). Green (first row), blue (2nd row), and yellow (third row) spheres indicate the Cu, Ag, and Au atoms, respectively. Gray and red balls represent cerium and oxygen atoms. Light green balls are the reduced cerium atoms.

Ce^{4+} to Ce^{3+} (see Fig. 3.4), as theoretically found also by Tang et al. [89]. Table 3.1 reports the calculated adsorption energy E_{ads}^{Ag}, the three metal-oxygen bond lengths, the metal - Ce^{3+} bond length, the transferred charge, and the magnetization of the reduced Ce^{3+} ion, resulting from the partial filling of the f orbital. In Fig. 3.5d we show the projected density of states of Ag/CeO_2: the appearance of the Ag s peak above the Fermi energy (E_F) and a new Ce f peak below E_F confirms the charge transfer. The new oxidation state of the Ag adatom is +1, with Ag - O distances slightly larger than the experimental values for Ag_2O [90]. The behaviors of Cu and Au are similar to that of Ag. Cu binds on top of a surface oxygen atom of the third layer (Fig. 3.3d), with a larger adsorption energy (E_{ads}^{Cu}=-2.62 eV) in comparison to Ag, but less than the cohesive energy [88], and Cu - O distances slightly larger than those observed in Cu_2O [91]. In contrast to Ag and Cu, Au prefers to adsorb on a bridge site between two surface oxygen atoms, but the adsorption energy difference between the bridge and on top sites is less than 0.10 eV. The Au adsorption energy is E_{ads}^{Au}=-1.12 eV, and, as for the other noble metal atoms, is less than the cohesive energy [88]. Similar to Ag, Cu and Au are oxidized to $Cu^+$and Au^+ upon adsorption on the CeO_2 surface, and at the same time one Ce atom is reduced to Ce^{3+}. As shown in Fig. 3.5a and

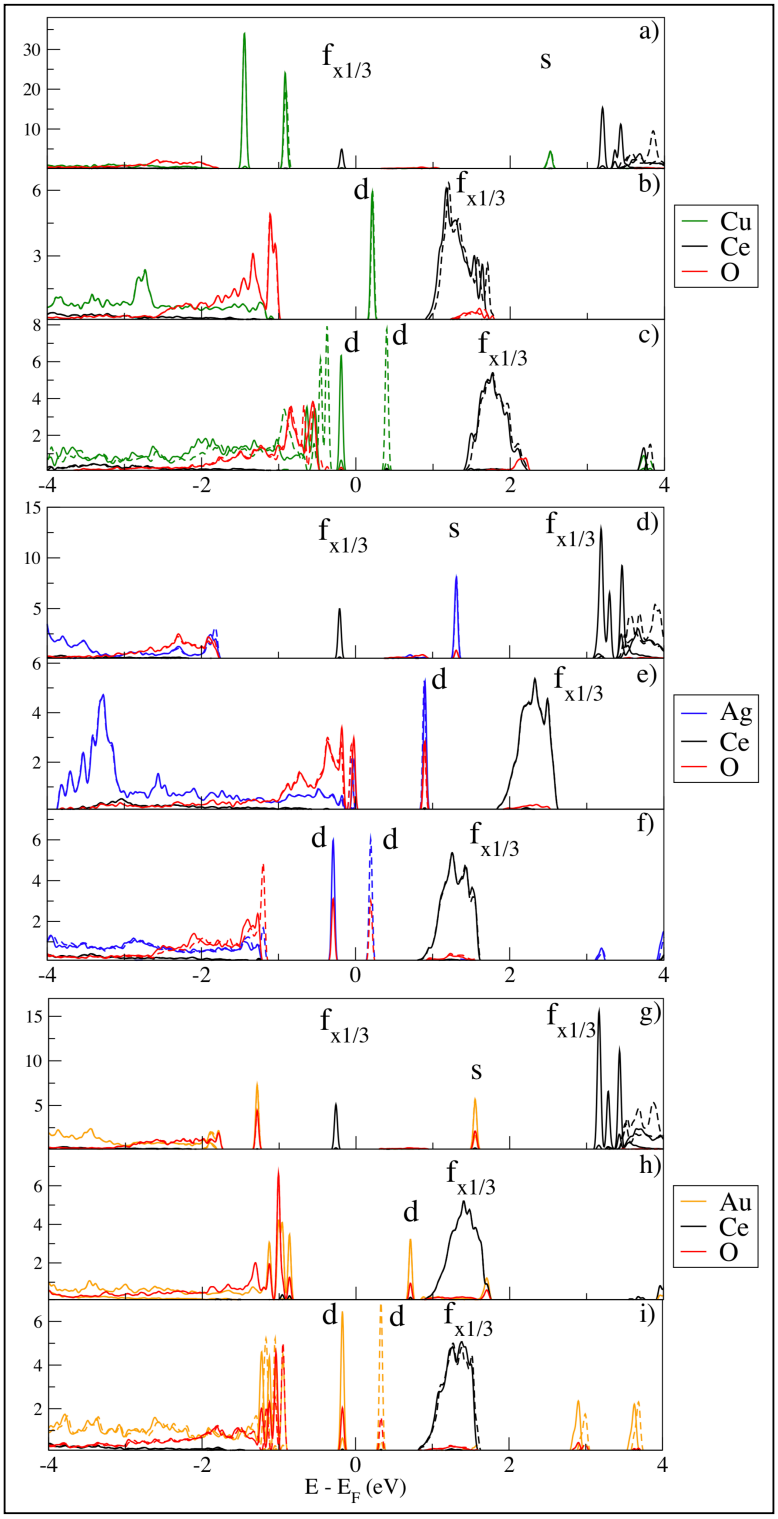

FIGURE 3.5: Projected Density of States of the model systems shown in Fig. 3.3: a) Cu/ CeO_2; b) Cu:H-CeO_2; c) Cu: CeO_{2-x}; d) Ag/ CeO_2; e) Ag:H-CeO_2; f) Ag: CeO_{2-x} ; g) Au/ CeO_2; h) Au:H-CeO_2; i) Au: CeO_{2-x}. Full and dashed lines refer to spin up and spin down contributions, respectively. f states have been multiplied by a factor 1/3.

3.5g, the metal s peak is indeed empty, and a new Ce f peak appears below E_F. The reduced Ce atom is a second neighbor of both Cu [89] and Ag, whereas it is a third neighbor in the case of Au (see Table 3.1), as found in other computational studies [89], [92]. However it is important to note that that the oxidation state of Au depends strongly on the computational method chosen [93].

TABLE 3.1: Adsorption energy of the metal adatom, in eV, magnetic moment of Ce^{3+} (μ_B), M-O distance (Å) between the metal (M) and neighboring O atoms, M- Ce^{3+} distance (Å) between the metal and the Ce^{3+} ion, charge transfer Δq (e) from the metal adatom to the surface.

M	E_{ads}	$\mu(Ce^{3+})$	M-O	M-Ce^{3+}	Δq
Cu	-2.62	0.89	2.02, 2.03(2)	4.82	0.55
Ag	-1.31	0.89	2.35, 2.41(2)	5.06	0.38
Au	-1.12	0.90	2.15,2.18	4.71	0.20

M:H-CeO_2

The second investigated model is the substitution of a Ce by an Ag atom. Cerium has oxidation state +4 in CeO_2, whereas the highest oxidation state that Ag can have is +3. To compensate for the missing charge, we have introduced an adsorbed H atom on a distant surface oxygen (see Figs. 3.3 and 3.4), which provides an additional electron without substantially affecting the interaction of Ag with the H_2 molecule. We found indeed that, in the absence of such a compensating charge, the H_2 molecule tends to react with an oxygen atom of the CeO_2 surface to form an H_2O molecule together with a surface oxygen vacancy, suggesting that the surface needs extra electronic charge to be stabilized. The optimized Ag:H-CeO_2 structure is shown in Fig. 3.3e. This surface termination is stable when the oxygen chemical potential μ_O is greater than -0.5 eV. This means that at room temperature, and p = 1 atm, this surface termination is stable. Increasing the temperature, for example T = 900 K, the surface is stable only if the pressure is greater than 10^5 atm. Ag is approximately at the same height of the Ce surface atoms, and the Ag-O bonds are 2.19 Å , slightly larger than those observed in Ag_2O_3 [94]. The three oxygen atoms bonded to the Ag metal, and the other oxygen atoms below, show a smaller amount of electronic charge (-0.2 e per oxygen atom) than in pure ceria, as found also in a previous computational study for Au [95]. Comparison of the PDOS of Ag:H-CeO_2 (Fig. 3.5e) and Ag/CeO_2 (Fig. 3.5d) shows a new Ag peak above E_F for Ag:H-CeO_2, which originates from empty d metal orbitals with some contributions from the p states of the less charged oxygen atoms. At the same time, the Bader and Löwdin charges show a depletion of both the s and d Ag orbitals with respect to the isolated atom. These findings suggest that the new Ag oxidation state is +3, as previously proposed in a theoretical study by Camellone et al. [92] for substitutional Au. This conclusion is also supported by the Ag - O bond lengths and by the value of the dihedral angle in Ag:H-CeO_2, which is comparable to the dihedral angle in Ag_2O_3 (174.5°). In contrast to the Ag/CeO_2 case, where one reduced Ce^{3+} ion was observed, here all Ce ions have oxidation state +4 (i.e. all f states are empty). The

optimized structures of Cu:H-CeO_2 and Au:H-CeO_2 are shown in Fig. 3.3b and 3.3h, respectively. Similar to Ag, Au does not introduce major distortions of the surface structure: it remains at the same height of the Ce atoms with Au-O bond lengths of 2.12 Å , in the range of the observed Au - O bond lengths in Au_2O_3 [96]. In contrast, the Cu atom moves down toward a subsurface site with Cu - O bond lengths of 1.89 Å , similar to the observed bond distances in Cu_2O [91]. The PDOS of Cu:H-CeO_2 (Fig. 3.5b) and Au:H-CeO_2 (Fig. 3.5h) show metal d states above the Fermi energy, as found for Ag (Fig. 3.5e). The changes of Cu and Au's Bader charges with respect to the adsorbed atoms are also similar to those found for Ag. All results are consistent with an oxidation state +3 in the case of Au. The picture is less clear for Cu, for which a +2 oxidation state was actually suggested in a computational study by Yang et al. [97].

M:CeO_{2-x}

When a surface Ce atom is replaced by Ag, the energy cost to form an oxygen vacancy is found to become negative, -0.69 eV. This implies that O-vacancy formation occurs spontaneously in the presence of substitutional Ag, as computationally predicted by Shapovalov et al. [98]. This is probably due to a charge compensation required when we dope the surface with a lower valence dopant. For comparison, our computed formation energy of a surface oxygen vacancy on metal-free CeO_2(111) surface is 2.05 eV, a value similar to those reported in previous theoretical studies [71], [99]. The configuration generated by removing one of the surface oxygen atoms bonded to the substitutional Ag is shown in Fig. 3.3f. The excess electrons that result from the creation of the vacancy are acquired by the Ag atom. Analysis of the DOS shows indeed that the spin up empty Ag d state of Ag:H-CeO_2 (Fig. 3.5e) becomes occupied in Ag:CeO_{2-x} (Fig. 3.5f), whereas the spin down d state remains empty (dashed lines). This indicates that the Ag oxidation state is +2 in Ag:CeO_{2-x}. A similar behavior was reported in computational studies by Szabova et al. [100] and Yang et al. [97] for Cu. In agreement with Yang et al. [97] and Shapovalov et al. [98], our calculations predict that the creation of an oxygen vacancy is thermodynamically favored also in the presence of a substitutional Cu, even though the energy gain (E_{form}= -0.12 eV) is smaller than in the Ag case. In contrast, the creation of an oxygen vacancy is computed to be slightly endothermic, E_{form}=+0.23 eV, in the presence of substitutional Au. Our result is in agreement with the theoretical value obtained by Kim et al. [101], whereas Shapovalov et al. [98] predicted a negative formation energy (-0.36 eV) also in the Au case. The PDOS of Cu:CeO_{2-x} and Au:CeO_{2-x} (Fig. 3.5c and 3.5i) are similar to that of Ag:CeO_{2-x}, indicating that both excess electrons from the vacancy are acquired by the noble metal. A different result was reported in a theoretical work by Camellone et al. [92], who found that one of the excess electrons of the oxygen vacancy in Au:CeO_{2-x} is acquired by a Ce atom, leading to a reduced Ce^{3+}.

3.2.4 Pathways of H_2 dissociation

Recent computational studies of H_2 dissociation on metal-free CeO_2 (111) have predicted an heterolytic mechanism leading to the formation of two adjacent OH and the reduction of two surface Ce^{4+} cations to Ce^{3+} [63], [102], [103]. Following those studies, we calculated the pathways of H_2 dissociation on all the model systems shown in Fig. 3.3 using the NEB method [45]. In each case, we considered an initial state (IS) where the H_2 molecule is physically adsorbed on the surface and a final

state (denoted FS_{NEB}) where the molecule is dissociated. For the IS, we always examined several possible configurations of H_2 on the relaxed surface and chose the one energetically most stable. Considering that H_2 dissociation is likely to occur at the metal site, for the FS_{NEB} we chose a configuration with one H atom of H_2 bonded to the noble metal atom and the other bonded to a surface oxygen atom, rather than the most stable configuration (denoted FS) with both H atoms adsorbed on surface oxygen atoms. FS_{NEB} was found however to evolve spontaneously to FS in the case M:H-CeO_2. For better clarity, in the following we will report two reaction energies: the first one, ΔE_{NEB}, is the energy difference between the final and initial states of the NEB calculation; the other, ΔE, is the energy of the "true" (most stable) final state with the two H atoms on surface oxygen atoms, referred to the non-interacting gas phase H_2 molecule and M-CeO_2 system.

H_2 dissociation on Ag/CeO_2

The minimum energy pathway (MEP) for H_2 dissociation on Ag/CeO_2(111) is shown in Fig. 3.6. In the IS, the H_2 molecule is weakly adsorbed on the Ag adatom, with a binding energy of 0.27 eV. The H_2 bond length is 0.80 Å (vs 0.75 Å in the gas phase) and the Ag-H distance is 1.91 Å . The PDOS shows no charge transfer from H_2 to the surface (Fig. 3.7a IS). As final state FS_{NEB}, we consider a configuration with one H bonded to Ag (bond length 1.62 Å), the other bonded to a surface oxygen Os (bond length 0.99 Å), and the Ag adatom bonded to only one surface oxygen (bond length 2.15 Å). The H atom adsorbed onto O_s transfers its electron to a surface Ce atom reducing it to Ce^{3+}, while the other H reduces the Ag adatom from Ag^+ to Ag^0, as shown by the PDOS in the bottom panel of Fig. 3.7a, where the Ag s peak is below the Fermi energy. From the MEP in Fig. 3.6, we can also see that in the initial stages of the reaction the Ag atom rotates towards O_s, and breaks one of its O-Ag bonds. At the transition state (TS), the bond length of the H_2 molecule has increased to 0.90 Å , and one H atom forms a hydrogen bond with Os (dashed line in Fig. 3.6), with a O_s - H bond length of 1.64 Å , while the other H remains bonded to the Ag atom. The Ag s orbital remains empty and a Ce^{3+} peak is still present in the PDOS (Fig. 3.7a, TS). This TS is only 0.23 eV higher in energy than the IS. We have also determined the barrier for H transfer from Ag (FS_{NEB}) to a near surface oxygen (FS), and found it to be 1.0 eV. This barrier is quite high in comparison to that for H_2 dissociation, suggesting that FS_{NEB} is an observable intermediate of the reaction. To test the dependence of the activation and reaction energies on the Hubbard U value [104], we have further calculated the MEP of H_2 dissociation on Ag/CeO_2 using a Hubbard U parameter U=4.5 eV, a value employed by several other authors 13 40 41. As shown in Fig. 3.8, the variation of the activation energy is negligible: E_a= 0.22 eV instead of 0.23 eV obtained with U=4 eV.

Similar mechanisms of H_2 dissociation are found on Cu/CeO_2 and Au/CeO_2, see Figs. 3.9, 3.10, 3.11 and 3.12. In the IS, H_2 is adsorbed on the metal atom with adsorption energies of -0.35 and -0.93 eV, for Cu and Au, respectively, and the molecule is more stretched than in the Ag case. On Au/CeO_2, the Au atom shifts from the bridge to the on-top site upon H_2 adsorption; a similar change of metal adsorption site was observed also in a theoretical study of CO oxidation on Au/CeO_2 by Camellone et al. [92]. The existence of a bond between Au and H was assumed also by Jaurez et al. [105] to explain their experimental results on H_2 dissociation on Au/CeO_2. The activation energy (E_a) and reaction energies (ΔE_{NEB} and ΔE) of H_2 dissociation on the three M/CeO_2 surfaces are compared in Table 3.2, which shows also results for metal-free ceria from previous DFT studies. The presence of the noble metal atom on

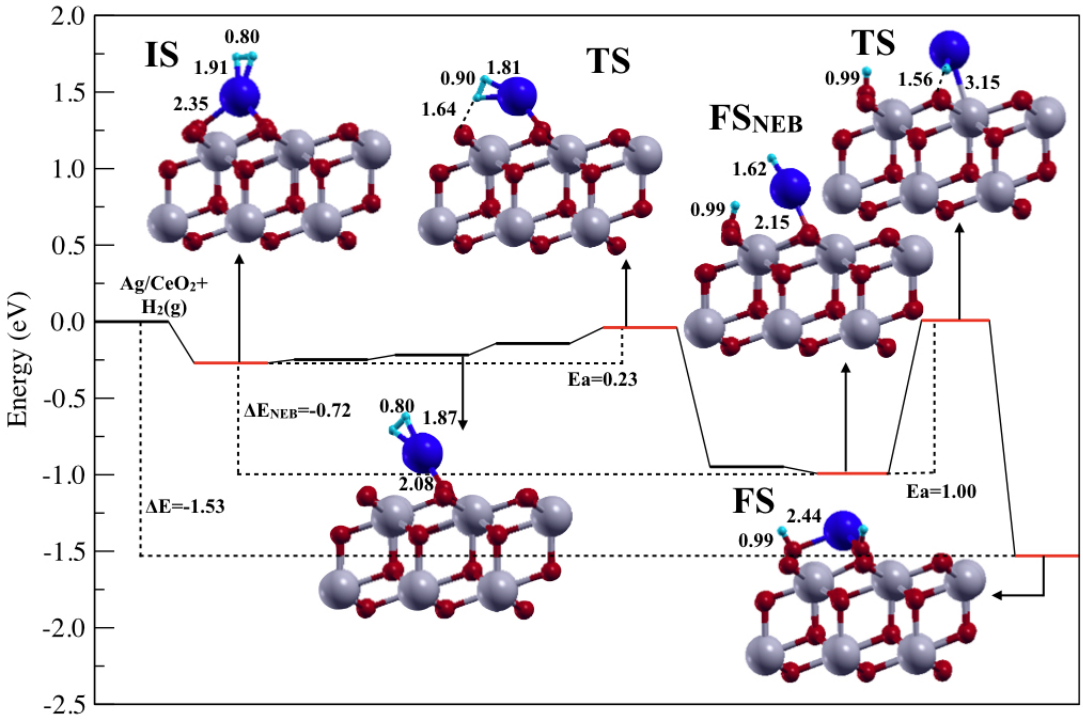

FIGURE 3.6: Potential energy profile along the Minimum Energy Pathway (MEP) of H_2 dissociation on Ag/CeO_2 (111), as obtained by CI-NEB calculations with seven images. Relevant distances are reported. Light blue, blue, gray, and red balls represent the hydrogen, silver, cerium, and oxygen atoms, respectively. All the distances are in Angstrom.

the CeO_2 surface decreases the barrier of H_2 dissociation (from 0.99 eV to 0.30 eV) and at the same time makes the reaction energy less negative, indicating that a single noble metal atom adsorbed on the CeO_2 (111) is an efficient catalyst for H_2 dissociation. The charge transfer from the metal adatom to the CeO_2 surface is crucial in favoring the initial binding of the H_2 molecule to the catalyst. This initial binding facilitates the dissociation with respect to the case of pure ceria where H_2 does not bind to the surface. The smaller absolute value of ΔE on M/CeO_2 relative to pure CeO_2 indicates that the H atoms are less strongly bound to the surface, which should facilitate the subsequent proton release during PEMFC operation.

H_2 dissociation on Ag:H-CeO_2

The MEP for H_2 dissociation on Ag-doped CeO_2 in the presence of an adsorbed H is shown in Fig. 3.13. In the initial state, H_2 is physically adsorbed (E_{ads}= -0.03 eV) with one of its H atoms at distance 2.75 Å from a surface oxygen, and the Ag oxidation state is +3 (Fig. 3.7b IS). As H_2 moves towards the surface, one of the Ag - O bonds with the surface breaks. At the TS, the H_2 molecule (bond length 0.80 Å) is adsorbed on the Ag atom (Ag-H distance 2.15 Å) while forming also a H-bond with a surface O atom (O_s) at distance 1.80 Å . From the PDOS it appears that the Ag oxidation state is still +3 at the TS (Fig. 3.7b TS). After the H-H bond breaks, one

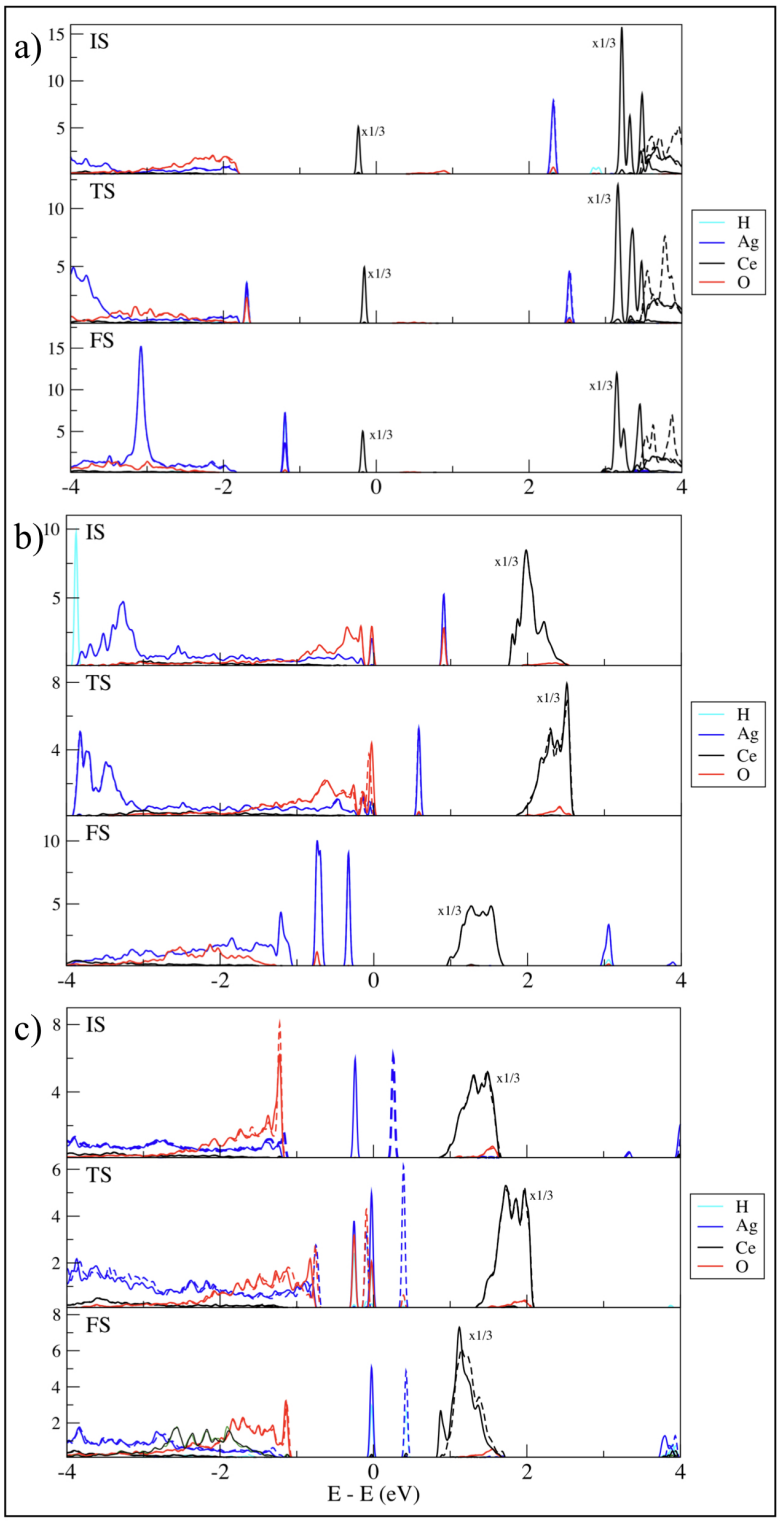

FIGURE 3.7: Projected Density of States for the IS, TS, and FS_{NEB} of H_2 dissociation on: a) Ag/CeO_2; b) Ag:H-CeO_2; c) Ag:CeO_{2-x}. Full and dashed lines represent the spin up and spin down contributions, respectively.

hydrogen atom moves directly to O_s while the other moves spontaneously from Ag to another nearby surface oxygen atom. The activation energy for dissociation, E_a =

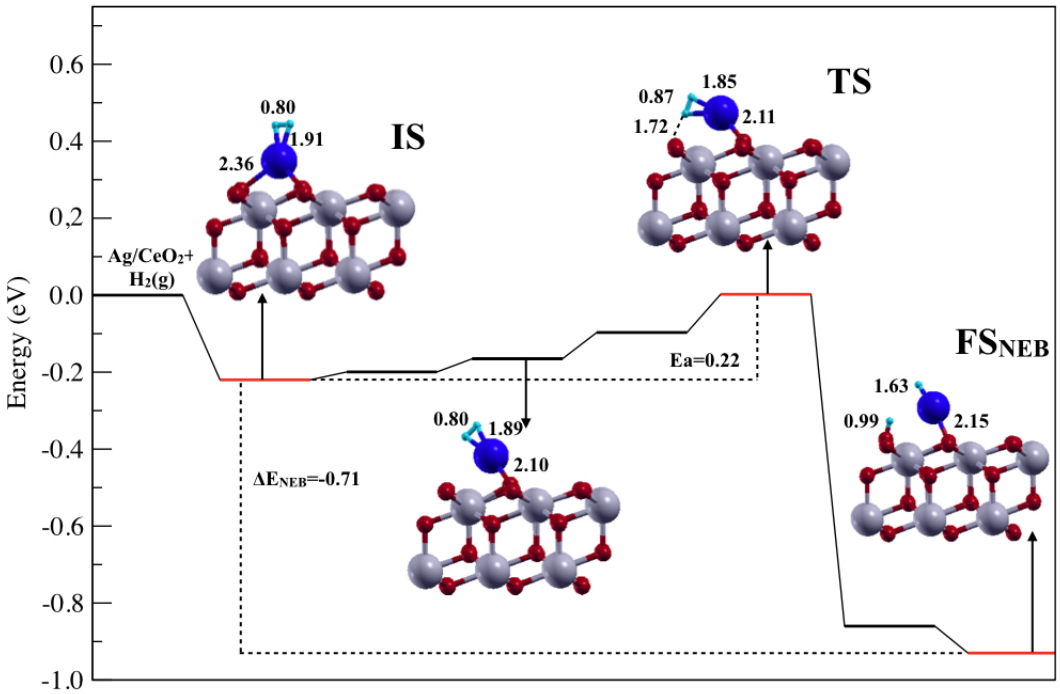

FIGURE 3.8: Potential energy profile along the Minimum Energy Pathway (MEP) of H_2 dissociation on Ag/CeO_2 (111), as obtained by CI-NEB calculations with seven images using U=4.5 eV. Relevant distances are reported. Light blue, blue, gray, and red balls represent the hydrogen, silver, cerium, and oxygen atoms, respectively. All the distances are in Angstrom.

0.33 eV, is significantly lower than in pure CeO_2. In this system the final state FS_{NEB} transforms spontaneously to (i.e. coincides with) FS, H_2 is dissociated with both H atoms adsorbed on surface oxygen atoms and Ag is reduced. As shown by the PDOS in the bottom panel of Fig. 3.7b, the Ag d states are indeed below E_F, while the CeO_2 surface remains oxidized, indicating that the Ag oxidation state is +1.

The analogous pathways on Cu:H-CeO_2 and Au:H-CeO_2 are qualitatively similar to those for Ag:H-CeO_2 (Figs. 3.14 and 3.15), but the charge transfers upon H_2 dissociation are different. In the Au case, the electrons of both H atoms are transferred not to the noble metal but to the surface, leading to the reduction of two Ce cations from Ce^{4+} to Ce^{3+}, while Au maintains an oxidation state +3 (Fig. 3.12b). On Cu:H-CeO_2, Cu is reduced to an oxidation state +2 after H_2 dissociation, as indicated by the PDOS in Fig. 3.11b. In Table 3.3 we compare the activation and reaction energies of H_2 dissociation on Ag, Au and Cu doped CeO_2 (M:H-CeO_2). Both the activation and reaction energies are much lower on the metal doped surfaces than on pristine CeO_2 (111), and the decrease is more significant for Ag than for Au and Cu. Charge transfers appear to have a key role in the reaction: Ag facilitates the dissociation of H_2 by becoming reduced from Ag^{3+} to Ag^{+}, its preferred oxidation state, whereas Au is already in its favorite oxidation state (+3) in the IS, so that its effect on H_2 dissociation is less pronounced. On the other hand, the strong stability of the final state of H_2 dissociation on M:H-CeO_2, especially in the Ag case, implies

TABLE 3.2: Activation energies (E_a) and reaction energies (ΔE_{NEB} and ΔE) for H_2 dissociation on pure CeO_2 (from previous computational studies, as indicated), Cu/CeO_2, Ag/CeO_2, and Au/CeO_2 (from this work). ΔE_{NEB} is the energy difference between the final and initial states of the NEB calculation, whereas ΔE is the energy of the H_2 dissociated state with both H atoms on surface oxygens relative to the non-interacting H_2 molecule and M/CeO_2 surface. All energies in eV. The hydrogen molecule dissociates without or with a very small energy barrier on the platinum (111) surface [106].

	CeO_2	Cu	Ag	Au
E_a	0.99 [63]			
	0.99 [103]	0.29	0.23	0.35
	1.08 [102]			
ΔE_{NEB}	-2.50 [63]			
	-2.34 [103]	-0.55	-0.72	-1.27
	-2.50 [102]			
ΔE	-2.50 [63]			
	-2.34 [103]	-1.99	-1.53	-2.32
	-2.50 [102]			

that it is difficult to break the bonds of the adsorbed H atoms with the surface and regenerate the catalyst as required in PEMFCs.

TABLE 3.3: Activation energies (E_a) and reaction energies (ΔE_{NEB} and ΔE) of H_2 dissociation on noble metal doped CeO_2 in the presence of adsorbed H (M:H-CeO_2) or an oxygen vacancy (M:CeO_{2-x}). ΔE_{NEB} is the energy difference between the final and initial states of the NEB calculation, while ΔE is the energy of the H_2 dissociated state with both H atoms on surface oxygens relative to the non-interacting gas-phase H_2 molecule and doped surface. All energies in eV.

	M:H-CeO_2			M:CeO_{2-x}		
	Cu	Ag	Au	Cu	Ag	Au
E_a	0.51	0.33	0.62	0.80	0.34	0.19
ΔE_{NEB}	-2.36	-4.11	-3.00	-0.55.	-0.72	-1.43
ΔE	-2.37	-4.14	-3.03	-2.13	-2.83	-2.89

H_2 dissociation on Ag:CeO_{2-x}

As discussed in Sec. 3.2.3, the substitution of a Ce atom by a noble metal favors the formation of oxygen vacancies, so that M:CeO_{2-x} is the actual stable configuration of M-doped CeO_2. The pathway and activation energy for H_2 dissociation on Ag:CeO_{2-x} (Fig. 3.16 and Table 3.3) are similar to those on Ag:H-CeO_2 (Fig. 3.13). The initial Ag oxidation state on Ag:CeO_{2-x} is +2 (Fig. 3.7c, IS), and the PDOS changes after H_2 dissociation (Fig. 3.7c, FS_{NEB}) suggest partial transfer of the hydrogen electrons to both Ag and the CeO_2 surface. This is confirmed by the Bader and Löwdin charges, which show an increase of the occupation of the Ag s orbital

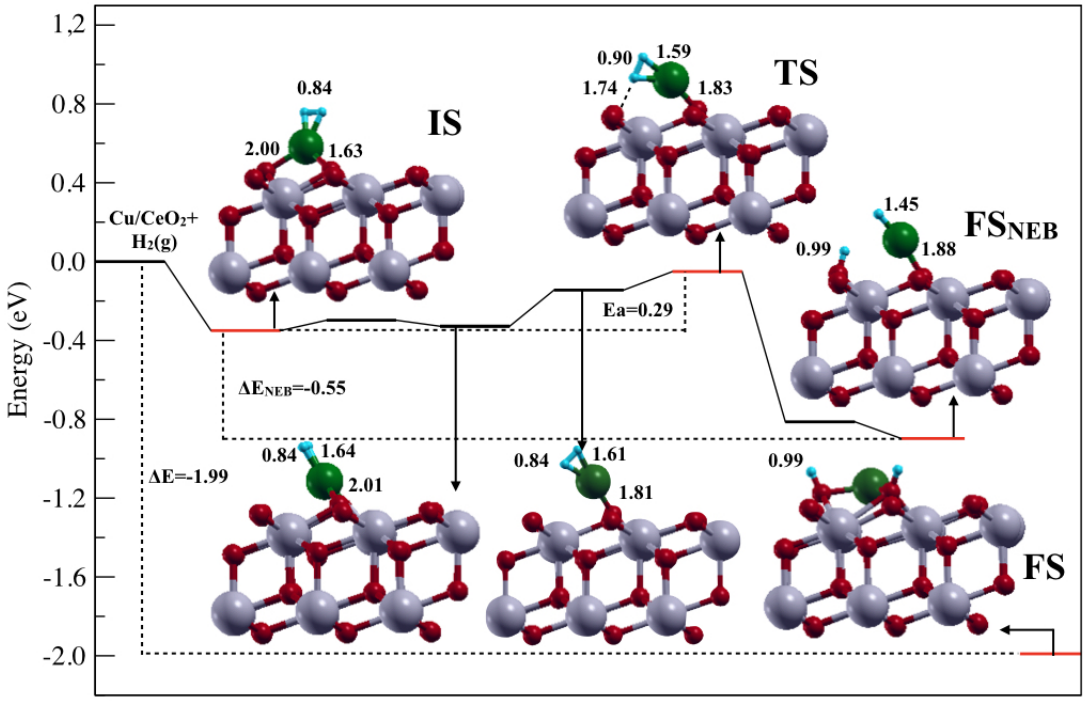

FIGURE 3.9: Potential energy profile along the Minimum Energy Pathway (MEP) of H_2 dissociation on Cu/CeO_2 as obtained by CI-NEB calculations with 7 images. Relevant lengths are reported. Light blue, orange, gray, and red balls are the hydrogen, copper, cerium, and oxygen atoms, respectively. All the distances are in Angstrom.

with respect to the IS. However, a clear Ag oxidation state of +1 is observed only after both H atoms are bonded to surface oxygen atoms. The computed barrier for H diffusion from Ag to a surface oxygen atom is 0.16 eV, a value significantly lower than the activation energy, 0.34 eV, of H_2 dissociation. The activation and reaction energies of H_2 dissociation on $Cu:CeO_{2-x}$ and $Au:CeO_{2-x}$ are summarized in Table 3.3, while pathways and PDOS are reported in Figs. 3.17, 3.18 and 3.11, 3.12, respectively. The barrier is low (0.19 eV) on $Au:CeO_{2-x}$, whereas it is quite high (0.80 eV) on $Cu:CeO_{2-x}$. A possible reason of this difference is that the initial +2 oxidation state is very stable for Cu whereas it is not as favorable for Ag and Au, which prefer to take an oxidation state +1, hence facilitating the dissociation of the H_2 molecule. On the other hand, the smaller H_2 dissociation barrier on $Au:CeO_{2-x}$ in comparison to $Ag:CeO_{2-x}$ may be related to the different TS geometries: on $Au:CeO_{2-x}$ the H_2 bond at the TS is only slightly longer than at equilibrium (0.78 Å), whereas on $Ag:CeO_{2-x}$ the H-H bond at the TS is stretched to 0.91 Å , thus requiring more energy. The low value of E_a predicted by our calculations for $Au:CeO_{2-x}$ appears to disagree with a recent study by Qiao et al. [27] showing that atomically dispersed Au on CeO_2 does not activate H_2 at temperatures below 100 °C. On the other hand, our value E_a = 0.62 eV for H_2 dissociation on H-Au:CeO_2 is both consistent with the experimental observation by Qiao et al. [27] and also agrees with their computed activation barrier of 0.69 eV for H_2 dissociation on atomically dispersed Au atoms at

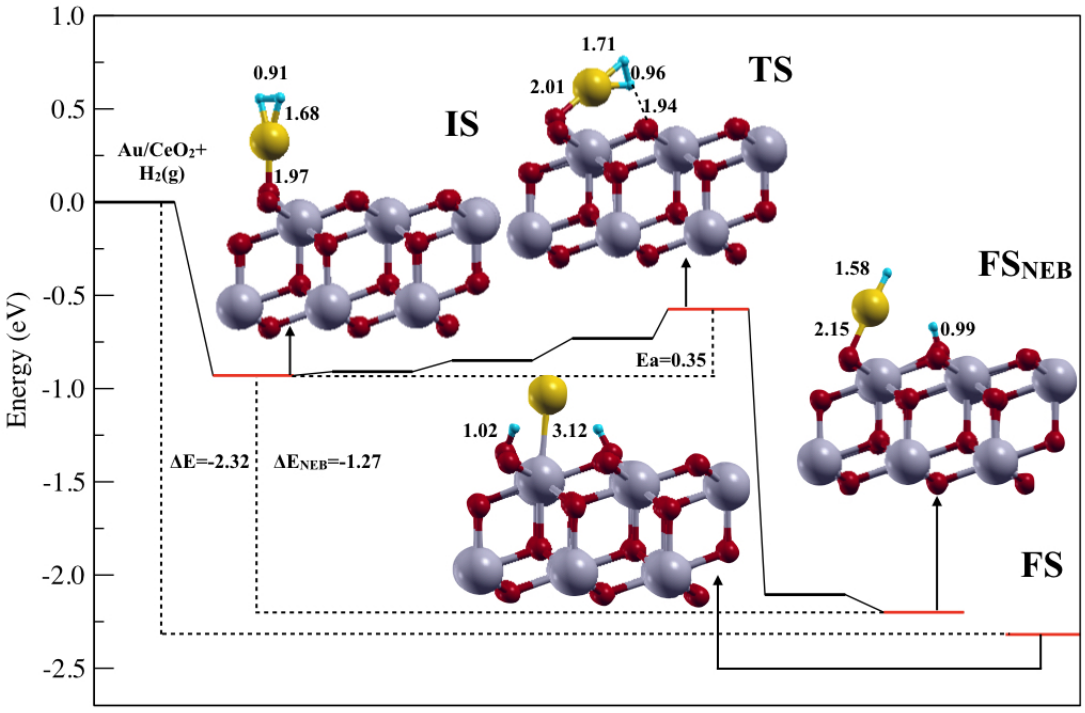

FIGURE 3.10: Potential energy profile along the Minimum Energy Pathway (MEP) of H_2 dissociation on Au/CeO_2 as obtained by CI-NEB calculations with 7 images. Relevant lengths are reported. Yellow, light blue, gray, and red balls are the gold, hydrogen, cerium, and oxygen atoms, respectively. All the distances are in Angstrom.

Ce sites (with no oxygen vacancy). Therefore, a possible explanation for the discrepancy of our results for $Au:CeO_{2-x}$ with experiment14 is the excessive reduction of the $Au:CeO_{2-x}$ model, as suggested also by the positive value of the corresponding O-vacancy formation energy in Sec. 3.2.3. Table 3.3 also shows that the reaction energies ΔE are in absolute value smaller on $M:CeO_{2-x}$ than on $M:H\text{-}CeO_2$, suggesting that the presence of oxygen vacancies improves the activity of noble metal doped CeO_2 as anode material for PEMFCs.

H_2 dissociation on Ag_2

The results in the previous sections show that the presence of a single adsorbed or substitutional noble metal atom on the CeO_2 surface facilitates the dissociation of H_2. However, it is experimentally difficult to synthesize dispersed single atoms on a supporting surface. We have studied the behavior of an Ag adatom on the doped $Ag:CeO_{2-x}$ surface and found that it is indeed energetically favorable for the adatom to bind to the Ag dopant. The resulting Ag-Ag dimer has a bond distance of 2.75 Å , slightly larger than the calculated bond length of an Ag_2 dimer in the gas phase. The computed H_2 dissociation pathway on the supported Ag dimer is shown in Fig. 3.19. Initially the hydrogen molecule is physically adsorbed (IS), whereas in the final state of the NEB calculation one H atom is bonded to a surface oxygen, and the other to the Ag adatom. Along the MEP, H_2 approaches the surface, until it binds to the

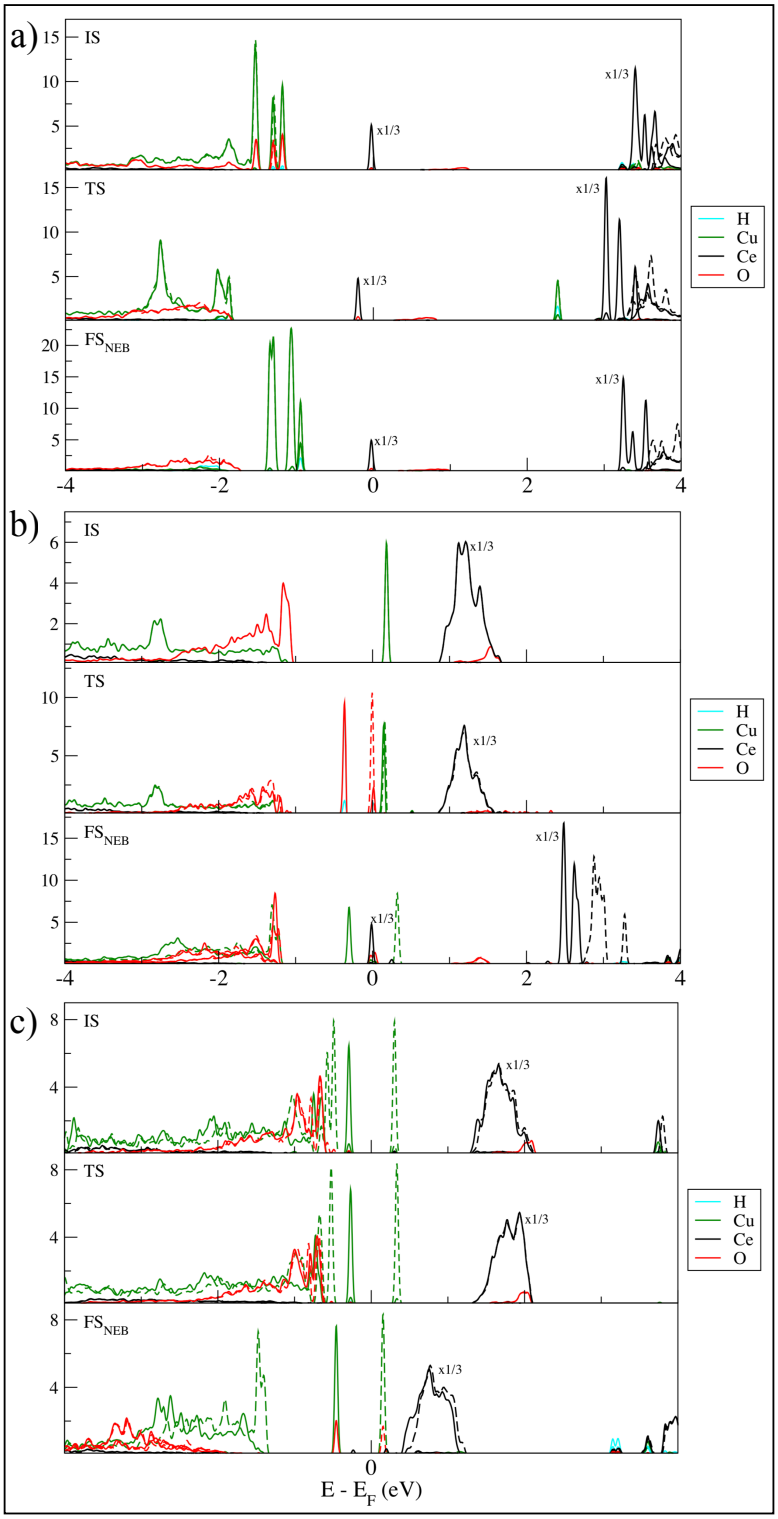

FIGURE 3.11: Pdos of: a) Cu/CeO_2(111) IS, TS, FS_{NEB}; b) Cu:H-CeO_2(111) IS, TS, FS_{NEB}; c) Cu:CeO_2 (111) IS, TS, FS_{NEB}. Continued and dashed lines are the spin up and down contributions, respectively. f states have been multiplied by a factor 1/3.

adsorbed Ag atom (TS) with a H-H bond length of 0.80 Å . Upon dissociation, one H atom moves onto the surface oxygen to which it was H-bonded while the other stays

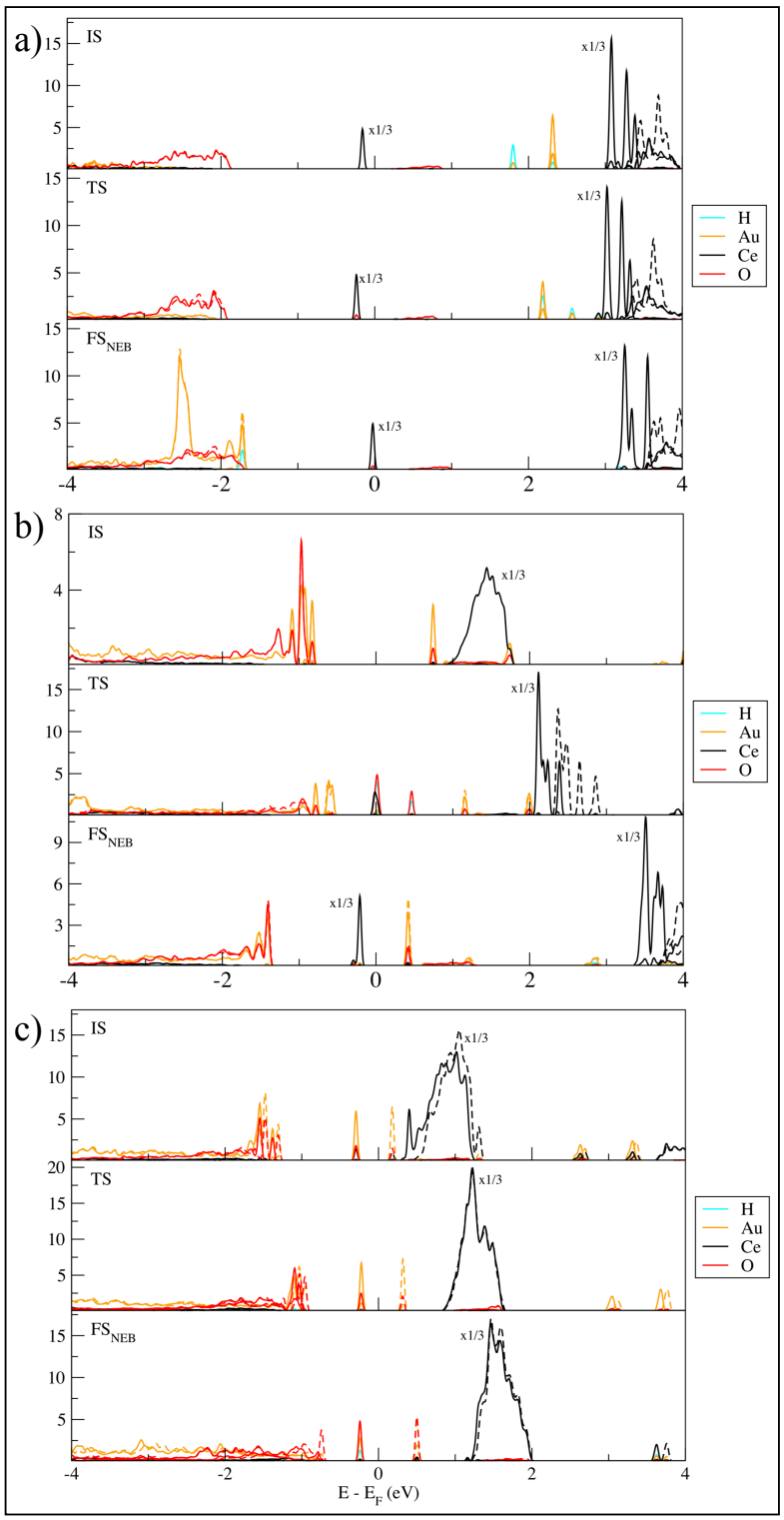

FIGURE 3.12: Pdos of: a) Au/Ce_2(111) IS, TS, FS_{NEB}; b) Au:H-CeO_2(111) IS, TS, FS_{NEB}; c) Au:CeO_2 (111) IS, TS, FS_{NEB}. Continued and dashed lines are the spin up and down contributions, respectively. f states have been multiplied by a factor 1/3.

on the Ag atom. The activation energy of the process, only 0.12 eV, is significantly lower than on pure ceria, as well as on Ag:H-CeO_2 and Ag:CeO_{2-x}. In a previous

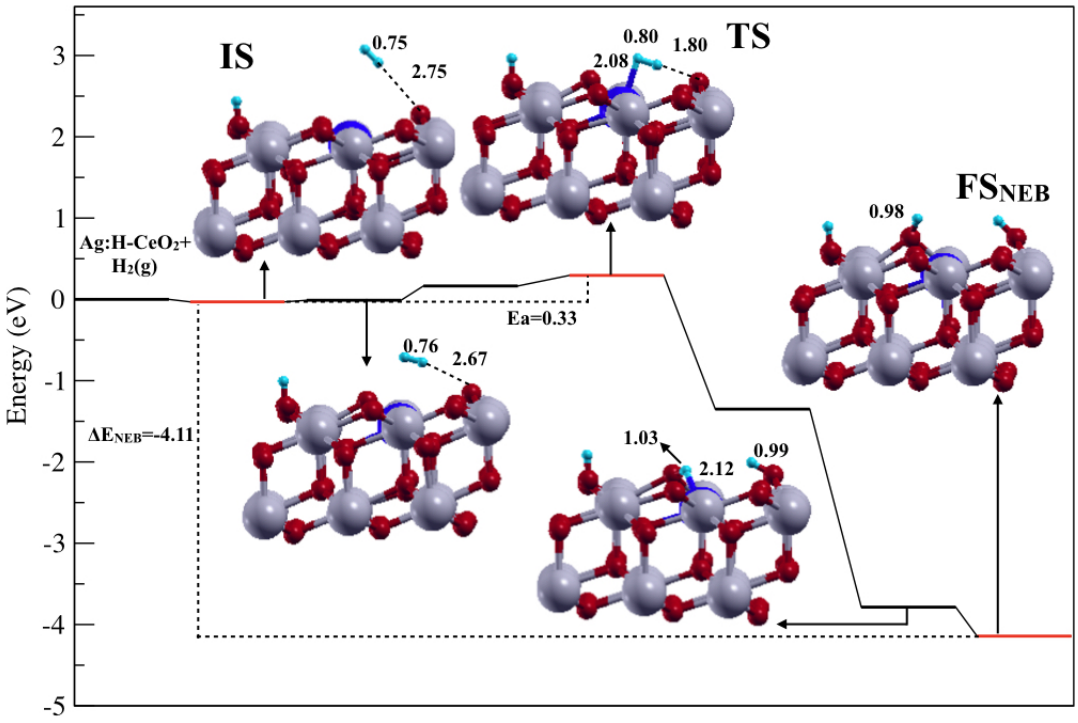

FIGURE 3.13: Potential energy profile along the MEP of H_2 dissociation on Ag:H-CeO_2(111). Relevant distances (in Å) are reported. The color code is the same as in Fig. 3.6.

theoretical work Wang et al. [107] have calculated the energy required to break the hydrogen molecule on the Ag-Ag dimer. The calculated energy is quite high, 2.14 eV, thus the interaction between Ag and CeO_2 is crucial to decrease the barrier energy.

3.2.5 Conclusion

In this work, we have used ab-initio calculations to investigate the mechanism of H_2 dissociation on single Ag, Au and Cu atoms deposited on or doped into CeO_2 (111). An important goal has been to identify an efficient hydrogen oxidation catalyst that might possibly replace Pt as anode material for PEMFCs. We have focused mainly on Ag, whose activity toward H_2 dissociation has been explored for the first time in this work, and considered different surface models, which has allowed us to investigate the effect of different initial oxidation states of the noble metal atom on the activation of H_2. Our results show that noble metal atoms generally induce a significant decrease of the H_2 dissociation barrier with respect to the pure ceria surface, and the charge transfers involved in the reaction play a crucial role in this decrease. For noble metal adatoms on pristine ceria (M/CeO_2), the initial metal oxidation state is +1 and the charge transfers involved in H_2 dissociation are the same for all metals. Ag/CeO_2 shows the lowest activation energy as well as the less negative reaction energy among the different supported metals (see Table 3.2), which makes it a potentially interesting material for PEMFC anodes. In the case where the noble metal is substitutional to a surface Ce atom, the formation of oxygen vacancies

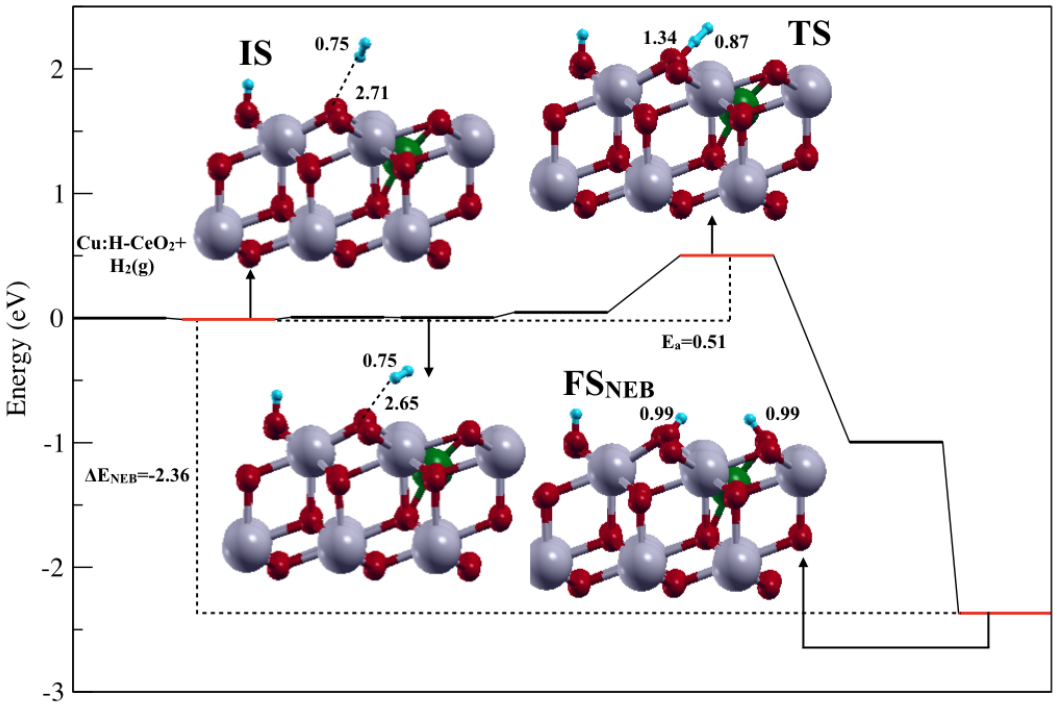

FIGURE 3.14: Potential energy profile along the Minimum Energy Pathway (MEP) of H_2 dissociation on Cu:H- CeO_2(111) as obtained by CI-NEB calculations with seven images. Relevant lengths are reported. All the distances are in angstrom. The color code is the same as in Fig. 3.9.

is highly favored (M:CeO_{2-x}). The initial metal oxidation state is +2, and among the different metals Au has the lowest activation energy, closely followed by Ag, which also shows a slightly less negative reaction energy (Table 3.3). Finally, as an alternative to the formation of an oxygen vacancy, we also considered the case where the missing charge of the substitutional noble metal atom is partially compensated by an adsorbed H (M:H-CeO_2). In this case the initial metal oxidation state is +3 and Ag induces the largest decrease of the activation energy with respect to pure ceria (Table 3.3). Ag plays an active role by acquiring the electrons of the dissociated H_2 molecule, so that its oxidation state changes from +3 to +1, which is the optimal one for Ag. In general, we found that when the noble metal atom is in its favored oxidation state in the initial state of the reaction, the energy barrier lowering with respect to pure ceria is small: this is the case of H_2 dissociation on Au:H-CeO_2 or Cu:CeO_{2-x}. Except for these cases, the noble metal participates actively in the reaction and contributes to the barrier lowering by accepting electrons from H_2 so as to reach its favorite oxidation state. Finally, our results indicate that CeO_2 modified with single Ag atoms is a promising candidate material for replacing Platinum in the anode of PEMFCs.

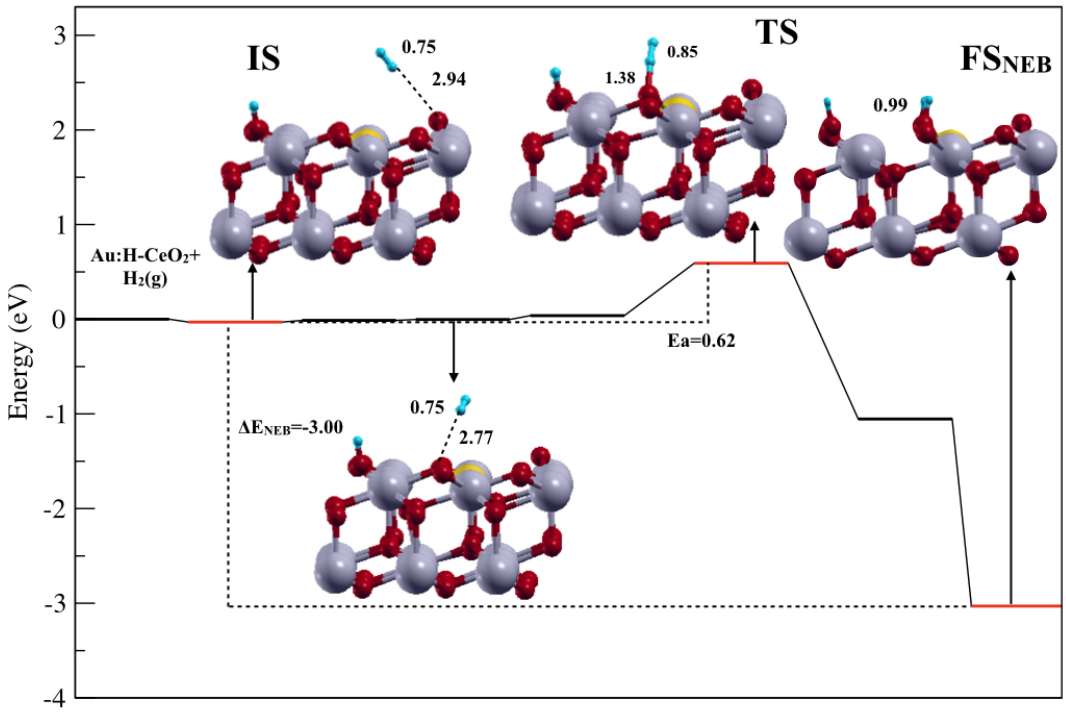

FIGURE 3.15: Potential energy profile along the Minimum Energy Pathway (MEP) of H_2 dissociation on Au:H- CeO_2 (111) as obtained by CI-NEB calculations with seven images. Relevant distances are reported. All the distances are in Angstrom. The color code is the same as in Fig. 3.10.

3.3 Comparison with the experimental results on H_2 exposed surfaces

3.3.1 Introduction

One of the possible methods adopted to experimentally detect H_2 activation on metal doped ceria films is to determine the oxidation states of both the dopant metal cation and of the Ce cations using photoemission spectroscopy [108]. Indeed, the results of several computational studies on H_2 dissociation on pristine ceria surfaces have shown that two hydroxyl groups are formed on the surface, and the simultaneous reduction of two Ce atoms occurs. Also in presence of isolated Pt species adsorbed on ceria, as found by a recent combined experimental and theoretical study, the reduction of Ce^{4+} cations to Ce^{3+} has been observed [108]. The number of Ce^{3+} is used also to quantify the number of oxygen vacancies: the removal of an oxygen atom leads, indeed, to the variation of the Ce oxidation state from 4+ to 3+. The excess of charge is, indeed, acquired by the localized f orbitals. Thus, a higher concentration of Ce^{3+} cations has been considered to be linked to a higher reactivity of the film to H_2 activation, and an higher reduction of the surface.
In the following, we provide new insights into the interaction between H_2 and the pristine and Ag-modified ceria surfaces. In particular, we will discuss the validity of assessing the reactivity of the surface towards H_2 dissociation by monitoring the

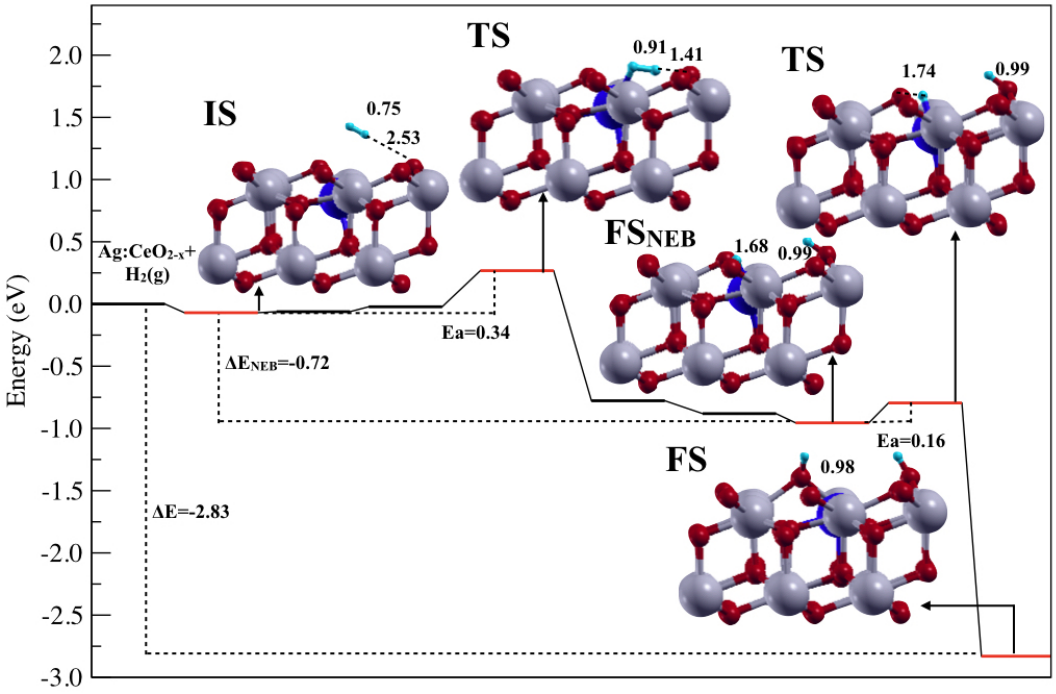

FIGURE 3.16: Potential energy profile along the MEP of H_2 dissociation on Ag:CeO_{2-x} (111), as obtained by CI-NEB calculations with seven images. The color code is the same as in Fig. 3.6. All the distances are in Angstrom

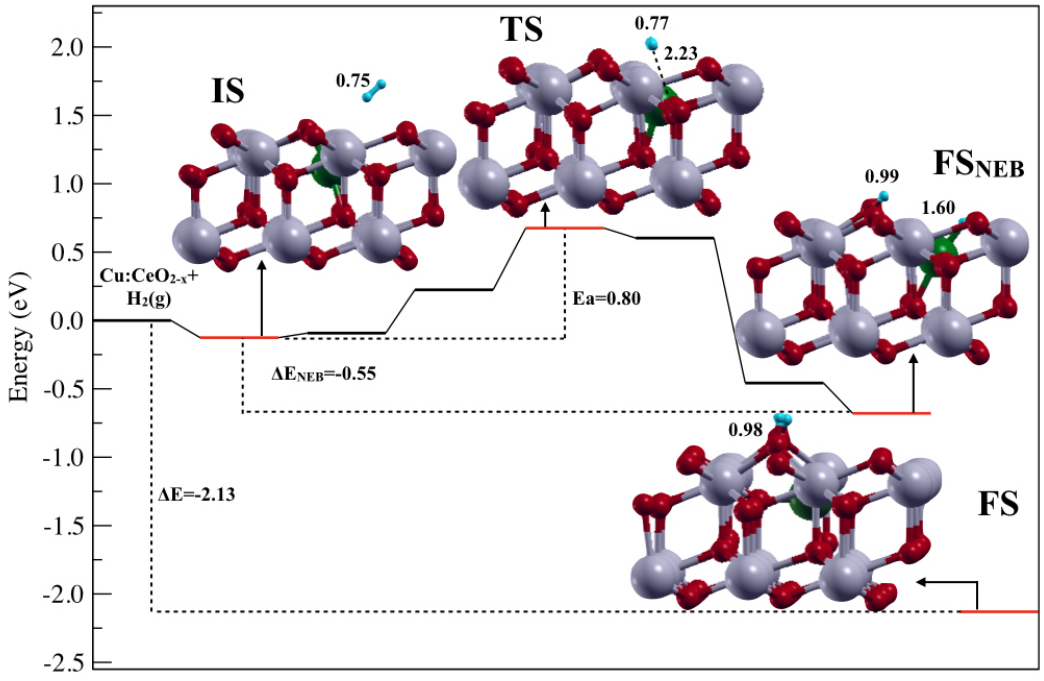

FIGURE 3.17: Potential energy profile along the Minimum Energy Pathway (MEP) of H_2 dissociation on Cu:CeO_{2-x} (111) as obtained by the CI-NEB calculations with seven images. Relevant distances are reported. All the distances are in Angstrom. The color code is the same as in Fig. 3.9.

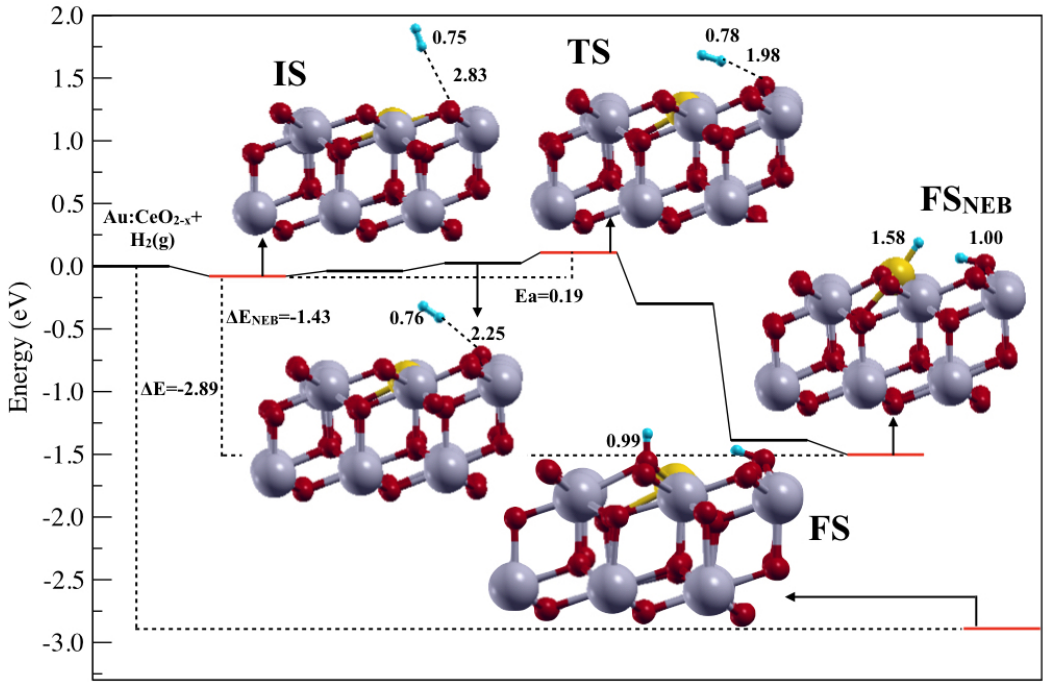

FIGURE 3.18: Potential energy profile along the Minimum Energy Pathway (MEP) of H_2 dissociation on Au:CeO_{2-x} (111), as obtained by CI-NEB calculations with seven images. Relevant distances are reported. All the distances are in Angstrom. The color code is the same as in Fig. 3.10.

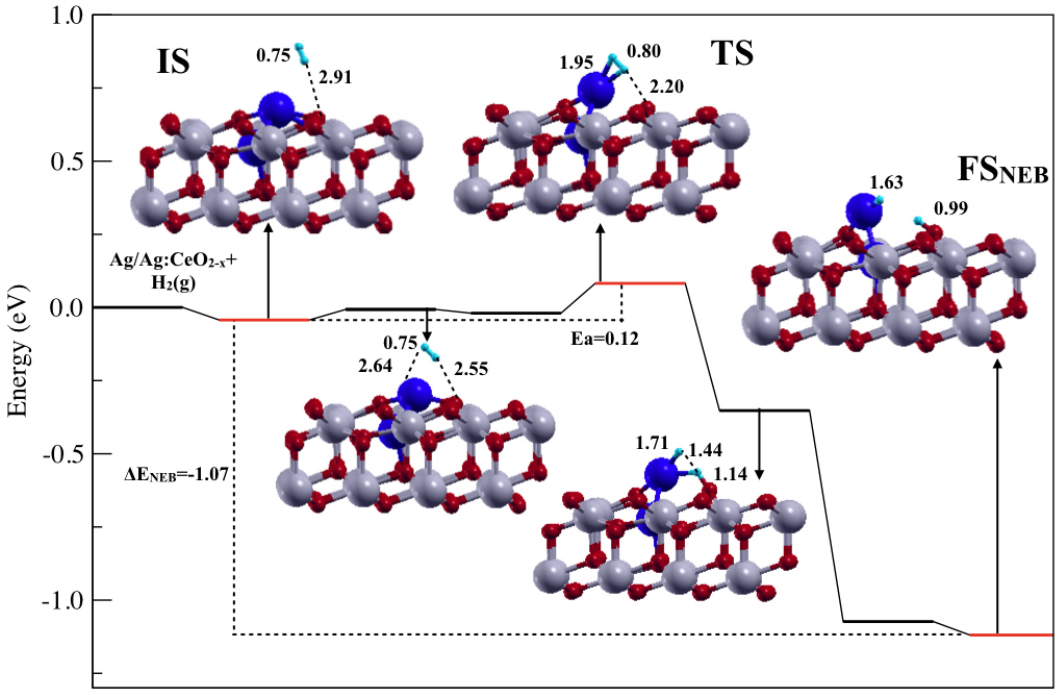

FIGURE 3.19: Potential energy profile along the Minimum energy Pathway (MEP) of H_2 dissociation on Ag on Ag:CeO_{2-x}(111) as obtained by CI-NEB calculations with seven images. The color code is the same as in Fig. 3.6. Reported distances are in Angstrom.

concentration of the Ce^{3+} reduced cations.
Motivated by the observations of the spectroscopy group at the SESAMO Lab. of UNIMORE and CNR-Nano here in Modena we have simulated the behavior of a ceria surface and Ag-modified ceria surface to hydrogen exposure. We have considered a slab formed by three O-Ce-O trilayers, with a (4×4) surface supercell to model the (111) surfaces. In particular, we used for the surface atomic structure the stable configuration with one missing oxygen atom near the Ag ion found in Ref. [109]. The Brillouin zone was sampled only at the Gamma point. We have calculated the adsorption energy of H atoms dissociated on the surface as E_{ads}^{2H}=$E_{2H/surface}$ - $E_{surface}$ -E_{H_2}, where $E_{2H/surface}$ is the energy of the slab with H atoms adsorbed in two separate sites, $E_{surface}$ is the pristine surface, and E_{H_2} is the energy of the hydrogen molecule. To determine the minimum energy paths (MEP) of H_2 dissociation, H diffusion, and H_2O formation on the pristine, and Ag-doped ceria surfaces we used the climbing image nudged method (CI-NEB) [45] with seven images.

3.3.2 Results

Experimental Results

We report here the results obtained at the SESAMO Laboratory (FIM). The modifications in a 4 ML pristine CeO_2 film, and in a film of the same thickness with Ag atoms in substitution of Ce atoms, due to thermal cycles in a reducing environment have been studied using the XPS and STM techniques. The Ce 3d spectra of the pure and doped CeO_2 films after the thermal treatment in UHV and H_2 have been invetsiagted. At room temperature only Ce^{4+} are present. In vacuum conditions the variation of the Ce 3d lineshape is negligible in the pristine film, whereas strong modifications are observed under H_2 as shown in Fig. 3.20a. These variations are due to the contribution of reduced Ce atoms (Ce^{3+}). For the doped surface, as shown in Fig.3.20b, the trend is the same, but an higher reduction under H_2 atmosphere is observed. They found that in UHV, both in the pristine and in the doped CeO_2 films, the concentration of Ce^{3+} is about 5%. As shown in Fig. 3.20c, in H_2 atmosphere, already at 470 K, a significant reduction is observed in the Ag modified oxide, whereas, only at 570 K, an increase of Ce^{3+} is observed in the pristine surface. Only at very high temperatures, larger than 620 K, the number of Ce^{3+} is greater in the pristine film than on the Ag-modified one.
Under H_2, the O 1s peak is modified due to the appearance of a new component due to the OH bond.

In Fig. 3.21a the ratio between the OH and OCe peaks as a function of temperature is shown. On the Ag modified CeO_2 films, the ratio starts to increase already at 470 K. Over the entire range of temperatures the ratio is greater for the doped films, which means that the number of OH groups is always greater on this surface. In Fig. 3.21b the O 1s peak intensity at different temperatures is shown. If we relate the decrease of the peak intensity to the increase of the number of oxygen vacancies O_V, we note that, in general, under H_2 atmosphere, the concentration of the vacancies is greater than in the vacuum. In UHV, at a high temperature ($\sim$ 770 K), for the doped surface, the number of O vacancies is greater than for the pristine surface, whereas in hydrogen atmosphere the number of oxygen vacancies is greater on the pristine ceria surface. A peculiar situation occurs at 470 K, where the O_V concentration in the modified oxide is larger in UHV than in H_2.
Using an ab-initio approach we have tried to interpret these experimental findings.

It is indeed surprising that the number of oxygen vacancies is greater on the pristine oxide under H_2 than on the doped one. We have started to compare the results in vacuum, and then we have considered the H_2 atmosphere.

Computational Results

We have calculated the energy required to create an oxygen vacancy (O_V) on the pristine and Ag-modified CeO_2(111) surface (Ag:CeO_{2-x}). On the pristine ceria surface (Figs. 3.22a and 3.22b) the O_V formation energy is E_{form}= 2.02 eV, a value similar to those reported in previous theoretical works [99], [71]. Following the creation of the oxygen vacancy we observe the reduction of two Ce atoms on second neighbor sites of the O_V. In Figs. 3.22c and 3.22d the side and top views of the most stable Ag-modified CeO_2 surface are shown. This surface is characterized by the contemporary presence of a single Ag atom and an oxygen vacancy located in the outermost layer. The two oxygen atoms closer to Ag have less electronic charge than the one corresponding to the canonical -2 oxidation state, and it is known that they are more reactive [78], [5]. The energy required to remove these oxygen atoms is only 0.78 eV. The excess of charge due to the creation of the vacancy, in this configuration, is acquired by Ag and by a single Ce, which is reduced to Ce^{3+}. Ag loses $\sim$ -0.5 e with respect to the charge in the gas phase, and we can speculate that the new oxidation state is +1.
It is important to note that the O_V formation energy is only the energy cost necessary to create the surface vacancy, and not the energy barriers, which the oxygen atoms have to overcome to break their bonds to the surface and be released. However, we can see that the calculated O_V formation energies alone can qualitatively explain most of the experimental observations in UHV. After thermal treatment, indeed, the number of oxygen vacancies is greater on the Ag doped CeO_2 oxide, and we have found that the energy required to remove a surface oxygen is smaller on this surface. Moreover, as found experimentally, the number of Ce^{3+} is greater on the pristine ceria since, on this surface, the formation of the oxygen vacancy causes the reduction of two Ce atoms, whereas on the Ag-modified surface, the creation of an oxygen vacancy leads to the reduction of only one Ce atom. Thus, despite the larger reactivity of the modified Ag-ceria surface the number of reduced cerium atom is smaller.

We pass now to investigate the reduction of the surfaces in H_2 atmosphere. A reaction frequently observed on reducible metal oxides under conditions of high H_2 pressure and temperature is:

$$H_2 + O_s \rightarrow H_2O + V_O, \tag{3.4}$$

where O_s and V_O are a surface oxygen atom and surface oxygen vacancy, respectively. Temperature programmed reduction measurements acquired by several groups on cerium oxide powdered catalysts indicate, indeed, that the dissociated H can be released from the surface in the form of H_2 O forming O vacancies on the surface around 770 K, whereas 1100 K are required to create bulk vacancies [110], [111]. We have investigated the pathway of this reaction on pristine and Ag doped CeO_2 surface assuming that in the initial state (IS) H_2 is already adsorbed in dissociated form on the CeO_2 surfaces (Figs. 3.23 and 3.24). As shown by recent computational studies, and reported in Fig. 3.23 (3.24) H_2 dissociation has an energy barrier E_a = 0.99 [63] (0.34) eV, and an energy release ΔE $\sim$ 2.5 [63] (2.83) eV on pristine CeO_2 [63], [102], [112] (Ag-doped CeO_2) [109]. The dashed rectangles, in the figures, indicate that intermediate states are present in this part of reaction. The adsorption of H_2

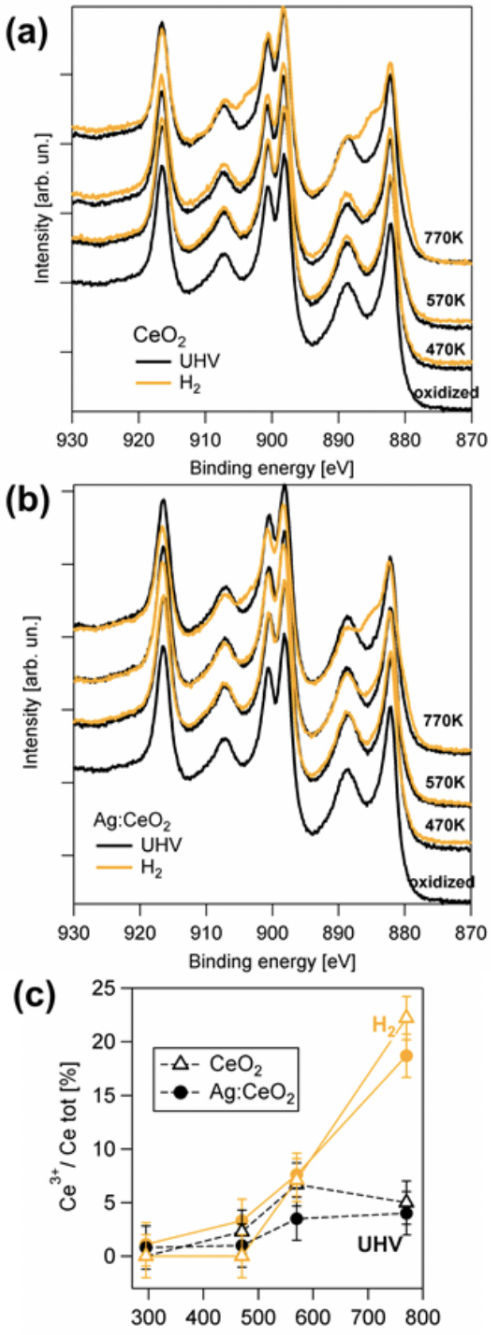

FIGURE 3.20: Ce 3d spectra for 4ML a) pristine CeO_2 b) Ag modified CeO_s films reduced at increasing temperature in vacuum (black) and in H_2 (orange). c) Concentration of Ce^{3+} as a function of the temperature for different films in vacuum and in H_2 as obtained from the Ce 3d fit.

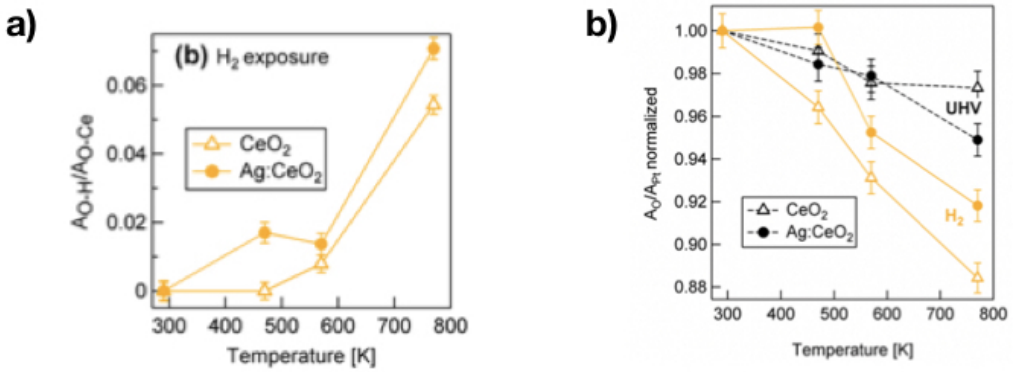

FIGURE 3.21: a) Ratio between HO and OCe peaks after H_2 exposure (as obtained by the fit) as a function of temperature, b) O1s/Pt4p3/2 peak intensity ratio as a function of temperature for pure and Ag modified CeO_2 films in vacuum and in H_2. The ratios have been normalized to the first point for comparison (to eliminate effects due to small differences in thickness).

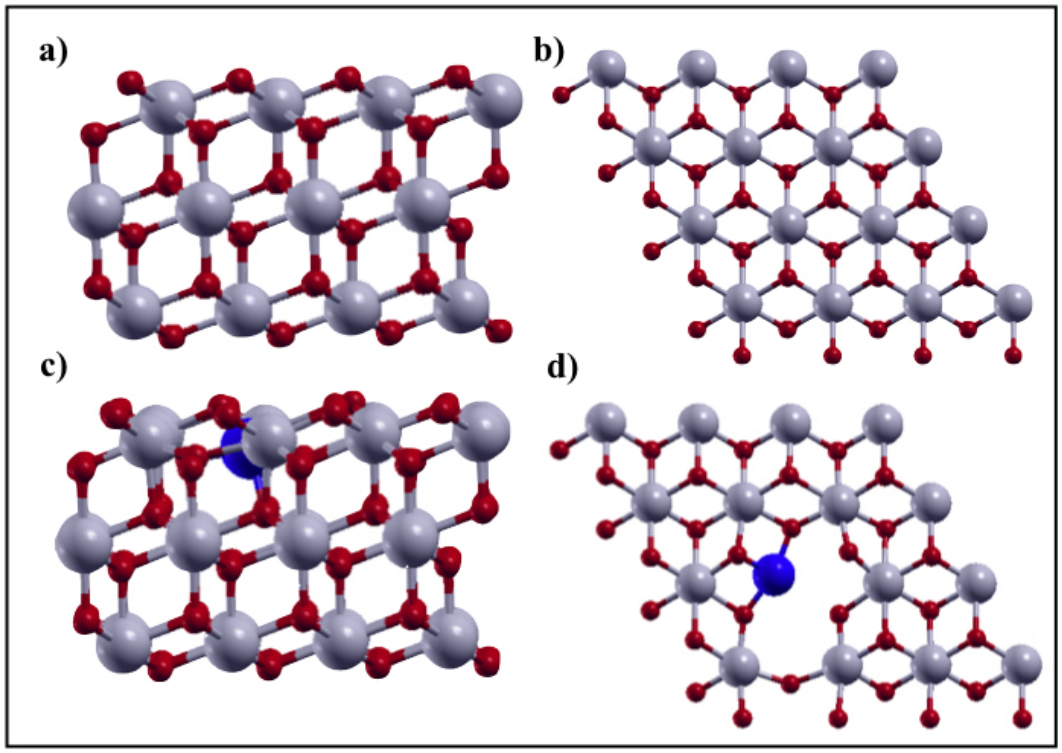

FIGURE 3.22: a) and b) Side and top view of CeO_2 (111) surface. c) and d) Side and top view of Ag:CeO_{2-x} (111) surface.

in a dissociative form on the surface leads to the reduction of cerium atoms: two and one Ce atom for the pristine and doped surface, respectively. For both surfaces, the large value of ΔE suggests that the H atoms will diffuse on the surface after H_2 dissociation. As a possible water formation pathway, we considered the diffusion of one hydrogen atom from the oxygen atom to which it is bonded to another surface hydroxyl, and divided the reaction in two steps. For the first step, we have followed the path proposed by Fernández-Torre et al. [112] who found that a H atom on pristine CeO_2(111) first diffuses from O_s to a subsurface oxygen (O_{sub}), reaching a metastable state (MS) before passing to a different O_s. For the second step, we assumed that H diffuses from O_{sub} to a surface hydroxyl, with which it reacts to form a H_2O molecule that desorbs from the surface (FS). For pristine CeO_2, our computed activation energies of the first (IS → MS) and second (MS → FS) step are 1.13 and 0.30 eV (Fig. 3.23), while the barriers for the inverse MS→ IS and FS→MS processes are 0.12 and 0.28 eV, respectively. The water formation pathway for Ag doped CeO_2 is reported in Fig. 3.24. Here, the energy barrier for H diffusion from a surface to a subsurface oxygen (IS→MS) is 0.77 eV, lower than that on pristine CeO_2, with an inverse (MS→ IS) barrier of 0.35 eV. On the other hand, the activation energy required to create a water molecule (MS→FS), 0.61 eV, is higher than on the pristine surface and the inverse (FS→ MS) barrier is only 0.14 eV. This suggests that the creation of a surface V_O through water formation is actually quite unlikely on Ag-doped CeO_2. An alternative pathway, where water formation occurs on the Ag dopant, is found to have an even higher MS → FS energy barrier, 1.05 eV, (Fig. 3.25).
The energy required to dissociate H_2 is less on the Ag:CeO_2 surface than on the pure CeO_2 surface, and this is in agreement with the appearance of a peak due to the OH bond (see Fig. 3.21a) at lower temperature (470 K) on the Ag modified surface than on the pristine surface (∼ 580 K), but the number of Ce^{3+} is less on the more reactive surface. Supposing that all the gain of energy due to the dissociation of the hydrogen molecule (ΔE) is transferred to the lattice, the hydrogen atoms adsorbed on both the surfaces (pristine and Ag doped) have enough energy to start to diffuse just after their adsorptions, and the rate of H diffusion is higher on the Ag-doped CeO_2. On the contrary, water formation is more favorable on the pristine surface since the activation energy is lower. Since water formation leads to oxygen vacancy creation, a higher number of oxygen vacancies can be expected on the pristine than on the Ag-doped CeO_2 surfaces as observed experimentally at high temperature. Moreover, easily H_2O dissociates again on the doped surface to reach a metastable state (MS). The formation of water leads to the reduction of two and one Ce atoms for CeO_2 and Ag:CeO_2, respectively, and this is in agreement with the experimental results, shown in Fig. 3.20, where the number of Ce^{3+} is higher on the pristine than on the doped CeO_2 surface.

3.3.3 Conclusions

Using an *ab − initio*, based on the density functional theory, approach we have investigated the reactivity of the pristine and Ag modified CeO_2 surfaces, in vacuum and H_2 atmosphere, in order to interpret the experimental findings obtained at the SESAMO Laboratory. We have discussed, in particular, the validity of evaluating the reducibility of the surfaces on the basis of the number of reduced cerium atoms.
We have found, as observed experimentally, that in vacuum the Ag doped CeO_2 surface is more reducible than the pristine one, but the presence of Ce^{3+} is not a good marker since the number of Ce^{3+} is smaller than on the pristine ceria surface.
We have found, as observed experimentally, that the Ag modified CeO_2 surface is

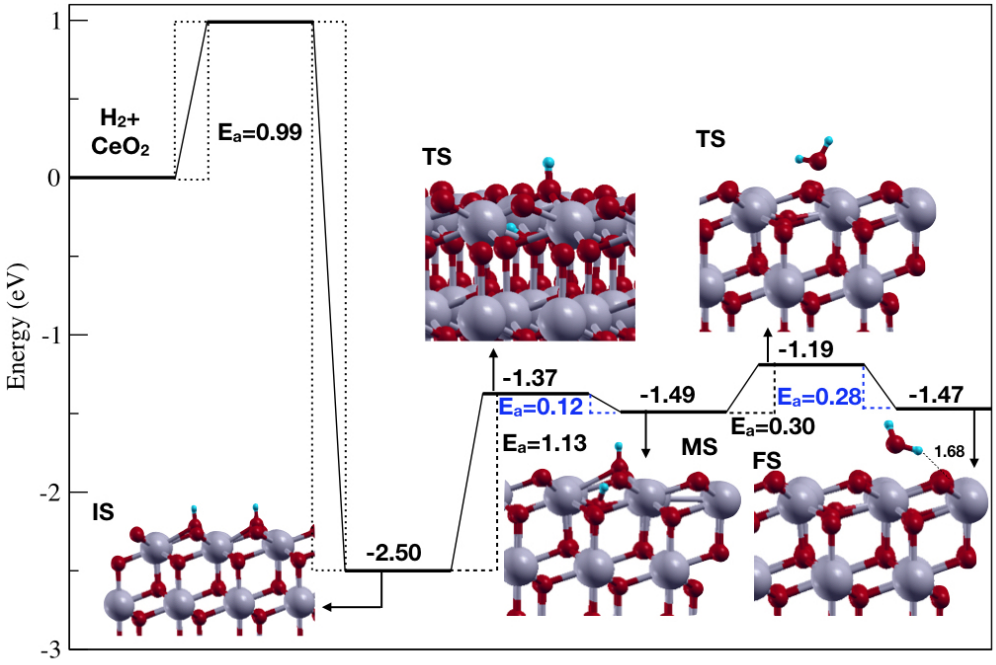

FIGURE 3.23: Minimum Energy Path (MEP) of H_2O formation on pristine CeO_2 surface. Gray and red balls are the Ce and O atoms, respectively. The light blue balls are the Hydrogen atoms. The activation energies reported in blue refer to the inverse processes. The distance reported is in Angstrom.

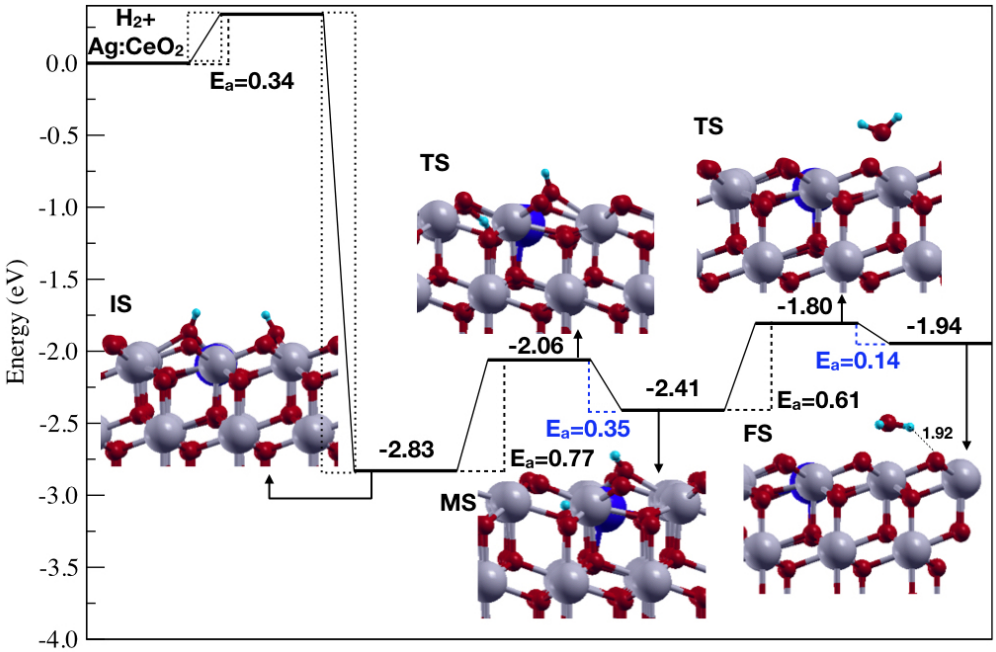

FIGURE 3.24: Minimum Energy Path (MEP) of H_2O formation on pristine $Ag:CeO_{2-x}$ surface. The color code is the same as in Fig. 3.23. The blue ball is the Ag atom. The activation energies reported in blue refer to the inverse processes. The distance reported is in Angstrom.

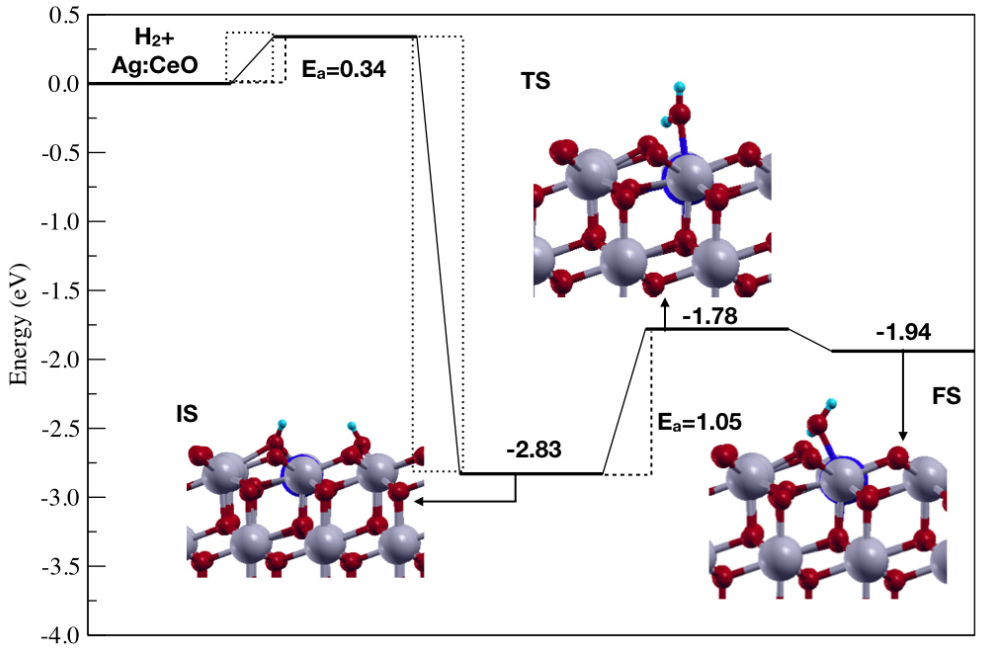

FIGURE 3.25: Minimum Energy Path (MEP) of H_2O formation on pristine Ag:CeO_{2-x} surface directly from two hydrogen atoms bonded to surface oxygens. The color code is the same as in Fig. 3.24. The distance reported is in Angstrom.

more reactive towards H_2 dissociation than the pristine one, but, once the dissociated H atoms are adsorbed on the surface, it is more difficult to form water, which leads to the formation of more surface oxygen vacancies. Consequently, the number of oxygen vacancies, as found experimentally, is smaller on the Ag modified surface than on the pristine ceria surface.
Thus, Ag modified CeO_2 surface seems to be a good candidate as anode catalytic materials for the PEMFCs, since, in these devices, it is necessary to increase the rate of H_2 dissociation, but then the hydrogen atoms have to remain on the surface, and then diffuse to the membrane.

Chapter 4

Methane activation on the pristine and Ag doped (111) and (100) CeO_2 surfaces

In this chapter we report a study of the performance of CeO_2 (111) and (100) surfaces pristine and Ag-doped, towards the dissociation of the methane molecules. This work has been done in collaboration with Prof. Annabella Selloni, of the Chemistry Department of the Princeton University.

4.1 Introduction

Methane (CH_4) is the main component of natural gas [113]. It's very cheap and abundant on earth, and, it is a good candidate as a source of clean fossil energy [114]. CH_4 can be employed in the production of many products, from biofuel [115], syngas [114], olefins [114] to methanol [116]. New reserves have been recently discovered [117] but they are located in isolated areas and the transportation, due to the lower density of CH_4 with respect to oil [118], is not economic [114]. Consequently, to employ CH_4, it is necessary to convert it to other energy sources more transportable.
CH_4 is a very stable molecule due to the strong C-H bonds (439KJ/mol) [119], and for this reason is quite inert, and breaking the first C-H bond is usually the rate limiting process of the entire reaction [120], [121], [122]. So, to activate the process at low temperatures it is necessary to use catalysts.
Ceria (CeO_2) plays an important role in the environmental catalysis [123]. In particular, CeO_2 supported noble metal systems have been extensively investigated for their catalytic activity towards CO oxidation [124], water gas shift reaction [58], and H_2 dissociation [63], [102]. Ceria has attracted an increasing attention due to its capacity to store and release oxygen atoms [25], which leads cerium atoms to pass from the Ce^{4+} to the Ce^{3+} oxidation state [125].
It has been shown that catalysts based on cerium oxides exhibit a great performance in the activation of the C-H bond [67], [30], [126], [127] , but the energy required to activate CH_4 on the more stable and exposed CeO_2 (111) facet is still quite high. In the attempt to lower this energy we can follow two paths: to change the exposed surface or to dope the surface with a metal.
Ceria's catalytic activity towards C-H activation has so far been investigated only for the (111) surface, but the surface catalytic activity is known to depend significantly on the orientation of the exposed surface [128] . For example, Zhou et al. have observed an high reactivity for CO oxidation in nanorods exposing the 100/110 planes [129] , whereas Zhao et al. have found an increased propene hydrogenation on the

CeO_2 (111) facets [130] with respect to other facet orientations. Concerning the C-H activation, Capdevila-Cortada et al. [131] in a recent theoretical work have found that the energy required to dissociate methanol was smaller on a CeO_2 (100) surface than on the (111) surface. Consequently, the (100) surface seems to be a promising surface also for CH_4 activation.
The second possibility is to dope the surface with metals: doping is indeed one way to increase the catalytic activity of the surfaces [5]. It has been shown that the presence of a single metal atom on ceria lowers the activation energies of reactions: Fu et al. [9] have observed experimentally the increased activity of nonmetallic Au and Pt atoms on ceria for water-gas shift reaction, and recently, it has been calculated that a single Ag atom doped CeO_2(111) surface lowers significantly the energy to dissociate the hydrogen molecule [109]. Single metal atoms on ceria have been recently synthesized [9], [6], [27], [28], and it has been observed that the metal atoms tend to occupy the cerium sites. In particular a single Ni [125] or Co [132] adatom on the CeO_2(111) surface, and single Pd [123], Pt [133], Rh [133] atoms in substitution of cerium atoms lower the energy needed to break the C-H bond with respect to the value it has on pristine ceria. In this work we consider the influence of single Ag atoms doping the CeO_2(111) and (100) surfaces on the activation of methane: as shown by Krcha [134] for the (111) surface, Ag seems to be a good candidate to promote CH_4 dissociation. However, Krcha et al. [134] for their calculations have not considered for the (111) orientation the most stable surface. Following the experimental observations, we consider Ag doped surfaces where one Ce atom per surface unit cell is substituted by one Ag atom. Methanol (CH_3OH) is extensively employed in chemical industries [135], or used as a fuel [136], and the possibility to produce it directly from methane is of fundamental importance. However, its production is not easy: to obtain methanol, as a stable product from CH_4, it is indeed, necessary to activate methane at low temperature (<500 $^\circ$ C) [136], [137]. Recently, it has been proposed to directly oxidize CH_4 to produce CH_3OH on molecular oxygen over copper-exchange zeolites [138] . On the pure ceria (111) surface, Knapp et al [139] have studied the production of methanol as $CH_4 + CeO_2 \rightarrow CH_3OH + CeO_{2-x}$, where CeO_{2-x} is the ceria surface with a surface oxygen vacancy, but they found that the activation energy is higher than the energy required to dissociate CH_4 as CH_3+H. It is interesting to find out what would happen on a doped surface.
By using first principles calculations based on the density functional theory, we have investigated both paths to increase the reactivity towards CH_4 dissociation. We have studied CH_4 oxidation on the pristine CeO_2 (100) ceria surface, and on the Ag-doped CeO_2 (111) and (100) surfaces comparing the results with those relative to the most studied CeO_2 (111) surface. For the (111) orientation of the Ag-doped surface we have considered a more stable surface than the one used by Krcha et al. [134]. For the Ag doped surfaces we have considered also the reaction mechanism to obtain methanol as final stable product.

4.2 Computational Details

The spin polarized calculations have been carried out using the density functional theory (DFT) as implemented in the Quantum Espresso (QE) code [82], [83]. The electron -ion interactions were described by ultrasoft pseudopotentials. The approximation of Perdew, Burke, and Ernzherof (PBE) [35] to the exchange and correlation functional was employed. In order to consider the dispersion interaction we have used the D2 correction proposed by Grimme [140] implemented in the code. The

energy and charge density cutoffs were set to 30 Ry and 240 Ry, respectively.
To describe the strongly correlated f electrons of Cerium we have used the Hubbard correction as implemented by Cococcioni et al. [43]. We have set U = 4 eV, since using this value we can reproduce the experimental and theoretical results of previous works. The structure of CeO_2 bulk was optimized using a $7 \times 7 \times 7$ Monkhorst-Pack (MP) [84] mesh grid, obtaining the lattice parameter a = 5.52 Å , in reasonable agreement with the experimental value ($\sim$ 5.41 Å [141], [142]).
CeO_2 surfaces were modeled with slabs supporting an in-plane (4×4) unit supercell, and the Brillouin zone was sampled at the Γ point.
The (111) oriented slabs contains three O-Ce-O trilayers. Previous theoretical studies have predicted an oxygen termination for the (100) surface [70]. Since the resulting slab is not stoichiometric, so, in order to avoid a dipole moment and obtain a stoichiometric surface slab, half of the surface oxygens are moved from the top to the bottom surface as suggested by Skorodumova et al. [70]. We have used a slab with the same number of atoms of the slab used to model the (111) surface.
The atoms of the two surfaces have a different coordination: on the (111) surface Ce and O bind to 7 and 3 atoms, respectively, whereas on the (100) surface Ce and O bind to only 6 and 2 atoms as shown in Fig. 4.1.

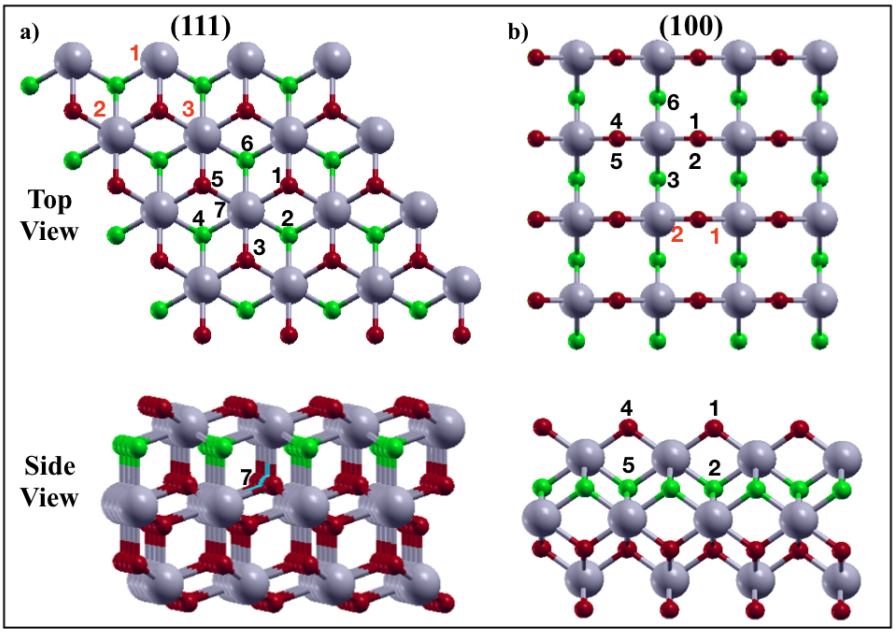

FIGURE 4.1: Top and side view of a) CeO_2 (111) and b) (100) surfaces. Gray balls are the cerium atoms. Red and green are the oxygen atoms of the first and second layer. The cyan ball is the oxygen of the second trilayer of the (111) surface bound to the surface cerium atom. Black and red numbers indicate the first neighbor of cerium and oxygen atoms, respectively.

A vacuum thickness of about 15 Å was used in order to avoid interactions between contiguous slabs. We have relaxed the atomic positions until the forces were less than 0.01 eV/Å ; the atoms of the last three layers were fixed to the bulk positions. The total energy criterion for the structure optimization was set to 10^{-5} eV.

In order to account for long range interactions we employed the D2 method proposed by Grimme et al. [140] as implemented in the QE code.
The adsorption energies of methane in the molecular (CH_4) and in the dissociative (CH_3+H) configurations have been calculated as E_{ads}=E_{CH_4} (or CH_3+H)/surface - E_{CH_4} - $E_{surface}$, where E_{CH_4} (or CH_3+H)/surface is the energy of the surface with adsorbed CH_4 or CH_3+H, $E_{surface}$ is energy of the pristine surface, and E_{CH_4} is the energy of the methane molecule in the gas phase. E_{CH_4} was determined using a cubic box with a 20 Å edge.
To test how the adsorption energies of methane on ceria change as a function of the coverage we have adsorbed CH_4 and CH_3+H also on a (3×3) surface unit cell. In this way the coverage Θ passes from 1/16 to 1/9.
In this last case the integration on the Brillouin Zone was accomplished using a (2 × 2 × 1) MP mesh grid [84]. To determine the minimum energy pathway (MEP) of the reactions we have used the climbing image nudge elastic method (CI-NEB) 50 with seven images.
We have estimated the charge transfers occurring during the reactions looking at the Bader charges [87] on the atoms and analyzing the projected density of electronic states (PDOS) on the atoms of the structure before and after the reaction.
We have calculated the change in the Gibbs free energy of the slab when one Ag atom per cell is added as

$$\Delta G(T,p) = E_{Ag:CeO_2} - E_{CeO_2} + N^{O}_{vac}\mu_O(T,p) + N^{Ce}_{vac}(E^{Bulk}_{CeO_2} - 2\mu_O(T,p)) - \mu_{Ag}, \quad (4.1)$$

where $E_{Ag:CeO_2}$ is the energy of the doped surface with one Ag per unit cell, E_{CeO_2} is the energy of the pristine surface, N^{O}_{vac} is the number of oxygen vacancies, N^{Ce}_{vac} is the number of Ce vacancies, μ_O (T,p) is the oxygen chemical potential at temperature T and pressure p, and μ_{Ag} is the Ag chemical potential which corresponds to the total energy of one Ag atom in the bulk.
We have calculated the constant dissociative rate k, following the work of Su et al. [143] , as

$$k = \frac{K_B T}{h}\frac{q_{TS}}{q_{CH_4}} e^{\frac{-E_a}{K_B T}}, \quad (4.2)$$

where q_{TS} and q_{CH_4} are the partition functions for CH_4 in the transition state and gas phase, respectively, and E_a is the activation energy. In this expression q_{TS}=$\frac{1}{1-e^{\frac{-h\nu}{K_B T}}}$, and q_{CH_4}=$\frac{1}{1-e^{\frac{-h\nu}{K_B T}}} \times \frac{32\pi^2}{3}(\frac{K_B T}{4\pi\varepsilon_{CH_4}})^{\frac{3}{2}} \times \frac{K_B T}{P_{CH_4}/P^{\Theta}} \times (\frac{2\pi m K_B T}{h^2})^{\frac{3}{2}}$, where ν is the vibrational frequency, ε_{CH_4} is the rotational constant, P_{CH_4} is the methane pressure, and P^{Θ} is standard pressure.

4.3 Results

4.3.1 Adsorption of CH_4 on pristine CeO_2(111) and (100) surfaces

We start by investigating the adsorption of methane on the pristine CeO_2 (111) and (100) surfaces. We have calculated the adsorption energies at different possible adsorption sites in order to locate the most favoarble ones. The molecular (MA) and dissociative (DA) adsorption structutre on the pristine CeO_2 (111) and (100) surfaces are shown in Fig. 4.2.
On the (111) surface CH_4 prefers to physisorb at a distance 3.28 Å above a Ce atom (E_{ads}= -0.04 eV), with one hydrogen atom pointing away from the surface. The C-H

distances are 1.10 Å , in good agreement with the experimental value 6 (1.09 Å) for the methane molecule. The physisorption of the molecule does not determine a net charge transfer from the molecule to the surface, and the projected density of states (pdos) of the CeO_2 surface is not changed with respect to the PDOS of the surface before the adsorption of methane as shown in Fig. 4.3a and b. No cerium atoms are reduced. In the dissociative adsorption, the methyl group (CH_3) and H are adsorbed on two surface Oxygen atoms as shown in Fig. 4.2 (DA). This state will be the final state of the dissociative reaction of CH_4 on the surface. The C-O and C-H distances of CH_3 are 1.42 and 1.11 Å , respectively. The C-H bond lengths are very similar to those of CH_4. Following the adsorption of the dissociated methane, two Cerium atoms are reduced to Ce^{3+}, as shown in Fig. 4.2. As a confirmation, we note the appearance of Ce f peaks below the Fermi energy at about -0.5 eV as shown in the PDOS of Fig. 4.3c. The dissociative adsorption is highly favored compared to the molecular one: the adsorption energy is now -0.89 eV. In order to take account of the dispersion interactions we have also calculated the adsorption energies using the D2 correction proposed by Grimme [140], and the results are reported in table 4.1 where we also compare the calculated adsorption energies with the results of previous works. We see that the van der Waals correction increases the adsorption energies for both the molecular and dissociative adsorption. In the table we have reported the values obtained for the (4×4) supercell but as shown in table 4.2 we note that the calculation of the adsorption energies at different coverages produce similar results.
On CeO_2(100), the molecule prefers to physisorb above a Ce atom as found on the (111) surface, but with a different orientation. As shown in Fig. 4.2: two hydrogens of CH_4 point towards the surface, and the other two are directed in the opposite direction. The C-Ce distance, 3.52 Å , is slightly larger than that calculated for the (111) surface. The adsorption energy is -0.02 eV. The PDOS, as occurs for the (111) surface, is not modified by the molecular adsorption of CH_4 as shown by the comparison between Fig. 4.3d and Fig. 4.3e. Also in this case no cerium atoms are reduced.
As for the dissociative adsorption, the adsorption of CH_3 and H on the surface leads to the reduction of two Ce atoms (see the f peak below E_F) in Fig. 4.3f. The adsorption energy is -2.25 eV, greater than the value calculated for the (111) surface. We can speculate that the larger adsorption energy on the (100) surface with respect to the (111) surface is due to due to the lower coordination of the surface atoms. The surface oxygen atoms are, indeed, less negative charged than on the (111) surface ($\sim$ -0.2 e), and this loss of charge of the surface oxygen atoms was found previously also by Nolan et al. [144] , The adsorption of the methyl group and of the hydrogen atom determines an increase of the negative electronic charge of two surface oxygen atoms, that reach their favorite -2 oxidation state, and this charge transfer makes the adsorption more favorable on the (100) surface than on the (111) surface where all the oxygens are already in their favorite oxidation state.

4.3.2 Adsorption of molecular and dissociated CH_4 on Ag doped CeO_2(111) and (100) surfaces

We now analyze how the doping of the surface with Ag atoms affects the adsorption of CH_4 and CH_3+H. To simulate Ag doped surfaces (Ag:CeO_2) we have substituted one Ce atom per unit cell with one Ag atom. On both (111) and (100) doped surfaces the creation of one oxygen vacancy is thermodynamically favored, and consequently the most stable surfaces are those without the surface oxygen atoms, Ag:CeO_{2-x}. We have studied the effect of pressure and temperature on the stability of the Ag:CeO_2

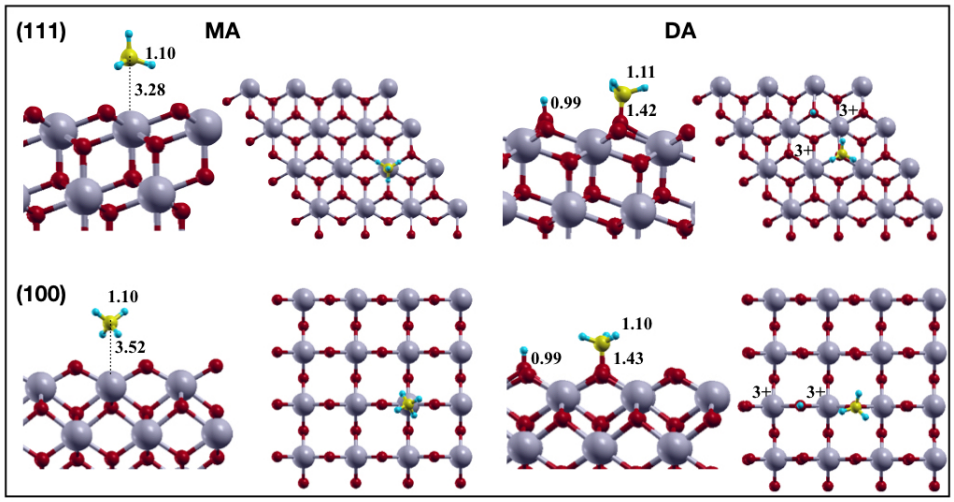

FIGURE 4.2: Side and Top views of the molecular (MA) and dissociative (DA) adsorption configurations of CH_4 on the CeO_2(111) and (100) surfaces. Gray and red balls are the cerium and oxygen atoms, respectively. Yellow and light blue balls represent the carbon and hydrogen atoms, respectively. The symbol 3+ indicates the reduced cerium atoms.

and Ag:CeO_{2-x} surfaces. The reduced surface is the most stable one over the entire range of oxygen chemical potentials as shown in Fig. 4.4, where we have plotted the Gibbs free energies of the Ag:CeO_2 and Ag:CeO_{2-x} surfaces. Thus, the adsorption of CH_4 and CH_3+H is studied on the reduced Ag:CeO_{2-x}(111) and Ag:CeO_{2-x}(100) surfaces. However, to compare our results with the only work present in the literature concerning the Ag dopant proposed by Krcha et al. [134], we have considered also the Ag:CeO_2(111) surface although it is not stable.
In Fig. 4.5 we show the PDOS of the Ag:CeO_{2-x} surfaces. As shown in Fig. 4.5a and 4.5d, for the Ag:CeO_{2-x} (111) and (100) surfaces, respectively, the s and one of the d orbitals of the Ag atom are empty, and from the analysis of the Bader charges on the Ag atom ($\sim$ - 0.8 e) with respect to the Ag atom in the gas phase, we can speculate that the Ag oxidation state is +2. Due to the presence of Ag, some surface oxygen atoms are less charged ($\sim$ - 0.2 e) with respect to their value on the pristine CeO_2 surface.
In Fig. 4.6 we show the side and top views of the configurations of the methane molecule in its most favorite adsorption sites on both surfaces for both the molecular and dissociative adsorption. In Fig. 4.7 we show the adsorption sites of CH_4 on the Ag doped CeO_2 (111) surface without the oxygen vacancy considered by Krcha et al. [134].

Molecular Adsorption On Ag:CeO_{2-x} (111) CH_4 prefers to adsorb above the surface oxygen vacancy site as shown in Fig 4.6, whereas in the absence of the vacancy CH_4 adsorbs above the Ag atom (Fig. 4.7). The adsorption energy is -0.76 eV. It increases significantly with respect to that calculated on the unstable Ag:CeO_2 surface, E_a= -0.23 eV, so the presence of the oxygen vacancy, which has not been considered in Ref. [134], is important for the reactivity of the surface. Even in the absence of a net charge transfer from CH_4 to the surface, we observe from the PDOS in Fig 4.5b that

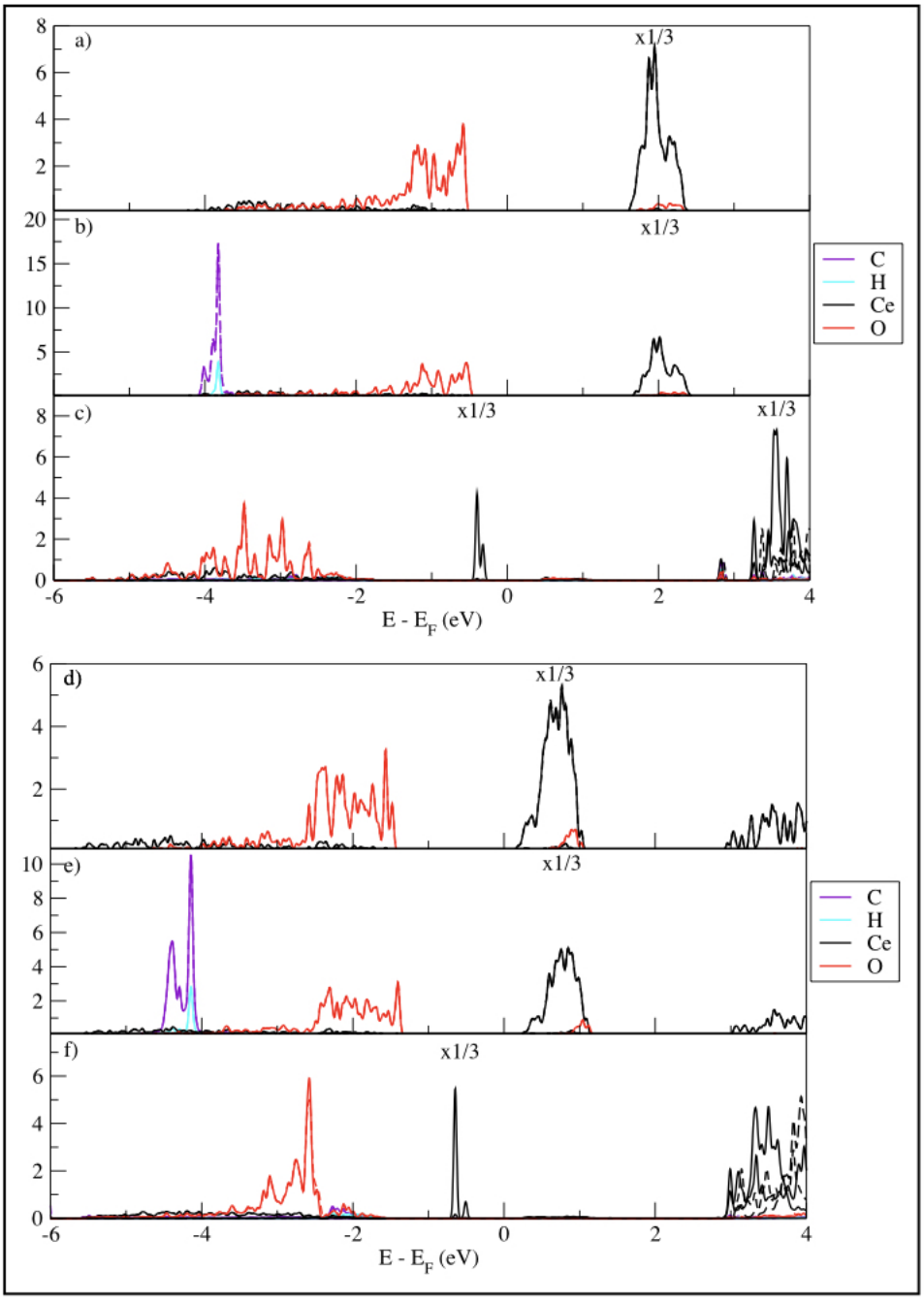

FIGURE 4.3: Projected Density of States (PDOS) of methane adsorbed on CeO2 surfaces. a) CeO_2 (111) surface; b) CH_4 on CeO_2(111); c) CH_3 and H on CeO_2(111); d) CeO_2(100) surface; e) CH_4 on CeO_2(100); c) CH_3 and H on CeO_2(100). Continued and dashed lines are the spin up and down contributions, respectively. The Cerium f states have been multiplied by a factor 1/3

TABLE 4.1: Adsorption energies (E_{ads}) (eV) of the methane molecule on the pristine (111) and (100) CeO_2 surfaces. The symbol * refers to adsorption energies obtained adding the van der Waals dispersion interaction.

	111		100	
	Molecular	Dissociative	Molecular	Dissociative
E_{ads}	-0.04	-0.89	-0.02	-2.25
E^*_{ads}	-0.38	-1.59	-0.32	-2.79
E_{ads} [139]	/	-2.23	/	
E_{ads} [67]	<0.05	-0.76	< 0.05	-1.52
E_{ads} [14]	-0.21	. -1.31		
E_{ads} [145]	/	-1.14	/	/
E_{ads} [134]	<0.05	-0.76	/	/

TABLE 4.2: Adsorption Energy (eV), without the long order range interactions, of the methane molecule in the molecular and dissociative form on pure Ceria (111) surfac. In order to test the effect of the coverage we have used two different surface unit cells: 4×4 (Θ=1/16) and 3×3 (Θ=1/9).

	CeO_2	
	Θ=1/16	Θ=1/9
Molecular	-0.04	-0.04
Dissociative	-0.89	-1.01

the energy distance between the p peaks of the less charged oxygens of the valence and conduction band increases compared to those calculated for the Ag:CeO_{2-x} surface without adsorbates. Also the energy distance between the d states of Ag and the f states of Ce decreases. The Ag d orbitals in the valence band now touch the Fermi Energy. These changes are due to the interaction between the molecule and the surface.
On the Ag:CeO_{2-x} (100) surface the adsorption energy, -1.01 eV, increases significantly with respect to the value calculated for the Ag:CeO_{2-x} (111) surface, so the Ag doped CeO_2 (100) surface seems to be more reactive towards CH_4. The preferential adsorption site is slightly different compared to that found for the Ag:CeO_{2-x} (111) surface since now CH_4 is closer to the Ag atom: the C-Ag distance is 3.42 Å , while on the (111) surface is 3.74 Å . Following the adsorption of CH_4, the PDOS (see Fig. 4.5e) changes significantly. The energy distance between the d states of Ag in the valence band and those in the conduction band decreases with respect to the surface before the adsorption, and indeed, we note the appearance of an Ag localized state in the valence band near the Fermi Energy (see Fig. 4.5d).

Dissociative Adsorption We turn now to study the dissociative adsorption of CH_4. We have considered three different final states: i) CH_3 adsorbed on Ag, and H on a surface oxygen atom (DA_1); ii) CH_3 and H bonded to the same surface oxygen atom

(DA_2), and iii) CH_3 and H adsorbed on two surface oxygen atoms (DA_3). In Table 4.7 we report the adsorption energies for the three possible final states on the different surfaces. The adsorption energies are greater when CH_3 and H are bonded to two surface oxygen atoms (DA_3), and for both the surfaces the adsorption energies follow the same trend $E_{DA_1} < E_{DA_2} < E_{DA_3}$. Also on the Ag:$CeO_2$(111) surface (see Table 4.7) the trend is the same. The value calculated by us for the DA_3 state on Ag:CeO_2(111), -3.68 eV, is greater than the value found by Krcha et al. [134] without the van der Waals correction, -3.29 eV.
In Fig. 4.6c and 4.6f we show the PDOS of the surface atoms in the most stable final state (DA_3). For both surfaces, Ag and some surface oxygens acquire an amount of charge following the adsorption. Now, only the Ag s states are in the conduction band. Comparing the PDOS of the DA_3 states with those calculated before the adsorption we can speculate that the new Ag oxidation state is +1, which is the favorite one for the Ag atom. We observe also the reduction of one Ce atom: the f peak is indeed now below E_F.
The different adsorption energies of DA_1, DA_2, and DA_3 can be related to the different charge transfers occurring during the adsorption. On Ag:CeO_{2-x} (111), in DA_1 , Ag acquires less charge compared to the two other possible final states. It is, consequently, less favored, since it doesn't reach its favorite oxidation state. In the other two final states (DA_2 and DA_3) Ag acquires the same amount of charge but on DA_2, contrary to what happens for DA_3, one oxygen remains less charged with respect to the ideal -2 oxidation state, and as a consequence of the not optimal charge redistribution, the adsorption energy of DA_2 is lower than that of DA_3 .
On the Ag:CeO_{2-x} (100) surface, in all the final states Ag acquires almost the same amount of charge, and the difference in the calculated adsorption energies is only due to the different charge transfers to the oxygens. Again, only in the DA_3 configuration two oxygen atoms increase their electronic charge, and, consequently, this configuration is more favored.

TABLE 4.3: Adsorption Energies (in eV) of the methane molecule in the molecular (MA) and dissociative (DA) forms with the van der Waals correction. In parenthesis the adsorption energies without the van der Waals correction for the MA and DA_3 states on the Ag:CeO_2(111), Ag:CeO_{2-x}(111), and Ag:CeO_{2-x}(100) surfaces are reported.

	MA	DA_1	DA_2	DA_3
Ag:CeO_{2-x} (111)	-0.76 (-0.28)	-1.10.	-1.23	-2.45 (-1.92)
Ag:CeO_{2-x} (100)	-1.01 (-0.63)	-1.53	-2.13	-3.20 (-2.94)
Ag:CeO_2 (111)	-0.23 (-0.03)	-1.57	-2.85	-4.25 (-3.68)

4.3.3 CH_4 dissociation pathways on the pristine CeO_2 (111) and CeO_2 (100) surfaces

We investigate now the reaction pathway to dissociate CH_4 to CH_3+H on the CeO_2 (111) and (100) surfaces. As shown in Fig. 4.8, in the transition states (TS) of both the reaction paths, CH_4 is already dissociated: H is bonded to a surface oxygen atom, whereas CH_3 is adsorbed $\sim$ 3.3 Å near a Ce atom. Then, the methyl group (CH_3)

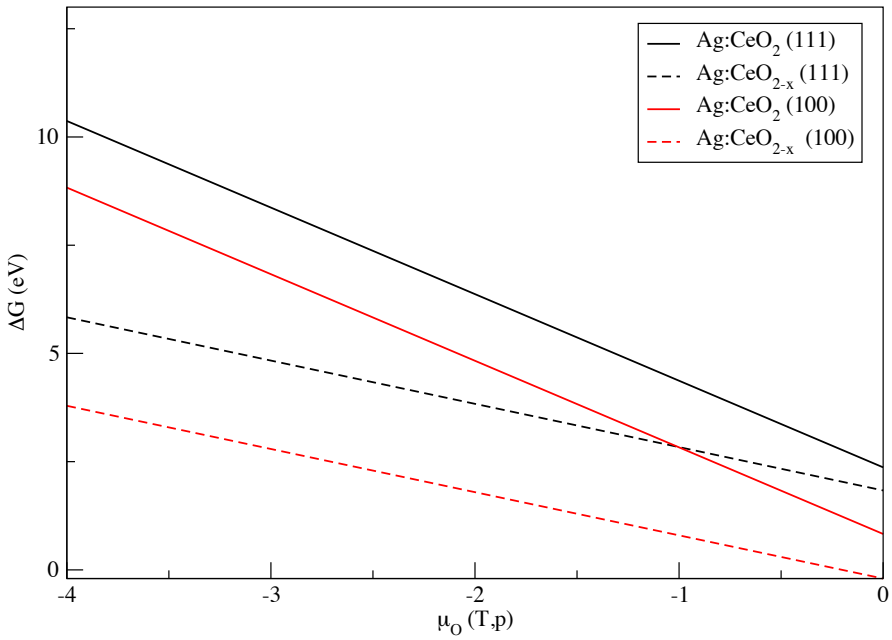

FIGURE 4.4: Change in the Gibbs free energy with the addition of one Ag atom per unit cell on the CeO_2(111) and CeO_2(100) surfaces as a function of the oxygen chemical potential μ_O (T,p). Black and red lines are the free energies of the Ag doped CeO_2 (111) and (100) surfaces, respectively. Continued and dashed lines are the stoichiometric and reduced surfaces, respectively.

moves to bind to a surface oxygen. The calculated activation energy on CeO_2(111) is 1.44 eV, which is similar to the values reported in previous works [143], [67], [139] , although those barriers were calculated without the van der Waals correction. The energy required to break the first C-H bond is significantly lower on the (100) surface. It is indeed 0.87 eV , thus, the (100) surface is more active towards C-H dissociation than the (111) surface. This is probably due to the less charged surface oxygen atoms present on the (100) surface, which are more reactive than the oxygen atoms on the (111) surface. Following the work of Su et al. [143] we have calculated the reaction rate constant k as a function of the temperature. At room temperature (300 K), and pressure P_{CH_4} = 0.1 atm, the rate constants for methane dissociation are 4.61*10^{-27} s^{-1} and 1.45*10^{-17} s^{-1} for the (111) and (100) surfaces, respectively. Increasing the temperature to 600 K the rates increase significantly: 1.03*10^{-15} and 7.67*10^{-9} s^{-1} for the (111) and (100) surfaces, respectively. Thus, the (100) orientation might considerably increase the activity of CH_4 dissociation. Additives as the decanoic acid can be used to increase the 100 exposed surface with respect to the 111 [128], leading to the formation of cube-like nanoparticles.

4.3.4 CH_4 dissociation pathways on the Ag doped CeO_{2-x} (111) and CeO_{2-x} (100) Ag surfaces

For both the Ag:CeO_{2-x} (111) and (100) surfaces we have considered only the two most stable final states (DA_2 and DA_3). In Fig. 4.9 we show the dissociation paths of CH_4 on the Ag:CeO_{2-x} (111) surface. On both pathways CH_4 moves from the oxygen vacancy towards the Ag atom, and in the TS the C-Ag distances are 4.05 Å and 3.25 Å for the DA_2 and DA_3 final states, respectively. Contrary to the pristine

surface in the TS the CH_4 molecule is not dissociated. The activation energies are very similar: 0.38 and 0.49 eV for DA_2 and DA_3 final states, respectively. The dashed blue rectangle in the figure indicates that, after the TS, CH_3 has to overcome another small barrier to reach the final state as shown in Fig. 4.10, where the entire reaction path to produce a methanol molecule (DA_2 final state) is shown.

CH_4, indeed, reaches the transition state, and then the dissociation occurs: one H binds to a surface O, whereas the methyl group is adsorbed on Ag. This metastable state corresponds to the less stable final state DA_1. Then, with a low barrier, 0.08 eV, CH_3 leaves Ag and binds to the same oxygen atom to which previously H was bonded to form CH_3OH, which will leave the surface, creating a surface oxygen vacancy on the surface. It is interesting to note that Ag plays an active role in the dissociation path, and it is fundamental in the production of CH_3OH. Since the activation energy is slightly lower for the path which leads to the production of a methanol molecule (DA_2) than that required to obtain the DA_3 final state, the production of CH_3OH is slightly more probable, although this state is less stable than DA_3. The energy required to dissociate CH_4 as CH_3+H is 0.95 eV less than on the pristine (111) ceria surface: doping is, consequently, a promising way to increase the rate of the reaction. The presence of isolated Ag atoms is sufficient to activate methane at a lower temperature (energy). The dissociation occurs near the noble metal atom, and the presence of less charged O_s, caused by its presence, is crucial to increase the adsorption energies and the reactivity of the surfaces. In Fig. 4.11 we show the dissociation of CH_4 on the unstable Ag:CeO_2 (111) surface. CH_4 will dissociate spontaneously to reach the DA_1 and DA_2 final states, whereas a small activation energy, E_a=0.23 eV, is required to reach the DA_3 final state. This value is smaller than the energy barrier, E_a = 0.39 eV, calculated by Krcha et al. [134] without the van der Waals correction. The less stable Ag:CeO_2 (111) surface is more reactive than the stable one: if it were possible to stabilize Ag:CeO_2 (111), the break of the first C-H bond, which is usually considered the rate limiting process, could occur without any energy cost. In Fig. 4.12 we show the CH_4 reaction pathways on the Ag:CeO_{2-x}(100) surface. As for the corresponding pristine surface, the Ag doped (100) surface is more active towards C-H activation than the (111) surface: indeed, the energy required to break the first C-H bond is only 0.21 eV against 0.49 eV or 0.38 eV. In the TS, the molecule is already dissociated with one H atom bonded to a surface oxygen and the methyl group adsorbed near a Ce atom. So, the presence of one single Ag atom in a Ce substitutional site increases significantly the reactivity of the surface: thus, to dope the CeO_{2-x} surface is the most efficient way to increase the reaction rate to obtain CH_3 + H from CH_4. Contrary to what happens on the (111) surface, here, the energy necessary to activate the molecule to produce methanol is 0.22 eV greater than the energy necessary to reach the most stable DA_3 final state so, it is more unlikely to obtain methanol on the (100) surfaces than to dissociate CH_4 into the DA_3 final state. Thus, contrary to the (111) surface, the (100) surface facilitates the activation of the CH_4 molecules, but it is not effective for the production of methanol.

4.3.5 Stability of a methanol molecule on the Ag:CeO_{2-x} (111) surface

We have found in the previous section that the energy necessary to activate one CH_4 molecule on the Ag:CeO_{2-x} (111) surface and produce one methanol molecule is slightly smaller than the energy necessary to obtain the DA_3 final state. Here, we want to investigate if the methanol molecule, once formed, does not dissociate into the most stable DA_3 configuration. As shown in Fig. 4.13 the barrier the

methanol has to overcome to reach the DA3 final state is quite high, 1.73 eV, and consequently the methanol molecule is a quite stable intermediate state which can then be observed. The CH_4 rate constant dissociation at T=400 K to produce methanol is k=7.73*10^{-8} s^{-1}. We have chosen this temperature because methanol as product of the reaction is stable only if it obtained at temperature below 500 ° C.
Once CH_3OH is formed, it is necessary to remove it from the surface as shown in Fig. 4.14. The energy required to desorb the methanol molecule, calculated as -E_{ads}, is 1.24 eV. As observed previously, the formation of a methanol molecule determines the formation of a surface oxygen vacancy, so to close the catalytic reaction, and to reobtain the catalyst as in its initial state, it is necessary to refill the vacancy as shown in Fig. 4.14. We examine the energetics of such process. We have calculated the formation energy of the second process (detachment of O) as E_{form}=$E_{O:Ag:CeO_{2-2x}}$+1/2 E_{O_2} -E_{O_2}:Ag:CeO_{2-2x}, where $E_{O:Ag:CeO_{2-2x}}$ is the energy of the surface where we have removed one oxygen atom of the oxygen molecule, $E_{O_2:Ag:CeO_{2-2x}}$ is the energy of the surface with the oxygen molecule adsorbed, and E_{O_2} is the energy of oxygen molecule. The adsorption of O_2 on the vacancy is strongly favored, -1.24 eV, and the energy to take away one of the two oxygens is only 0.07 eV.
Thus, once the methanol molecule is formed, it is easy to reobtain the catalyst under oxygen pressure.

4.4 Conclusions

Using an *ab − initio* approach, based on the density functional theory, we have investigated the dissociation of methane on the pristine and Ag doped CeO_2 surfaces. We have considered two surface orientations, the (111) and the (100), to determine which would be more efficient in the activation of methane. In both the pristine and Ag doped ceria surfaces, the (100) surface enhances the methane dissociation, decreasing significantly the energy required to break the first CH bond, which is usually considered the rate limiting step of the reaction. This is probably due to the presence of less charged surface oxygen atoms, which are more reactive than the oxygen atoms on the (111) surface.
Single Ag atoms dispersed on both the ceria surfaces lower significantly the barrier energies with respect to that calculated for the pristine CeO_2 surfaces. Ag favors significantly the CH_4 activation, since, following the breaking of the molecule, it acquires one H electron, reaching, in this way, its favorite +1 oxidation state. Moreover, Ag allows for the direct conversion of methane into methanol, and, for the (111) surface, the calculated energy required for this reaction is less than the energy required for the dissociation of CH_4 as CH_3 +H. Methanol is a quite stable product of the reaction, although it is not the most stable final state.
Finally, single Ag atoms dispersed on ceria surfaces seem to be good candidates as single atom catalysts to increase the methane activation rates.

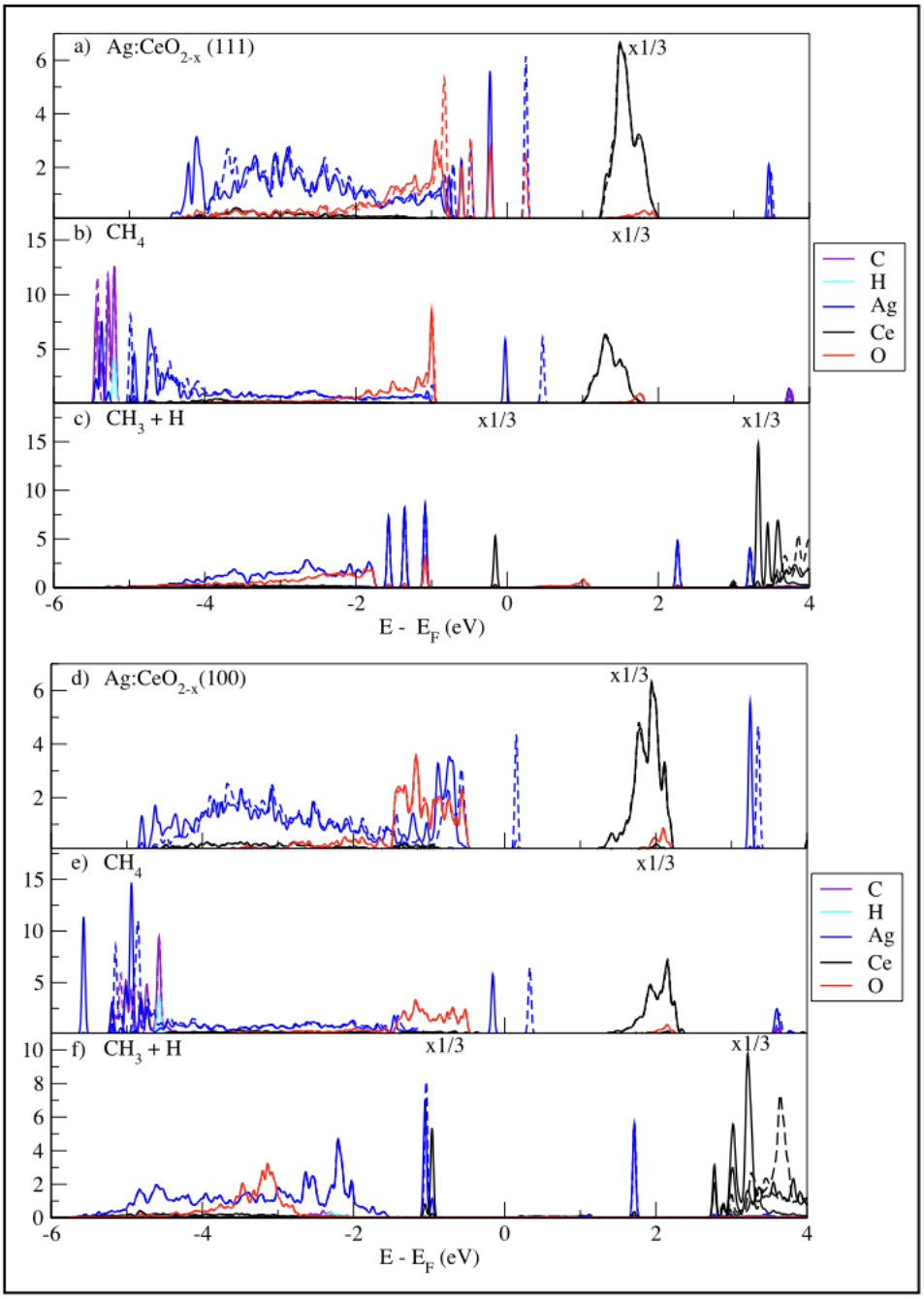

FIGURE 4.5: Projected density of states of a) Ag:CeO2-x (111) surface; d) Ag:CeO_{2-x} (100) surface; CH_4 adsorbed on b) Ag:CeO_{2-x} (111); e) Ag:CeO_{2-x} (100) surfaces; and CH_3+H adsorbed on two surface oxygens on c) Ag:CeO_{2-x} (111) and f) Ag:CeO_{2-x} (100) surfaces. The cerium f states have been multiplied by a factor 1/3.

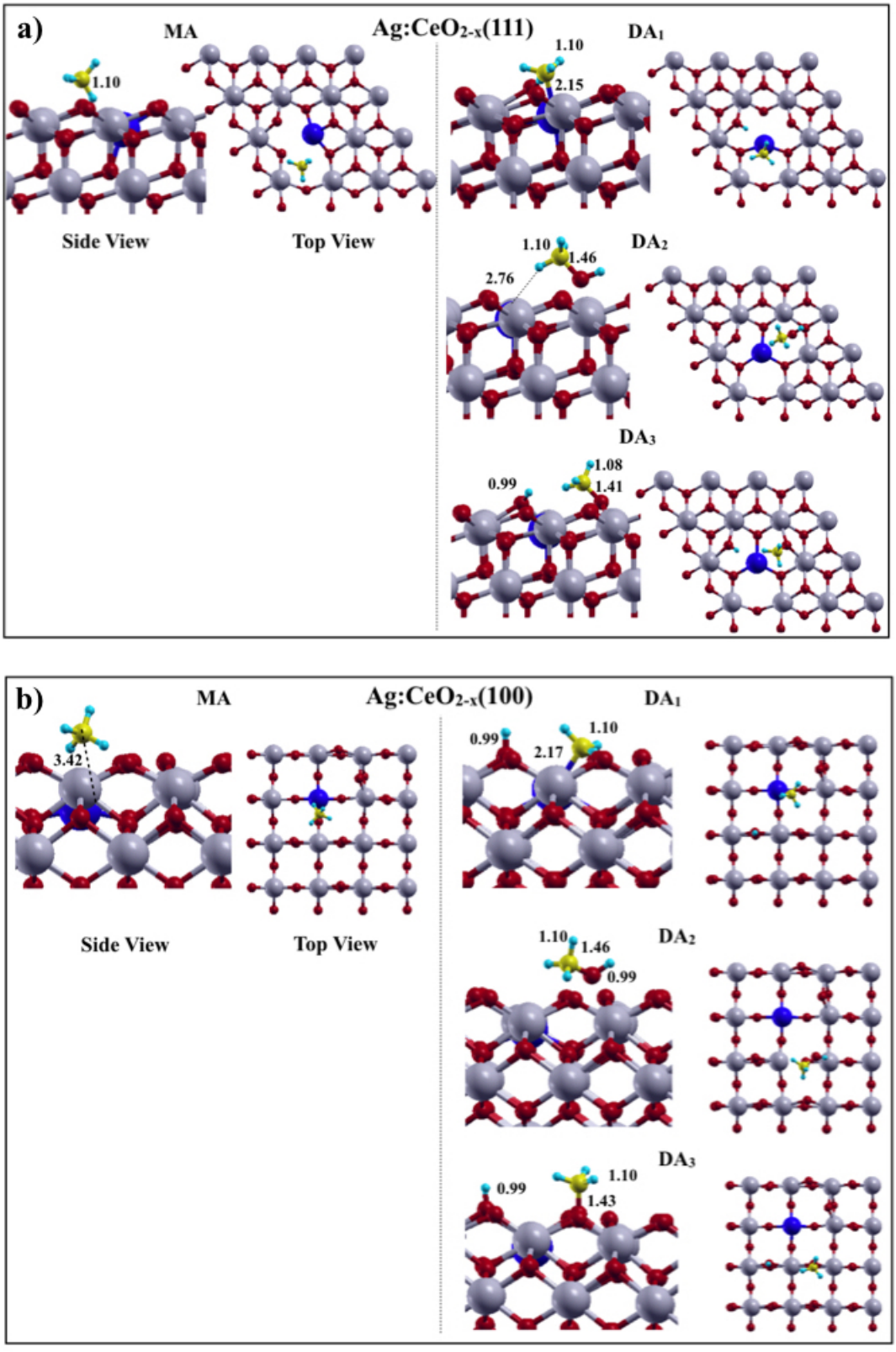

FIGURE 4.6: Side and Top view of the molecular and dissociative adsorption of CH_4 on Ag:CeO_{2-x} (111) and Ag:CeO_{2-x} (100). Yellow and cyan balls are the Carbon and Hydrogen atoms. Blue, gray, and red balls represent Silver, Cerium, and Oxygen atoms.

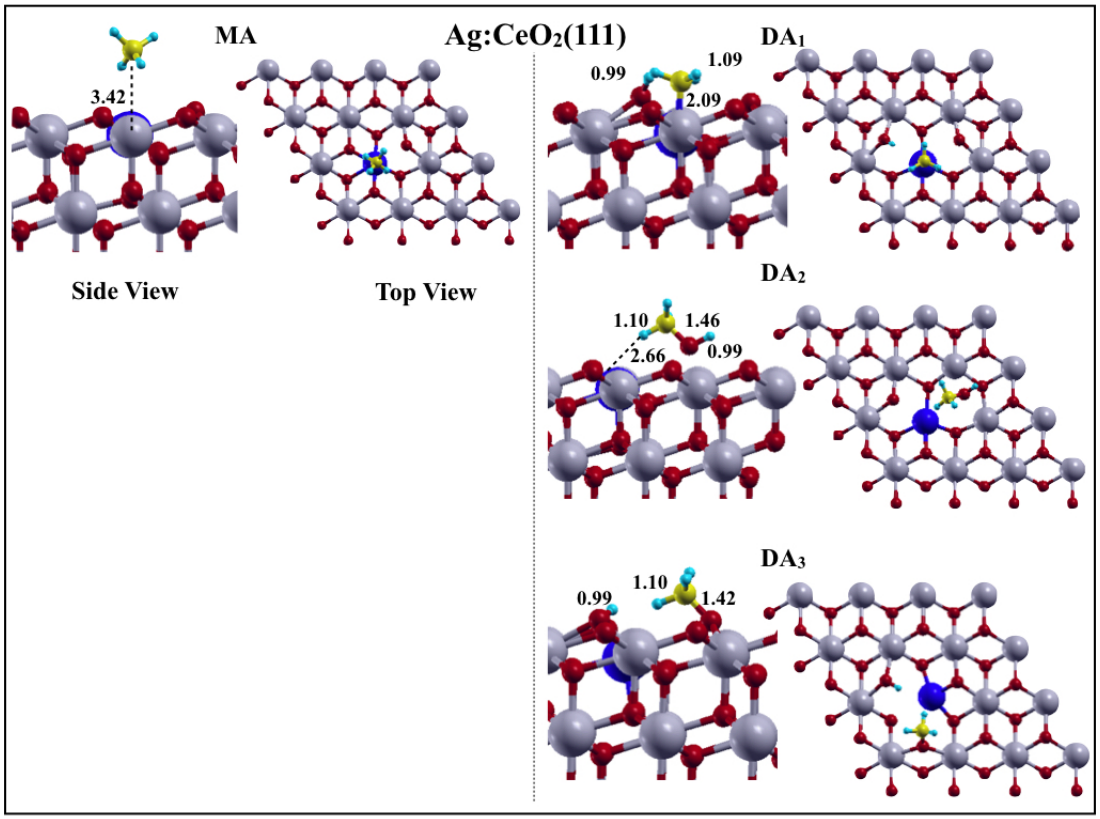

FIGURE 4.7: Molecular and Dissociative adsorption of CH_4 on $Ag:CeO_2(111)$ surface. Yellow and cyan balls are the Carbon and Hydrogen atoms. Blue, gray, and red balls represent Silver, Cerium, and Oxygen atoms.

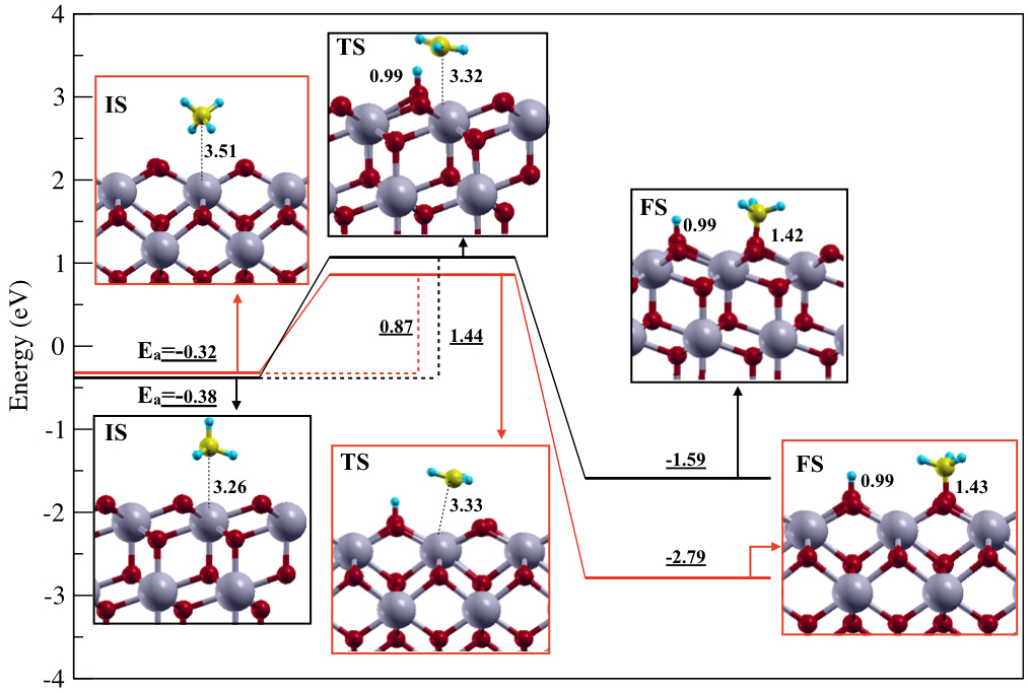

FIGURE 4.8: Minimum Energy Pathway (MEP) of CH_4 dissociation on the CeO_2(111), black line, and on the CeO_2(100), red line, surfaces. The relevant distances are given are in angstrom. The color code is the same as in Fig. 4.2.

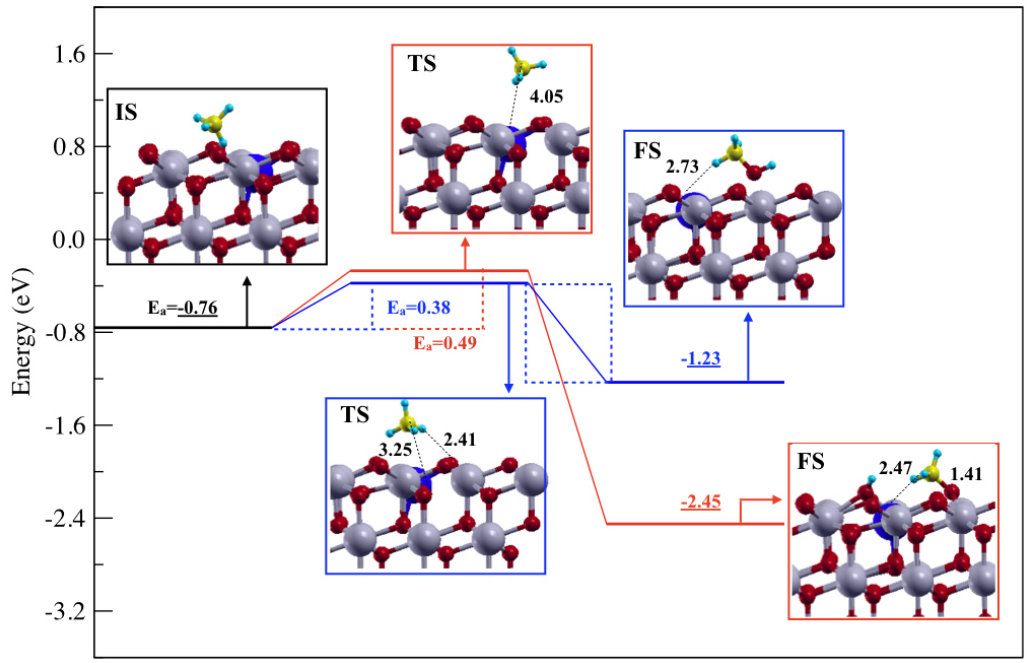

FIGURE 4.9: Minimum reaction pathways (MEP) for the activation of CH_4 on Ag:CeO_{2-x}(111). The blue line, and the red line represent the reaction pathways to DA_2, and DA_3, respectively. All the distances are in Angstrom. The color code is the same as in Fig. 4.6.

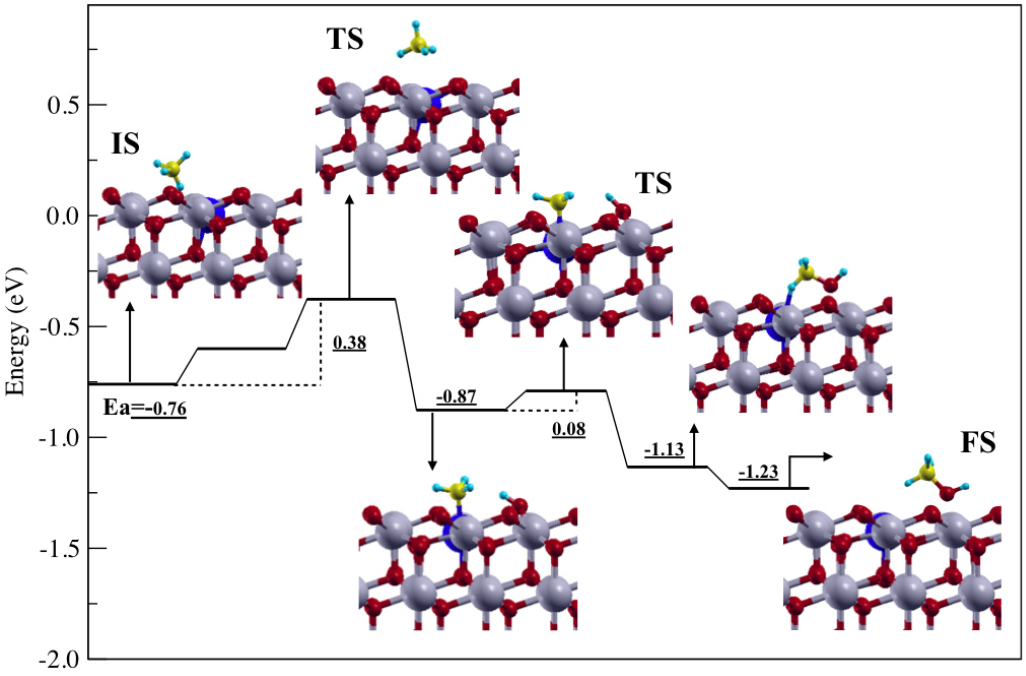

FIGURE 4.10: Reaction Pathway of the dissociation of CH_4 on Ag:CeO_{2-x}(111) to form methanol. All the distances are in angstrom. The color code is the same as in Fig. 4.6.

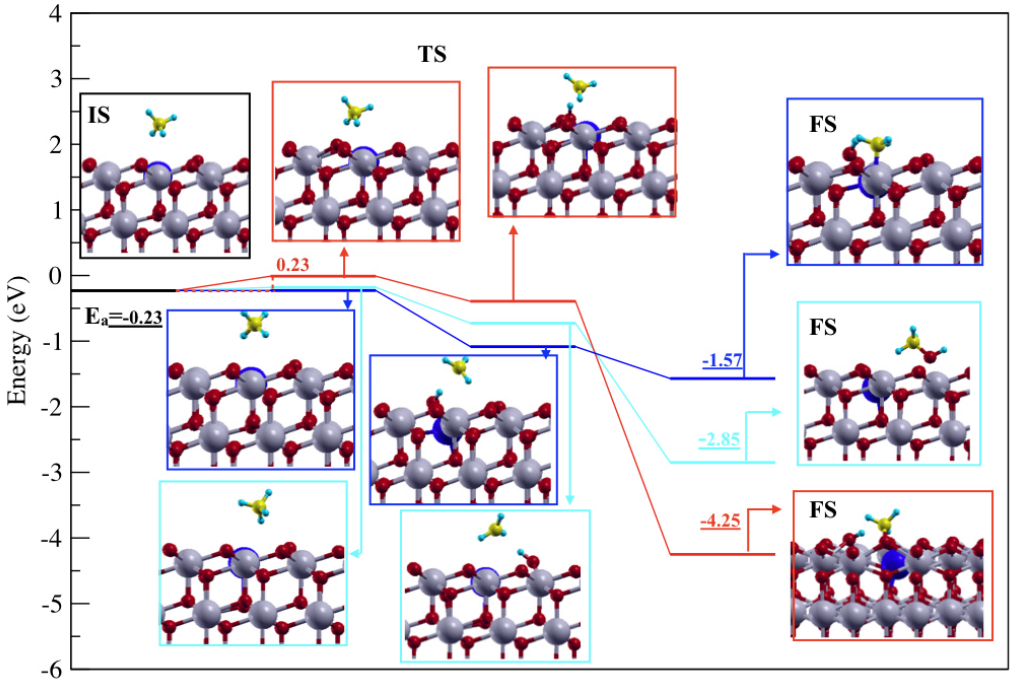

FIGURE 4.11: Minimum Energy Pathways (MEP) of the CH_4 dissociation on the Ag:CeO_2(111) surface with three different possible final states. The color code is the same as in Fig. 4.6.

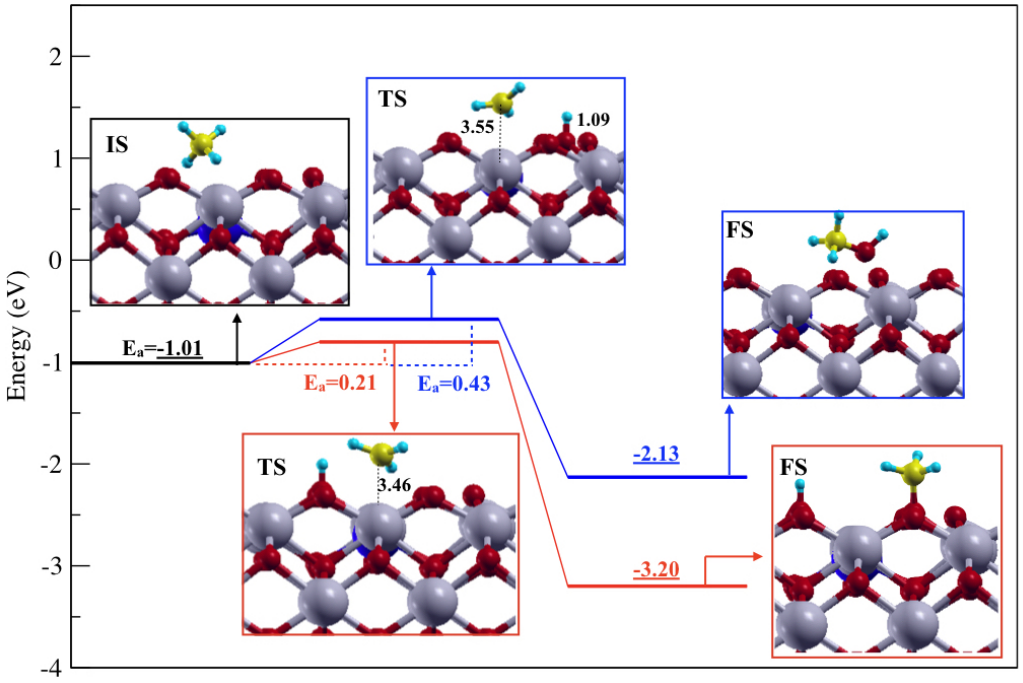

FIGURE 4.12: Minimum reaction pathways (MEP) for the activation of CH_4 on Ag:CeO_{2-x}(100). The blue lines and red lines represent the reaction pathways to the DA_2 and DA_3 final states, respectively. All the distances are in Angstrom. The color code is the same as in Fig. 4.6.

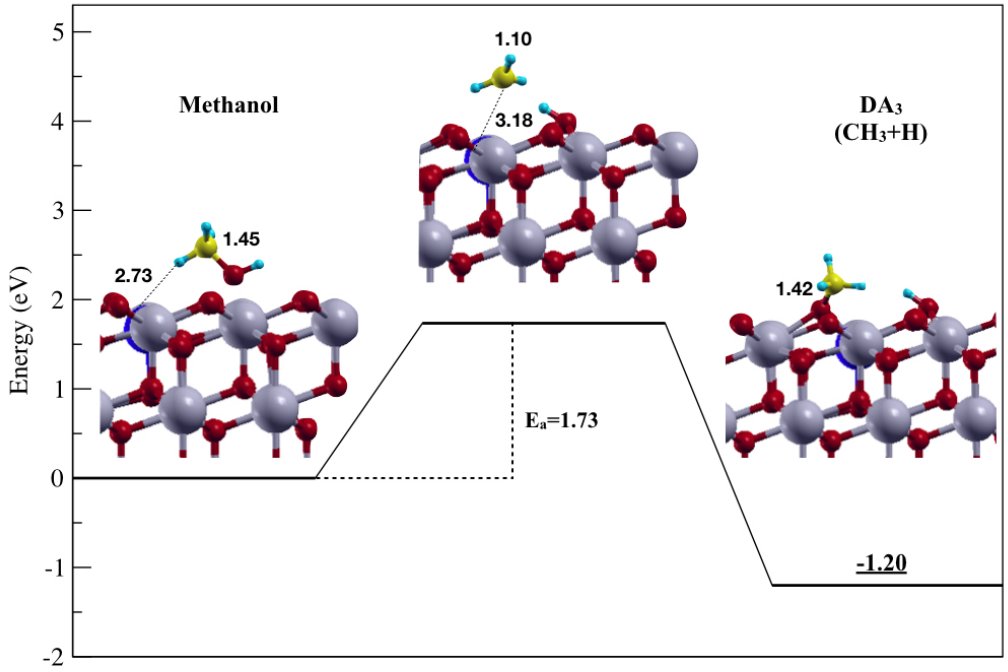

FIGURE 4.13: Minimum Energy Pathway (MEP) of the reaction of methanol dissociation ($DA_2 \rightarrow DA_3$) on Ag doped CeO_2 surface in presence of an oxygen vacancy. All the distances are in angstrom. The color code is the same as in Fig. 4.6.

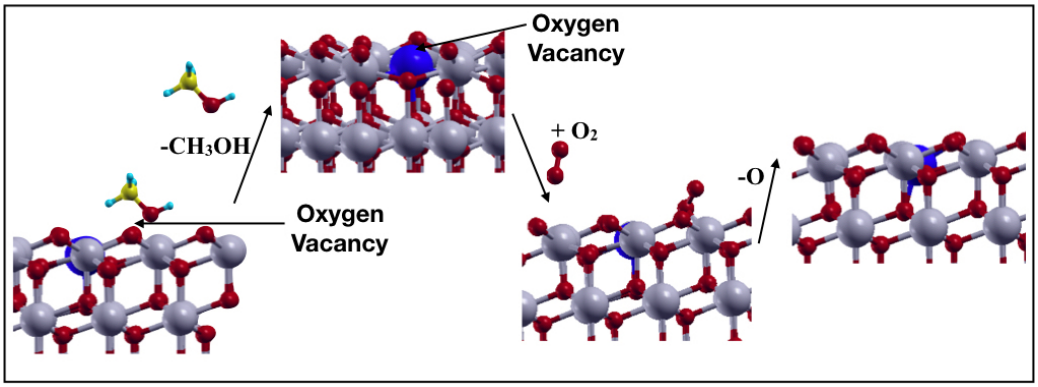

FIGURE 4.14: The removal of CH_3OH and the adsorption of O_2 on the Ag:CeO_{2-x}(111) surface. The color code is the same as in Fig. 4.6.

Chapter 5

Reduction and Oxidation of Maghemite (001) Surfaces: the Role of Iron Vacancies

In this chapter we investigate the properties of another important class of reducible oxides: the iron-oxides, and, in particular, the less studied, but commonly employed in catalytic applications, Fe_2O_3 in the maghemite structure. In Sec. 5.1, we briefly present the general properties of iron oxides, and their applications. In particular, we will focus on experiment concerning CO oxidation. In Sec. 5.2, motivated by the experimental findings, a study related to the role of the iron vacancies on the redox properties of the maghemite surface is reported.

5.1 Iron oxides

Iron oxides are compounds of iron and oxygen, and they are common everywhere in the earth [146]. The weathering of rocks, containing Fe, naturally, originates iron oxides [146].
The use of iron oxides has an ancient origin. In the prehistory, ochre pigments, which are present in the iron oxides, have been used to color the cave walls [26], and since 850 AD, the magnetic properties of iron oxides have been used to build compasses [26]. Recently, it has been proposed to employ iron oxides in different fields of applications due to their high stability and low cost. Energy storage and heterogenous catalysis are two of the most important application fields. As catalysts, iron oxides are used, for example, for Fenton [147], and water splitting reactions [148], or for CO oxidation [149].
Iron oxides are used as catalysts towards some reactions, or as cheap supports for metal nanoparticles, but it has been shown that also the role of the support is fundamental in the reactions [150].
In this context, in a recent article, Najafishirtari et al. [151] studied the catalytic activity of iron oxide nanodumbells, one of which is shown in Fig. 5.1a. In Fig. 5.1b a schematic picture of the samples is shown. The samples are constituted by a metal (yellow balls) and a metal oxide domain (brown balls) of the same size. It has been possible to obtain metal oxide domains with a hollow interior. A number of samples then have been considered with a different percentage of hollow domains. Three samples have been characterized with a number of hollow size domains (transparent areas) increasing from D_1 to D_3. The CO oxidation activity of the three samples was found to be different. It decreases from D_1 to D_3 as shown in Fig. 5.2a. A very complete characterization of the samples revealed that the only relevant difference between the samples is that D_1 and D_2 are composed only by maghemite (γ-Fe_2O_3),

whereas, the D_3 sample contains also a small fraction of hematite (α-Fe_2O_3). This difference was found using X-Ray diffraction (XRD), and the results are shown in Figs. 5.2b and 5.2c. The ratio of the two phases has been obtained performing a semi quantitative analysis based on the Reference Intensity Ratio (RIR) .
Assuming that the CO oxidation reaction follows the Mars-van Krevelen mechanism [24], the removal from the surface and the adsorption of an oxygen atom on the surface are both crucial reactions which may affect the reactivity of the system. Since D_1 is the most active, and it is formed only by maghemite, whereas D_3 has also a fraction of hematite, a possibility is that there is a difference in the reduction and oxidation activity of maghemite and hematite. Maghemite and hematite differ each other for crystal symmetry. Maghemite, indeed, has a cubic symmetry, whereas hematite has an hexagonal symmetry. Another difference is the presence in maghemite of iron vacancies which are absent in hematite. We have focused our attention on this second difference trying to understand the role of iron vacancies in the redox activity. To do this we have compared maghemite and magnetite, which have both a cubic symmetry, but with the iron vacancies present only in maghemite. The aim is to identify the role of the iron vacancies on the redox activity of, for example, the (001) surface of maghemite.

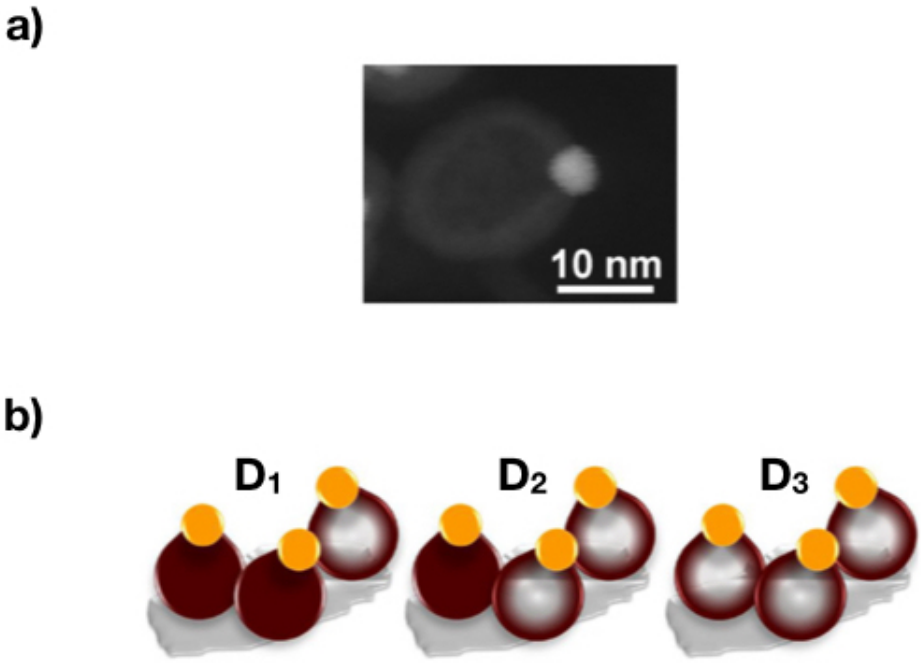

FIGURE 5.1: a) HAADF-STEM image of the sample; b) schematic picture of the nanodumbell structures. Yellow and brown balls are the metal and metal oxide domains. The transparent areas are the hollow domains. Adapted from Ref. [151].

5.2 Reduction and Oxidation of Maghemite (001) Surfaces: the Role of Iron Vacancies

The text of this section has been copied by the article "Reduction and Oxidation of Maghemite (001) Surfaces: the Role of Iron Vacancies", G. Righi and R. Magri, The Journal of Physical

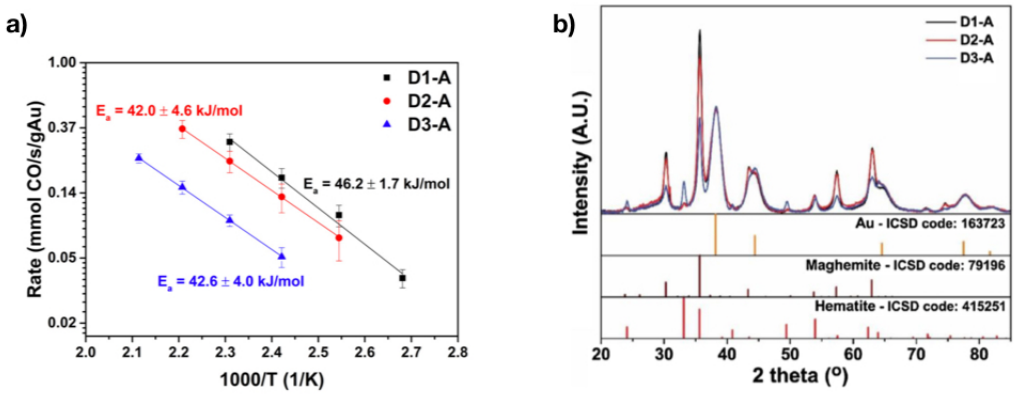

c)

Phase Quantification from RIR			
Sample	Au	Maghemite	Hematite
D_1	20.8	79.2	-
D_2	24.1	75.9	-
D_3	27.5	55.4	17.1

FIGURE 5.2: a) CO oxidation rate obtained by kinetic measurements; b) X-ray diffraction patterns of the different samples; c) ratio of the phases of the samples. Adapted from Ref. [151].

Chemistry C, 12325, 15648-15658 (2019), https://doi.org/10.1021/acs.jpcc.9b03657. Adapted with permission from The Journal of Physical Chemistry C. Copyright 2019 American Chemical Society.

5.2.1 Introduction

Iron and oxygen are two of the most plentiful elements on the Earth, and, consequently, many studies have been aimed to investigate the potential of iron oxides for a large number of applications. Iron oxides have been indeed proposed for sustainable energy storage [148], [147], biotechnology [152] , data sensors, and biomedicine [153]. In the field of clean energy production, an important role is played by electrochemical devices for the utilization of alternative, environmentally friendly fuels, and iron-oxides have the potential to make a substantial contribution as electrodes in such devices. The possibility to use iron oxides as new catalytic electrode materials as substitutes for the existing costly and rare raw materials (i.e., platinum), without losing in efficiency and maintaining a high level of performance is highly attractive. Many catalytic reactions, for example, CO oxidation, follow the Mars-van Krevelen mechanism [24]. In this mechanism, the surface is reduced with a surface oxygen atom transferred to an adsorbed fuel molecule. This reaction is then followed by the surface re-oxidation with the refilling of the oxygen vacancy from an O_2 molecule from the gas-phase. The mechanism, thus, requires an easy transfer of oxygen atoms from and to the catalyst surface. Reducible oxides, such as iron

oxides, can thus be effective catalysts for these reactions. In this article, we study the reduction and oxidation properties of the maghemite (γ-Fe_2O_3) iron oxide as determined by the extraction and addition of oxygen atoms from and to the surface. Maghemite surfaces have been shown to have a high potential for applications. Recently, Qiu et al. [154] have shown experimentally that maghemite exhibits promise for oxygen reduction reaction, a fundamental reaction taking place in living systems and at the cathodes of electrochemical devices [153]. Najafishirtari et al. [151] have observed that larger the percentage of the maghemite phase over the hematite one, α-Fe_2O_3, in dumbbell-shaped metal/iron-oxide nanocrystalline catalysts, more reactive were the catalysts toward CO conversion. Furthermore, iron oxides in the maghemite phase have recently been proposed as cathode or anode materials for lithium-ion batteries, which need to be improved for their extensive use in hybrid electric vehicles and new devices [148] ,[155]. Maghemite (γ-Fe_2O_3) is the second most stable iron oxide [156]. It is obtained by the oxidation [157] or as a weathering product [158] of magnetite (Fe_3O_4), which is the most stable (in conditions of ultravacuum) and studied iron oxide. Maghemite and magnetite are structurally correlated [146].They both have an inverse spinel crystal structure with two kinds of differently coordinated Fe atoms: iron atoms coordinated to oxygen atoms in octahedral sites, and iron atoms with a tetrahedral coordination to oxygen atoms. In contrast to magnetite, where all tetrahedral iron atoms have oxidation state Fe^{3+} and an equal number of Fe^{3+} and Fe^{2+} cations occupy the octahedral sites, in γ-Fe_2O_3, all of the iron atoms are in a trivalent oxidation state. To guarantee the neutrality of the bulk structure, some Fe vacancies are required that have experimentally been found to be located at the octahedral sites [159]. Several experimental works [160], [161], [162] , [163] suggested that the iron vacancies of maghemite are arranged in an ordered structure corresponding to the tetragonal space group, $P4_122$, with a = 8.347 Å and c = 25.042 Å . Recently, Grau-Crespo et al. [158] using a density functional theory (DFT) approach and a supercell containing three magnetite bulk unit cells, compared the total energies of all structures obtained by occupying differently the 24 Fe octahedral sites with 8/3 vacancies. They found that the structure with space group $P4_122$ is indeed the most stable. The supercell corresponded to thrice the cubic unit cell of the magnetite bulk, replicated along the [001] direction, so as to accommodate an integer number of iron vacancies. Along the [001] direction of this crystalline structure, the maghemite and magnetite bulks correspond to the alternation of octahedral Fe and oxygen planes and of tetrahedral Fe planes. In the ordered structure with $P4_122$ space group, the Fe vacancies are located in two (octahedral Fe?oxygen) planes out of three as shown in Figure 5.3.

To study the thermodynamics of oxygen release and adsorption on the maghemite (001)-oriented surfaces, we have considered two surfaces terminated with octahedral iron atoms and oxygen atoms obtained by truncating the bulk. These surface terminations have been shown in magnetite to be more stable than the surfaces terminated in tetrahedral iron atoms [164], thus, because of the structural similarity between the two phases, we assume that this is also true for maghemite. Of the two considered surfaces, one, termed A, has the iron vacancies on the outermost plane, whereas the other, termed B, has the iron vacancies located in the third plane below the outermost plane. We have also considered an additional surface reconstruction related to a new stable reconstruction of the (001) magnetite surface found recently in a joint experimental and theoretical work [32]. We have investigated the reduction and oxidation properties of these surfaces in order to understand the role of the iron vacancies and analyzed the corresponding changes in the electronic properties and related charge transfers. We have compared the results obtained for the maghemite

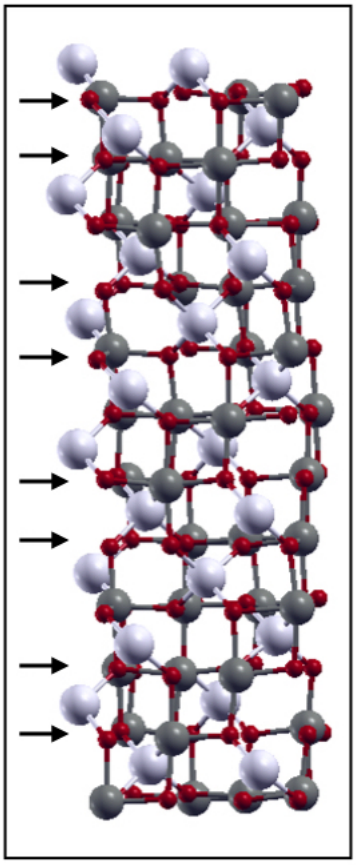

FIGURE 5.3: Maghemite (γ-Fe_2O_3) bulk. Dark and light grey balls are the octahedral and tetrahedral iron atoms, respectively. Red balls are the oxygen atoms. Arrows indicate the planes where the iron vacancies are located.

surfaces with those of analogous calculations performed for the correspond- ing (001) surfaces of magnetite, where the iron vacancies are absent. These are the first calculations for maghemite surfaces, which take account explicitly of the iron vacancies beyond a mean-field approximation treatment [165], [166] .

5.2.2 Method

Computational Details

Calculations based on the density functional theory (DFT) have been carried out using the Quantum Espresso Package [82], [83]. We have used ultrasoft pseudopotentials to describe the interaction between the iron and oxygen ions and the valence electrons, and the approach of Perdew, Burke, and Ernzerhof (PBE) [35] for the exchange-correlation functional. We used a 4 x 4 x 1 Monkhorst - Pack (MP) grid of k-points to integrate the electronic charge [167]. The energy cutoffs for the wavefunction and charge density expansions were set to 40 Ry and 420 Ry, respectively. The calculations were spin polarized. To describe the electronic properties of the localized electron states in iron oxides we have used the Hubbard correction (DFT+U) using the implementation of Cococcioni et al. [168]. The U value for the iron atoms was set to 4 eV, a value which allows us to reproduce the experimental

bulk properties. We have calculated the maghemite bulk lattice parameters obtaining a = 8.42 Å , and c = 25.19 Å . The calculated magnetic moment per unit cell is 2.5 μ_B. These values are in agreement with those calculated by Crespo et al. [158] and with the experiments [161], [162], [169]. In order to estimate the charge transfers caused by the creation of oxygen vacancies, or by the addition of oxygen atoms to the surfaces, we have calculated the Bader charges 30 on the atoms in the different structural configurations. To investigate the occupation of the orbitals we have used the Löwdin charge [170], [171] . The surfaces have been modeled through periodically arranged symmetric slabs separated by 21 Å of vacuum, sufficient to make negligible the couplings between the periodic replicas. The x,y dimensions of the unit cell were kept fixed to the optimized bulk parameter. The atomic positions in the slabs were optimized using the Broyden-Fletcher-Goldfarb-Shanno algorithm (BFGS) as implemented in the PW.x code until the forces were less than 0.01 eV/ Å . The atoms of the central plane were kept fixed to their bulk positions. The total energy criterion for the structural optimization was set to 10^{-5} eV.

To model the bulk-truncated surfaces we have extracted portions of bulk (which by itself contains 160 atoms per unit cell). We have considered a sequence of (001) bulk planes stacked, starting from a given central plane, in the same way towards the two surface planes, as shown in Fig. 5.4. The atom arrangement in the upper and the lower half parts of the slab are the same less an in-plane rotation. In Fig. 5.4a we show the side views of the slabs corresponding to the two different surface terminations termed A and B. The slabs are formed by 11 and 13 atomic layers, respectively. The planes are labeled O, Ov, and T to indicate octahedral Fe cation and oxygen planes without iron vacancies (O), similar planes but containing iron vacancies on the octahedral sites (Ov), and planes of tetrahedral iron cations (T). The top views of the surfaces are shown in Fig. 5.4b. They are both terminated with planes containing octahedral iron cations and oxygen atoms, but, in the A slabs, the iron vacancies (black circles) are in the outermost plane Ov, whereas in the B slabs the iron vacancies (blue circles) are in the third atomic layer below the outermost atomic plane. Both surface terminations are not stoichiometric: indeed the ratio between the number of iron and oxygen atoms is different from the value 2/3 of the maghemite bulk. In the A slab the ratio is 5/8, which is Fe-poorer than the bulk, whereas in the B slab the ratio is 3/4 which is more Fe-richer than the bulk, and it is the same stoichiometry of the magnetite bulk. The main effect of structural relaxation on the bulk-truncated surfaces is to decrease the octahedral iron and oxygen bond lengths, and to increase the tetrahedral iron and oxygen bond lengths. This leads to a considerable decrease in the total energy. We have performed calculations for slabs of different thicknesses constructed following the same prescription and supporting the same terminations on the two sides, and found that the convergence of the calculated surface energies with the slab thickness was better than 0.01 eV/Å ^{2} . To study the surface reduction we have calculated the oxygen vacancy formation energies as:

$$E_{form} = \frac{1}{2}[E_{slab}(-2O) + E_{O_2} - E_{slab}], \tag{5.1}$$

where E_{slab} (-2O) is the energy of the slab with two oxygen vacancies where we have removed one oxygen atom from the top and one from the bottom planes to maintain unchanged the symmetry of the slab, E_{O_2} is the energy of the oxygen molecule, and E_{slab} is the energy of the unreduced surface. To study the oxidation of the surfaces and determine the most favorable positions for oxygen adsorption, we have calculated the potential energy surfaces (PES) for the oxygen adatom by relaxing the z

coordinate of the adatom together with the surface atoms, and keeping fixed the x and y coordinates of the adatom. The x and y coordinates belonged to a grid on the surface having a step of 1.05 Å . Once we have individuated the positions closer to the minima of the energy, we have completed the relaxation releasing further the oxygen atom in the proximity of those positions, thus finding the precise adsorption site and energy. In correspondence of the adsorption site we have calculated the adsorption energy as:

$$E_{ads} = \frac{1}{2}[E_{slab}(+2O) - E_{O_2} - E_{slab}], \tag{5.2}$$

where E_{slab}(+2O) is the energy of the slab with two oxygen atoms adsorbed, one on the top plane and the other one on the bottom plane of the slabs at corresponding positions. E_{O_2} is the energy of the oxygen molecule, and E_{slab} is the energy of the pristine surface.

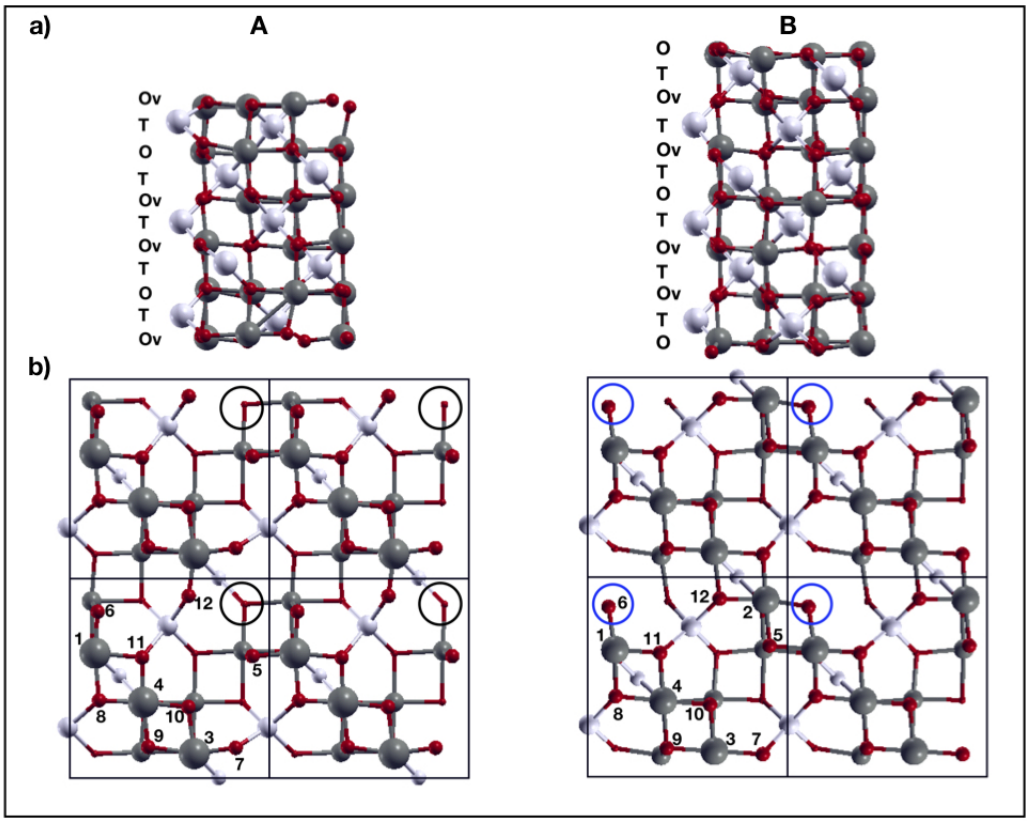

FIGURE 5.4: a) Side view of the slabs used to model the A and B surfaces; b) top view of the (2×2) unit cells of the A and B surfaces. Dark and gray balls are the octahedral and tetrahedral iron atoms, respectively. Red balls are the oxygen atoms. Black and blue circles indicate the sites of the octahedral iron vacancies on the surface (case A), and on the third layer below the outermost plane (case B), respectively. The numbers label the atoms on the outermost layer as explained in the text.

Calculation of the surface energies

Following the work of Reuter et al. [172], [173] , we have calculated the surface energies as functions of the oxygen chemical potential using a thermodynamic formalism combined with the DFT calculations. We summarize here the main equations in relation to maghemite surfaces. The maghemite surface energy $\gamma(T,p)$ at temperature T and pressure p is defined as:

$$\gamma(T,p) = \frac{1}{2}A[G(T,p,N_{Fe},N_O) - N_{Fe}\mu_{Fe}(T,p) - N_O\mu_O(T,p)], \tag{5.3}$$

where $G(T,p,N_{Fe},N_O)$ is the Gibbs free energy per unit area at temperature T and pressure p, N_{Fe} and N_O are the numbers of iron and oxygen atoms in the system, μ_{Fe} and μ_O are the iron and oxygen chemical potentials appropriate to the physical situation, and A is the surface area. We have neglected the vibrational contribution, negligible at not too high temperatures, so we can approximate $G(T,p,N_{Fe},N_O)$ with the total energy of the slab. We have divided by $2A$ since we have considered symmetric slabs with two equal surfaces. To derive the chemical potentials of Fe and O we have considered that the surface is in thermodynamic equilibrium with both its bulk and with the gaseous environment. Under this assumption the iron and oxygen chemical potentials are not independent, but they are related by the Gibbs free energy of the maghemite bulk oxide: $G^{Bulk}_{Fe_2O_3}$=$2\mu_{Fe}(T,p)$+$3\mu_O(T,p)$. It is conventional to express the surface energies as a function of the oxygen chemical potential, whose values have to satisfy some constraints. Indeed, the possible values of $\mu_O(T,p)$ have to obey the inequality $\frac{1}{3}\Delta H_f(0,0) < \Delta\mu_O < 0$, with $\Delta\mu_O = \mu_O(T,p)$ - $\frac{1}{2}E_{O_2}$. ΔH_f (0,0) is the heat of formation of the bulk maghemite oxide Fe_3O_2 in the low temperature limit, and E_{O_2} is the energy of the oxygen molecule. The lower boundary is related to the chemical potential of oxygen bonded to Fe in bulk $G^{Bulk}_{Fe_2O_3}$. The chemical potential of oxygen on the surface, being less coordinated than in the bulk, tends to be less negative. The higher boundary reflects a condition of supersaturation of oxygen on the surface which exists only in a gaseous O_2 phase. In correspondence of this value of the oxygen chemical potential, the Fe chemical potential corresponds to that of Fe metal. As previously seen the lowest limit of $\Delta\mu_O$ is one third of the heat of formation of the maghemite bulk (ΔH_f (0,0)). Our calculated ΔH_f (0,0) is -703.67KJ/mol. This value is in good agreement with the result experimentally obtained by Parkinson et al. [26], -711.1 KJ/mol . These considerations apply to the case of zero Kelvin temperature. However, since oxygen is normally in the gas phase, its properties are more subjected to variations of temperature and pressure. It is therefore necessary to determine how the oxygen chemical potential depends on temperature T and pressure p. We assume that the O_2 gas is an ideal gas which acts as a reservoir. We can, consequently, write the dependence of the oxygen chemical potential on the pressure p at temperature T as $\mu_O(T,p)$=$\mu_O(T,p^0) + \frac{1}{2}kTln(p/p^0)$, where p^0 is a reference pressure. For the dependence on temperature at the reference pressure p^0, we can write $\mu_O(T,p^0)$ as the sum of two terms: $\mu_O(T,p^0) = \frac{1}{2}E_{O_2} + \frac{1}{2}\Delta G_{O_2}(T,p^0)$ [174]. The first term is the value at T = 0 K, whereas the second is half the difference between the Gibbs free energies of the oxygen molecule at 0 K and at finite temperature T. $\Delta G_{O_2}(T,p^0)$ is linked to the entropy and enthalpy of the O_2 gas. The values for the entropy and the enthalpy of the oxygen gas are tabulated in Ref. [175] for p^0= 1 atm. In Fig. 5.5 we show how the oxygen chemical potential changes as a function of temperature and pressure. Low temperature and high pressure conditions correspond to high values of the oxygen chemical potential, whereas high temperature and low pressure conditions correspond to low values of the oxygen chemical

potential. Thus, each value of $\Delta\mu_0$ in the range indicated above can be made to correspond to a given temperature T and a given pressure p of the oxygen gas to which the surface is exposed.

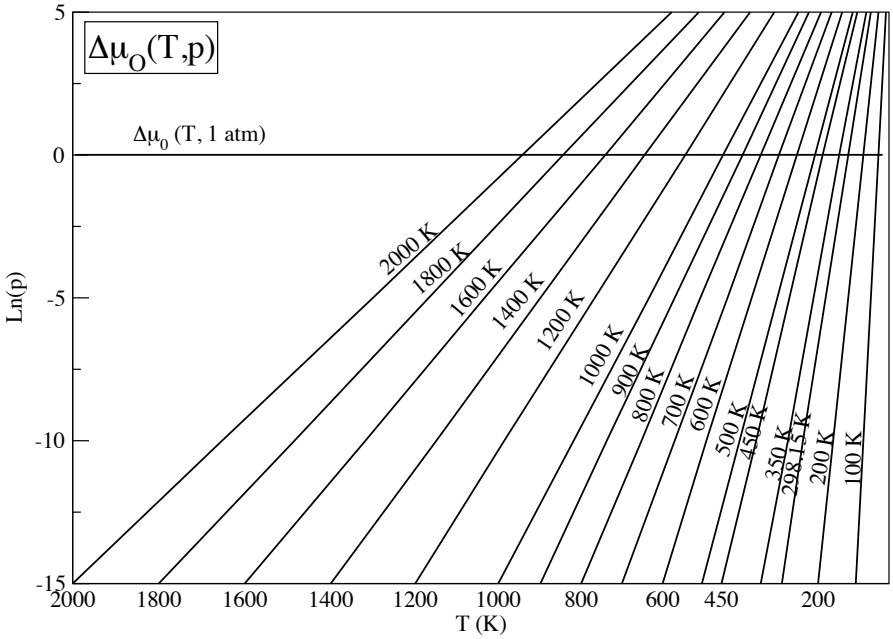

FIGURE 5.5: Variation of the oxygen chemical potential $\Delta\gamma_O$ (T, p) as function of the temperature (T) and pressure (p)

5.2.3 Results

Reduction and Oxidation of the (001) maghemite and magnetite surfaces

The reduction and oxidation properties of maghemite and magnetite surfaces are crucial for estimating their catalytic potential. Consequently, in this section we have investigated the energy required to remove and to add one oxygen atom from/to the surfaces. We have considered two Fe_3O_4(001) surfaces: the $R45(\sqrt{2}\times\sqrt{2})$ one, which has been considered for many years as the most stable, and it was suggested on the basis of experiments [164], [176], [177], and DFT calculations [178], and the recent reconstruction observed by Bliem et al. [32]. We have considered this last reconstruction because the authors [32] have found that this surface is more stable than the $R45(\sqrt{2}\times\sqrt{2})$ over a wide range of oxygen chemical potential values. Following their notation, we term this surface SCV. In Fig. 5.7 we show the side (a, b) and top (c, d) views of the two Fe_3O_4 surfaces. Both surfaces are terminated with a plane containing octahedral iron and oxygen atoms. We model the $R45(\sqrt{2}\times\sqrt{2})$ surface with slabs having the same sequence of planes as for the maghemite surfaces, but with all the iron sites occupied, since there are not iron vacancies in magnetite. In the SCV surface an additional tetrahedral iron atom is inserted in the second layer while two octahedral iron atoms are removed from the third layer below the outermost plane. Due to the stability of the SCV Fe_3O_4 (001) surface reconstruction, we have considered the same reconstruction also for the (001) maghemite surface that we term SCV_M . As shown in Fig. 5.6, there are two octahedral iron vacancies (blue circles) in the third layer below the surface, and an additional tetrahedral iron atom above them in the second layer.

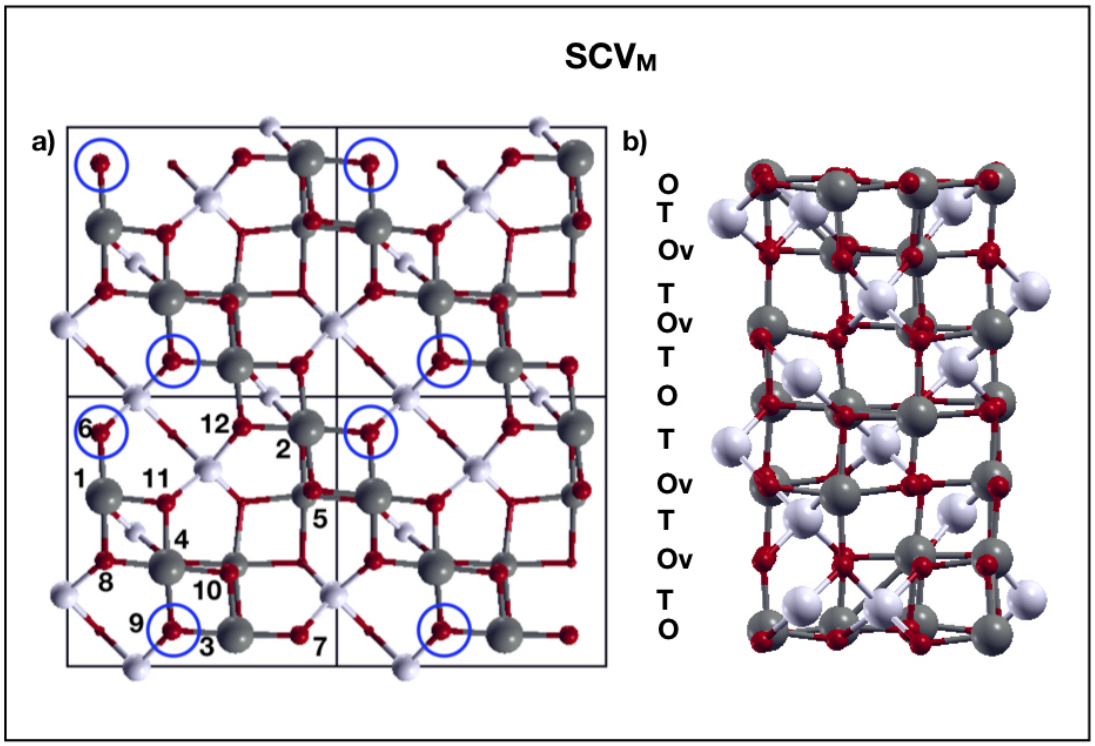

FIGURE 5.6: a)Top view of the (2×2) unit cell of the SCV_M reconstruction of the γ-Fe_2O_3 (001) surface; b) side view of the slab used to model the SCV_M reconstruction of the γ-Fe_2O_3 (001) surface. The color code is the same as in Fig. 5.4. Blue circles indicate the location of the Fe vacancy in the third layer below the outermost plane. The numbers label the atoms on the outermost layer as explained in the text.

Reduction properties of the maghemite surfaces

First, we report the results on the calculations of the formation energies of the oxygen vacancies on the bulk-truncated A and B maghemite surfaces. We have classified the surface oxygen atoms according to their oxygen-iron first-neighbor bonds. The Fe - O bonds were considered first-neighbor if the atom distances were comprised between 1.7 Å and 2.1 Å . On the surface plane the four Fe atoms are labeled from 1 to 4 (see Fig. 5.4) and the 8 oxygen atoms are labeled from 5 to 12. On both A and B surfaces the oxygen atoms labeled as O_9 and O_{10} are bonded to three octahedral iron atoms (two iron atoms in the same surface layer, and one in the third atomic layer below), while the oxygen atoms labeled O_8 and O_{11} are bonded to two octahedral and one tetrahedral iron atoms. The other four oxygen atoms have a different first-neighbor coordination on the two A and B surfaces. In the case of the A surface, due to the presence of the iron vacancy on the outermost layer, the atoms O_5 and O_6, are only bonded to two octahedral iron atoms (one on the surface layer and one in the third layer). O_7 and O_{12} also have only two bonds: one to one octahedral iron atom and the other one to one tetrahedral iron atom. On the B surface, instead, atom O_5 is bonded to three octahedral iron atoms, whereas O_6 is the only one with only two bonds to two octahedral irons. Atoms O_7 and O_{12} have the same bonding configuration as atoms O_8 and O_{11}, but their positions with respect to the iron vacancy in the third layer below is different, thus, they are not equivalent to atoms

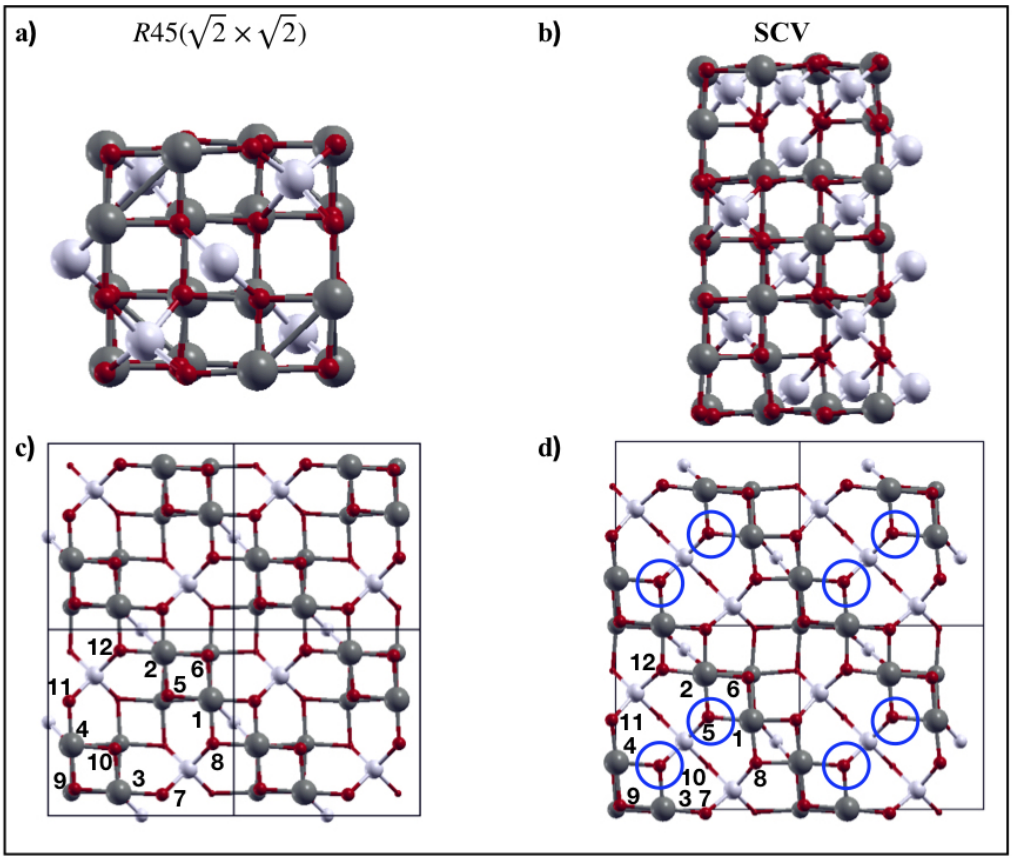

FIGURE 5.7: a) Side view of the slab used to model the $R45(\sqrt{2}\times\sqrt{2})$ (001) Fe_3O_4 surface; b) side view of the slab used to model the SCV reconstruction of the (001) magnetite surface proposed by Bliem et al. [32] ; c) top view of the (2×2) unit cell of the $R45(\sqrt{2}\times\sqrt{2})$ (001) Fe_3O_4 surface; d) top view of the (2×2) unit cell of the SCV reconstruction of the Fe_3O_4 (001) surface. Dark and light grey balls are the octahedral and tetrahedral iron atoms, respectively. Red balls are the Oxygen atoms. Blue circles indicate the location of the Fe vacancies in the third layer below.

O_8 and O_{11}. Their vacancy formation energies are reported in Table 5.1. The oxygen atoms that we have indicated in the Table as equivalent have formation energies for their removal that differ at most of ± 0.01 eV. On the magnetite $R45(\sqrt{2}\times\sqrt{2})$ surface reconstruction, due to the absence of iron vacancies, there are only two kinds of oxygen atoms: atoms bonded only to octahedral iron atoms, and atoms bonded to both octahedral and tetrahedral iron atoms (see Fig. 5.7). In the SCV magnetite reconstruction, if we consider again only the first neighbor atomic environment, we have three kinds of oxygen atoms since two oxygen (O_5 and O_{10}) are above the octahedral iron vacancies in the third layer below. In Table 1 we report the calculated oxygen vacancy formation energies E_{form} also for the magnetite surfaces. The oxygen vacancy formation energies calculated for the oxygen atoms bonded only to the octahedral iron atoms in the $R45(\sqrt{2}\times\sqrt{2})$ Fe_3O_4 (001) surface are in agreement with the value, 1.11 eV, calculated by Yu. et al. [179].

We can observe that, in general, it is easier to remove the oxygen atoms bonded only to octahedral iron atoms, i.e. the atoms indicated as O_5-O_6-O_9-O_10 in the A,

TABLE 5.1: Formation energy E_{form} of oxygen vacancies on the maghemite A, B, B′, and SCV_M surfaces, and on the $R45(\sqrt{2}\times\sqrt{2})$ and SCV magnetite surfaces. The labels of the oxygen atoms are shown in Figs. 5.4, 5.6, and Fig. 5.7. The numbering of the oxygen atoms on the B′ surface is the same as for the B surface apart from the removed oxygen O_5. All the formation energies are in eV.

Maghemite		Maghemite		Maghemite		Maghemite		Magnetite		Magnetite	
A		B		B′		SCV_M		$R45(\sqrt{2}\times\sqrt{2})$		SCV	
O	E_{form}	O	E_{form}	O	E_{form}	O	E_{form}	O	E_{form}	O	E_{form}
5-6	0.41	5-6	-0.13	6	2.53			5-6	1.09		
7-12	1.10					6-9	0.38			5-10	1.77
8-11	2.09	8-12	1.83	8-12	2.22	8-12	1.47	8-12	2.08	8-12	2.32
		7-11	2.50	7-11	2.42	7-11	1.47	7-12	2.08	7-11	2.32
9-10	0.42	9-10	0.85	9-10	1.57	5-10	1.47	9-10	1.09	6-9	1.68

B, and $R45(\sqrt{2}\times\sqrt{2})$. The energy cost is, indeed, almost 1 eV less than the energy required to extract the oxygen atoms bonded also to tetrahedral iron atoms. Also Yu et al. [179] and Mulakaluri et al. [180] have found that the energy required to create a vacancy on the $R45(\sqrt{2}\times\sqrt{2})$ increases if the oxygen is bonded to tetrahedral iron atoms. The only exception is provided by the SCV_M and SCV reconstructions where the two oxygen atoms above the octahedral iron vacancies have a lower E_{form} despite being bonded also to the additional tetrahedral iron. It is, indeed, the proximity of the Fe vacancies that reduces E_{form} . We have found that the initial electronic charge rearrangement at the surface with respect to the bulk plays a key role in determining the reducibility of the surfaces. In Table 5.2 we show the variation of the electronic charge of the oxygen atoms at the surfaces compared to the value in the bulks.

TABLE 5.2: Variation of the surface oxygen electronic charge in (e) with respect to the their bulk value on the studied surfaces.

Maghemite		Maghemite		Maghemite		Maghemite		Magnetite		Magnetite	
A		B		B′		SCV_M		$R45(\sqrt{2}\times\sqrt{2})$		SCV	
O	e	O	e	O	e	O	e	O	e	O	e
5-6	-0.30	5-6	-0.30	6	< - 0.10			5-6	< -0.10		
7-12	-0.25					6-9	-0.11			5-10	<0.10
8-11	-0.10	8-12	-0.11	8-12	<0.10	8-12	-0.10	8-12	<-0.10	8-12	<-0.10
		7-11	-0.10	7-11	< -0.10	7-11	< -0.10	7-12	<-0.10	7-11	<-0.10
9-10	-0.30	9-10	-0.11	9-10	<-0.10	5-10	-0.18	9-10	<-0.10	6-9	<-0.10

Comparing Table 5.1 and 5.2 we note that it is easier to remove the oxygen atoms whose charge is most diminished with respect to the bulk value. The presence of the iron vacancies on the outermost layer on the A surface causes most of the charge loss for the surface oxygens. On the B and SCV_M surfaces, instead, only the oxygen atoms above the iron vacancies, have less charge. On the other hand, on the

$R45(\sqrt{2} \times \sqrt{2})$ magnetite surface, just because of the lack of Fe vacancies, the variation of the electronic charge is not significant for all oxygen atoms, and the vacancy formation energy is always larger. On the SCV Fe_3O_4 (100) reconstruction two octahedral iron vacancies are present in the third layer below, (see Fig. 5.7), but still there is not a significant variation of the surface oxygen charges with respect to the bulk values. In this case we have found that electronic charge has been transferred to the surface oxygen atoms from the octahedral iron atoms below, which become Fe^{3+} from Fe^{2+}. Fe^{2+} are present only in magnetite and not in maghemite. This explains the lower E_{form} found for SCV_M maghemite reconstruction compared to the SCV magnetite reconstruction for the removal of the corresponding surface oxygen atoms. Following this rule, it is easier to remove oxygen atoms from the A surface than from the B surface, but there is an important exception. On the B surface the two less charged oxygen atoms will tend to spontaneously leave the surface. The creation of the oxygen vacancies is, indeed, thermodynamically favored since their formation energies are negative. Thus, a more stable reconstruction for the maghemite (001) surface can be obtained from the bulk-truncated B surface by removing one of these oxygen atoms. We term B′ this new surface termination. We also consider the analogously reduced surface structure obtained from the A surface by removing atom O_{10}. This surface is less stable at the temperature $T = 0$ K than the bulk-truncated A surface but it is one of those having the lowest surface energy among the reduced surfaces of the A surface. By analogy with the B′ surface we term this reduced surface A′. We have also found a correlation between the value of the vacancy formation energy and the change in the oxidation states of the Fe atoms. The rule is the following: the vacancy formation energy is larger if the electronic charge left behind by the removed oxygen atoms goes to reduce the iron atoms (see Table 5.3, where the symbol asterisk indicates the Fe atoms that have acquired the oxygen charge). If, instead, the excess charge is acquired by the other less charged oxygen atoms, which become thus closer to the -2 nominative oxygen oxidation state, the creation of the oxygen vacancy is more favored. On the magnetite surfaces, as shown in Table 5.2, all the surface oxygen atoms are charged as in the bulk, where they are already in their favorite -2 oxidation state. Thus, the excess of charge, due to the removal of the oxygen atom, always leads to the reduction of Fe atoms. Yu et al. [179] have, indeed, found that, following the creation of the vacancy on the $R45(\sqrt{2} \times \sqrt{2})$ surface, two iron atoms increase their electronic charge (+0.39 e), changing their oxidation state. For the same surface, we have calculated an increase of 0.40 e (see Table S1), a value which is in good agreement with theirs. Since the maghemite B′ surface, which has one less oxygen atom, O_5 or, equivalently O_6, see Fig. 5.4, is more stable than the B surface, we have calculated the formation energy of an oxygen vacancy also for this surface. The results are reported in Table 5.1. As shown in the table, the creation of the oxygen vacancy on this surface is more unfavored than on the A and B surfaces. In particular, the oxygen O_6, whose vacancy formation energy is small on the A and B surfaces, becomes harder to remove on the B′ surface. It is interesting to examine the reconstructed B′ surface shown in Fig. 5.8. O_6, the oxygen partner of the removed one, because bonded to the same Fe atoms (blue balls in Fig. 5.8), moves in a bridge position between the two iron atoms, shortening the bond to them. This bond shortening is an indication of bond strengthening. Thus, above the Fe vacancy in the third layer this new structural motif develops on the surface. A similar reconstruction occurs also on the A′ surface, but in this case, the partner of the removed oxygen is located in a neighboring position to the surface Fe vacancy, and its shift to the bridge position is not complete, as shown in Fig. 5.9.

TABLE 5.3: Variation of the Bader charges of the octahedral and tetrahedral iron atoms following the creation of the oxygen vacancy on the surfaces. The symbol asterisk indicates the Fe atoms that have acquired more electronic charge. The labels of the oxygen and iron atoms on the surface outermost layer refer to Figs. 5.4, 5.6, 5.8 and 5.7.

Atom	A				R45($\sqrt{2}\times\sqrt{2}$)		SCV		
	10	6	12	11	5	8	6	12	10
Atom	Δe	Δe	Δe	Δe	Δe	Δe	Δe	Δe	Δe
Fe_1	0.01	0.10	-0.01	0.03	0.02	0.10	0.38 *	-0.02	-0.03
Fe_2	/	/	/	/	0.03	0.01	0.12	0.01	0.03
Fe_3	0.05	-0.03	0.14	0.00	0.36*	0.00	0.01	0.38 *	0.06
Fe_4	0.10	0.06	0.00	0.15	0.40 *	0.40*	0.01	0.00	0.08
Fe_T	0.03	0.01	0.38*	0.39*	0.01	0.40*	0.01	0.41*	0.01
Fe_T	0.00	0.00	0.00	. 0.02	0.00	0.02	0.02	0.01	0.00
Fe_T	/	/	/	/	/	/	-0.01	-0.02	0.38*
Fe_O	0.05	0.00	0.02	0.01	0.18	-0.16	0.35*	-0.02	0.00
Fe_O	-0.01	0.03	0.00	-0.02	-0.13	0.19	-0.02	-0.02	0.34*
Fe_O	0.01	0.00	-0.01	0.01	-0.03	-0.01	/	/	/
Fe_O	0.03	0.01	-0.01	0.01	0.09	0.00	/	/	/

	B					B′			
	5	6	9	11	12	9	6	11	12
Atom	Δe	Δe	Δe	Δe	Δe	Δe	Δe	Δe	Δe
Fe_1	0.09	0.09	0.02	0.32*	0.00	0.00	0.45*	0.40*	0.04
Fe_2	0.11	0.09	0.05	0.02	0.10	0.00	0.43*	0.01	0.42*
Fe_3	0.02	0.05	0.07	0.03	0.11	0.37*	0. 00	0.03	0.12
Fe_4	-0.01	0.01	0.05	0.28*	0.00	0.43*	0.06	0.12	0.05
Fe_T	0.00	0.00	0.00	0.11	0.40*	0.00.	0.01	0.42*	0.42*
Fe_T	0.00	0.00	0.01	0.01	0.02	0.00	0.01	0.01	0.02
Fe_O	-0.01	0.00	-0.01	0.02	0.01	0.00	-0.01	-0.02	0.02
Fe_O	0.01	0.01	0.37*	0.00	-0.01	0.06	0.00	0.00	0.00
Fe_O	0.06	0.05	-0.03	0.00	0.01	0.00	0.00	0.02	-0.04

	SCV_M			
	5	6	7	8
Fe_1	0.07	0.04	0.01	0.07
Fe_2	0.06	0.05	0.11	0.02
Fe_3	0.06	0.07	0.08	0.04
Fe_4	0.04	0.05	0.03	0.11
Fe_T	0.00	-0.03.	0.00	0.00
Fe_T	0.00	0.00	0.05	0.05
Fe_T	0.02	-0.01	0.00	0.01
Fe_O	0.00	0.06	0.01	0.00
Fe_O	0.03	0.03	0.03	0.01

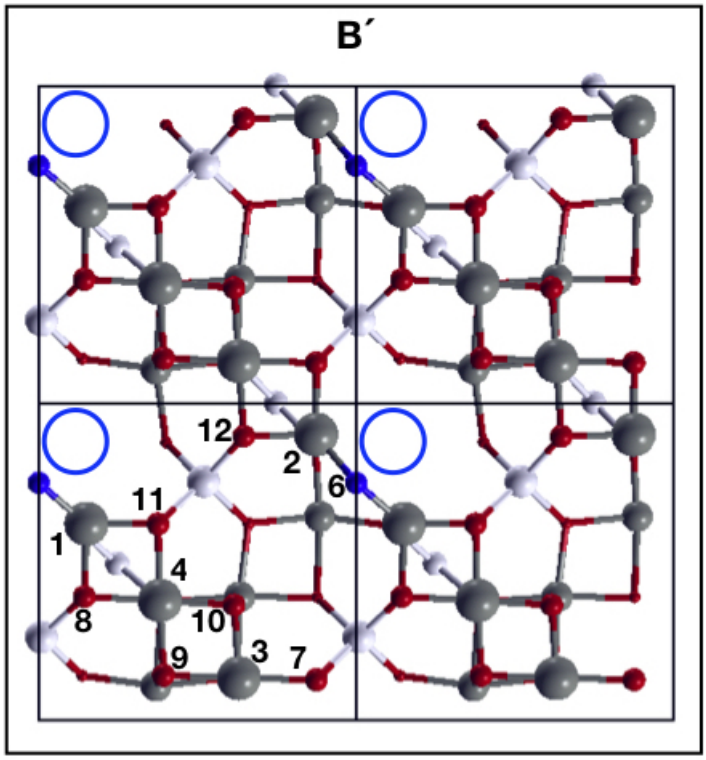

FIGURE 5.8: Top view of the (2×2) unit cell of the B′ surface. Blue circles indicate the Fe vacancy in the third layer below. The blue balls represent the oxygen atoms partner of the removed oxygens. The color code is the same as in Fig. 5.4. The numbers label the atoms on the outermost layer as explained in the text.

The variation of the charge on the iron atoms following the oxygen removal from the B′ surface is reported in Table 5.3. By comparing the vacancy formation energies calculated for the maghemite and magnetite surface reconstructions, we have found that it is easier, in general, to create one oxygen vacancy on the maghemite surfaces than on the corresponding magnetite surfaces (bulk-truncated A-B vs $R45(\sqrt{2}\times\sqrt{2}$), SCV_M vs SCV, and most stable B′ vs SCV). Thus, the maghemite (001) surfaces tend to be more reducible than the corresponding magnetite ones. The Fe vacancies and the absence of Fe^{2+} cations play a key role in increasing the reducibility of the maghemite surfaces.

Oxidation properties of the (001) maghemite surfaces

We have calculated the oxidation properties of the maghemite bulk-truncated A and B surfaces, and the reduced B′ surface. In order to determine the preferential adsorption sites for the oxygen atom, we have calculated the Potential Energy Surface (PES) for one oxygen atom adsorbed on the surface. The calculated PES are shown in Fig. 5.10 where we have reported the positions of the atoms of the first atomic layers. In all the PES the level 0 corresponds to the lowest calculated adsorption energy, and the dark blue areas indicate the most favorite adsorption sites. For the A surface, one adsorption site sees the added oxygen atom bonded to an octahedral iron atom (Fe_4), in the position indicated by the red cross in Fig. 5.10a. Following the adsorption, the

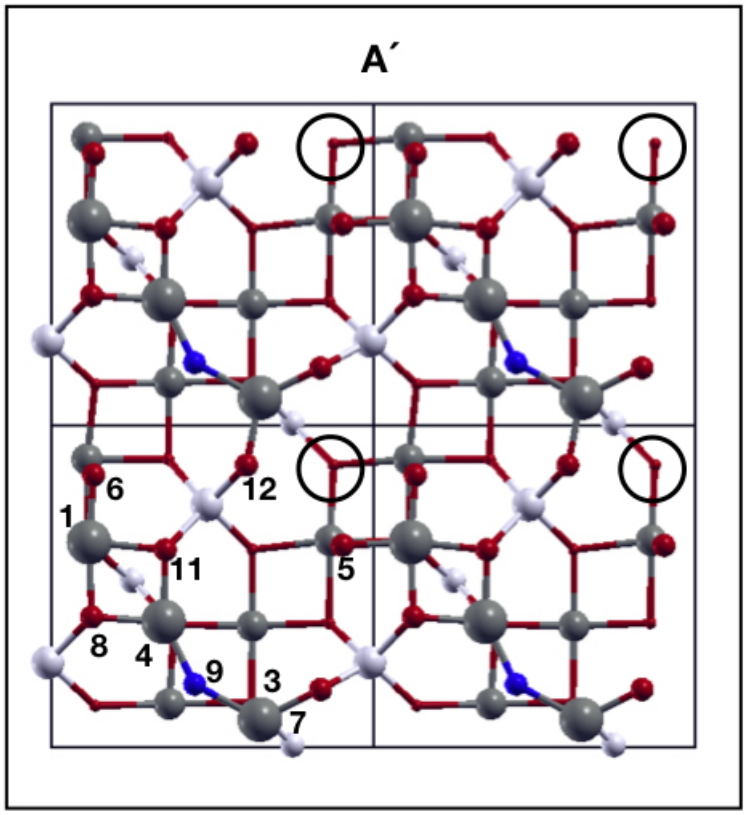

FIGURE 5.9: Top view of the (2×2) A′ surface. Dark and gray balls are the octahedral and tetrahedral iron atoms, respectively. Red balls are the oxygen atoms. Blue balls are the oxygen atoms partners of the removed oxygen atom. Black circles indicate the Fe vacancies on the outermost layer.

O_9 atom breaks its bonds with Fe_3 and Fe_4, and creates a new bond with the added oxygen atom forming a dimer as shown in Fig. 5.11a with an O-O distance of 1.26 Å, slightly larger than the O_2 bond (1.24 Å). The adsorption energy, calculated using Eq. 5.2, is only 60 meV. Another possible adsorption site is near the iron Fe_3, in the position symmetric to Fe_4 with respect to O_9. In general, as we see from Fig. 5.10a, other preferential adsorption sites are closer to some of the less charged surface oxygen atoms. In the case of the B surface, the adatom prefers to bind to the octahedral Fe_4 atom and to a near surface oxygen as indicated by the red cross in Fig. 5.10b. Following the adsorption, the surface oxygen moves upwards, almost at the same height of the adatom, but, differently than for the A surface, both oxygens remain bonded to their Fe atoms, as shown in Fig. 5.11b. The O-O distance is now 1.34 Å , larger than the O_2 bond length. The calculated adsorption energy E_{ads} is 0.31 eV, larger than the energy required to adsorb the oxygen on the A surface. Thus, we see that the adsorption of an oxygen atom on the A and B surfaces leads to the formation of an O-O bond on the surface. The situation is different on the stable B′ surface, obtained by the B surface by removing O_5. The preferential adsorption site, indicated by the red cross in Fig. 5.10c, is near the position of the partner oxygen O_6 (blue ball in Fig. 5.10c). The added oxygen binds to Fe_1, Fe_2, and to O_6 as shown in Fig. 5.11c. The adsorption energy is 0.61 eV, significantly larger than the values calculated on

the bulk truncated surfaces. To recover the original B termination, an energy barrier needs to be overcome by the added atom since the oxygen O_6 needs to be pushed to the position of the previous removed oxygen. It is interesting to look at the charge transfer caused by the adsorption and its relation to the adsorption energy. On the A surface, where most surface oxygens are less charged than on the B surface, one oxygen atom gains a charge +0.2 e becoming closer to the -2 oxidation state. This charge transfer makes the process more favorable. On the contrary on the B and B'' surfaces no oxygen atoms gain electronic charge following the oxygen adsorption. We have studied the same adsorption process also on the $R45(\sqrt{2} \times \sqrt{2})$ Fe_3O_4 surface. In this case the added oxygen binds not to oxygen atoms, but to an octahedral iron atom, as shown in Fig. 5.11d. The adsorption energy is 0.74 eV, slightly larger than the adsorption energy calculated for the maghemite B′ surface. This behavior is explained by the fact that on the magnetite surface the oxygen atoms are already closer to the -2 oxidation state, and do not need to acquire extra charge. Thus, our results show that also oxidation is more favored on the maghemite surfaces than on the magnetite one.

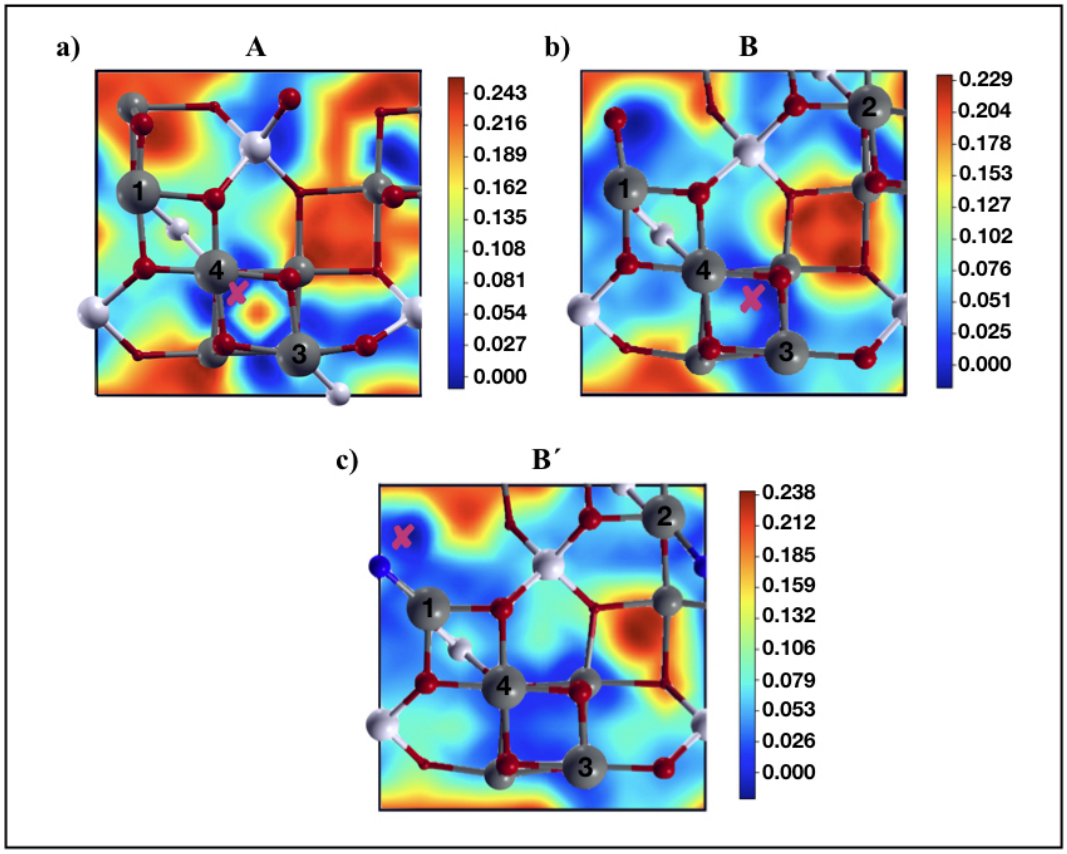

FIGURE 5.10: Potential Energy Surfaces (PES) for one oxygen adatom on the maghemite A, B, and B′ surfaces. The positions of the atoms of the first four layers are shown. Dark and light gray balls are the octahedral and tetrahedral iron atoms, respectively. Red balls are the oxygen atoms. The blue ball is the oxygen atom on B′ , that defines the new stable maghemite reconstruction. The crosses on the PES indicate the most favorite adsorption sites. The energy scale is in Ry.

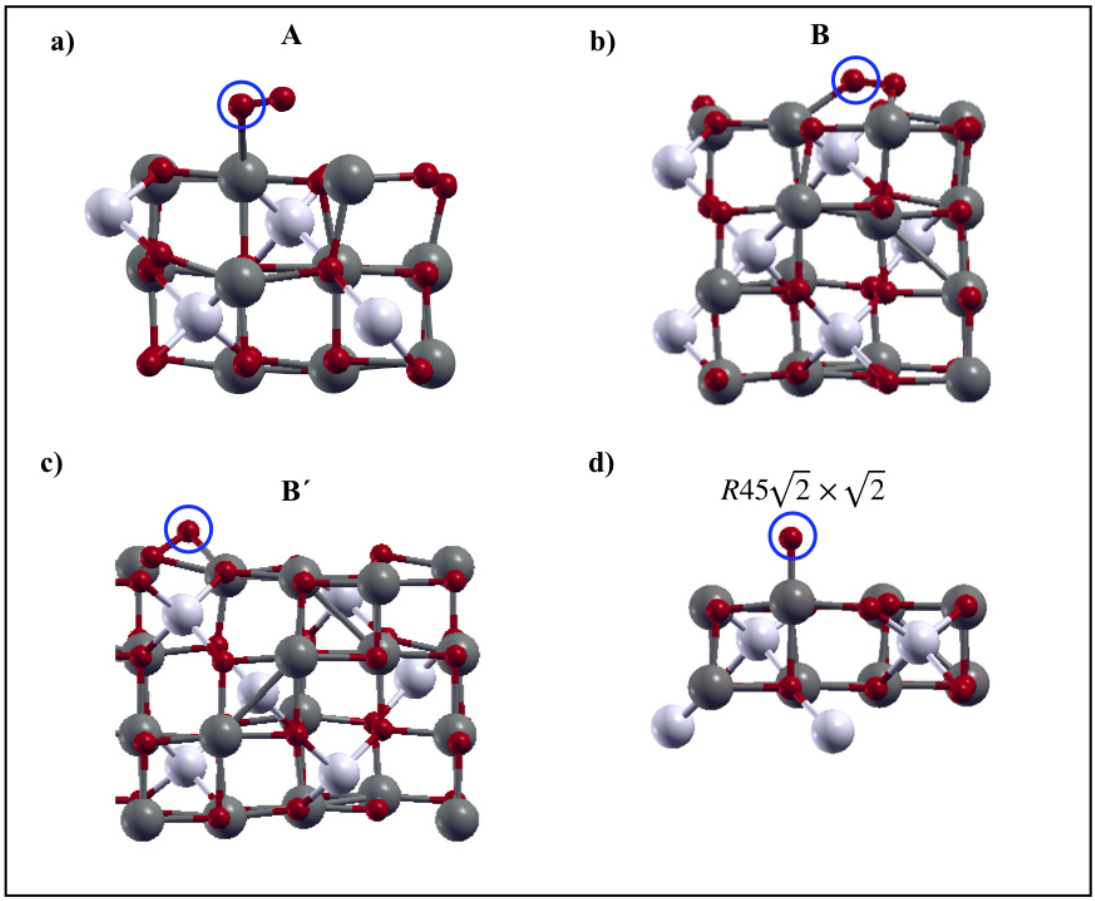

FIGURE 5.11: a) Side view of the upper half of the slab used to describe the A surface after the adsorption of an additional oxygen atom; b) side view of the upper half of the slab used to describe the B surface after the adsorption of an extra oxygen atom; c) side view of the upper half of the slab used to describe the B′ surface with an additional adsorbed oxygen atom; d) side view of the upper half of the slab used to describe the $R45(\sqrt{2} \times \sqrt{2})$ magnetite surface with an additional adsorbed oxygen atom The blue circles show the oxygen atom adsorbed on the surface. The atom color code is the same as in Fig. 5.4.

Surface Energies

We now correlate the reduction properties of the maghemite and magnetite surfaces with their relative stability under ambient conditions. In Fig. 5.12 a we plot the energies γ of the studied maghemite surfaces: the bulk-truncated A and B surfaces, their reduced A′ and B′ surfaces, B″ which is the reduced B′ surface, the SCV_M and its reduced $SCV_{M'}$ reconstructions, as a function of the oxygen chemical potential $\Delta\mu_O$. The plot allows us to compare the relative stability of the surfaces, since they have not the same stoichiometry, at the ambient conditions (temperature and pressure of the oxygen gas to which the surface is exposed).

In the figure we have indicated the interval of the oxygen chemical potential values corresponding to a range of pressure p at a fixed T = 600 K. Different experimental groups have indeed synthetized maghemite films [157], [181] at this temperature. We see that over the range of pressures of interest, the B′ surface is the most stable

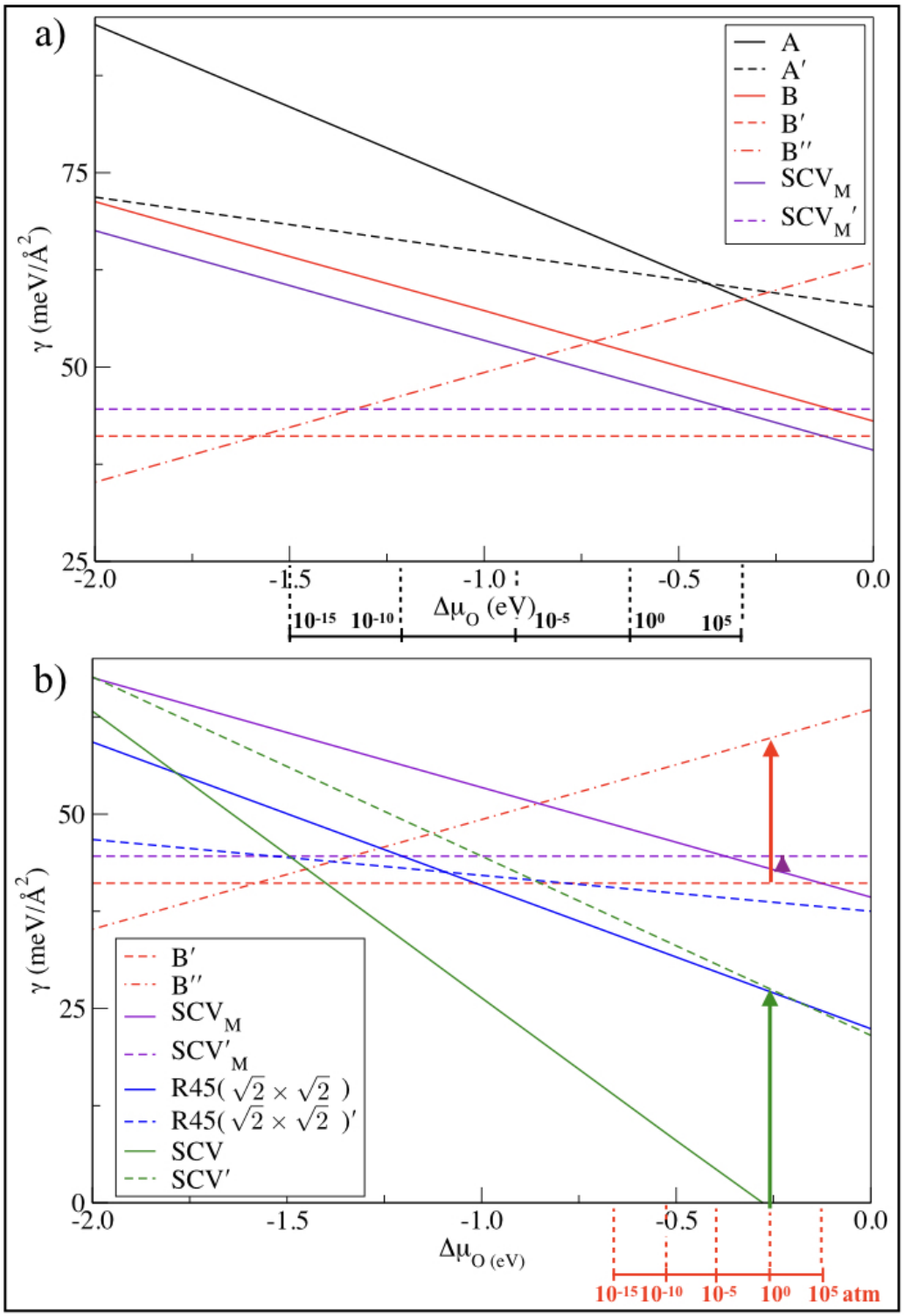

FIGURE 5.12: a) Surface Energies γ of maghemite surfaces as a function of the oxygen chemical potential $\Delta\mu_O$. Above the plot we have indicated the values of $\Delta\mu_O$ corresponding to a wide range of pressures (in atm) at the fixed temperature T = 600 K. b) Surface Energies γ of the pristine and reduced maghemite and magnetite surfaces as a function of the oxygen chemical potential $\Delta\mu_O$. Below the plot we have indicated the values of $\Delta\mu_O$ corresponding to a wide range of pressures (in atm) at the temperature T = 300 K. A and B are the bulk-truncated surfaces, A′ and B′ their reduced surfaces, and B″ is the reduced B′ surface. SCV'_M is the reduced SCV_M surface. $R45(\sqrt{2}\times\sqrt{2})$ and SCV are two Fe_3O_4 (001) surfaces, and $R45(\sqrt{2}\times\sqrt{2})$ SCV′ are their reduced surfaces. The arrows indicate the energy $\Delta\gamma$ required to pass from a surface to its reduced one.

surface. Also the bulk-truncated B surface is more stable than the A one, and this is true also for their reduced surfaces A′ and B′. Thus, the presence of the iron vacancies on the outermost layer tends to destabilize the surface. The reduced surfaces (A′ and B′) are more stable than their corresponded bulk-truncated A and B surfaces, so maghemite surfaces will tend to loose surface oxygen atoms. The oxidized surfaces are more unstable than the pristine surfaces, and, thus, are not reported in the figure. The SCV_M reconstruction is more stable than the bulk truncated surfaces over all the indicated range of oxygen chemical potentials. At 600 K its reduced SCV'_M surface is even more stable, but not as stable as the B′ surface. From Fig. 5.12 it can been seen that the B″ and SCVM surfaces can become stable at given values of the oxygen chemical potentials. The reduced B″ is the most stable surface only at high temperatures, $T > 600$ K, and low pressures, i.e at T=1000 K, p must be lower than 10^{-5} atm. In contrast, the SCV_M surface is stable only at low temperatures, for example at T=300 K, p must be at least 105 atm, whereas at lower temperatures, lower pressures are permitted. In Fig. 5.12b we compare the surface energies of the more stable maghemite B′ and SCV_M surfaces with the magnetite $R45(\sqrt{2} \times \sqrt{2}$ and SCV ones, together with those of their reduced surfaces. Below we show the range of oxygen chemical potentials corresponding to a range of pressure value p at the temperature T = 300 K. At this temperature experimental groups [149], [182] have performed catalytic experiments concerning CO oxidation [149] and hydrogen peroxide decomposition [182] . The length of the vertical arrows at p = 1 atm represents the reducibility of the surfaces at this pressure. For the most stable maghemite and magnetite surfaces, B′ and SCV, the energy required to reduce the surface is less for the maghemite (18.4 meV/Å ^{2}) than for magnetite surface (28.3 meV/Å ^{2}). It is interesting to note that at p = 1 atm the reduction energy $\Delta\gamma$ is very small for the SCV_M surface (1.5 meV/Å ^{2}), which has a surface energy slightly larger than B′. Our results have shown that the reduction and oxidation reactions are in relation with the stability of the surfaces. Indeed, the oxygen vacancy formation energies and the adsorption energies tend to be higher on the most stable maghemite and magnetite surfaces.

Electronic properties of the surfaces

To understand the trends in surface stability and reduction properties is instructive to look also at the electronic properties of the surfaces. We report in Figs. 5.13 and 5.14 the atomic projected density of states (apdos) of the maghemite bulk, of the maghemite bulk-truncated A and B surfaces, and of the most stable B′ surface. The total density of states (dos) and the band structure are shown in Figs. 5.15 and 5.16, respectively. We have also analyzed the variation of the related magnetic moments due to the surface modifications, a phenomenon which is at the heart of the use of iron-oxide nanoparticles as markers in diagnostic biomedicine, since iron-oxides are biocompatible materials 46. In the apdos we distinguish the electronic states of the spin up and spin down channels, and the contributions due to the surface atoms (indicated with *) and the bulk atoms. We define as bulk atoms the atoms in the center layer of the slabs that we have used to model the surfaces. As shown in Figs. 5.13a 5.15a, and 5.16a we see that the maghemite bulk is a semiconductor with different energy gaps for the spin up and down channels: 1.80 eV and 1.75 eV, respectively, in reasonable agreement with the experimental value, -2 eV 47. As for most reducible oxides, the top of the valence band is composed of the oxygen p states, while the bottom of the conduction band is formed by the cation d states. The calculated magnetic moments of the octahedral and tetrahedral iron atoms of the

maghemite bulk are 3.73 μ_B and -3.50 μ_B, respectively, and the magnetic moment of the bulk formula unit is 2.5 μ_B, in agreement with the experimental measurements 29. These values are related to the electronic states of the Fe atoms as shown in the apdos of Fig. 5.13a. The spin up states of the octahedral and tetrahedral iron atoms are in the valence and conduction band, respectively; and the opposite is true for the spin down states.

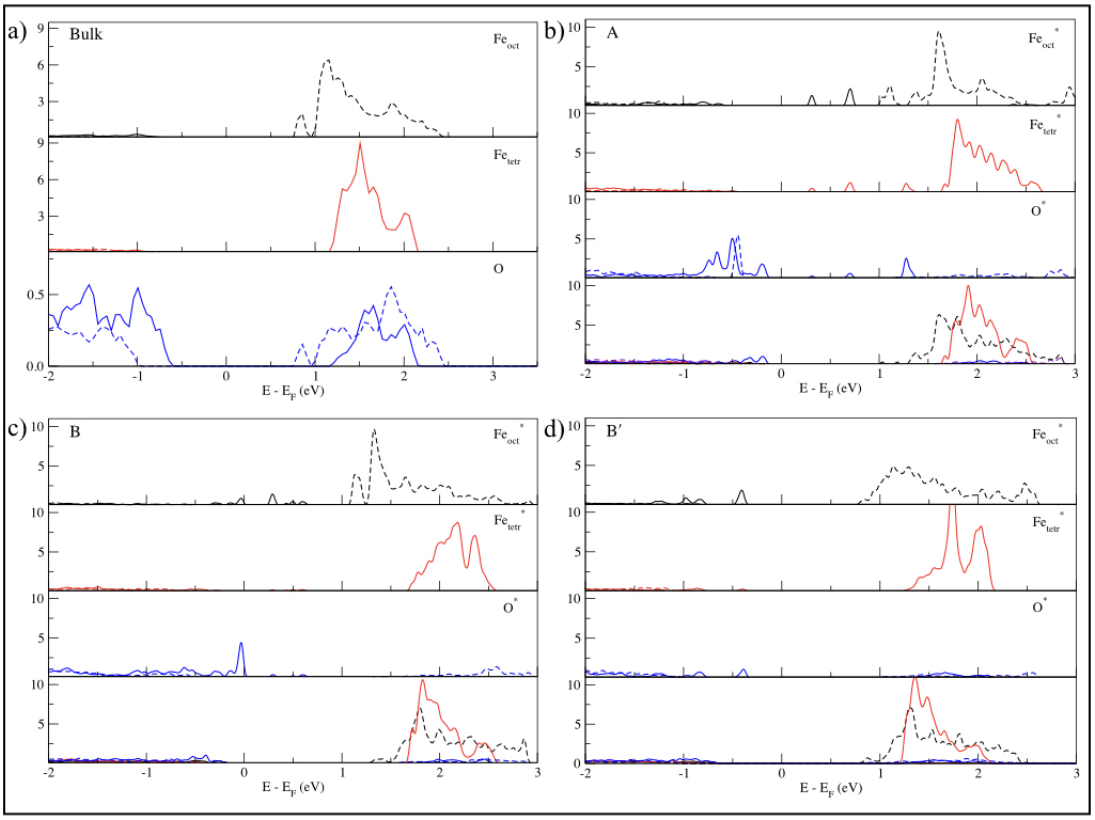

FIGURE 5.13: Atomic projected density of states (apdos) of: a) maghemite bulk, b) A surface, c) B surface, d) and B′ surface. Fe^*_{oct}, Fe^*_{tetr}, and O* are the surface atoms. Fe_{oct}, Fe_{tetr}, and O are the bulk atoms. Continued and dashed lines are the spin up and down contributions, respectively. The last panel of b), c), and d) shows the apdos of the bulk atoms (middle layer of the slab), and the color code is the same used in a). In panel a) different scales have been used to increase the visibility.

In the apdos of the bulk-truncated A and B surfaces we notice the appearance of new peaks at the bottom of the conduction band related to localized states. To these states contribute only surface atoms, so they are surface states. The A surface is semiconducting with different energy gaps for the spin up and down components: 0.35 and 1.33 eV, respectively, as shown in Figs. 5.13b, 5.15b, and 5.16b. These energy gaps are both smaller than those calculated for the bulk due to the presence of the surface states. Contrary to the A surface, the B surface is not semiconducting. Thus, moving the Fe vacancy from the outermost layer to the third layer below the outermost one causes the surface electronic structure to change significantly. As shown in Figs. 5.13c, 5.15c, and 5.16c , the spin up surface states of the Fe atoms and of the surface oxygen atoms touch the Fermi Energy. For the spin down contribution we have calculated an energy gap of 1.48 eV, also smaller than in the maghemite bulk.

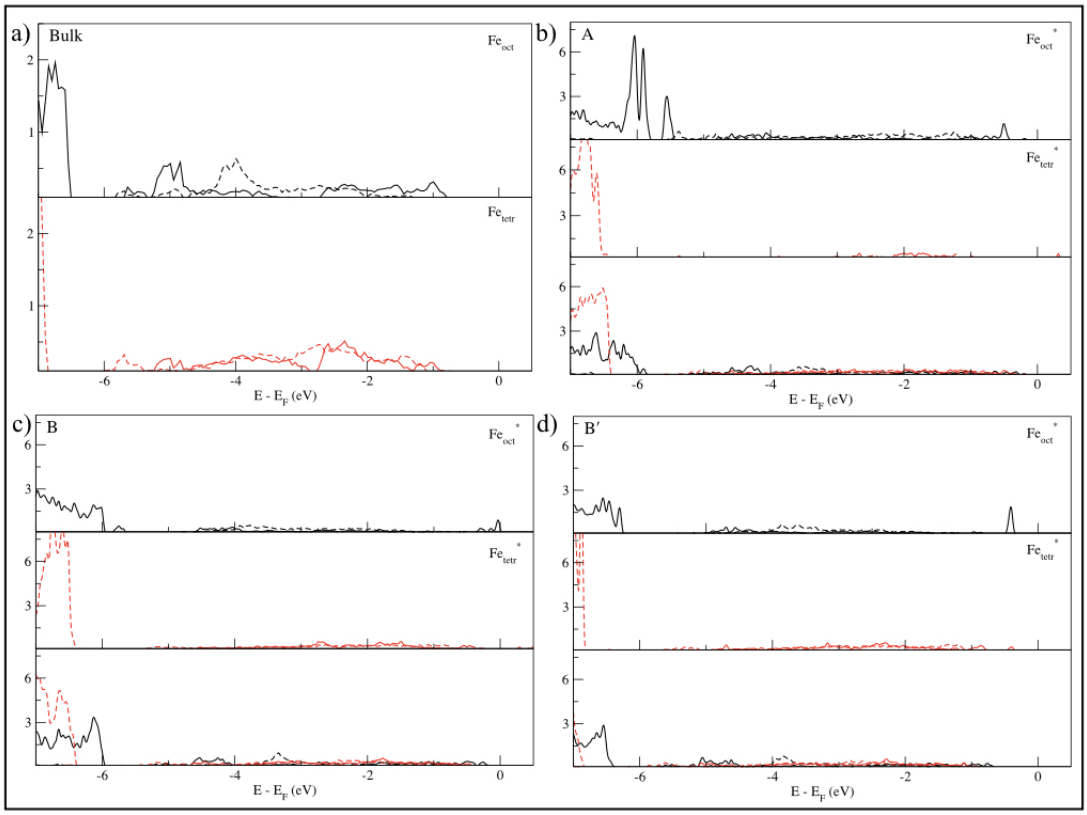

FIGURE 5.14: Atomic projected density of states (apdos) of the iron atoms where only the occupied states are shown. Fe^*_{oct} and Fe^*_{tetr} are the surface octahedral and tetrahedral iron respectively. a) Bulk, b) A surface, c) B surface, and d) B′ surface. The last panel of b),c), and d) shows the apdos of the bulk atoms.

The magnetic moments of the surface Fe atoms change with respect to the bulk. In particular, on the A surface, the magnetic moments of the Fe atoms decrease significantly as shown in Table 5.4. This is due to the decrease in the occupation of the spin up states of the octahedral iron atoms in the valence band, and to the simultaneous increase of the occupation of the spin down states which in the bulk were in the conduction band. Also two oxygen atoms increase slightly their magnetic moments (0.25 μ_B): this increase is related to the loss of the electronic charge of these oxygen atoms with respect to the bulk. This loss concerns the charge of only one spin channel.

On the B surface only the magnetic moments of two Fe atoms, those that are above the iron vacancy in the third layer, decrease. The reason is the same as for the A surface. As for the A surface, two oxygen atoms acquire a small magnetic moment (0.35 μ_B) but for a process similar to that of the Fe atoms: charge is transferred from the spin down channel to the spin up one. Now we pass to investigate the electronic properties of the reduced B′ surface. As shown in Fig. 5.13c the main effect of the oxygen vacancy is the opening of the electronic gaps: 1.51 eV and 1.66 eV, for the spin up and down gaps, respectively. This is due to the octahedral iron and oxygen states, as shown in Figs. 5.13d, 5.15d, and 5.16d which are now well below the calculated Fermi Energy. The localized surface states in the conduction band disappear, and localized surface states formed instead at the top of the valence band. The B′ surface

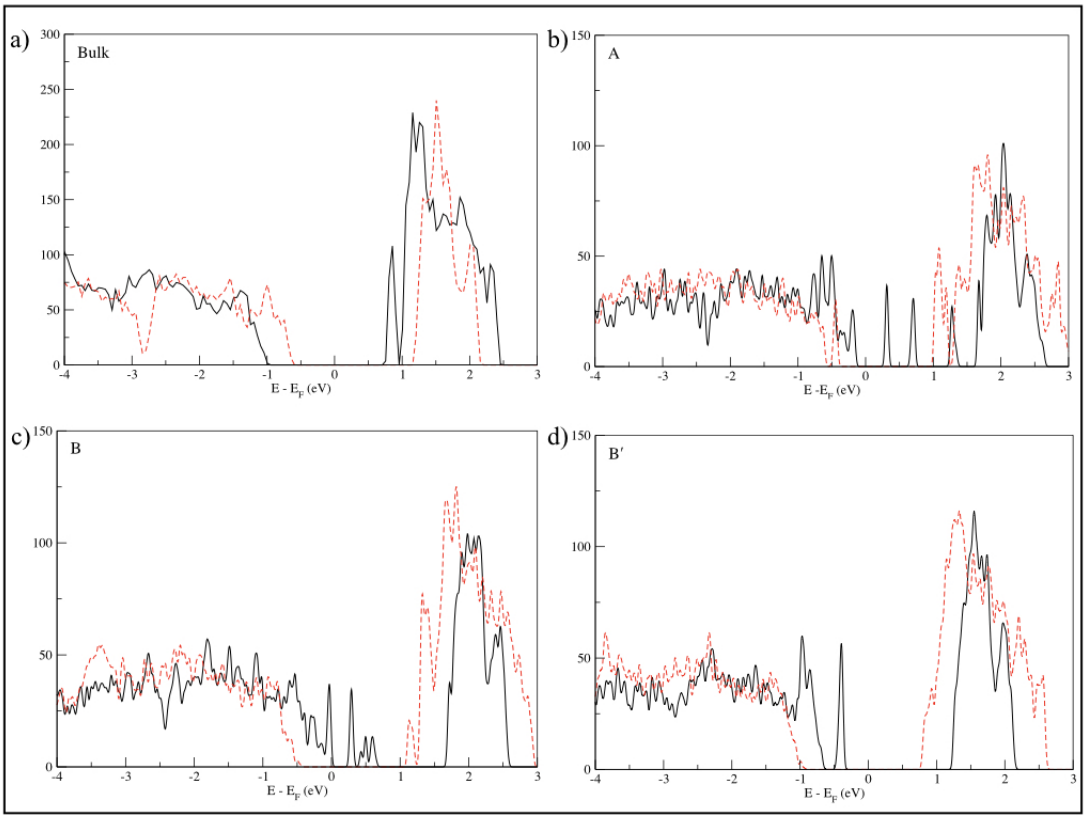

FIGURE 5.15: Density of states (dos) of a) maghemite bulk, b) A surface, c) B surface, and d) B′ surface. Continued black lines and dashed red lines are the spin up and down contributions, respectively.

TABLE 5.4: Magnetic Moments (μ_B) and variation of the spin up (↑) and down (↓) contributions of the Löwdin charge with respect to the bulk value for the maghemite surfaces.

	Maghemite A			Maghemite B			Maghemite B′		
	μ_B	↑	↓	μ_B	↑	↓	μ_B	↑	↓
Fe_1	2.93	-0.28	+0.39	3.29	-0.20	+0.20	3.54	-0.03	+0.03
Fe_2	/	/	/	3.31	-0.18	+0.19	3.55	-0.02	+0.04
Fe_3	2.90	-0.30	+0.52	3.61	-0.01	0.00	3.54	+0.00	-0.01
Fe_4	3.12	-0.21	+0.24	3.62	-0.03	+0.01	3.60	-0.01	0.00

is semiconducting. The modifications of the band structure from B to B′ are related to the enhanced stability of the reduced B′ structure. Also for the reduced A′ surface the empty localized surface states (not shown) disappear, and the surface is still a semiconductor as the A surface but with larger band gaps. The magnetic moments of the Fe atoms on the B′ surface are not substantially changed with respect to the bulk, while three oxygen atoms acquired a small magnetic moments (0.40 μ_B). The analysis of the electronic structure of the investigated surfaces show that the stable maghemite (001) B′ surface is the one whose electronic states and magnetic moment distribution are more similar to the bulk ones.

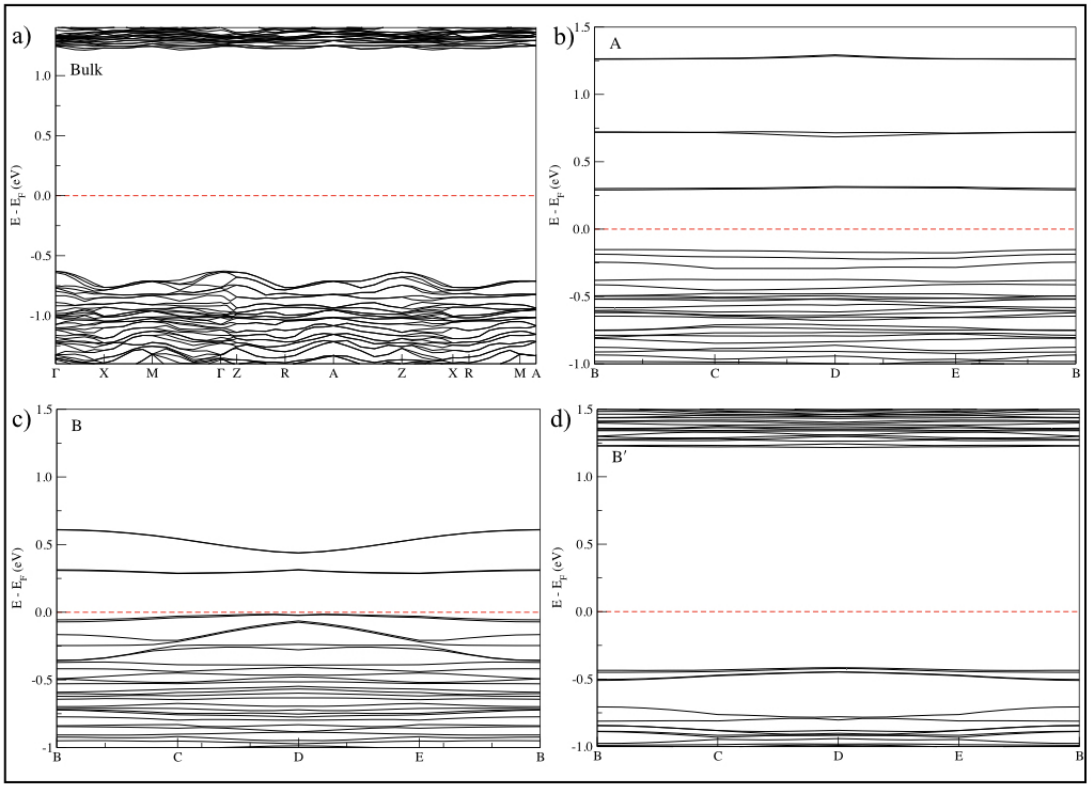

FIGURE 5.16: Electronic band structure of a) bulk, b) A surface, c) B surface, and d) B′ surface of maghemite. The dashed red line indicates the Fermi Energy.

5.2.4 Conclusions

In this paper we have investigated, using an ab-initio approach based on the density functional theory, the reduction and oxidation properties of maghemite γ-Fe_2O_3 (001) surfaces. The aim of this work has been to enlighten the role of Fe vacancies on the redox properties of the surfaces. We have considered the Fe vacancies fully beyond the mean-field approach by constructing the surfaces from the maghemite bulk, for which we have taken the lowest energy structure proposed by Crespo et al. 12, whose point group was also found experimentally. We have found that the presence of the Fe vacancies in maghemite increases both the reducibility and the oxidation efficiency of the surfaces. To reach these conclusions we have compared our results for the maghemite surfaces with those for the magnetite ones, that have not iron vacancies in the bulk. The main effect of the iron vacancies in the proximity of the maghemite surfaces is to decrease the electronic charge of the surface oxygen atoms, both respect to the bulk and to the magnetite surfaces. The consequence is that the oxygen atoms become easier to remove from the surface, and also easier to adsorb on the surface since the adsorbed atom can lend it some charge. The removal of one surface oxygen from the B surface produces a stable reconstruction which we have termed B′ . We have calculated the surface stability as a function of temperature and pressure and found that the B′ reconstruction is indeed the most stable termination for the maghemite (001) surfaces. We have also considered another reconstruction, termed SCV_M, based on the most stable SCVs magnetite reconstruction, but we have found that it is slightly less stable than B′. Another result that we

have obtained is the lower stability of maghemite surfaces with Fe vacancies on the outermost layer. Thus, iron vacancies on the outermost layer tend to destabilize the surfaces. We have also found that the reducibility of the surfaces is strictly related to their stability: more the surface is stable less is reducible. We have examined the charge transfers and the modifications in the electronic structure caused by the reduction of the surfaces. Our results on the (001) surfaces indicate that maghemite might be a better material than magnetite to use in catalysts for oxidation reactions.

Chapter 6

Structural and Electronic properties of single Cu, Ag, and Au atoms on the (001) maghemite surface

In this chapter we provide a theoretical insight into the modifications induced in the structural and electronic properties of the maghemite (001) surface by the additional of noble metal atoms. We have also tested how the presence of the noble metal atoms influences the surface reducibility, and the adsorption of CO molecules.

6.1 Introduction

Iron oxides are promising materials for catalytic applications as also shown in Chapter 5. We have shown in the case of ceria that the addition of dispersed noble metal atoms can improve some catalytic applications. It is interesting to see if this is also the case for iron oxides. Several metal atoms such as Au, Pt, Pd, and Ag have been stabilized on the (001) magnetite (Fe_3O_4) surfaces [32], [183], [184], [185], and single Pt atoms have been also synthesized on the (0001) hematite surface [12]. It is known that single atoms are stabilized by their interactions with the surface atoms of the support [7]. Consequently, in order to design better catalysts, it is important to obtain theoretical insight on how the species of noble metal or its position on the surface may affect the catalytic activity. In this chapter, using an ab-initio approach based on the density functional theory, we investigate the structural and electronic properties of dispersed atoms of three noble metals (Cu, Ag, and Au) on the (001) maghemite surfaces. Three different metal configurations for the metal atoms have been considered: i) atom adsorbed on the surface; ii) atom in a Fe substitutional site, and iii) atom in a O substitutional site. We have analyzed the charge transfers, and the change in the electronic and magnetic properties of the surfaces. We have also tested the reactivity of the modified metal on metal-oxide surfaces for CO adsorption and compared the results to that of the pristine maghemite surface.

6.2 Methods

6.2.1 Computational Details

The details of the computational methods, and the description of the maghemite surface are reported in the previous chapter. Here, we report only the new equations for the modification (adsorption, substitutional, reduction) energies that we have used. The energy gain or cost due to the adsorption of metal atoms, or the substitution of surface atoms with metal atoms, or again the removal of oxygen atoms has been

calculated as:

$$E(N_M^{ad}, N_{Fe}^{sub}, N_O^{sub}, N_O^{rem}) = \frac{1}{N_M^{sub} + N_M^{ad}}[E_{B'*} - E'_B - (N_M^{sub} + N_M^{ad})\mu_M + \frac{1}{2}N_{Fe}^{sub}\mu_{Fe_2O_3}^{bulk} + (N_O^{sub} - \frac{3}{2}N_{Fe}^{sub})\mu_O(T,p) + N_O^{rem}\mu_O(T,p)], \tag{6.1}$$

where $E_B'^*$ is the energy of the modified slab, E'_B is the energy of the slab of the pristine B′ surface, $\mu_{Fe_2O_3}^{bulk}$ is the energy of a maghemite bulk unit, μ_M is the metal chemical potential which has been set equal to the energy of the metal atom in the gas phase, and $\mu_O\ (T,p)$ is the oxygen chemical potential. N_M^{ad} is the number of adsorbed metal atoms, N_{Fe}^{sub} is the number of metal substituted Fe atoms, N_O^{sub} is the number of metal substituted oxygen atoms, and N_O^{rem} is the number of removed surface oxygen atoms (O vacancies). The sum of substituted Fe and O atoms must be equal to the number of metal atoms present in substitutional sites, N_M^{sub}= N_{Fe}^{sub}+N_O^{sub}. At each E(N_M^{ad},N_{Fe}^{sub},N_O^{sub},N_O^{rem}) is associated the modified surface indicated as M(x,y,w,z)@Fe_2O_3(001), where M is the kind of noble metal atoms, and x, y, w, z the number of adsorbed atoms, the number of substituted Fe, the number of substituted O, and the number of removed oxygen atoms, respectively. For example, M(1,0,0,0)@Fe_2O_3(001) means that a single metal atom M is adsorbed on the B′ surface, indicated as (0,0,0,0). In the following the modified surfaces will be indicated in this way. We have supposed that the surface is in thermodynamic equilibrium with its bulk and the environment, and, consequently, we have used the equality $\mu_{Fe_2O_3}^{Bulk}$=$2\mu_{Fe}$+$3\mu_O$, where μ_{Fe} is the Fe chemical potential. Since molecular oxygen may be present in the atmosphere above the surface, the oxygen chemical potential is a function of both temperature and pressure. Consequently, it is important to understand how it depends on these parameters since the properties of the gas are strongly affected by the variation of T and p. Assuming that the oxygen gas is an ideal gas, we can write

$$\mu_O(T,p) = \frac{1}{2}E_{O_2} + \frac{1}{2}\Delta G_{O_2}(T,p^0) + \frac{1}{2}KTln(p/p^0), \tag{6.2}$$

where p^0 is the reference pressure, E_{O_2} is the energy of the oxygen molecule at T = 0 K, and $\Delta\ G_{O_2}$ (T,p^0) is the variation of the Gibbs free energy of O_2 at temperature T from its value at 0 K. This term is linked to the entropy and enthalpy contributions of the O_2 molecule, and for p^0 =1 atm the values are tabulated in Ref. [175]. We have neglected any vibrational contribution. Equation 6.1 is a general expression which is valid if all the surface atoms sites are equivalent, otherwise it is necessary to specify it for each inequivalent site.
The oxygen vacancy formation energy, in the case the modifications involve a single atom per unit cell, has been evaluated as:

$$E_{form}^{(0,0,0,1)} = E_{(0,0,0,1)} - \frac{1}{2}E_{O_2} - E_{(0,0,0,0)}, \tag{6.3}$$

instead the O vacancy formation energy in the presence of one adsorbed metal atom is:

$$E_{form}^{(1,0,0,1)} = E_{M(1,0,0,1)} - \frac{1}{2}E_{O_2} - E_{M(1,0,0,0)}. \tag{6.4}$$

If the noble metal substitutes an iron atom the O vacancy formation energy becomes:

$$E_{form}^{(0,1,0,1)} = E_{(M(0,1,0,1)} - \frac{1}{2}E_{O_2} - E_{M(0,1,0,0)}. \tag{6.5}$$

The adsorption energy of the CO molecule on the surface has been calculated as:

$$E_{ads}^{CO} = E_{CO/surface} - E_{CO} - E_{surface}, \tag{6.6}$$

where $E_{CO/surface}$ is the energy of the slab with the adsorbed CO, E_{CO} is the energy of the CO molecule in the gas phase, and $E_{surface}$ is the energy of the slab without adsorbed CO.

6.3 Results

6.3.1 Adsorption

We have adsorbed a single Cu, Ag, and Au atom on the B′ surface. The preferential adsorption site for all noble metals is a bridge position between two surface oxygen atoms, aligned along the surface [1,1] diagonal with the tetrahedral Fe atoms of the second layer below the outermost layer as shown in Fig. 6.1, where the top and side views of the surface termination are reported. These adsorption sites were also found by Meier et al. [31] on the structurally correlated magnetite oxide. The energy $E_M(1,0,0,0)$ of Eq. 6.1 is named adsorption energy. In Table 6.1 the adsorption energies (E_{ads}), the metal-oxygen (M-O) bond lengths, the noble. metal oxidation states (M_{OX}), and the number of reduced Fe (Fe^{2+}) are reported. The adsorption of the noble metals on the surface is favored. The adsorption energy, in absolute value, is greater for Cu. In particular, the Cu adsorption energy, -3.65 eV, is higher than the cohesive energy of Cu bulk, whereas for Ag and Au the adsorption energies are less than their respective bulk cohesive energies, and consequently their adatom configurations are not stable against sintering. Following the adsorption of Cu, Ag, and Au on the B′ surface, the metal *s* electron of the noble metal is transferred to the substrate, reducing one iron atom from Fe^{3+} to Fe^{2+}. Indeed, as shown in Figs. 6.3a, 6.3d, and 6.3g, a spin down *d* peak of Fe has moved to the valence band. The metal adatoms are positively charged: Cu, Ag, and Au transfer to the surface 0.52 *e*, 0.41 *e*, and 0.47 *e*, respectively. We can speculate that their new oxidation state is +1. This is also confirmed by the calculated M-O distances, which are slightly larger than the experimental values in Cu_2O [91], Ag_2O [186], and Au_2O [187]. As shown in Table 6.2, the presence of the noble metal atom decreases the spin up and down energy gaps with respect to those of the B′ surface (1.55 eV and 1.66 eV for spin up and down, respectively). The decrease is greater for the Cu surface than for the other two noble metals. On Cu(1,0,0,0)@Fe_2O_3(001) , see Fig. 6.3a, the top of the valence band is constituted by *d* orbitals of Fe, *p* orbitals of O, and, mainly, by *d* states of Cu. The bottom of the conduction band is formed by the spin down states of octahedral Fe as in the case of the pristine surface whose DOS is shown in Fig. 6.2. Contrary to Cu, the surfaces with Ag and Au adatoms have the top of the valence band formed mainly by the *d* Fe and *p* O states, and less by the metal states, as shown in Figs. 6.3d and 6.3g. Also the magnetic properties of the surface change with the presence of the adsorbed metal. This is an important aspect for the use of maghemite nanoparticles in diagnostic medicine. The adsorption of the noble metals leads to the decrease of the magnetic moment ($\sim$ -0.5 μ_B) of the octahedral Fe atom that has acquired the metal *s* electron, due to the increase of the occupation of the spin down states. The

noble metals have not a magnetic moment, contrary to the gas phase, due to the transfer of the *s* electron to the surface.

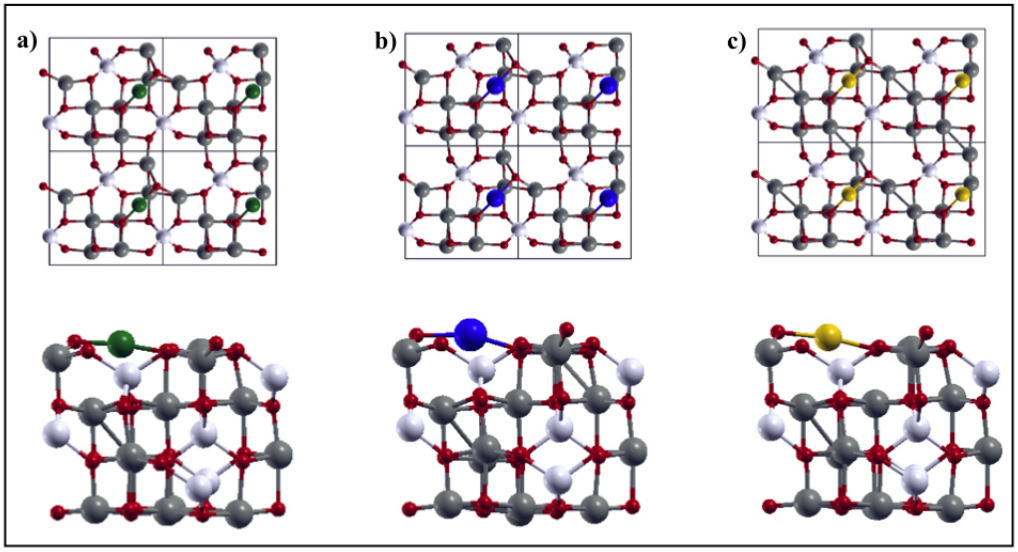

FIGURE 6.1: Top view of the (2 × 2) (first row) and side view (second row) of a) Cu(1,0,0,0)@Fe_2O_3(001), b) Ag(1,0,0,0)@Fe_2O_3(001), and c) Au(1,0,0,0)@Fe_2O_3(001) surfaces. Dark and light gray balls are the octahedral and tetrahedral iron atoms, respectively. The red balls are the oxygen atom. The green, blue, and yellow balls are the Cu, Ag, and Au atoms, respectively.

6.3.2 Metal in a substitutional Fe atom

We have investigated the changes in the geometrical, electronic, and magnetic properties of the maghemite B′ surface when a single Fe atom is substituted with a noble metal atom. As shown in Fig. 6.4, we have identified three inequivalent kinds of iron atoms: i) octahedral Fe_4 and Fe_2 irons, bonded to the O_5 oxygen, ii) octahedral Fe_1 and Fe_3 irons, not bonded to the oxygen O_5, and iii) tetrahedral Fe_{12} and Fe_{13} atoms, in the second layer below. We have assumed that the Fe atom with the lowest vacancy formation energy is the one with the highest probability to be substituted. Thus, the substitution reaction is modeled as a two steps process: first, a Fe vacancy is created, second, the noble metal atom is adsorbed into the vacancy site. The Fe atom vacancy formation energy E^{Fe}_{form} has been evaluated as E^{Fe}_{form}=$E_{B'_-}$ + $\frac{1}{2}\mu^{Bulk}_{Fe_2O_3}$-$E_{B'}$ -$\frac{3}{4}E_{O_2}$, where $E_{B'_-}$ is the energy of the slab without the iron atom, $E_{B'}$ is the energy of the pristine slab, $\mu^{Bulk}_{Fe_2O_3}$ is the energy of a maghemite bulk unit, and E_{O_2} is the energy of the oxygen molecule in the gas phase. The energy required to remove the Fe atoms is lower for the octahedral iron atoms not bonded to O_5. It is 2.31 eV, whereas it is 3.03 eV for Fe_2 and Fe_4 and 5.09 eV for the tetrahedral irons. Thus, we substituted Fe_1 as indicated by the black crosses in Fig. 6.5. The creation of the Fe vacancy determines a decrease of the energy gaps. In particular, the spin up energy gap is only 0.09 eV, with valence states touching the Fermi Energy, as shown in Fig. 6.6, whereas the spin down energy gap is 1.52 eV. Following the creation of the vacancy the magnetic moments of the octahedral Fe atoms (Fe_3 and Fe_4) near the iron vacancy decrease significantly to $\sim 2.9\ \mu_B$, whereas Fe_2 is $\sim 3.4\ \mu_B$.

TABLE 6.1: Oxidation number (M_{OX}), Metal-Oxygen (M-O) distances in angstrom, Metal-Iron (M-Fe) distances in angstrom, adsorption energies (E_{ads}) in eV, substitutional energy (E_{sub}), and number of reduced Fe atom (Fe^{2+}).

	Cu		
	(1,0,0,0)	(0,1,0,0)	(0,0,1,0)
M_{OX}	+1	+3	+0
M-O	1.87	1.93(2)	/
	1.88	1.86(2)	
M-Fe	/	/	2.53(2)
			2.58
E_{ads}	-3.65	/	/
E_{sub}	/	-5.02	-0.46
Fe^{2+}	1	0	2
	Ag		
	(1,0,0,0)	(0,1,0,0)	(0,0,1,0)
M_{OX}	+1	+3	0
M-O	2.13	2.16	2.35
	2.17	2.10(2)	
		2.03	
M-Fe	/	/	3.00(2)
			2.71
E_{ads}	-2.41	/	/
E_{sub}	/	-2.80	-0.39
Fe^{2+}	1	0	2
	Au		
	(1,0,0,0)	(0,1,0,0)	(0,0,1,0)
M_{OX}	+1	+3	-1
M-O	2.05	2.08(2)	/
	2.08	2.02(2)	
M-Fe	/	/	2.65(2)
			2.75
E_{ads}	-2.49	/	/
E_{sub}	/	-3.48	-0.54
Fe^{2+}	1	0	1

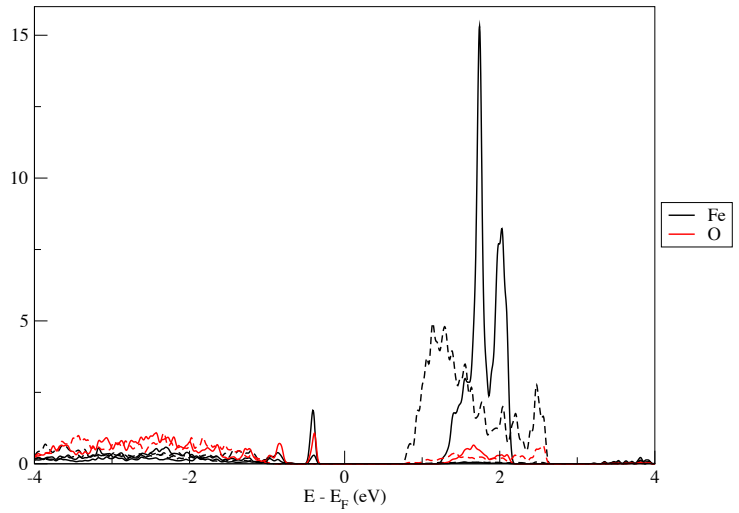

FIGURE 6.2: PDOS of the pristine B′ maghemite surface. The continuous and dashed lines are the spin up and down contributions respectively.

TABLE 6.2: Spin up (↑) and down (↓) energy gaps E_g in eV for the different M(x,y,w,z)@Fe_2O_3(001) surfaces

			Cu			
Surface	(1,0,0,0)		(0,1,0,0)		(0,0,1,0)	
Spin Orientation	↑	↓	↑	↓	↑	↓
E_g	1.21	0.91	0.66	1.17	0.89	1.32
			Ag			
Surface	(1,0,0,0)		(0,1,0,0)		(0,0,1,0)	
Spin Orientation	↑	↓	↑	↓	↑	↓
E_g	1.31	1.05	0.57	1.71	1.32	1.27
			Au			
Surface	(1,0,0,0)		(0,1,0,0)		(0,0,1,0)	
Spin orientation ↑	↓	↑	↓	↑	↓	
E_g	1.30	0.91	1.42	1.68	0.33	1.35

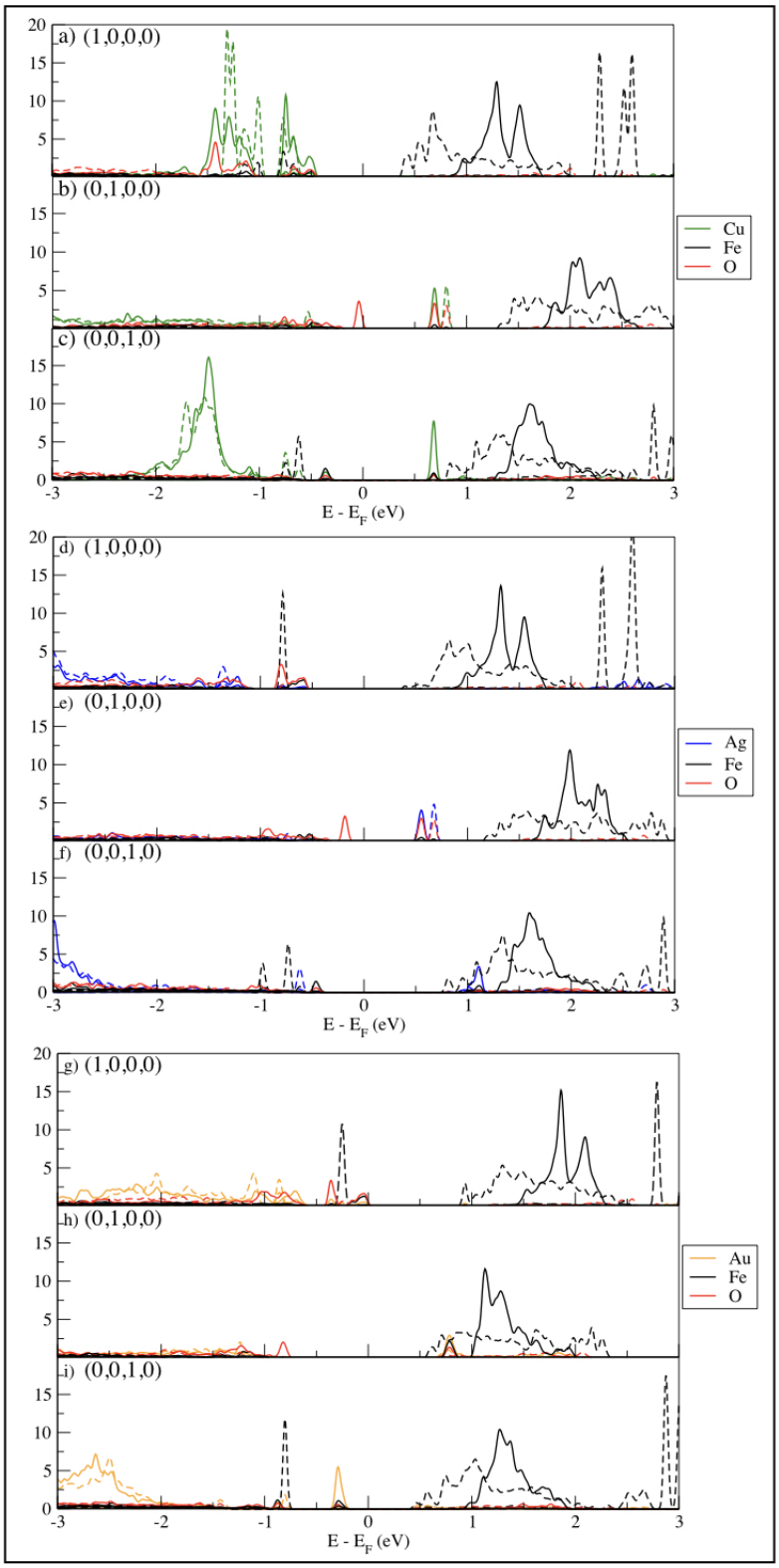

FIGURE 6.3: Projected density of states of a) Cu(1,0,0,0)@Fe_2O_3(001), d) Ag@(1,0,0,0)Fe_2O_3(001), g) Au(1,0,0,0)@Fe_2O_3(001); b) Cu@(0,1,0,0)Fe_2O_3(001); e) Ag(0,1,0,0)@Fe_2O_3(001); h) Au@(0,1,0,0)Fe_2O_3(001); c) Cu(0,0,1,0)@Fe_2O_3(001); f) Ag(0,0,1,0)@Fe_2O_3(001), and i) Au(0,0,1,0)@Fe_2O_3(001). Continuous and dashed lines are the spin up and down contributions, respectively.

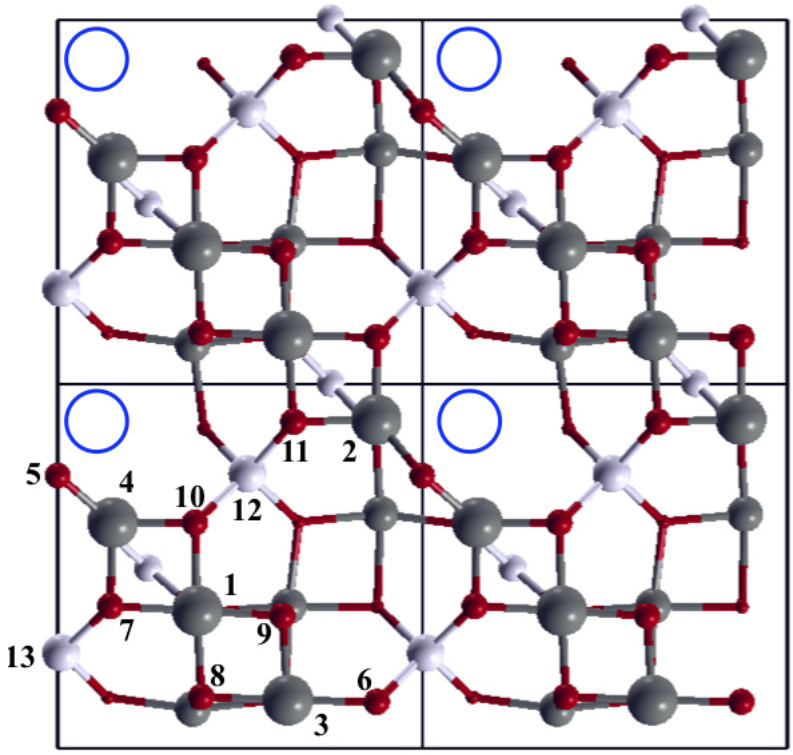

FIGURE 6.4: Top view of the (2×2) of the most stable B′ maghemite surface reconstruction. Dark and light gray balls are the octahedral and tetrahedral iron atoms. Red balls are the oxygen atoms. Blue circles indicate the Fe vacancy located in the third layer below the outermost layer. The numbers label the surface atoms.

On this iron empty site, we have adsorbed a single Cu, Ag, and Au atom as shown in Fig. 6.7, where the top and side views of the M(0,1,0,0) configurations are reported. When the noble metal atom substitutes one atom of the substrate, the energy of Eq. 6.1, E(0,1,0,0), is named substitutional of energy. The substitutional energies E_{sub} are reported in Table 6.1. In general, we note that the substitution of an iron atom with the noble metal is a thermodynamically favored reaction, and the substitutional energies follow the same trend as the adsorption energies (see Table 6.1). They decrease from Cu to Au to Ag. For all metals, the substitution energies are greater than the adsorption energies, but the difference is significantly low for Ag, only 0.39 eV. Surface cation vacancies are very important sites to trap single atoms, however, it is important to keep in mind that to have the substitution is necessary to overcome an energy barrier, which is not evaluated in this work. The noble metal atoms in Fe substitutional sites lose a significant amount of charge, -1.13 e, -1.01 e, and -1.26 e, for Cu, Ag, and Au, respectively. Two d states and the s state of the noble metal atoms appear, indeed, in the conduction band as shown in the PDOS of Figs. 6.1b, 6.1e, and 6.1h. The Ag-O and Au-O distances (see Table 6.1) are slightly larger than the experimental values found for the Ag_2O_3 and Au_2O_3 oxides [94], [96]. These results suggest that the oxidation state of the noble metal atoms is $\sim$ +3. Also two oxygen atoms bonded to the metal atom, and to two octahedral irons lose an amount of charge ($\sim$ -0.2 e). The magnetic moments of the Fe atoms don't change with respect to the pristine B′ surface, and all the Fe atoms are still in a 3+ oxidation state. These magnetic moments are however larger than than those of the surface of

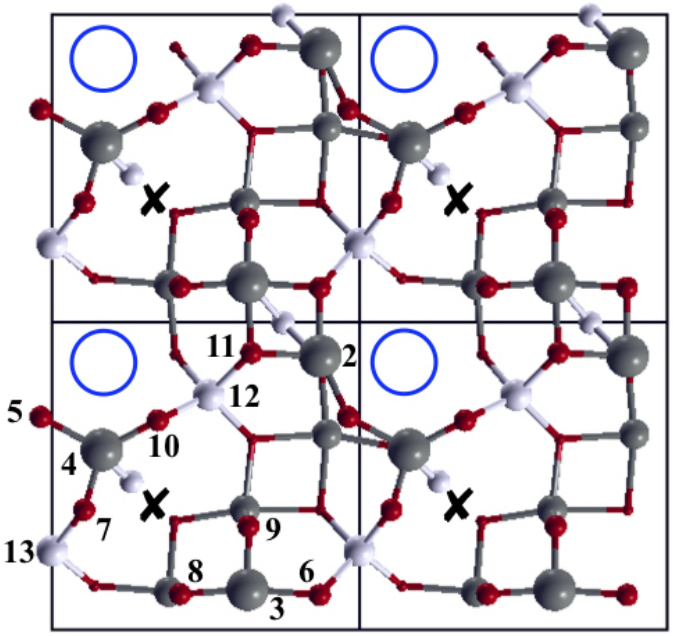

FIGURE 6.5: Top view of the (2×2) B′ surface where octahedral Fe atoms of the outermost layer whose position is indicated by black crosses, have been removed. The blue circles indicate the Fe vacancy in the third layer below the outermost layer.

the surface with the octahedral Fe vacancy. On the Cu(0,1,0,0)@Fe_2O_3(001) surface, as on the Cu(1,0,0,0)@Fe_2O_3(001) surface, the band gaps decrease with respect to those of the pristine surface as reported in Table 6.2. Contrary to the Cu case, on the Ag(0,1,0,0)@Fe_2O_3(001) surface, only the spin up energy gap decreases of 63%, whereas the spin down gap remains the same. A similar trend has been calculated for the Au(0,1,0,0)@Fe_2O_3(001) surface, but for this surface the decrease of the spin up energy gap is only 8%. The significant decrease of the spin up gaps calculated when substituting Fe with Cu and Ag is due to the appearance at the top of the valence band, and at the bottom of the conduction band of p peaks due to the less charged oxygens. At the bottom of the conduction band we note also the appearance of metal states. On Au(0,1,0,0)@Fe_2O_3(001) the oxygen p states, which are at the top of the valence band, are at lower energies than on the Cu(0,1,0,0)@Fe_2O_3(001) and Ag(0,1,0,0)@Fe_2O_3(001) surfaces. Comparing the gaps reported in Table 6.2 with those of the surface with the Fe vacancy the presence of the noble metal atoms in the vacancy site increases the spin up energy gaps, and also the spin down gaps in the case of Ag and Au atoms.

6.3.3 Noble Metal atom substituting an O atom

In this section we report our results on the properties of a noble metal doped surface where one surface oxygen atom is substituted by a Cu, Ag, or Au atom. We have tested also this substitution due to the high reducibility of the maghemite surface. As for the cation substitution we have supposed that the noble metal is adsorbed after the oxygen atom with the lowest vacancy formation energy is removed. As shown in Ref. [188], and reported in Table 6.3, the energy required to remove the surface oxygens is not the same. We have chosen to substitute O_8, which is one of

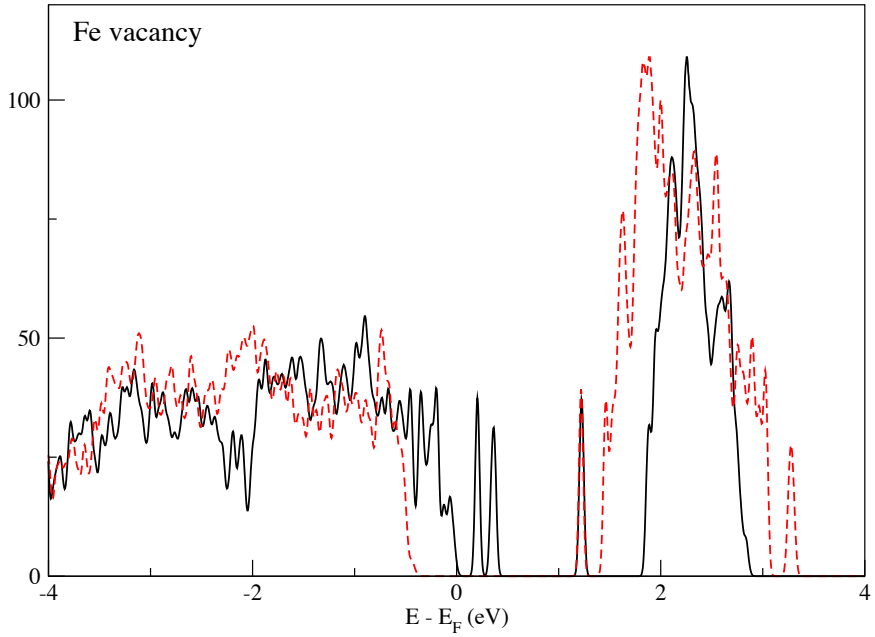

FIGURE 6.6: Density of states of the surface. with an iron vacancy in site Fe_1. Black and red lines are the spin up and down contributions, respectively.

the two atoms with the lowest formation energy. Its sites are indicated by crosses in Fig. 6.8. Following the creation of the O vacancy the spin up gap remains constant, whereas the spin down gap decreases to 1.10 eV, as shown in the DOS of Fig. 6.9. Two octahedral Fe atoms acquire the excess of charge, passing from Fe^{3+} to Fe^{2+}, and consequently their magnetic moments decrease from 3.60 μ_B to 3.13 μ_B The magnetic moments of the other two Fe atoms don't change with respect to the pristine surface.

In Fig. 6.10 the top and side views of the M(0,0,1,0) surfaces are shown. The substitution M→O is favored for all the metals but much less than the Fe→M substitution, as can be noted from the energies reported in Table 6.1. In particular, contrary to the previous configurations, the substitution of O with Au is more favored than the substitution of O with Cu or Ag. Cu and Au bind only to octahedral Fe atoms, whereas the Ag atom binds also to a surface oxygen atom as shown in Fig. 6.10. On the Cu(0,0,1,0)@Fe_2O_3(001) and Ag(0,0,1,0)@Fe_2O_3(001) surfaces we don't observe any charge transfer from (to) the metal and the substrate: we note indeed a spin down (up) *s* peak in the valence (conduction) band as occurs for the levels of the atoms in the gas phase. The absence of charge transfers is due to the similarity of copper, silver, and iron electronegativity. On the Cu(0,0,1,0)@Fe_2O_3(001) and Ag(0,0,1,0)@Fe_2O_3(001) surfaces we have found that two iron atoms are still reduced, as in presence of the single O vacancy, with magnetic moments lower than those on the pristine maghemite surface. Au, instead, is more electronegative than Fe, and consequently a net charge transfer occurs from Fe to Au. In particular, electronic charge is transferred from reduced Fe^{2+} to Au (+0.41 *e*). We notice, indeed, that both the spin up and down s peaks are now present in the valence band as shown in Fig. 6.3i. Au is, consequently, negatively charged, Au^{-1}. For all the modified surfaces we have calculated a decrease of the energy gaps with respect to the pristine surface as reported in Table 6.2. It is interesting to note that the spin up energy gap decreases with respect to that of the simply reduce surface, whereas the spin down

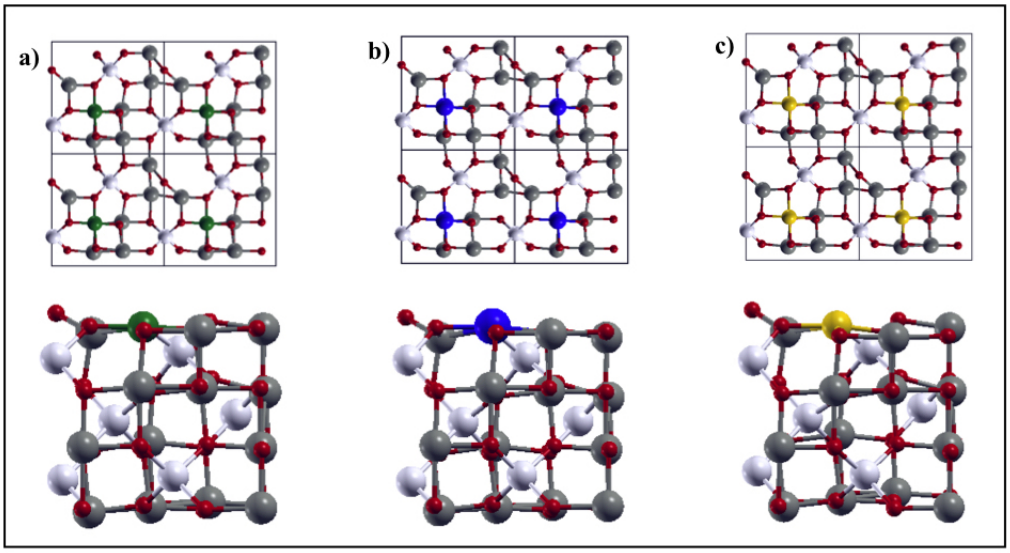

FIGURE 6.7: Top view, first row, of the (2×2) and side view, second row, of: a) Cu(0,1,0,0)@Fe_2O_3(001), b) Ag(0,1,0,0)@Fe_2O_3(001), and c) Au(0,1,0,0)@Fe_2O_3(001). The color code is the same as in Fig. 6.1.

increases slightly. On Cu(0,0,1,0)@Fe_2O_3(001) and Ag(0,0,1,0)@Fe_2O_3(001) the top of the valence band is composed by Fe and O states, whereas the bottom of the conduction band is formed by localized metal states. On the contrary, on Au(0,0,1,0) @Fe_2O_3(001) the top of the valence band is formed by Au states, due to the occupation of the *s* state, whereas the bottom of the conduction band is formed by Fe states.

6.3.4 Reducibility of the surfaces

In this section we have investigated how the presence of Cu, Ag and Au atoms as adsorbates or in Fe substitutional sites influences the reducibility of the surfaces. The M(0,0,1,0)@Fe_2O_3(001) surfaces, where O is substituted by the noble metal atom, are not considered since these surfaces are already reduced compared to the B′ pristine surface. The oxygen vacancy formation energies have been evaluated using Eqs. 6.3, 6.4, 6.5 and are reported in Table 6.3 where they are compared with those of the pristine B′ maghemite surface. The oxygen atoms are labelled as in Fig. 6.4.

As a general rule we note that it is easier to remove the oxygen atoms from the doped surfaces than from the surfaces with adatoms. The presence of the metal dopant causes two surface oxygen atoms, O_8 and O_9, bonded to the noble metal atom, to be less charged than on the pristine surface, and, thus, easier to remove. It is indeed well known that the less charged electrons are also the more reactive ones [5]. The Ag doped surface is the most reducible one. Indeed, the energy required to remove the most reactive oxygens is only 0.59 eV, whereas it is more than 1 eV for the other two doped surfaces. On the M(0,1,0,0)@Fe_2O_3(001) surfaces, if we remove an oxygen atom bonded to the noble metal atom, all or part of the excess charge left behind by the oxygen removal is acquired by the noble metal atom. In particular, the Ag atom acquires almost all the charge ($\sim$ +0.50 *e*), reaching in this way its favorite +1 oxidation state. A small amount of charge is acquired also by one Fe atom ($\sim$ +0.15 *e*), and by other surface oxygens $\sim$ +0.10 *e*),. The same charge transfer to the

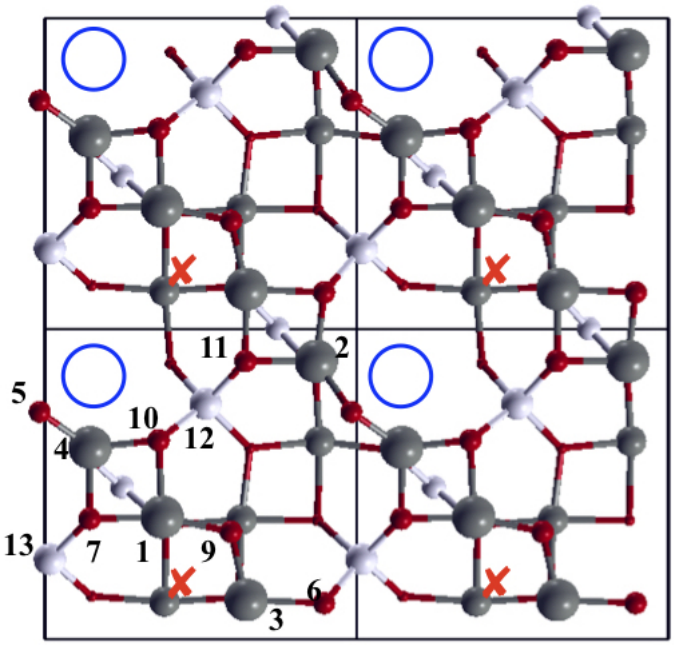

FIGURE 6.8: Top view of the (2×2) B′ surface with oxygen vacancies indicated by red crosses. The color code is the same as in Fig. 6.4.

noble metal atom is observed also for Au, but in this case the charge transfer to oxygen atoms is negligible. Contrary to the Ag and Au cases, Cu acquires only one of the two electrons in excess ($\sim$ +0.35 e), reaching in this way its favorite +2 oxidation state. The remaining electron is acquired by one Fe atom ($\sim$ +0.22 e),and by oxygen atoms. In the case of noble metal atom adsorbed on the surface, the reducibility of the surface doesn't change significantly with respect to the pristine surface as shown in Table 6.2. However, we can note that the oxygen vacancy formation energy is slightly smaller for Ag(1,0,0,0)@Fe_2O_3(001) than for the other two surfaces. The greater oxygen vacancy formation energies calculated for the adsorbate case compared to the doped case are probably due to the more favorable charge transfers occurring in the second case. In the adsorbate configurations, indeed, the oxygen atoms are already in the -2 oxidation state, and following the creation of the oxygen vacancy the two electrons left behind by the removed oxygen can be acquired only by two Fe atoms ($\sim$ +0.40 / +0.50 e, reducing them from Fe^{3+} to Fe^{2+}. This is unfavored as found previously for the pristine surface in Ref. [188]. Moreover, the noble metal atoms are already in a +1 oxidation state, and they don't favor further charge transfers. On these surfaces an iron atom is already reduced, and a further reduction is therefore more costly. Ag, as a dopant, increases the reducibility of the surface more than the other two noble metal atoms, and, consequently it seems to be the most promising dopant to use as a catalyst in the reactions where the creation of an oxygen vacancy is required, i.e. the reactions following the Mars van Kreevelen mechanism [24], or as oxygen carrier in the chemical looping combustion where the activity depends on the redox capacity activity [189].

6.3.5 Stability of the surfaces

In this section we examine the stability of the investigated modified surfaces in different environments characterized by different values of temperature and pressure.

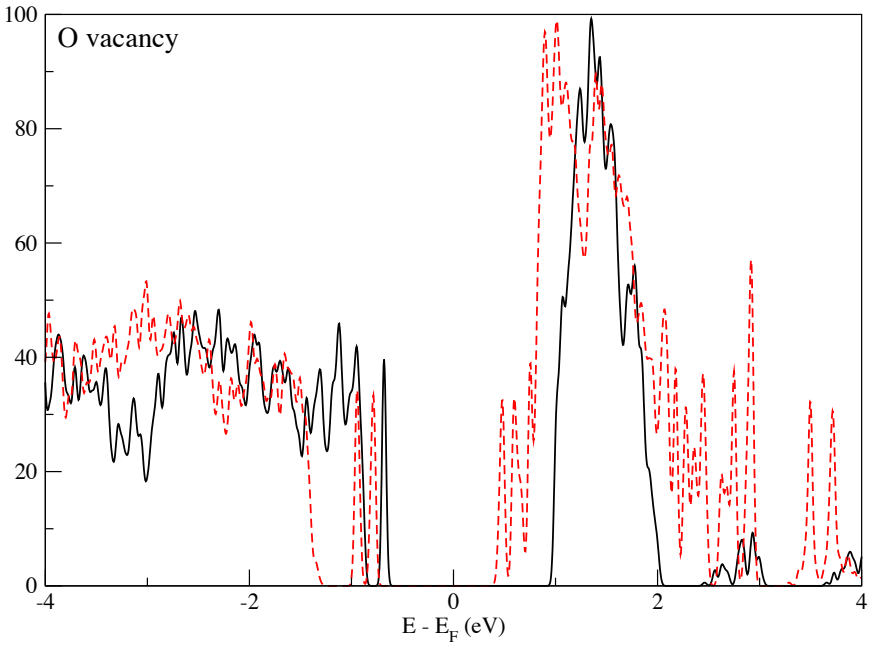

FIGURE 6.9: Density of states of the reduced pristine surface. Black and red lines are the spin up and down contributions, respectively.

In Figs. 6.11a, 6.11b, and 6.11c we show the surface energies versus the oxygen chemical potential, which is a function of T and p as shown in Eq. 6.2. We have reported explicitly the oxygen chemical potential values corresponding at a wide range of pressure p at room temperature. The energies have been calculated using Eq. 6.1. In general, we can identify three different stable phases: i) for μ_O less than -1.5 eV (reduced conditions), the adatom configurations in the presence of an oxygen vacancy, M(1,0,0,1)@Fe_2O_3(001), are the most stable ones, ii) at intermediate values of μ_O, the adatom configurations M(1,0,0,0)@Fe_2O_3(001), are the most favorite, and iii) at higher values of μ_O (> -0.92 for Cu, > -0.25 for Ag, > -0.65 for Au), oxidation conditions, the doped configurations, M(0,1,0,0)@Fe_2O_3(001) are the most stable. The M(0,1,0,1) @Fe_2O_3(001) and the M(0,0,1,0)@Fe_2O_3(001) surfaces are unstable over the entire range of oxygen chemical potentials. It is very interesting to note that the range of stability of the adatom configurations is different for the three noble metals: it decreases from Cu to Au, to Ag. At room temperature, and p=1 atm, which are the typical conditions of catalytic reactions, μ_O is $\sim$ -0.27 eV, Cu and Au, will tend to occupy the iron sites. This can explain the observations of Najafishirtari et al. [151], where they have found Cu atoms occupying the positions of octahedral iron atoms. It is interesting to note that for Ag, instead, the energy difference between the substitutional and adatom configurations, at μ_O = -0.27 eV, is only 0.02 eV. Thus, it is possible to observe both configurations. Single Ag adatoms have been indeed observed on the magnetite (001) surface using scanning tunneling microscopy (STM) [184].

6.3.6 CO adsorption on the noble metal modified surfaces

We have investigated the interaction of the CO molecule with the M(1,0,0,0)@Fe_2O_3(001) and M(0,1,0,0)@Fe_2O_3(001) surfaces, which are the most stable in a wide range of oxygen chemical potentials. Firstly, we have considered the pristine surface and

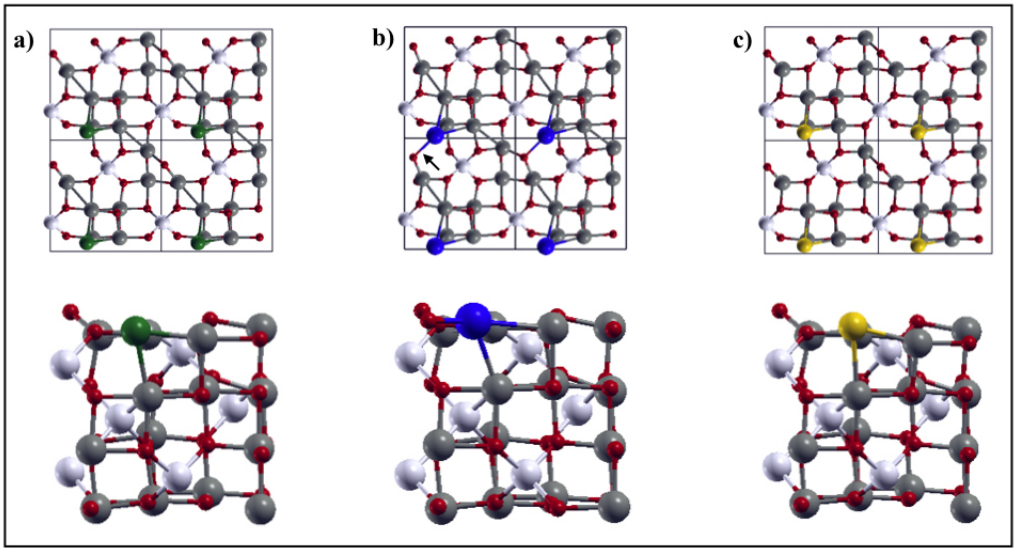

FIGURE 6.10: First row: top view of the (2×2) and side view. Second row: of a) Cu(0,0,1,0) @Fe_2O_3(001), b) Ag(0,0,1,0)@Fe_2O_3(001), and c) Au(0,0,1,0)@Fe_2O_3(001). The black arrow indicated the Ag-O bond. The color code is the same as in Fig. 6.1.

then we have compared the results obtained for it with those obtained for the surfaces with dispersed noble metal atoms. In Fig. 6.12 we show the preferential adsorption sites of CO on the different surfaces. On the pristine surface, CO adsorbs above an octahedral iron atom, E_{ads}=-0.25 eV, and its bond length is slightly shorter than the CO bond length in the gas phase (1.142 Å) as reported in Table 6.4. We have not found any charge transfer from CO to the surface, and vice versa. The presence of CO doesn't determine any modification of the maghemite electronic structure, shown in Fig. 6.13a, with respect to the PDOS of the pristine maghemite surface, shown in Fig. 6.2. The only difference we notice is the presence of empty orbitals of CO in the conduction band. The spin up and down energy gaps remain the same. The presence of noble metal atoms modifies the interaction between CO and the surface. We have started considering the adatom configurations.

The presence of single noble metal atoms adsorbed on the maghemite surface increases significantly the adsorption energy of the CO molecule compared to the pristine surface. Cu, in particular, seems to be the most reactive noble metal towards CO adsorption. CO binds directly to the Cu and Ag atoms, whereas, on the Au(1,0,0,)@Fe_2O_3(001) surface, CO binds to an octahedral Fe atom of the outermost layer. In Table 6.4 the adsorption energies E_{ads}^{CO}, the C-Fe distance for the M(0,1,0,0)@Fe_2O_3(001), and Au(1,0,0,0)@Fe_2O_3(001) surfaces, the C-M bond lengths for the Cu(1,0,0,0)@Fe_2O_3(001) and Ag(1,0,0,0)@Fe_2O_3(001) surfaces, and the C-O bond lengths of the CO molecule are reported. On the Cu(1,0,0,)@Fe_2O_3(001) surface, CO increases slightly its bond lengths, and it is adsorbed perpendicular to Cu. Cu maintains both its bonds with the surface oxygens, and it moves 0.09 Å upward. On the contrary, the adsorption of CO on Ag(1,0,0,)@Fe_2O_3(001) leads to the breaking of one of the two Ag-O bonds in a similar way to what was observed by Parkinson et al. [185] for Pd on magnetite. Also, Ag, as Cu, moves 0.08 Å upward, but in this case the CO molecule bends with respect to the surface plane. From an electronic point of view, the presence of CO increases slightly the gaps: the new up (down) gaps are 1.51 (1.22) eV, 1.40 (1.12) eV, and 1.52 (1.25) eV for Cu, Ag, and Au adatom

TABLE 6.3: Oxygen vacancy formation energies, in eV, on the pristine and on the noble metal modified surfaces. The numbering of the oxygen atoms is shown in Fig..6.4

	B′	M(0,1,0,0)			M(1,0,0,0)		
O		Cu	Ag	Au	Cu	Ag	Au
5	2.53	2.53	2.40	2.41	3.69	2.93	2.82
6	2.42	2.40	2.36	2.36	2.53	2.32	2.34
7	2.22	2.36	1.84	2.46	1.97	1.94	1.84
8	1.57	1.23	0.59	1.12	1.59	1.49	1.53
9	1.57	1.23	0.59	1.12	2.05	1.87	1.85
10	2.22	2.67	2.21	2.77	2.53	2.32	2.34
11	2.22	2.27	2.22	2.22	1.97	1.94	1.84

TABLE 6.4: Adsorption Energy of the CO molecule, E_{ads}^{CO} in eV, distance between the carbon atom and a octahedral Fe atom C-Fe (Å), the carbon-metal bond length C-M (Å), and the C-O bond length (Å).

	B′	Cu(1,0,0,0)	Ag(1,0,0,0)	Au(1,0,0,0)	Cu(0,1,0,0)	Ag(0,1,0,0)	Au(0,1,0,0)
E_{ads}^{CO}	-0.25	-0.71	-0.51	-0.37	-0.27	-0.24	-0.25
C-Fe	2.40			2.13	2.39	2.42	2.20
C-M		1.80	2.00				
C-O	1.1388	1.152	1.144	1.142	1.138	1.138	1.137

surfaces, respectively. On the Cu@Fe_2O_3(001) surface, following the CO adsorption, Cu transfers a small amount of charge to C, and, in this way, it reaches its preferential +2 oxidation state. On the other two surfaces no charge transfers take place. On the doped surfaces, CO is adsorbed above a surface octahedral Fe atom as on the pristine surface. The adsorption configurations are shown in Fig 6.12. The CO adsorption energies are similar to those calculated for the pristine surface as shown in Table 6.4. The energy gaps change, in particular the spin up gaps decrease their value: the new up (down) gaps are 0.40 (1.12) eV, 0.38 (1.12) eV, and 1.20 (1.65 eV) for Cu, Ag, and Au, respectively. For Cu and Ag, (see Figs. 6.13c and 6.13e), we observe peaks formed by the O *p* and noble metal *d* states at the bottom of the conduction band. In summary, we have found that the configurations with noble metal atoms adsorbed on the maghemite surface are the most effective in terms of CO adsorption. The metal atoms, indeed, allow for the formation of stronger bonds between CO and the surface atoms, Cu, Ag, and Fe, increasing, in this way, the adsorption energy with respect to the pristine and doped surfaces. A similar behavior was found previously in the case of H_2 adsorption on the CeO_2(111) surface with Cu, Ag, and Au single atoms adsorbed on it [109].

6.4 Conclusions

In this article we have studied, using an *ab − initio* approach, the structural and electronic properties of single Cu, Ag, and Au atoms adsorbed on the pristine (001)

maghemite surface, or substituting a surface Fe or O atom.
This work provides a theoretical insight on the noble metal atom modified maghemite surfaces. To understand how the catalytic activity depends on the different noble metal atom, and on its position is crucial to increase the performance of the catalysts.
We have found that the preferential adsorption site of all the three noble metals is a bridge position between two surface oxygens, and that they are aligned with the tetrahedral Fe atoms of the layer below. We have calculated that following adsorption of the noble metal atom, one electron is transferred to the oxide, leading to the formation of a positively charged noble metal ion. On the other hand, when the noble metal is adsorbed on the Fe vacancy, three electrons are transferred to the oxide. When instead the noble metal atoms are adsorbed on a surface oxygen vacancy, we have calculated a charge transfer from the surface oxide only to Au, which becomes a negatively charged ion.
We have also investigated the reducibility of the surfaces, and have found that, in general, the noble metal atoms substituting Fe atoms, decrease the energy required to remove surface oxygen atoms. In particular, among the three noble metal atoms, Ag seems to be the best candidate to increase the reducibility of the surfaces.
We have also investigated the stability of the modified surfaces as a function of temperature and pressure, and we have found that at room temperature and pressure the M(0,1,0,0)@Fe_2O_3(001) surfaces are the more stable ones, but for Ag the energy difference between the Ag(1,0,0,0)@Fe_2O_3(001) and Ag(0,1,0,0)@Fe_2O_3(001) surfaces is very small.
We have also found that the adsorption of CO on the surfaces is more favored when single Cu, Ag and Au atoms are adsorbed on the surface, and, in particular, Cu adsorbates increase CO adsorption energy of 184%.
In order to confirm our predictions concerning the stability of the surfaces scanning tunneling microscopy (STM) measurements of the surface should be performed. Moreover, STM images can be acquired to verify the adsorption of CO on the surfaces, and to test the catalytic activity of the surfaces CO-TPR measurement can be done to investigate the CO oxidation. Finally, our results indicate that noble metal atoms dispersed on the (001) maghemite surfaces may improve the catalytic properties of the maghemite surface and that the performance depends strongly on the kind of noble metal atom, its position, the degree of reduction of the surface, and if it is adsorbed or substitutional to surface Fe or oxygen atoms.

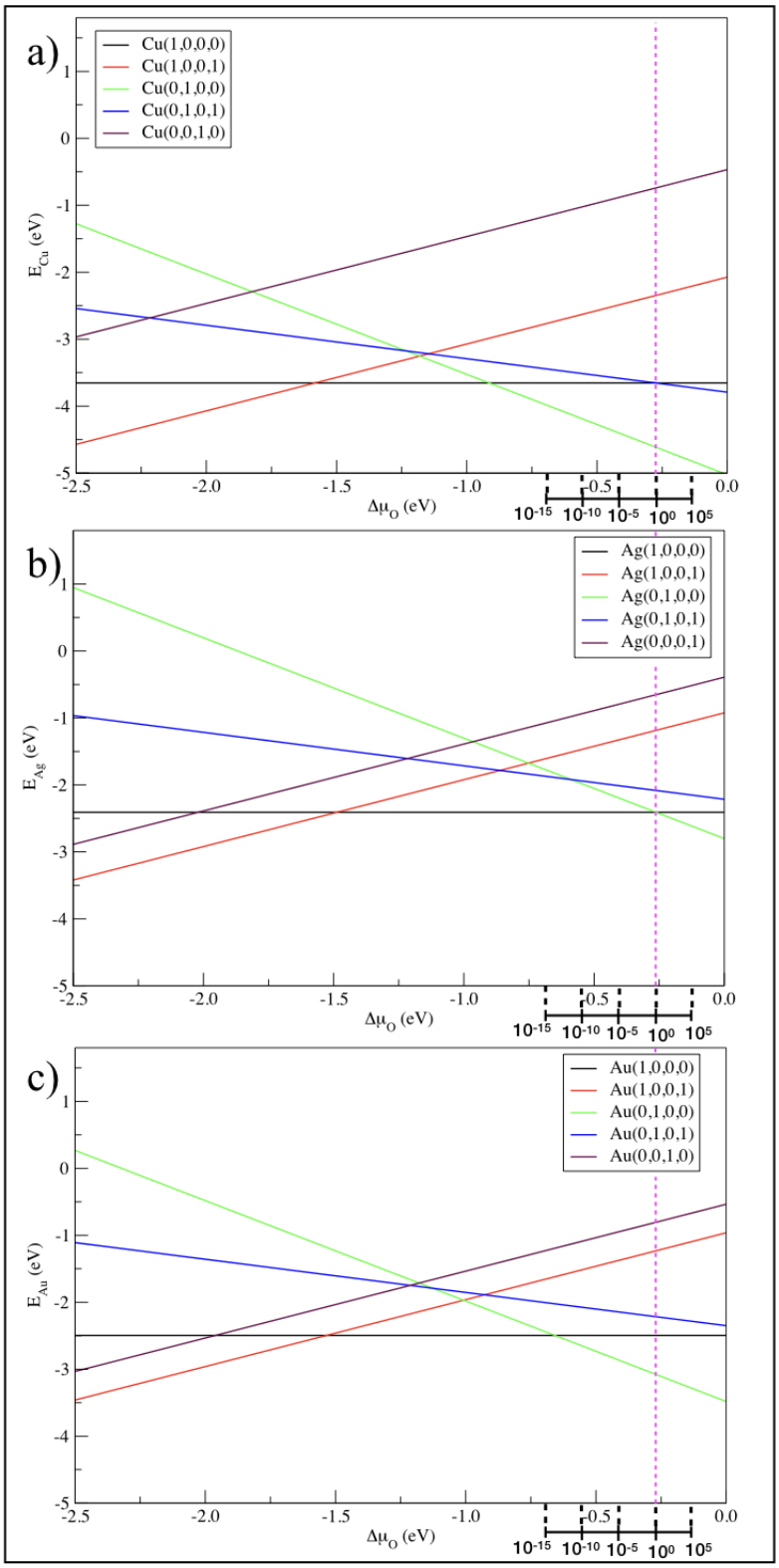

FIGURE 6.11: Adsorption and substitutional energies of maghemite surfaces with of a single a) Cu, b) Ag, and c) Au atom, as a function of the oxygen chemical potential. The purple dashed lines indicate μ_O=-0.27 eV. The values of oxygen chemical potential corresponding to a range of pressure (in atm) at room temperature are reported.

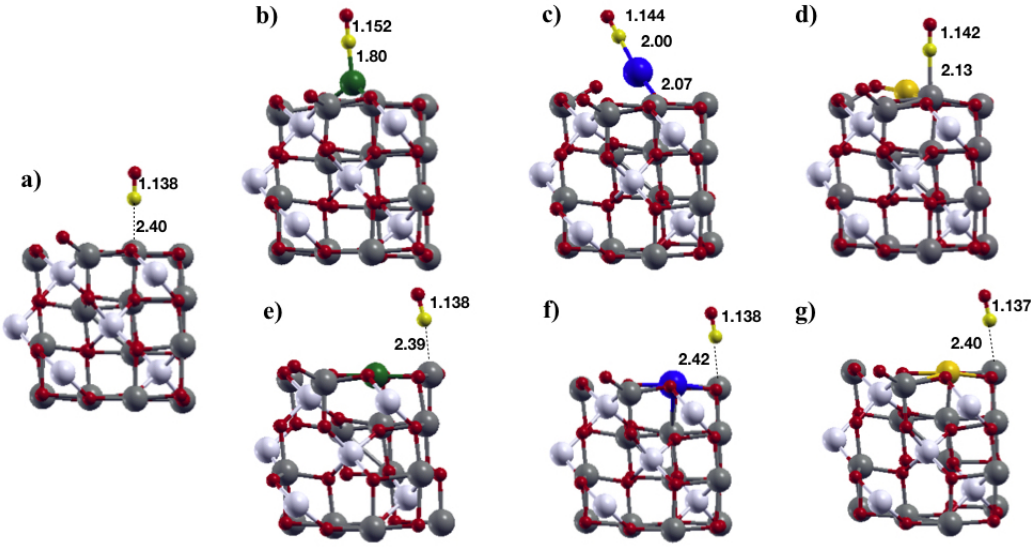

FIGURE 6.12: CO preferential adsorption sites on a) pristine maghemite surface, b) Cu(1,0,0,0)@Fe_2O_3(001), c) Ag(1,0,0,0)@Fe_2O_3(001), d) Au(1,0,0,0)@Fe_2O_3(001), e) Cu(0,1,0,0)@Fe_2O_3(001), f) Ag@Fe_2O_3(001), and g) Au@Fe_2O_3(001). All the distance are in angstrom. In Figure only half slabs are shown.

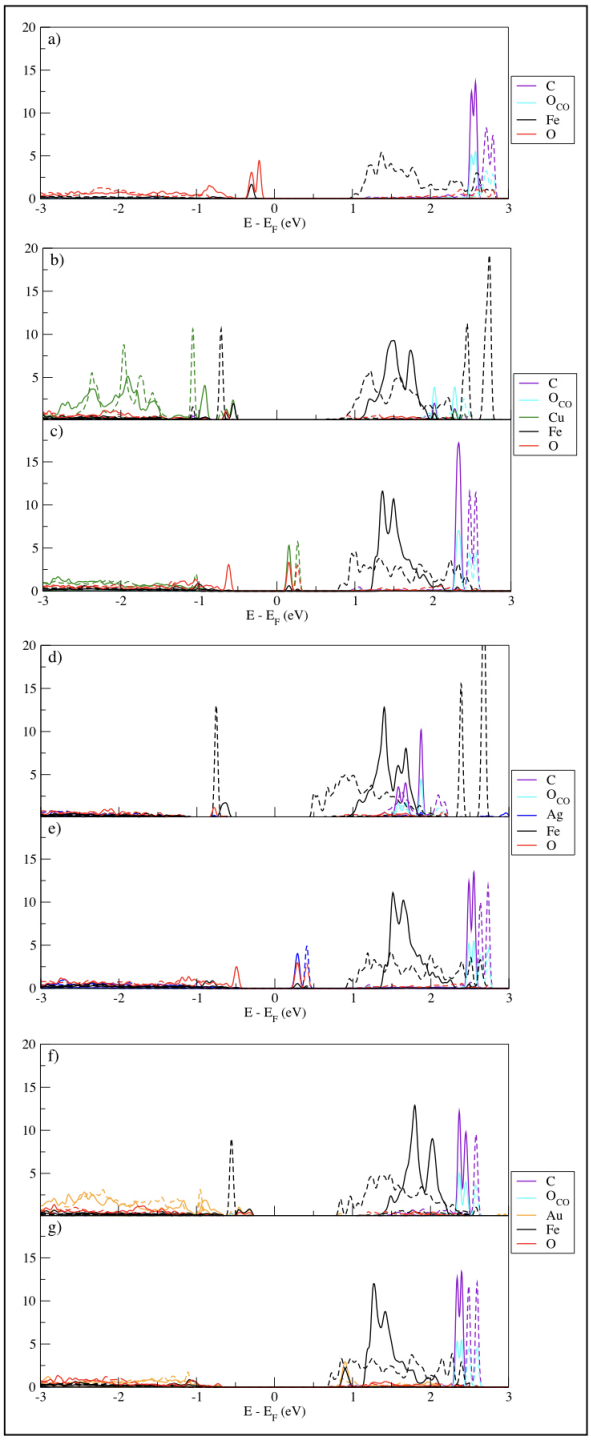

FIGURE 6.13: Atomic Projected Density of states of CO adsorbed on the different surfaces: a) B′, b) Cu(1,0,0,0)@Fe_2O_3(001), c) Cu(0,1,0,0)@Fe_2O_3(001), d) Ag(1,0,0,0)@Fe_2O_3(001), e) Ag(0,1,0,0)@Fe_2O_3(001), f) Au(1,0,0,0)@Fe_2O_3(001), and g) Au(0,1,0,0)@Fe_2O_3(001). Continuous and dashed lines are the spin up and down contributions, respectively.

Chapter 7

Conclusions

7.1 Summary

The aim of this thesis is to propose new catalysts, which are fundamental to the majority of the industrial processes. Using an *ab − initio* approach, based on the density functional theory, we have investigated how noble metal atoms dispersed on the surface and/or surface defects affect the catalytic activity.
In the first part of the thesis we have investigated cerium oxide as an active support for single noble metal atoms. In Chapter 3 we have studied how single Cu, Ag, and Au atoms, dispersed on the CeO_2 (111) surface, influence H_2 dissociation, an important reaction which occurs at the anode of the proton exchange membrane fuel cells (PEMFCs). Different configurations, which correspond to different noble metal oxidation states, have been studied. In general, the presence of noble metal atoms decreases the activation energy required to dissociate H_2, and the noble metals oxidation states play a key role in the determination of the activation energy. If the noble metal atoms are not initially in their preferential oxidation states, they contribute actively to the reactions acquiring the H_2 electrons, so as to reach at the end their preferential oxidation states. In this case, the activation energy is significantly diminished. On the contrary, when the noble metal atoms are already in their preferential oxidation state, the decrease of the activation energy is smaller. Moreover, CeO_2 modified with single Ag atoms seems to be a promising anode material, since, in all the configurations, the activation energy is significantly lower than on the pristine ceria surface, and the reaction energy (ΔE) for the adatom configuration is smaller than on pure ceria.
We have found that contrary to the common belief, the number of Ce^{3+} is not always a good marker to estimate the reducibility of surfaces in vacuum and under H_2 atmosphere. In vacuum, in agreement with the experiments, the number of O vacancies is, indeed, greater on Ag doped surfaces than on pristine ones, but the number of Ce^{3+} is smaller than on the pristine surface. On Ag doped surfaces, the H_2 activation energy is lower than on pristine ceria surfaces, although the number of Ce^{3+} is smaller. Also, the diffusion of a single H atom, on the pristine CeO_2 surface, requires more energy than on the Ag modified one, but then, very easily, it binds to the hydroxyl group to form water, which leads to the formation of more surface oxygen vacancies. On the other hand, on the Ag modified ceria surface, contrary to expectation, the number of oxygen vacancies is smaller, because the energy required to form water molecules is higher.
From an application point of view, the tendency of hydrogens to remain on the Ag doped ceria surface is an important result since a good catalytic material for a fuel cell anode needs to increase the rate of H_2 dissociation, but then the dissociated H atoms have to stay on surface, and longer to increase the probability of diffusion to the PEMFC membrane.

In Chapter 4, the addition of single Ag atoms to the ceria surface has been investigated also in relation to another reaction: the activation of methane, the main component of natural gas, which plays an important part in the global energy production and consumption [190] . Two ceria surface orientations have been considered, the (111) and the (100), and we have found that the (100) surface is more active in the dissociation of CH_4 into CH_3 + H. Ag favors the breaking of CH_4, since, acquiring the H electron, it can reach its favorite +1 oxidation state, and also the less charge oxygens, located near the Ag atom, can reach their favorite -2 oxidation states. Moreover, we have found that the presence of a single Ag atom allows for the direct conversion of CH_4 to methanol, an important fuel used to produce formaldehyde and another possible fuel for PEMFC. It is important to note that the energy required to produce methanol, on the Ag:CeO_2 (111) surface, has been calculated to be less than energy required to dissociate CH_4 into CH_3 + H, and methanol is a quite stable final product of the reaction.
In the second part of the thesis we have studied maghemite γ-Fe_2O_3, one of the less studied iron oxides. For the first time, the iron vacancies have been treated explicitly, see Chapter 5, beyond the mean-field theory. We have found that the presence of Fe vacancies increases the reduction and oxidation activity of the surface when compared to the analogous surface of magnetite Fe_3O_4. Our results go in the directions to explain the experimental results obtained by Najafishirtari et al. [151]. They have, indeed, observed that the rate of CO oxidation, which is strongly correlated to the removal, and adsorption of oxygen atoms from/to the surface, was greater for the sample with the largest content of maghemite, which is characterized by the presence of iron vacancies.
The increase of the reduction activity is due to a redistribution of the electronic charge on the surfaces compared to the bulk. The surface oxygen atoms in the proximity of the Fe vacancies are less charged with respect to those in the bulk, and these oxygen atoms are more active. On the magnetite surface, instead, where the Fe vacancies are not present, all the oxygen atoms are fully charged, and it is more difficult to remove them. Thus, maghemite is a good candidate for making a catalytic material following the Mars van-Krevelen mechanism of reaction.
The adsorption of a isolated Cu, Ag, and Au atoms on the most stable (001) maghemite surface is favored as reported in Chapter 6. In particular, at room temperature and pressure the configurations with the noble metal atoms in substitution of iron atoms are the most stable ones. The presence of noble metal atoms modifies the reducibility of the surfaces: if the noble metal atoms are in substitution of iron atoms, the reducibility of the surfaces increases significantly. This is a very promising result for catalytic reactions, which require the creation of oxygen vacancies, and, among the noble metal atoms, Ag seems to be the best candidate as single atom catalyst for these kinds of reactions. Also the adsorption of carbon monoxide is influenced by the presence of the noble metal atoms: the adsorption energy increases significantly if the noble metal atoms are only adsorbed on the surface, and the binding energy is particularly high for Cu.

7.2 Future Perspective

In Chapter 4 we have studied the activation of a single methane molecule on Ag doped CeO_2 surfaces. Recently, Xie et al. [28] have found experimentally that single Pt atom catalysts dispersed on ceria preferentially converted methane in C_2 products. It should be very interesting to study if also single Ag atoms, dispersed on

the ceria surface, convert selectively methane in the presence of more than one CH_4 molecule per surface unit cell. Moreover, once the activation energies have been calculated, kinetic Monte-Carlo simulations can be performed to simulate the kinetics of the reactions in time and extract the performance catalyzer parameters.
In Chapter 5 we have investigated the reduction and oxidation properties of the (001) maghemite surfaces, a possible next step towards the simulation of realistic iron oxide nanoparticles is to study how the redox activity varies if the exposed surface orientation changes from (001) to (111). Moreover, the surface energies can be investigated to determine the most stable surface terminations and therefore the shape of stable nanoparticles.
In Chapter 6 we investigated the adsorption of CO. The next step would be to determine the activation energies required to oxidate the CO molecules comparing the results obtained on the pristine surfaces with those modified by the presence of dispersed noble metal atoms in the different possible configurations.

Appendix A

The choice of the Hubbard parameter U

In this Appendix the geometric, electronic, and magnetic properties of cerium dioxide and trioxide have been calculated to determine the kind of pseudopotential, and the Hubbard U parameter to use in the calculations.

The Hubbard parameter U plays a crucial role in describing the localized electron in the *f* orbital. In order to determine the U value, we have calculated the geometric, electronic, and magnetic properties of cerium dioxide and trioxide for different value of U, and compared our results with the experimental and theoretical values present in the literature. We have chosen the value which approximates better the experimental results. We have considered three different pseudopotentials, projector augmented wave method (PAW), ultrasoft (US) and full relativistic, with the same Perdew- Burke -Ernzerhof (PBE) approximation [35] to the exchange correlation functional . The cerium atom has twelve valence electrons ($4f^1 5s^2 5p^6 5d^1 6s^2$) for the PAW and the ultrasoft pseudopotential, instead it has twenty two valence electrons ($5s^2 6s^2 5p^2 5p^4 4d^4 4d^6 5d^{1.5} 4f^{0.50}$) for the full relativistic one.

A.1 Cerium Dioxide

We have started our analysis from cerium dioxide. In this oxide, the *f* states of Ce are empty. Before testing the properties, it is necessary to determine the kinetic energy cut-off: to find this value we have calculated the total energy as a function of the lattice parameter for the three pseudopotentials, and we have observed where the variation was negligible. We can see that for the PAW and ultrasoft pseudopotentials the energy cut-off at convergence is 80 Ry, instead for the full relativistic one the energy cut-off required is 175 Ry. These energy cut-offs have been used to calculate the bulk properties.

A.1.1 Structural Properties

We have calculated the cerium dioxide's structural properties (lattice parameter and bulk modulus) for the three different pseudopotentials, as shown in Fig. A.4. The black, red and blue values are obtained using the PAW, ultrasoft and full relativistic pseudopotential, respectively. We have compared our results with the experimental values calculated by Duclos et al. [141] (orange line), Gerward et al. [191] (cyan and green lines) and Nakajima et al. [192] (yellow line). In general, increasing the value

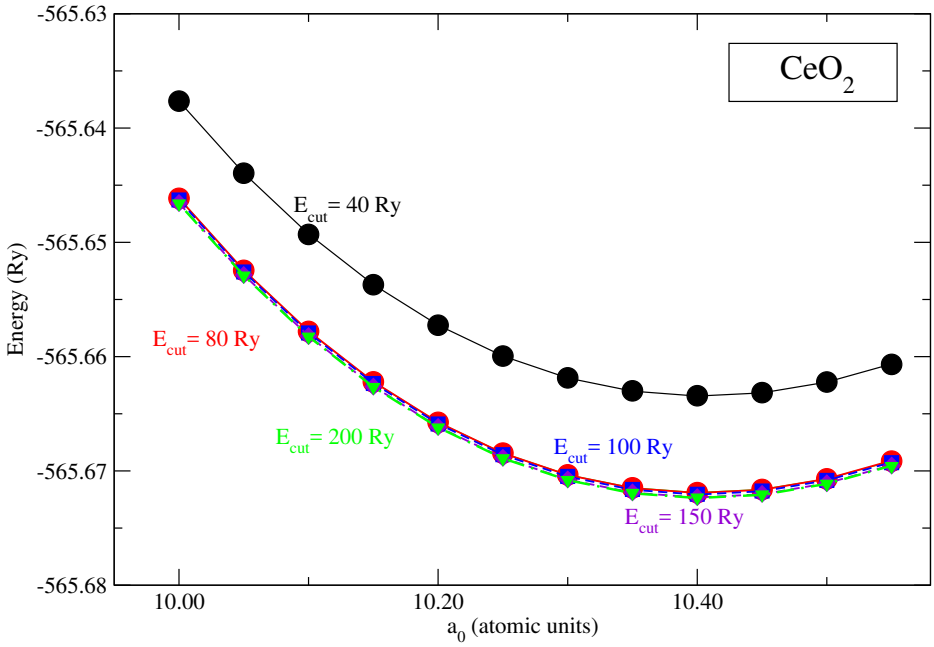

FIGURE A.1: Total energy as a function of the lattice parameter for different values of the cut-off energy calculated with the PAW pseudopotential.

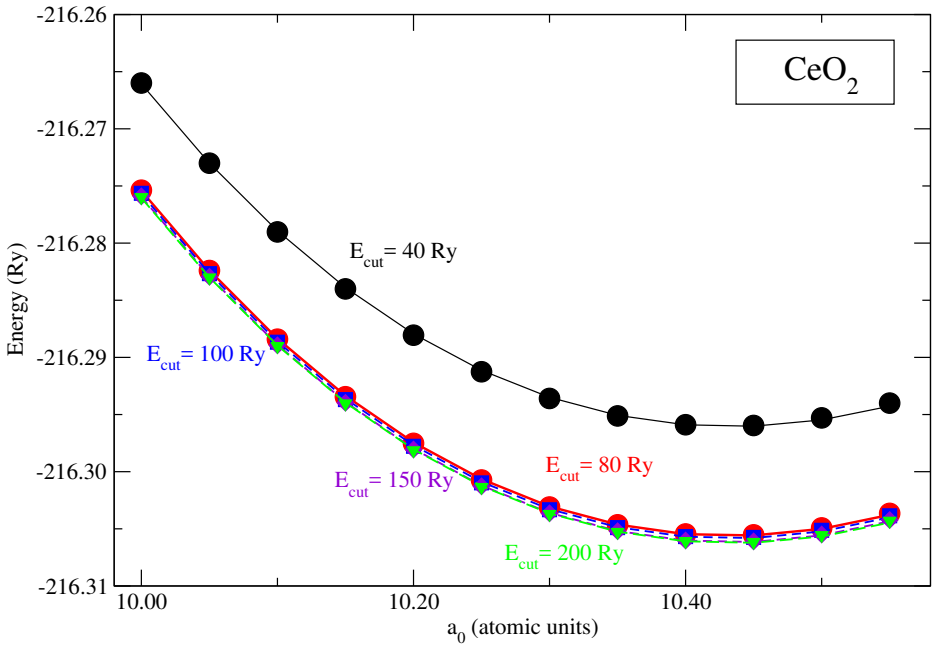

FIGURE A.2: Total energy as a function of the lattice parameter for different values of the cut-off energy calculated with the ultrasoft pseudopotential.

of U, the lattice parameter a_0 increases linearly as found, previously, by Andersson et al. [75] and Loschen et al. [193].

In Table A.1 we have compared our results with the theoretical values present in literature. Our lattice parameters are larger than the experimental value, see Fig. A.4, but they are agreed with the calculated values which are present in literature obtained with the same kind of pseudopotential. It is, indeed, known that the PBE

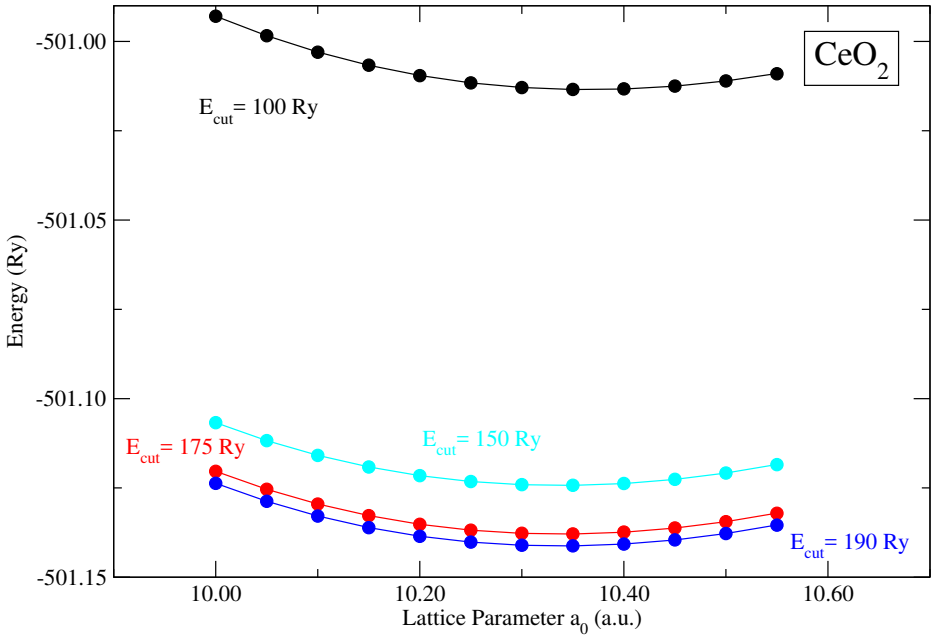

FIGURE A.3: Total energy as a function of the lattice parameter for different values of the cut-off energy calculated with the full relativistic pseudopotential.

approximation overestimates the structural parameters, as found in our calculation. The bulk modulus calculated values are agreed with the experimental value measured by Duclos et al. [141], but they are smaller than the other measured values. As for the lattice parameter, our results are similar to the theoretical values calculated with the same pseudopotentials.

A.1.2 Electronic Properties

It was noted in the literature that cerium dioxide is an insulating material. We have calculated the band structure, the density of states (DOS) and the partial density of states (PDOS) using the three different pseudopotentials.
In Figs. A.5, A.6, and A.7 the band structures, calculated for different values of the parameter U with the PAW, ultrasoft and full relativistic pseudopotentials, respectively, are shown. The variation of the band structure due to the change of the parameter U is very small for all the three pseudopotentials. In Figs. A.8, A.9, and A.10 we show the density of the states of CeO_2 changing the value of the U parameter, calculated with the PAW, ultrasoft and full relativistic pseudopotentials, respectively. The principal effect of the on-site correction is the shift of the f states's peak: increasing the value of U the f-peak moves towards higher energy for all pseudopotentials. However, as for the band structures, the variation of the density of states, due to the change of the U parameter, is small.
In Fig. A.11 we have compared the Ce_{4f} - O_{2p} and Ce_{5d} - O_{2p} gaps, and the width of the oxygen band (indicated in Fig. A.23, A.24, A.25) with the experimental results measured by Wuilloud et al. [200], whereas in Table A.2 we have compared our results with the theoretical values which are present in literature. Our results underestimate the experimental values of the gap, but they are in agree with the other theoretical values calculated using a DFT + U approach. The underestimation of the experimental gaps is an intrinsic problem of DFT calculations. In Figs. A.12, A.13, and A.14 we show the density of states projected onto the wavefunctions (PDOS)

TABLE A.1: Calculated values of the CeO_2 lattice parameter and bulk modulus.The lattice experimental value is a_0 = 5.38 Å[191], 5.40 Å[191] and 5.41 Å[141]. The Bulk Modulus experimental value is B = 220 GPa [191], 176.9 GPa [191] and 204 GPa [192].

Method	U (eV)	a_0 (Å)	B (GPa)	References
PAW LDA+U	5.0	5.40	213.7	[193]
PAW GGA+U	3.0	5.48	187.0	[193]
LDA+U	3.0	5.38	210.7	[194]
GGA+U	1.5	5.48	178.0	[194]
FP-LMTO LDA		5.39	214.7	[195]
FP-LMTO GGA		5.48	187.7	[195]
PAW LDA+U	6.0	5.40	217.0	[196]
PAW LDA+U	5.30	5.40	210.0	[197]
PAW PBE+U	4.50	5.49	180.0	[197]
PBE0		5.40		[198]
GGA+U	3.0	5.48		[198]
Hybrid Density Functional HSE		5.40	206.1	[199]
Ultrasoft (PBE)	3.0	5.50	179.8	This work
Ultrasoft (PBE)	4.5	5.52	175.1	This work
Ultrasoft (PBE)	5.0	5.52	178.5	This work
PAW (PBE)	3.0	5.49	175.2	This work
PAW (PBE)	4.5	5.50	175.1	This work
PAW (PBE)	5.0	5.50	175.0	This work
Full relativistic (PBE)	3.0	5.48	177.9	This work
Full relativistic (PBE)	4.5	5.49	179.2	This work
Full relativistic (PBE)	5.0	5.49	179.7	This work

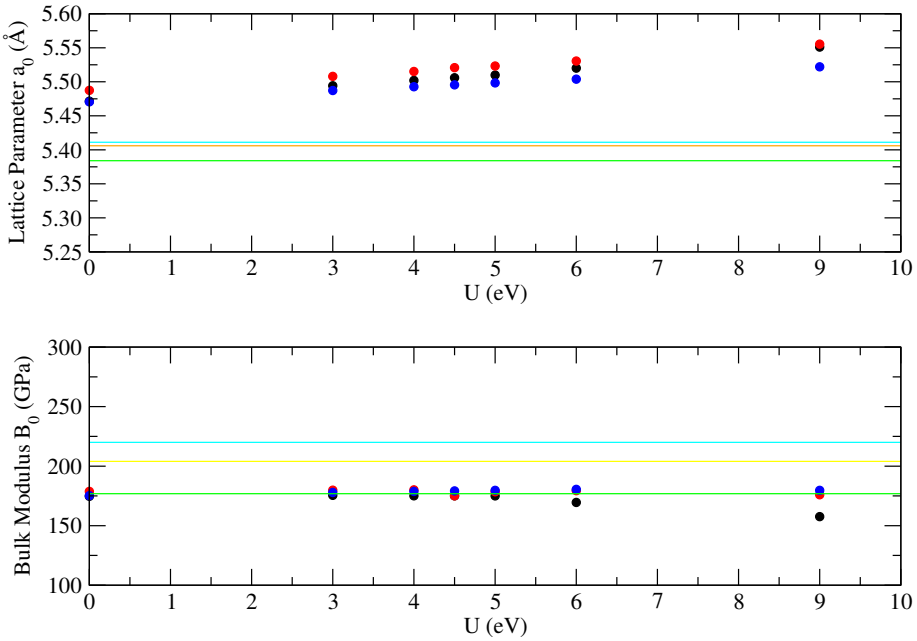

FIGURE A.4: Dependence of the lattice parameter and the bulk modulus on U (eV) value. Black, red and blue are the values obtained by the PAW, ultrasoft, full-relativistic pseudopotential, respectively. The continued green, cyan, orange yellow lines are the experimental values from Gerward et al. [191], Duclos et al. [141] and Nakajima et al. [192], respectively.

for all the pseudopotentials. In (a) the PDOS of Ce *f* states (continued line) and of O *p* states (dotted line) and, in (b), the PDOS of Ce *d* states (continued line) and of O *p* states (dotted line) are shown. The PAW and the ultrasoft pseudopotentials show the same trend, instead the full relativistic shows a shift of Ce *d* and O *p* peaks in the conduction band.

A.1.3 Charge Transfer

When the cerium atom binds to the oxygen atoms to form CeO_2, the valence electrons ($4f^1 5d^1 6s^2$) move from cerium to oxygen, and, consequently, Ce should have a theoretical charge of +8 if all the charge is completely transferred to oxygen, considering 12 valence electrons. We have studied the transfer of electrons analyzing the Bader charge [87] (see Figs. A.15, A.16), and the occupation of the Ce *f* orbitals and O *p* orbitals using the Löwdin charge [170], [171] (see Fig. A.17) for all the pseudopotentials. In general, we note that increasing the value of U the charge transfer increases slightly: a contemporary decreases (increase) of Ce (O) charge is calculated. The Bader charge analysis shows us that the 4 electrons are not transferred completely from the Ce atoms to the oxygen atoms: $\sim 9.5e$ are still on cerium instead of the theoretical $8e$. The charge transfers calculated using ultrasoft and full relativistic pseudopotentials are almost the same, whereas for the PAW pseudopotential the charge transfer is less, as shown in Fig. A.17.

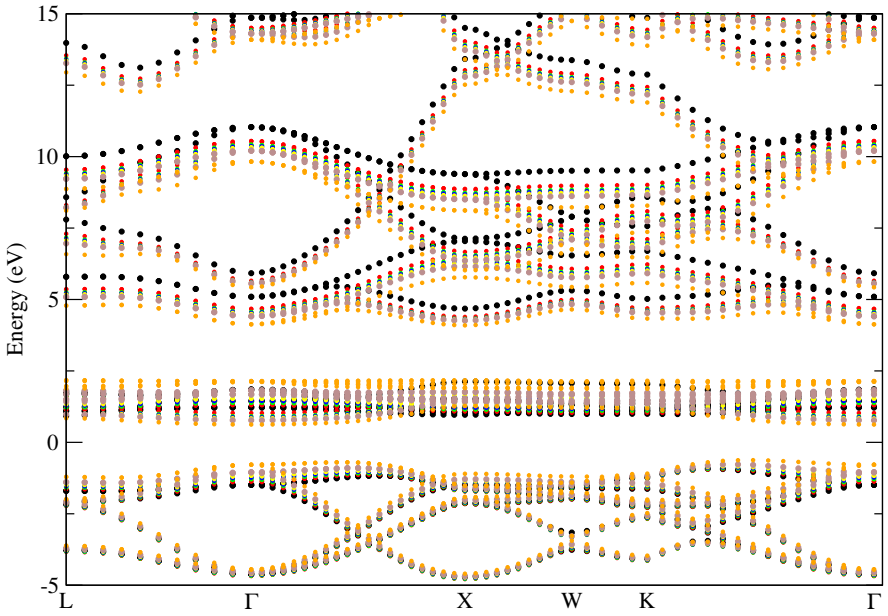

FIGURE A.5: Dependence on the U value of the band structure of CeO_2 obtained using the PAW pseudopotential. Black, red, green, blue, yellow, brown and orange are the values obtained using U= 0 eV, U = 3 eV, U = 4 eV, U = 4.5 eV, U = 5 eV, U = 6 eV and U = 9 eV, respectively.

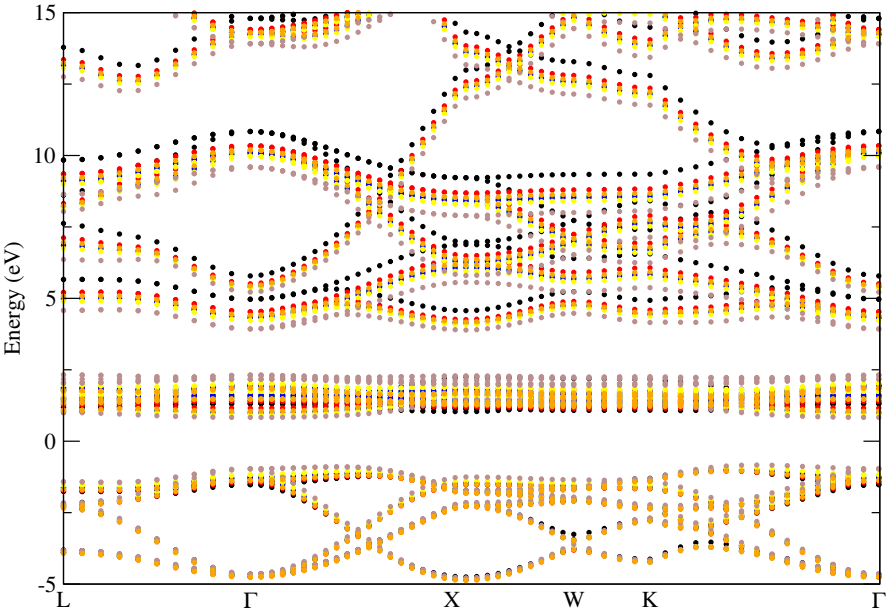

FIGURE A.6: Dependence on the U value of the band structure of CeO_2 obtained using the ultrasoft pseudopotential. Black, red, green, blue, yellow, brown and orange are the values obtained using U = 0 eV, U = 3 eV, U = 4 eV, U = 4.5 eV, U = 5 eV, U = 6 eV and U = 9 eV, respectively.

A.2 Cerium trioxide

Cerium trioxide (Ce_2O_3) has an hexagonal sesquioxide A-type structure. Experiments on the electronic and magnetic properties of Ce_2O_3 have shown that the oxide is an antiferromagnetic insulator. Through the standard DFT approach we can not

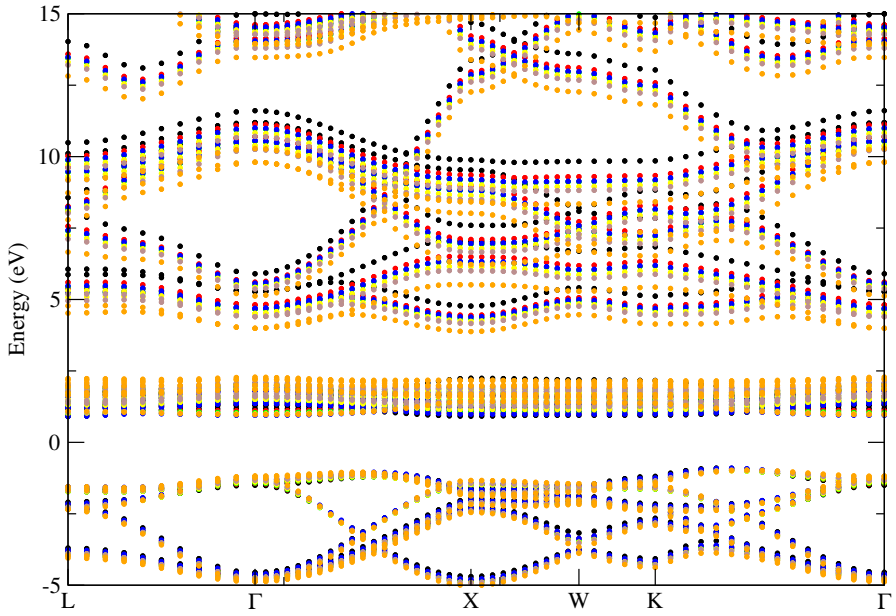

FIGURE A.7: Dependence on the U value of the band structure of CeO_2 obtained using the full relativistic pseudopotential. Black, red, green, blue, yellow, brown and orange are the values obtained using U = 0 eV, U = 3 eV, U = 4 eV, U = 4.5 eV, U = 5 eV, U = 6 eV and U = 9 eV, respectively.

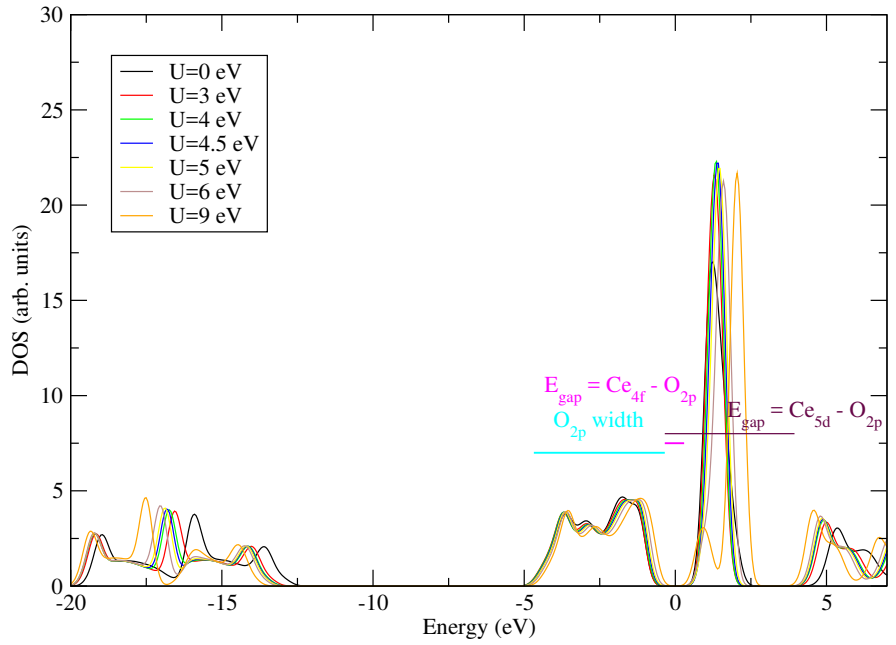

FIGURE A.8: Density of states of CeO_2 obtained by the PAW pseudopotential with different values of U. The calculated electronic gaps are shown.

describe correctly the Ce_2O_3's properties due to the difficulties to localize the cerium f states appropriately, since the cerium f states are now occupied by one electron. As for the CeO_2 oxide we have tested the structural, electronic properties using different pseudopotentials.

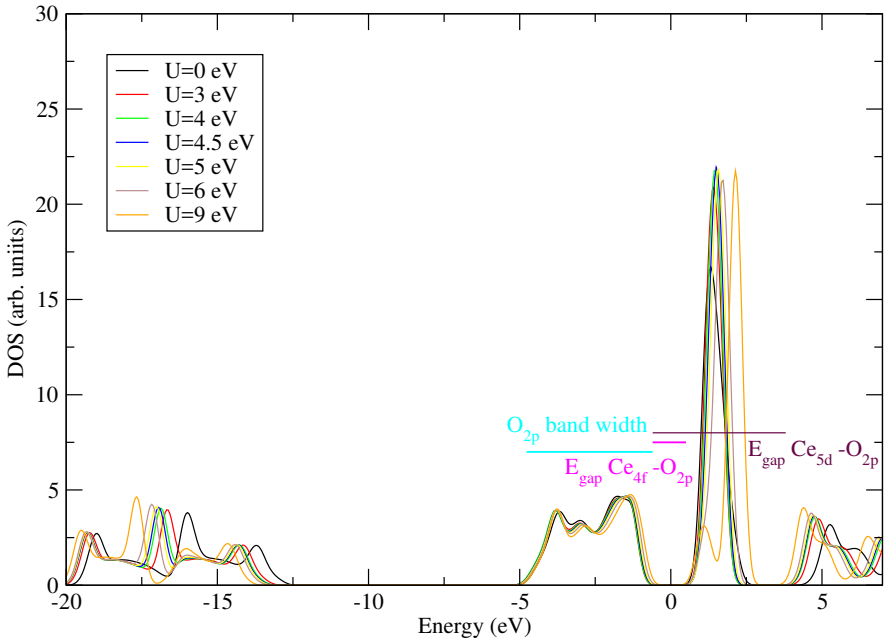

FIGURE A.9: Density of states of CeO_2 obtained by the ultrasoft pseudopotential with different values of U. The calculated electronic gaps are shown.

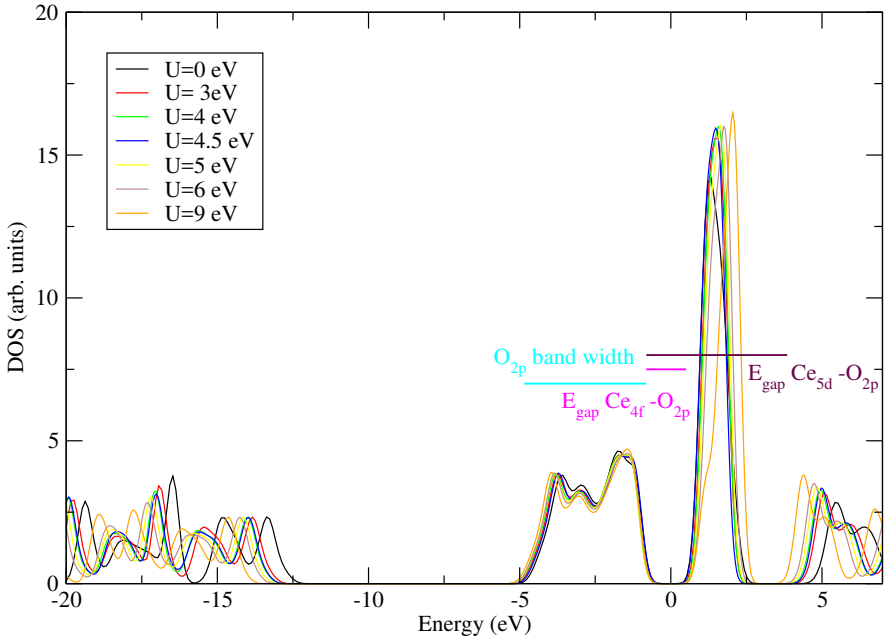

FIGURE A.10: Density of states of CeO_2 obtained by the full-relativistic pseudopotential with different values of U. The calculated electronic gaps are shown.

A.2.1 Structural properties

We show in Fig. A.18 the equilibrium lattice parameters for different values of the Hubbard parameter. The black, red and blue values are obtained using the PAW, ultrasoft and full relativistic pseudopotentials, respectively, and the green lines are the experimental values measured by Pinto et al. [201]. The lattice parameter a_0 increases linearly with U, but we can observe two exceptions U= 3 eV for the PAW

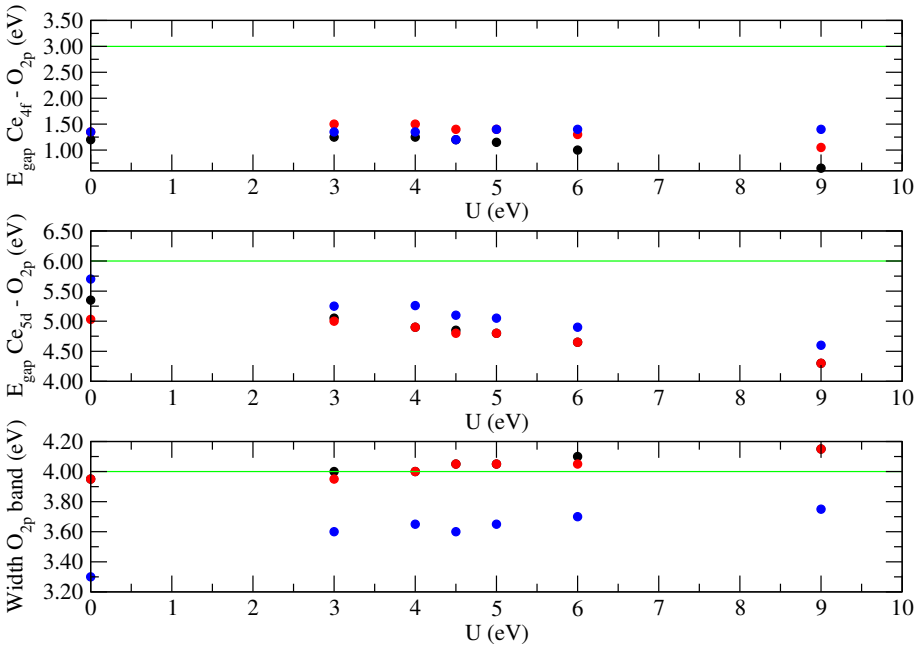

FIGURE A.11: Ce_{4f} - O_{2p} gap (top), Ce_{5d} - O_{2p} gap (middle) and the width of the oxygen band (bottom). Black, red, blue points are obtained by the PAW, ultrasoft anf full-relativistic pseudopotential. The green line shows the experimental value from [200].

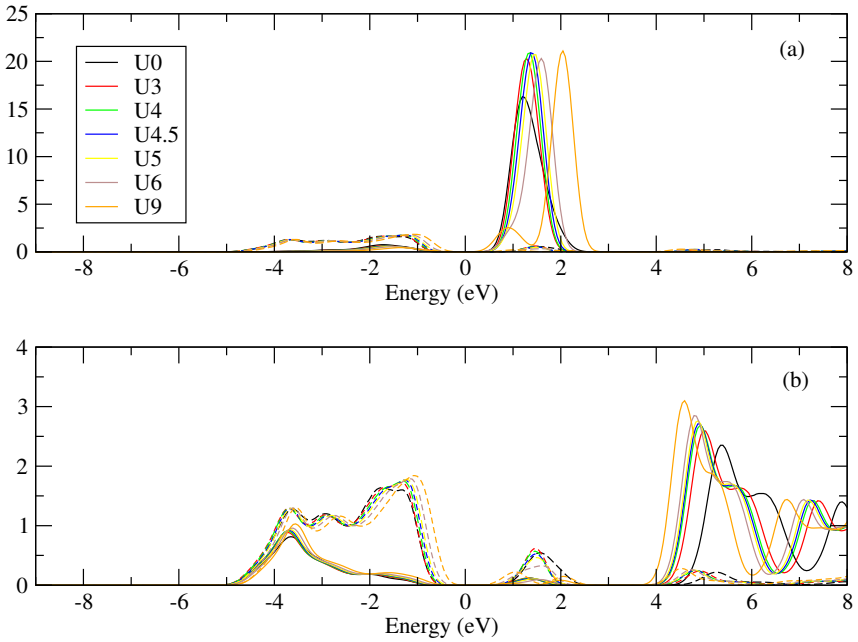

FIGURE A.12: (a) Partial dos of the Ce(4f) and O(2p) states obtained by different values of U. The Ce *f* states and the O *p* states are the continued and the dotted lines, respectively. (b) Partial dos of the Ce(5d) and O(2p) states obtained by different values of U. The Ce *d* states and the O *p* states are the continued and the dotted lines, respectively. The values are calculated with the PAW pseudopotential.

pseudopotential, and U=6 eV for the ultrasoft one. The higher difference in the lattice parameter is observed between U=0 eV and U=3 eV: this variation corresponds to the transition from a metal (U = 0 eV) and isolant (U = 3 eV). The linear trend

TABLE A.2: Theoretical CeO_2 energy gap. In the third column the energy gap between the Ce(5d) states and the O(2p) states, in the fourth he energy gap between the Ce(4f) and the O(2p) states. In the fifth column the width w of the O(2p) states is reported. All the values are in eV. The experimental values are $E_{gap_{dp}}$= 6 eV, $E_{gap_{fp}}$= 3 eV, and the width of O(2p) band , w,is 4 eV.

Method	U (eV)	$E_{gap_{dp}}$	$E_{gap_{fp}}$	w	Reference
LDA	0	5.5	2.5	4	[195]
LDA	0	5.61	2.0		[197]
PBE	0	5.64	2.0		[197]
LDA+U	-	≈ 5	1.3-2.3		[193]
GGA+U	-	$\approx$5	1.3-2.3		[193]
PAW	3	5.05	1.25	4	This work
PAW	4.5	4.85	1.2	4.05	This work
PAW	5	4.8	1.15	4.05	This work
Ultrasoft	3	5.0	1.5	3.95	This work
Ultrasoft	4.5	4.8	1.4	4.05	This work
Ultrasoft	5	4.8	1.4	4.05	This work
Full relativistic	3	5.25	1.35	3.6	This work
Full relativistic	4.5	5.1	1.20	3.6	This work
Full relativistic	5	5.05	1.40	3.65	This work

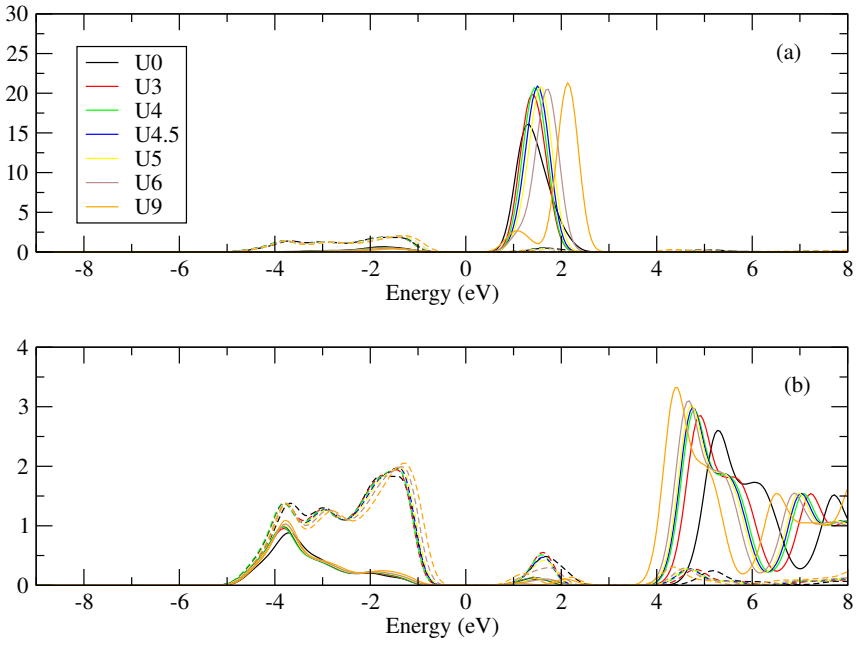

FIGURE A.13: (a) Partial dos of the Ce(4f) and O(2p) states obtained by different values of U. The Ce f states and the O p states are the continued and the dotted lines, respectively. (b) Partial dos of the Ce(5d) and O(2p) states obtained by different values of U. The Ce d states and the O p states are the continued and the dotted lines, respectively. The values are calculated with the ultrasoft pseudopotential.

was also observed by Niu et al. [202] and Andersson et al. [75]. We can note that

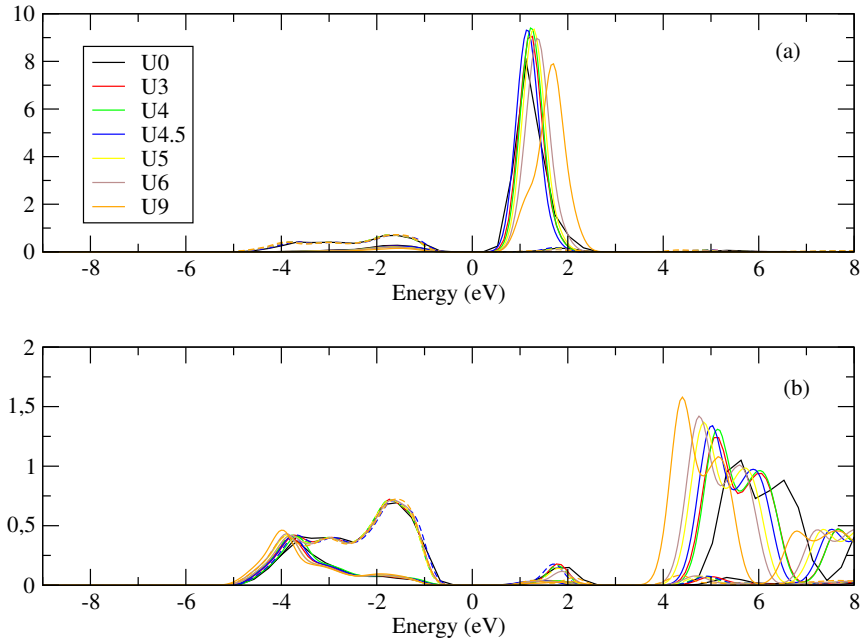

FIGURE A.14: (a) Partial dos of the Ce(4f) and O(2p) states obtained by different values of U. The Ce *f* states and the O *p* states are the continued and the dotted lines, respectively. (b) Partial dos of the Ce(5d) and O(2p) states obtained by different values of U. The Ce *d* states and the O *p* states are the continued and the dotted lines, respectively. The values are calculated with the full relativistic pseudopotential.

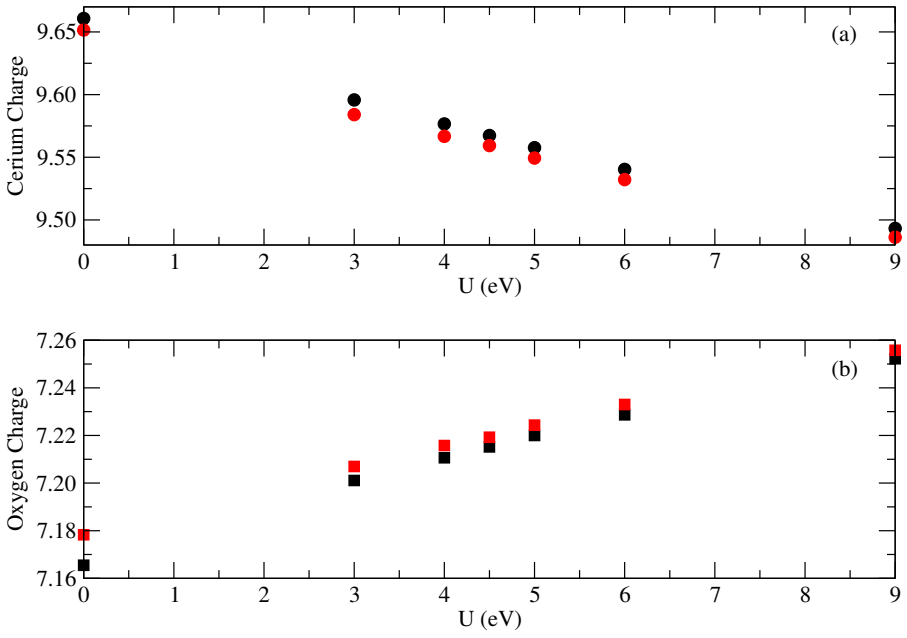

FIGURE A.15: Bader charge for Ce(4f) atom, at the top, and O(2p) atom, at the bottom, for different value of U. Black and red points are the values obtained by PAW and ultrasoft pseudopotential, respectively.

all the pseudopotentials reproduce correctly the experimental values of the lattice parameters of the oxide, especially at intermediate value of U, 3<U<5. The values of the bulk modulus do not show a regular behavior but there are not experimental

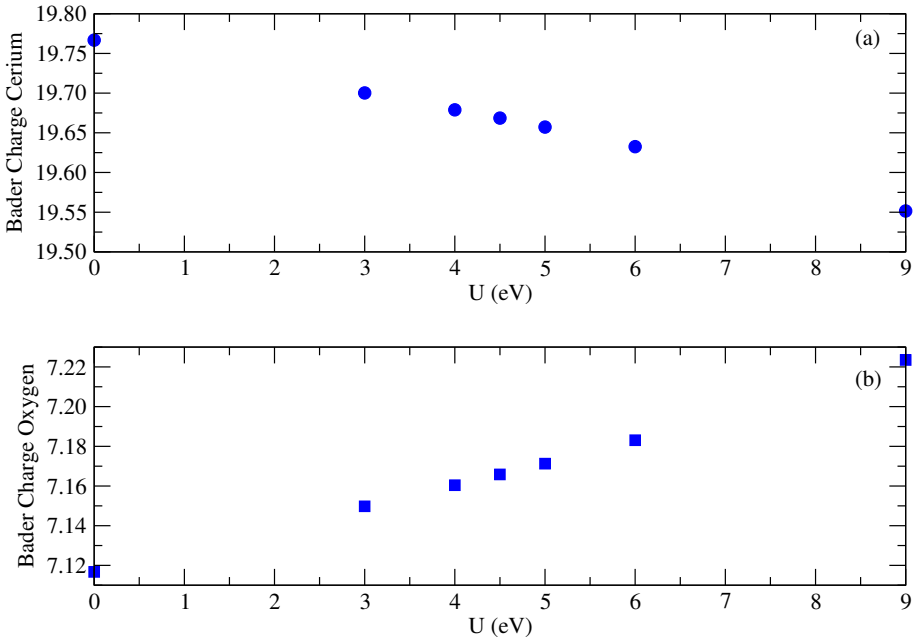

FIGURE A.16: Bader charge for $Ce(4f)$ atom, at the top, and $O(2p)$ atom, at the bottom, for different value of U. The values are obtained by the full-realtivistic pseudopotential.

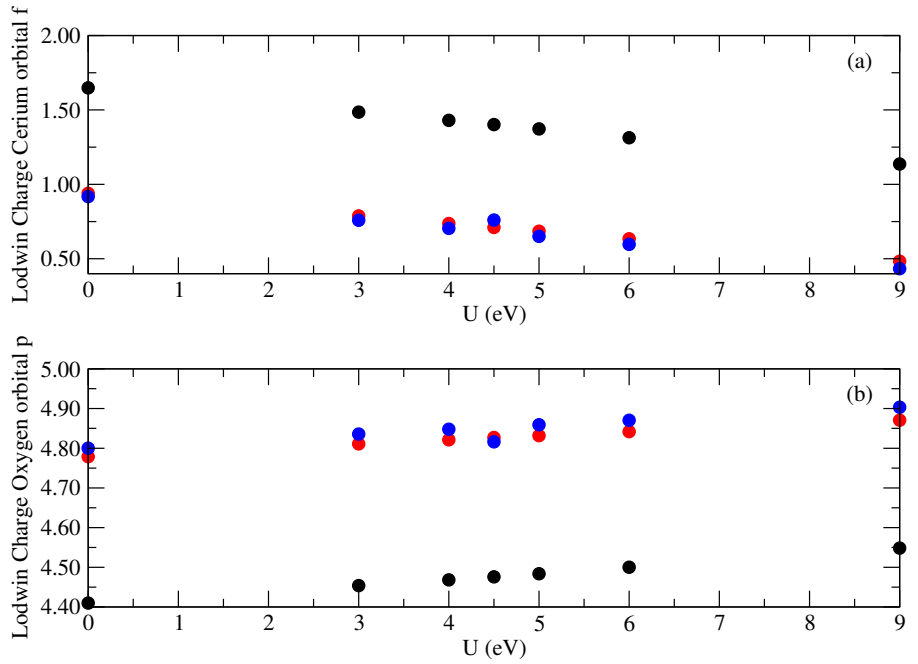

FIGURE A.17: Dependence of Löwdin charge of the Ce(4f) state and O(2p) state on U value. Black, red and blue values are obtained by PAW, ultrasoft and full-relativistic pseudopotential, respectively.

values to compare with. The lattice parameter a_0 is in good agreement with the other theoretical values present in literature, as shown in Table A.3.

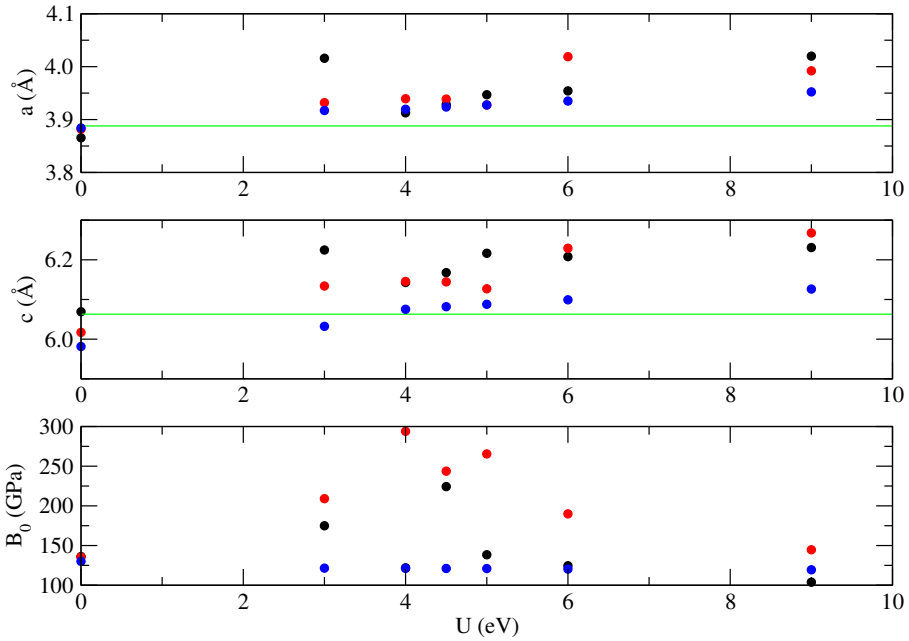

FIGURE A.18: Dependendence of Ce_2O_3 lattice parameters and bulk modulus B_0 on the value of the parameter U. Black, red and blue are values are obtained with PAW, ultrasoft and full relativistic pseudpotentials, respectively. These values have been obtained for the ferromagnetic case. The green lines are the experimental value measured by Pinto et al. [201].

A.2.2 Electronic and Magnetic Properties

We have tested the electronic and magnetic properties of the Ce_2O_3 oxide obtained with the three different pseudopotentials. We have found, in agreement with the literature, that the antiferromagnetic ground state is more stable than the ferromagnetic one. In the majority of cases the difference between the two configurations is 0.2/0.3 eV as found by Fabris et al. [194] using a LDA approximation. In Fig. A.19 we show the dependence of the absolute magnetization of the oxide in the antiferromagnetic ground state varying the value of the U parameter. We can see that the ultrasoft and PAW pseudopotentials underestimate slightly the experimental value measured by Pinto et al. [201] (2.17 μ_B), instead the full relativistic pseudopotential overestimates it for two values of the parameter U. We have associated an error bar to the absolute magnetization values obtained with the full-relativistic pseudopotential since the convergence required was less. This has been necessary to make a SCF cycle. For U equal to 3 eV and 5 eV the values obtained with the PAW and ultrasoft pseudopotentials fall inside the error bars. In Table A.4 we have also compared our results with the values reported in literature, and our values are in good agreement with the other theoretical values. To conclude this analysis about the magnetic properties we have compared the magnetic moment of Ce for different values of the parameter U as shown in Fig. A.20. The black, red and blue values are obtained with the PAW, ultrasoft and full relativistic pseupotentials, respectively. For the full-relativistic pseudopotential we have inserted the error bars since the values are less accurate. The continued line is the experimental value measured by Pinto. et al. [201]. In Figs. A.21, and A.22 we show the Ce_2O_3 band structure, calculated with the PAW and ultrarsoft pseudopotentials, in the antiferromagnetic case, and in Figs.

TABLE A.3: Ce_2O_3 lattice parameters. The lattice experimental values are a_0=3.888 Åand c_0=6.063 Å.

Method	U (eV)	a_0 (Å)	B_0 (GPa)	Reference
LDA + U	5.0	3.85	144.7	[193]
GGA + U	3.0	3.92	128.5	[193]
LDA + U	3.0	3.84	150.9	[194]
GGA (PBE) + U	1.5	3.94	131.3	[194]
LDA + U	6.0	3.877		[202]
PAW (PBE0)		3.87		[197]
PAW (PBE)	4.50	3.92	111 (AF)	[197]
PAW (LDA + U)	5.30	3.86/7	130 (AF)	[197]
PAW (PBE)	3.0	3.94	195.7	Present Work
PAW (PBE)	4.5	3.93	224	Present Work
PAW (PBE)	5.0	3.95	138.4	Present Work
Ultrasoft (PBE)	3.0	3.93	209.0	Present Work
Ultrasoft (PBE)	4.0	3.94	293.9	Present Work
Ultrasoft (PBE)	5.0	3.93	265.4	Present Work
full relativistic	3.0	3.90	121.4	Present Work
full relativistic (PBE)	4.5	3.92	121.1	Present Work
full relativistic (PBE)	5.0	3.92	121.0	Present Work

A.23, A.24, A.25 the density of states obtained with the three different pseudopotentials. We note that increasing the value of the parameter U the Ce(5d) and O(2p) bands tend to move both to higher energies. It is interesting to note that for U less than 5 eV the *f* states are separated from the other, whereas, increasing U, they tend to merge with the oxygen band state valence. In particular, the *f* peak tends to move to higher energies for U=3 eV and U=4 eV, and then it moves back to lower energies until it merges with the oxygen states for the PAW and the ultrasoft pseudopotentials. This mixing was hypothesized by Andersson [75] although occurring at higher values of U.

In Fig. A.26 we show the Ce(4f) - Ce(5d), Ce(4f)- O(2p) and Ce(5d) - O(2p) gaps, indicated in Figs. A.23, A.24, A.25. The gaps have been obtained with the three different pseudopotentials, and compared with the experimental values. The black, red and blue values are calculated with PAW, ultrasoft and full relativistic pseudopotential, respectively. The green line shows the experimental values measured by Prokofiev et al. [204] and Mullins et al. [205]. Increasing U the valence-conduction gap (Ce(4f) - Ce(5d)) increases progressively as observed previously by Jiang et al. [206], and in the range 4<U<5, the gap is similar to the experimental value. The Ce(4f) - O(2p) gap tends to decrease increasing U, and for U>5 it is almost zero. The last considered gap is between the O *p* states and the Ce *d* states: the gap is almost constant until U is less than 6 eV, and then it tends to decrease. In Figs. A.28, and A.29 we show the PDOS on Ce(4f), Ce(5d) and O(2p) for two different values of U obtained with the PAW and ultrasoft pseudopotentials. We can see the shift of *d* and *f* states towards higher energies introducing the correction of Hubbard. In Fig. A.30 we show the PDOS of Ce_2O_3 calculated with a full relativistic pseudopotential with the Hubbard correction.

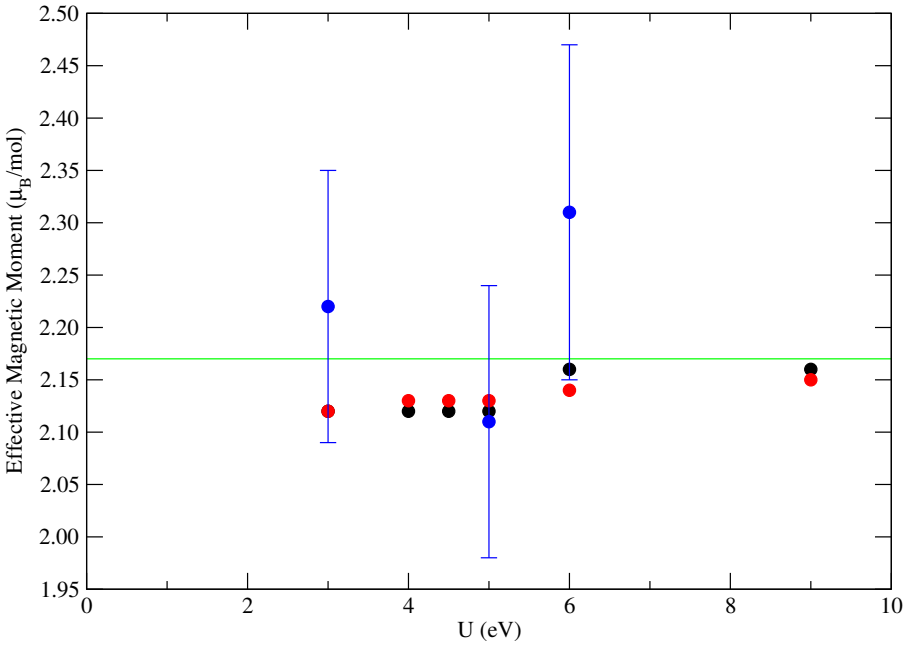

FIGURE A.19: Ce_2O_3 absolute magnetization. The black, red and blues values are obtained by PAW, ultrasoft and full relativistic pseudopotential, respectively. We have associated an error bar (blue lines) to the absolute magnetization values obtained with the full-relativistic pseudopotential since the convergence required was less. The green line is the experimental value measured by Pinto et al. [201].

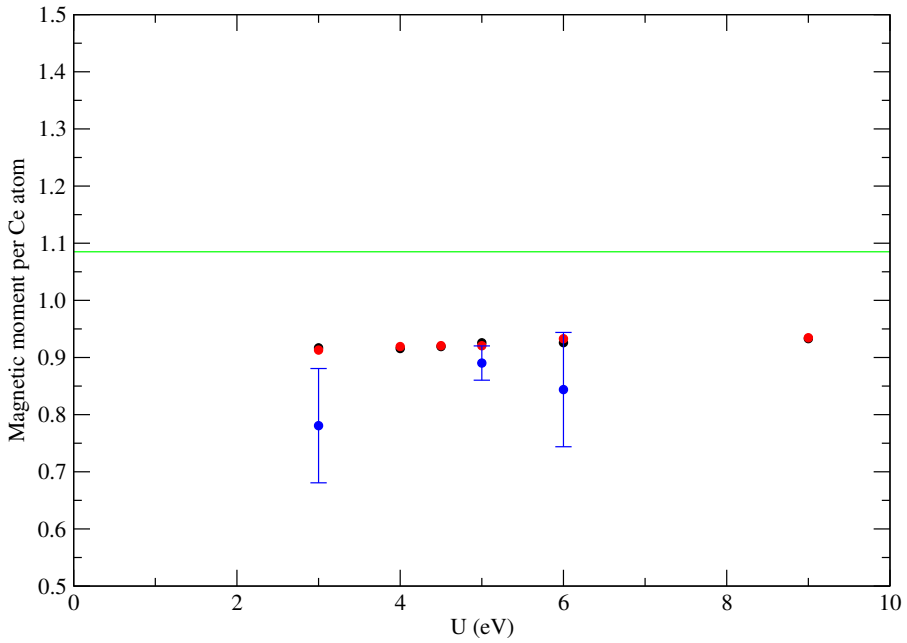

FIGURE A.20: Ce magnetic moment. The black, red and blues values are obtained by PAW, ultrasoft and full relativistic pseudopotential, respectively. We have associated an error bar (blue lines) to the absolute magnetization values obtained with the full-relativistic pseudopotential since the convergence required was less. The green line is the experimental value measured by Pinto et al. [201].

TABLE A.4: Theoretical values of the absolute magnetization of Ce_2O_3. * f electron in the core, ** f electron in the valence. The experimental value is 2.17 μ_B/mol measured by Pinto at al. [201].

Method	U	μ_B/mol	Reference
FP-LMTO*		2.13	[195]
FP-LMTO**		0.72	[195]
LDA		2.29	[194]
LDA +U	3	2.25	[203]
PAW (PBE) + U	3	2.12	Present Work
PAW (PBE) + U	4.5	2.12	Present Work
PAW (PBE) + U	5	2.12	Present Work
ultrasoft (PBE) + U	3	2.12	Present Work
ultrasoft (PBE) + U	4.5	2.13	Present Work
ultrasoft (PBE) + U	5	2.13	Present Work
full relativistic (PBE) + U	3	2.22	Present Work
full relativistic (PBE) + U	5	2.11	Present Work
full relativistic (PBE) + U	6	2.31	Present Work

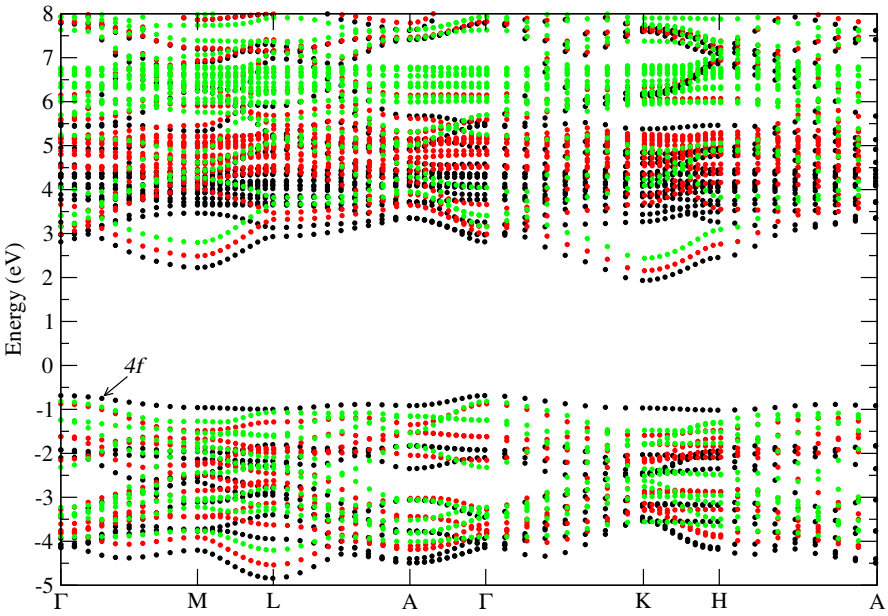

FIGURE A.21: Ce_2O_3 band structure obtained with the PAW pseudopotential. The black, red and green points are the energy obtained with U = 4.5 eV, 6 eV, 9 eV.

A.2.3 Charge Transfer

We have studied the transfer of charge from cerium to oxygen due to the difference of the electronegativity of the two elements occurring when the cerium atoms binds with the oxygen atoms. Each unbounded cerium atom has 12 valence electrons, and we would expect that 3 electrons, for each Ce atom, get transferred to the oxygen atom after the binding (each O receiving 2 electrons). The Bader charges of Ce and O atoms, calculated with different pseudopotentials, are shown in Figs. A.31, and A.32, whereas the Löwdin charges are shown in Fig. A.33. The Bader charge of

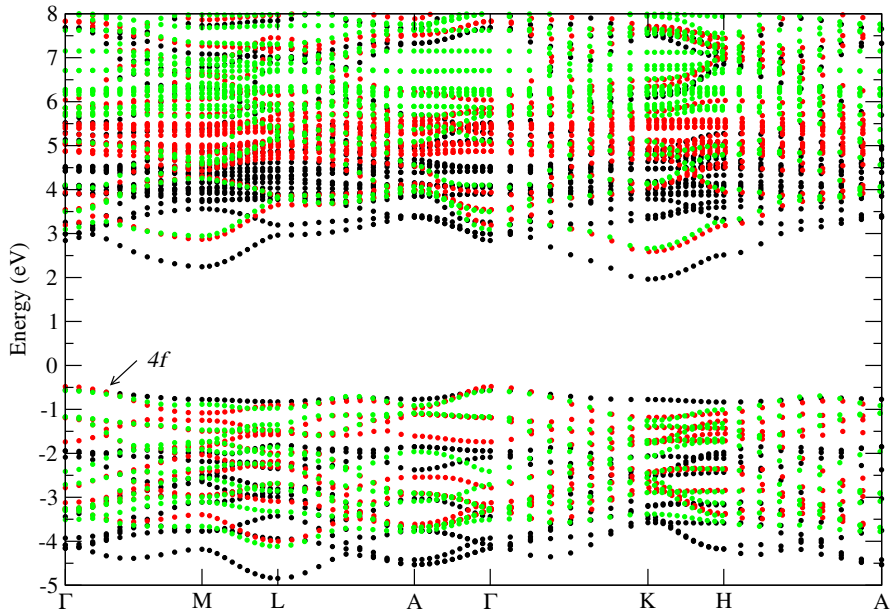

FIGURE A.22: Ce_2O_3 band structure obtained with the ultrasoft pseudopotential. The black, red and green points are the energy obtained with U = 4.5 eV, 6 eV, 9 eV

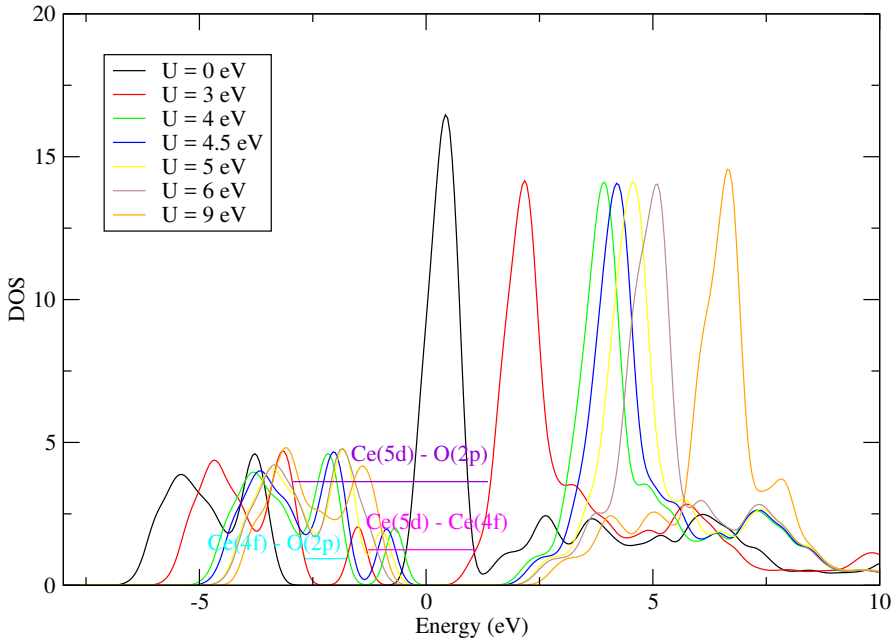

FIGURE A.23: Dependence of Ce_2O_3 on the value of parameter U. The values are obtained with PAW pseudopotential

two oxygens is reported since two of the three oxygens present in the bulk are not equivalent. The Bader charge analysis shows us that the theoretical 3 electrons are not transferred completely from the Ce atoms to the oxygen atoms: $\sim 9.9e$ indeed are still on Cerium, instead of the of the predicted $9e$. A charge transfer of $2.01e$ with respect to the the gas phase is calculated. Increasing the value of the parameter U, we can see a decrease of cerium charge and an increase of oxygen charge. Thus, increasing U, the calculated charge transfer increases. This behavior is also confirmed by the occupation of Ce and O states as reported in Table A.5.

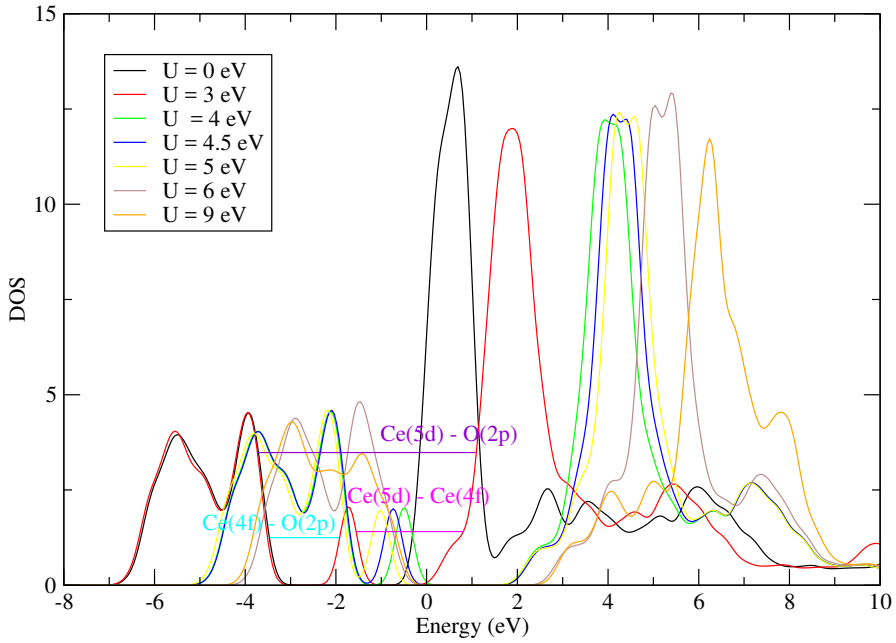

FIGURE A.24: Dependence of Ce_2O_3 on the value of parameter U. The values are obtained with ultrasoft pseudopotential.

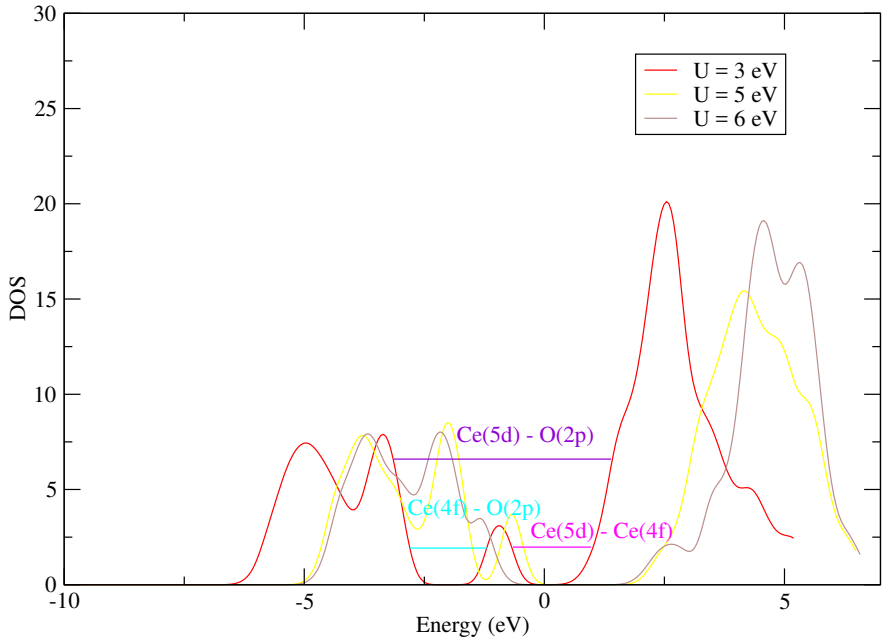

FIGURE A.25: Dependence of Ce_2O_3 on the value of parameter U. The values are obtained with full relativistic pseudopotential.

We have chosen to set the Hubbard value to 4 eV. Indeed, for this value of U we can reproduce, in the better way, the experimental gaps of both CeO_2 and Ce_2O_3 oxides.

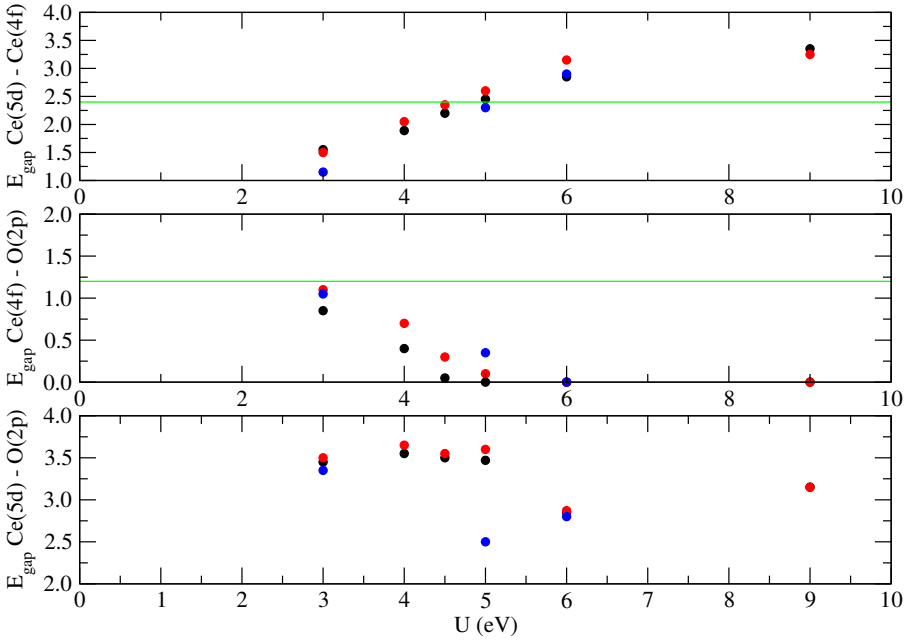

FIGURE A.26: Ce_2O_3 bands gap. At the top we show Ce(4f) - Ce(5d) gap, at the middle Ce(4f) - O(2p) gap, and at the bottom Ce(5d) - O(2p). Black, red and blue are the values obtained with PAW, ultra-soft and full relativistic pseudopotential, respectively. The green line shows the experimental values measured by Prokofiev et al. [204] and Mullins et al. [205].

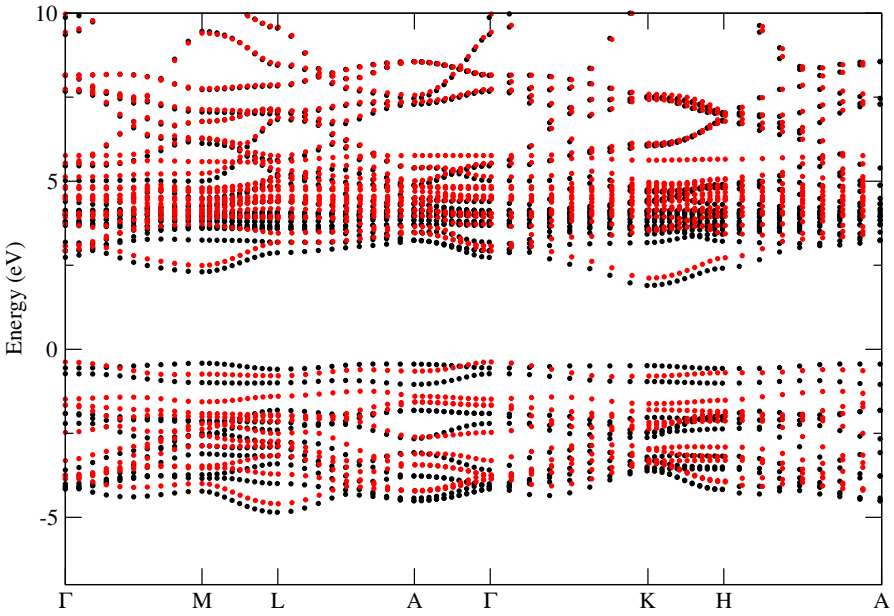

FIGURE A.27: Ce_2O_3 band structure with a ferromagnetic ground state calculated with a PAW pseudopotential. Black, red and green values are obtained with U = 4.5 eV and 6 eV, respectively.

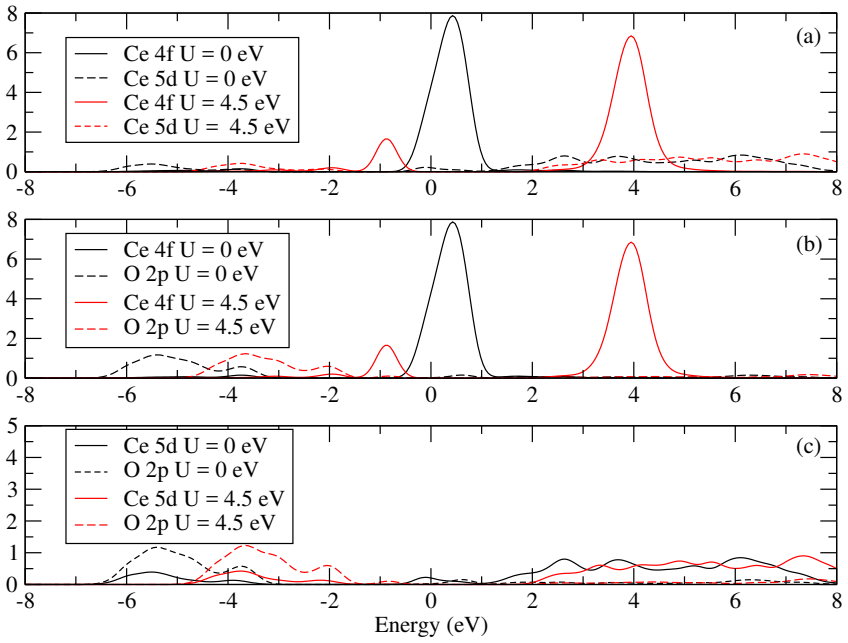

FIGURE A.28: Dependence of PDOS on the parameter value U. (a) PDOS on Ce(4f) atom and Ce(5d) atom. (b) PDOS on Ce(4f) and O(2p). (c) PDOS on Ce(5d) and O(2p). All the values are obtained wih PAW pseudopotential.

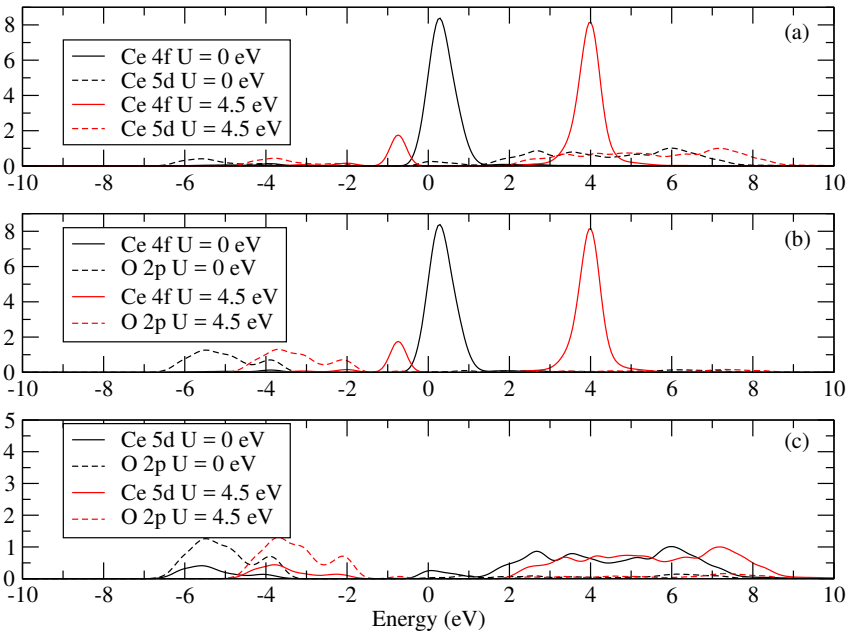

FIGURE A.29: Dependence of PDOS on the parameter value U. (a) PDOS on Ce(4f) atom and Ce(5d) atom. (b) PDOS on Ce(4f) and O(2p). (c) PDOS on Ce(5d) and O(2p). All the values are obtained wih PAW pseudopotential.

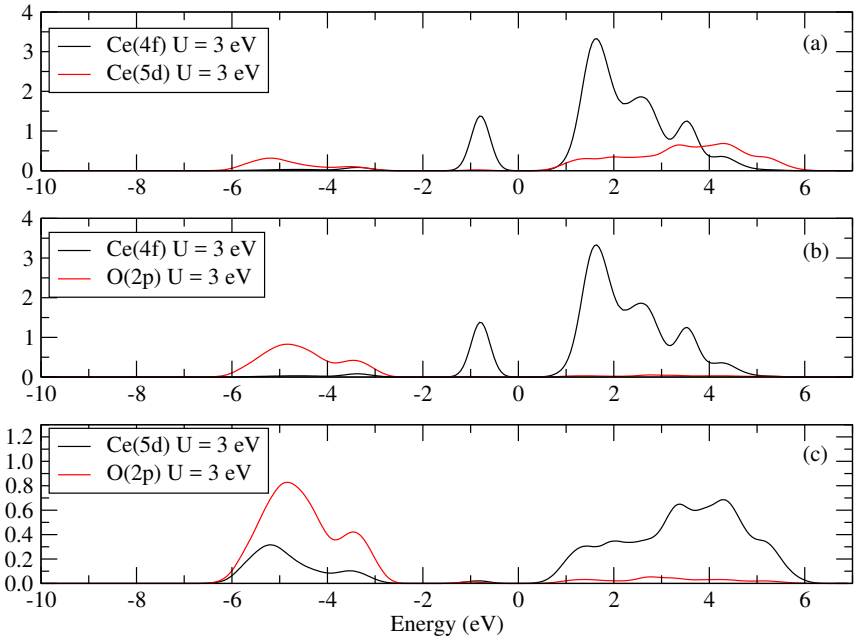

FIGURE A.30: Ce_2O_3 PDOS calculated with full relativistic pseudopotential.(a) PDOS on Ce$(4f)$ atom and Ce$(5d)$ atom. (b) PDOS on Ce$(4f)$and O$(2p)$. At the bottom PDOS on Ce(5d) and O(2p).

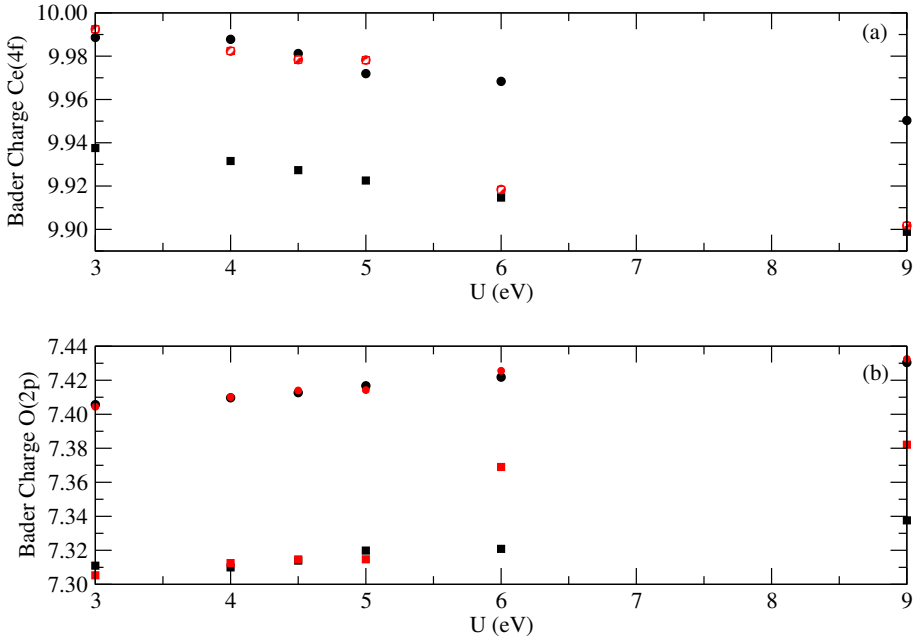

FIGURE A.31: Ce_2O_3 Bader charge. (a) Ce(4f) Bader charge, (b) the O(2p) Bader charge the black and the red values are obtained by PAW and ultrasoft pseudopotential, respectively.

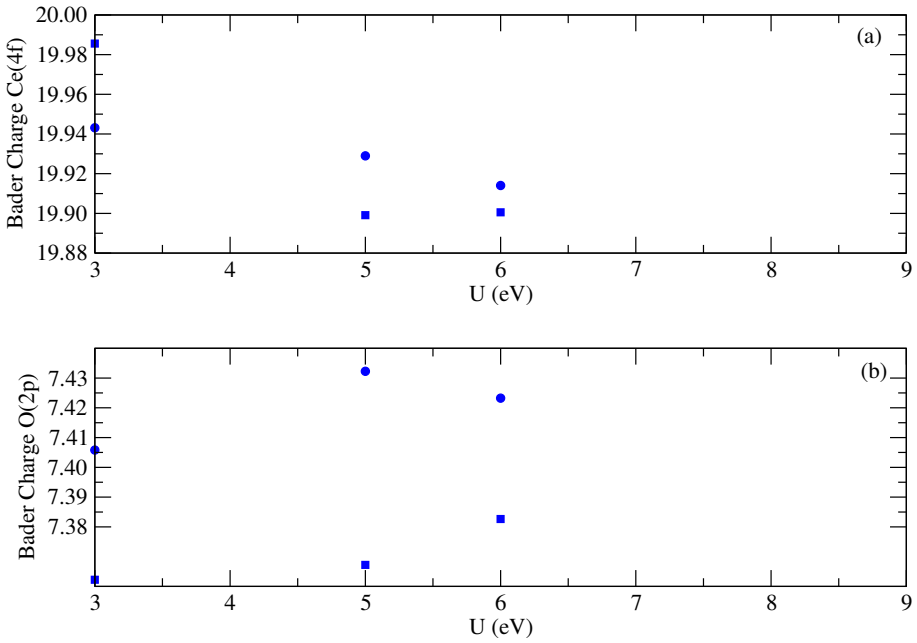

FIGURE A.32: Ce_2O_3 Bader charge. (a) Ce(4f) Bader charge, (b) the O(2p) Bader charge calculated with full relativistic pseudopotential.

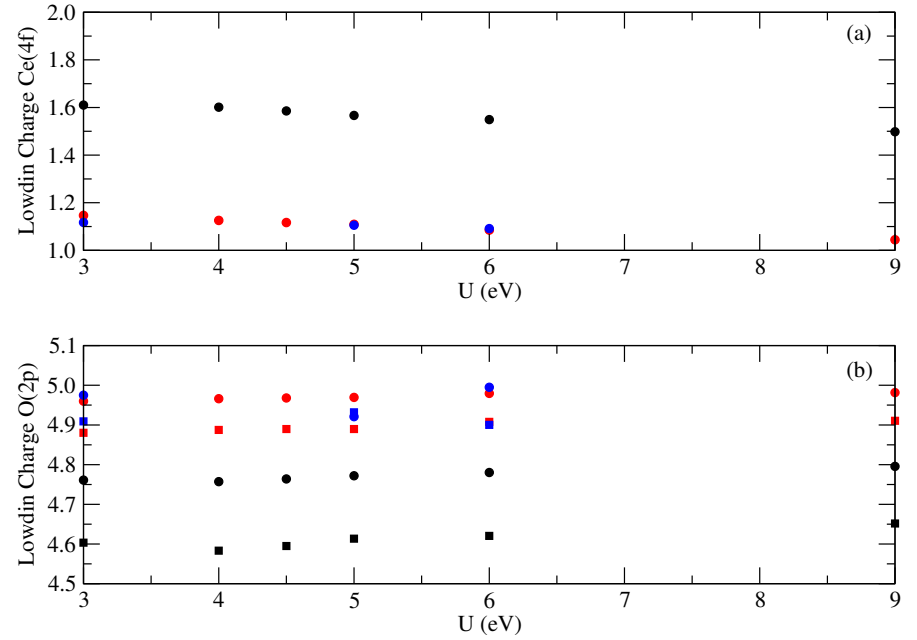

FIGURE A.33: Ce_2O_3 Löwdin charge. (a) Lödwin charge of Ce(4f) states, (b) Löwdin charge of O(2p) states. Black, red and blue are values obtained with PAW, ultrasoft and full relativistic pseudopotential.

TABLE A.5: Ce_2O_3 orbital occupation in a isolated atom and in the Oxyde.

	U	*s*	*p*	*d*	*f*	Total
Isolated cerium atom	-	4	6	1	1	12
Oxide	3	2.2768	5.9437	1.6357	1.466	11.0028
Oxide	4	2.2784	5.9449	1.6400	1.1258	10.9891
Oxide	6	2.2890	5.9518	1.6078	1.0854	10.9341
Isolated oxygen atom	-	2	4	-	-	6
Oxide, atom 1	3	1.7718	4.9600	-	-	6.7318
Oxide, atom 2	3	1.6989	4.8803	-	-	6.5792
Oxide, atom 1	4	1.7734	4.9662	-	-	6.7396
Oxide, atom 2	4	1.7006	4.8875	-	-	6.5881
Oxide, atom 1	6	1.7883	4.9795	-	-	6.7678
Oxide, atom 2	6	1.7164	4.9078	-	-	6.6242

Appendix B

Reduced cerium configurations in CeO_2/Ag inverse catalysis

In this Appendix we investigate the reduction cerium configurations for thin layer of CeO_2 and CeO_{2-x} adsorbed on Ag. Thin layers of oxides supported on metal surfaces form inverse catalysts. The text of this appendix has been submitted to Material Letters.

B.1 introduction

Ceria (CeO_2) is an important metal oxide with a large application potential for catalytic reactions and in the field of energy conversion [25]. The interest stems from its ability to exchange easily oxygen atoms with its environment, with the consequent change of the oxidation state of the metal cations from Ce^{4+} to Ce^{3+} and vice versa. Recent studies have shown that ceria thin films grown on metal substrates (named inverse catalysts) can achieve a higher activity for reactions such water-gas-shift WGS and CO oxidation than conventional catalysts [207], [208]. They have been shown to have unique catalytic properties different from those of ceria bulk [209]. The reason for this behavior lies in the relevant electronic charge transfer taking place between the ceria layers and the metal support [210]. While some theoretical studies have tried to quantify this charge transfer, a detailed investigation of the induced reduction patterns of the cerium atoms under different situations (number of ceria monolayers, position of the oxygen vacancies) has never been carried out. In this letter we provide a detailed investigation of this issue for the cases of one and two monolayers of ceria deposited on a Ag support, a metal that has been little considered so far in the literature [210], in contrast to Pt and Cu.

B.2 Method

The spin-polarized calculations were based on the density functional theory (DFT) using the exchange and correlation functional proposed by Perdew-Burke-Ernzerhof (PBE) [35] and the DFT+U approach [43] as implemented in the plane-wave pseudopotential PW code of the Quantum Espresso package [82], [83]. For the Ag, Ce and O atoms we used ultrasoft pseudopotentials. For the 4f states of Ce the U parameter was set to U = 4 eV. The energy cut-off for the plane-wave expansions of the wave functions and the charge density were set at 30 and 240 Ry, respectively. For the charge density integration we employed a $2\times2\times1$ k-point mesh. The calculations were iterated until the forces were less than 0.01 eV/Å. The total energy criterion for the geometric optimization was set to 10^{-5} eV. To model the CeO_2/Ag(111) interface we have used the slab method. The slabs, shown in Fig. B.1, consist of 4 layers of Ag, of which the last two layers were kept fixed at the bulk equilibrium positions,

plus one monolayer (ML) of CeO_2 (case (a) of Fig. B.1) or two MLs of CeO_2 (case (b) of Fig. B.1). The slabs were separated along the [111] direction by 15 Å of vacuum. For the charge density integration we employed a 2×2×1 k-point mesh. The interface is constructed by a 3×3 surface unit cell of CeO_2(111) and a 4×4 unit cell of Ag(111). This choice optimizes the lattice register and minimizes the strain in the ceria overlayer. With this registry the ceria lattice is expanded of only 0.375% with respect to the bulk lattice. The lattice parameter of the ceria oxide depends also on the oxidation state of the cerium atoms. The full reduction from Ce^{4+} to Ce^{3+} expands the lattice parameter of 0.282%, thus almost cancelling the slight mismatch at the interface. Thus, whatever the oxidation state of the cerium oxide, the strain is reduced at a minimum. We have considered three possible vertical alignments between the Ag and CeO_2 segments: (a) given an Ag atom at the interface, a Ce atom of the first CeO_2 ML is aligned along [111] with the Ag atom; (b) an O atom of the layer below the Ce layer is aligned with the same Ag atom; (c) an O atom of the layer above the Ce layer is aligned with the same Ag atom. We have calculated the adhesion energy of the three structures as: E_{adh} = [E(CeO_2/Ag)-E(CeO_2)-E(Ag)]/A, where E(Ag) is the energy of the free-standing four-layers Ag slab, E(CeO_2) the energy of a slab with 1 or 2 CeO_2 MLs, and A is the interface area. E_{adh} measures the strength of the interface bonding between CeO_2 and Ag. We obtained for the three configurations similar values: -3.585, -3.547, and -3.585 eV/nm^2 for the cases (a), (b), and (c), respectively. In the following we will consider only the (c) interface.

We have considered three possible vertical alignments between the Ag and CeO_2 segments: (a) given an Ag atom at the interface, a Ce atom of the first CeO_2 ML is aligned along [111] with the Ag atom; (b) an O atom of the layer below the Ce layer is aligned with the same Ag atom; (c) an O atom of the layer above the Ce layer is aligned with the same Ag atom. We have calculated the adhesion energy of the three structures as: E_{adh} = [E(CeO_2/Ag)-E(CeO_2)-E(Ag)]/A, where E(Ag) is the energy of the free-standing four-layers Ag slab, E(CeO_2) the energy of a slab with 1 or 2 CeO_2 MLs, and A is the interface area. E_{adh} measures the strength of the interface bonding between CeO_2 and Ag. We obtained for the three configurations similar values of E_{adh}: -3.585, -3.547, and -3.585 eV/nm^2 for the cases (a), (b), and (c), respectively. In the following we will consider only the (c) interface.

B.3 Results

B.3.1 1 ML CeO_2 on Ag

Before the formation of the interface with Ag the cerium atoms in the CeO_2 monolayer are all Ce^{4+} cations. After the interface formation electrons are transferred to CeO_2 from the Ag interface layer. Ag oxidation and electron transfer to ceria were evaluated calculating the Bader charges [87] on the atoms before and after interface formation. These electrons are not equally distributed among the Ce atoms but go to fill the f orbitals of only some of them. In our surface cell we have 9 Ce atoms. Of these cations, six are reduced to Ce^{3+} cations and three remain Ce^{4+}. In Fig. B.2 we show the arrangement of the Ce^{3+} and Ce^{4+} cations in the CeO_2 monolayer. It is interesting to note that the arrangement forms a new $(\sqrt{3}\times\sqrt{3})$ R30 periodicity with 3 atoms per surface unit cell (2 Ce^{3+} and 1 Ce^{4+}) instead of the 1×1 surface unit cell with 1 atom of unreduced CeO_2. The reduction of the Ce atoms is accompanied by a structural relaxation where the Ce-O bond lengths around Ce^{3+} become longer. We have investigated the energy required to remove one surface or interfacial oxygen atom, and how the number of Ce^{3+} changes as a consequence of oxygen removal.

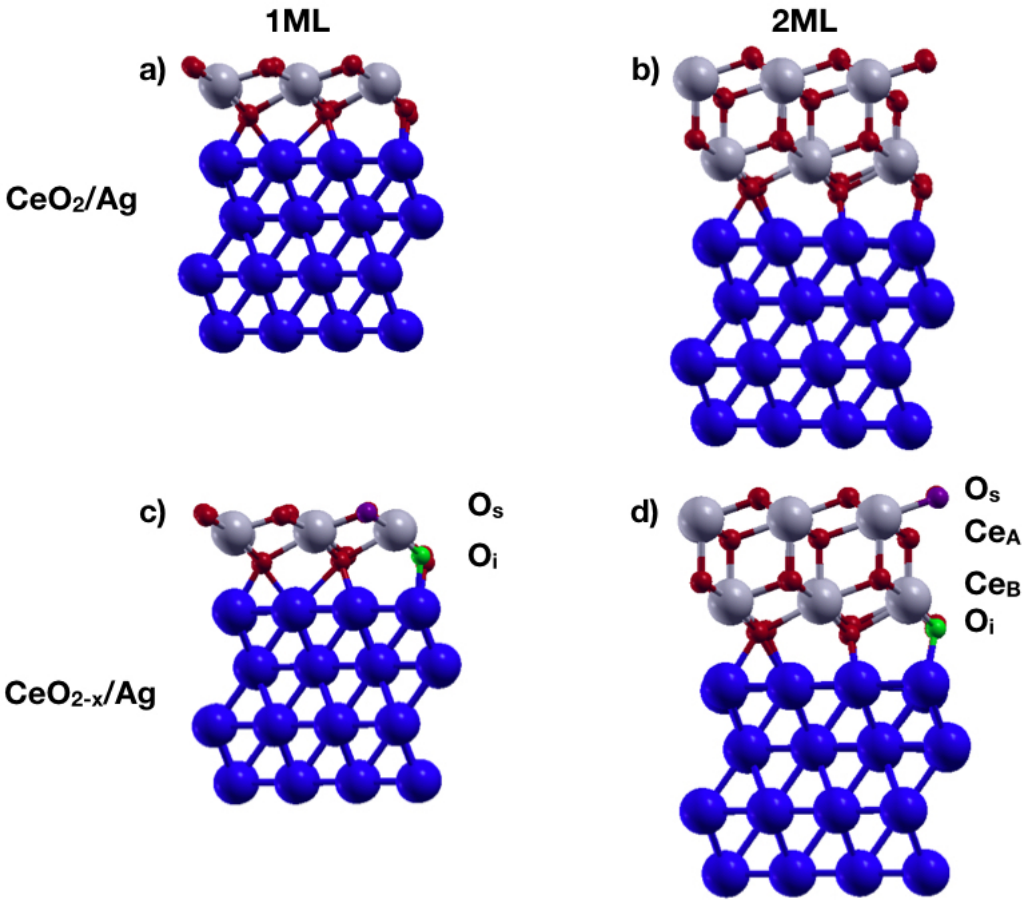

FIGURE B.1: Side views of the structures considered in this work. (a) 1 ML of CeO_2 on Ag; (b) 2 MLs of CeO_2 on Ag; (c) 1 ML CeO_{2-x}/Ag with 1 oxygen vacancy at the interface; (d) 2 MLs CeO_{2-x}/Ag with 1 oxygen vacancy at the interface. The blue balls indicate the Ag atoms, the grey balls the Ce atoms, the small red balls the oxygen atoms, the green balls interface oxygens, and the purple balls is surface oxygen atoms.

The oxygen vacancy formation energy has been evaluated as E_{form}=E(Ag/CeO_{2-x})-0.5*E(O_2)-E(Ag/CeO_2) , where E(Ag/CeO_{2-x}) is the energy of the slab without the oxygen atom, E(Ag/CeO_2) is the energy of the slab before the oxygen removal, and E(O_2) is the energy of the oxygen molecule. In Table B.1 we report the calculated oxygen vacancy formation energies. The oxygen atom is removed from the CeO_2 surface layer (O_s) or from the interface layer with Ag (O_I). We have considered oxygen atoms in two different positions: i) on top of an Ag atom, and ii) in a bridge position between two Ag atoms. All the oxygens are bonded to two Ce^{3+} atoms and to one Ce^{4+}. We have found that it is easier to remove an interfacial oxygen atom than a surface one, and E_{form} is slightly less when the oxygen atom is on top of an Ag atom. The oxygen vacancy formation energy for an interface oxygen is less than our calculated value for pristine ceria, 2.02 eV. The lower formation energy of the interface oxygen can be due to the increase of the Ce-O_I bond length, which is usually an indication of the decrease of the strength of the bond. The removal of an oxygen atom, both at the interface or at the surface, doesn't change the number of reduced cerium atoms. Thus, the excess of charge caused by the creation of the vacancy is transferred back to the Ag atoms of the support.

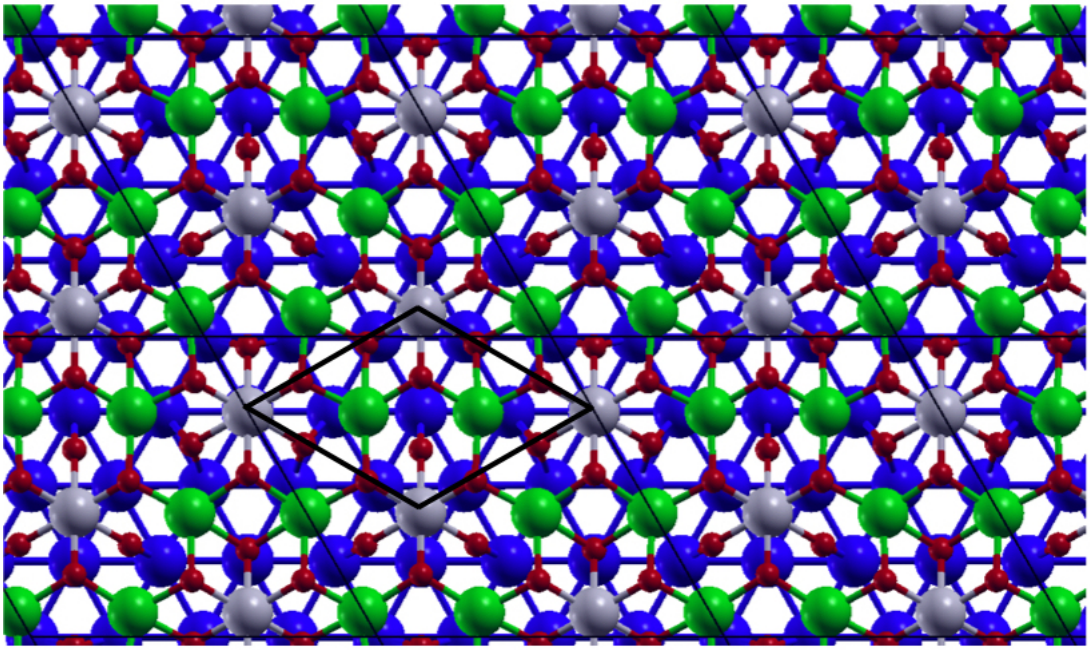

FIGURE B.2: 1 ML CeO_2 on Ag. Green balls are the Ce^{3+} atoms. The Ce^{4+}, Ag, and O color codes are the same as in Fig. B.1. The black lines indicate the new in plane periodicity.

B.3.2 2 MLs CeO_2 on Ag

Also in the case of 2MLs of CeO_2 electronic charge is transferred from the Ag support to the oxide. The charge is transferred only to the Ce atoms that belong to the Ce_B layer (see Fig. B.1), in particular to five of the nine Ce atoms, as shown in Fig. B.3a, where the arrangement of the reduced atoms is shown. Since there are not reduced cerium atoms in the Ce_A surface layer, O_s are all bonded to Ce^{4+} atoms, whereas the interface oxygens can be bonded to one, two, or three Ce^{3+}, and their E_{form} is different. Contrary to what occurs for the case of the single monolayer, it

TABLE B.1: Oxygen vacancy formation energy E_{form} (eV) for 1 and 2 MLs of CeO_2 on Ag, nCe^{3+} indicates the number of reduced cerium atoms to which the oxygens are bonded.

	O_s				O_I			
	Top		Bridge		Top		Bridge	
	nCe^{3+}	E_{form}	nCe^{3+}	E_{form}	nCe^{3+}	E_{form}	nCe^{3+}	E_{form}
1ML	2	2.25	2	1.85	2	1.40	2	1.49
2ML	0	1.52	0	1.63	0	2.33	2	2.21
					1	2.06	3	2.18
					2	2.09		

is easier to remove a surface oxygen than the oxygen atoms at the interface layer. The creation of a surface oxygen vacancy leads to the reduction of two Ce_A atoms, second neighbours of the removed oxygen as shown in Fig. B.3b. E_{form} is still less than on the pristine ceria surface, and it is slightly less for the oxygen atom on top of Ag. When the interfacial oxygen is removed, instead, no further cerium atoms are reduced. The excess of charge is, consequently, transferred back to Ag. We note that the oxygen vacancy formation energy becomes smaller when the number of Ce^{3+} cations to which the oxygen atom is bonded is larger. This is probably due to the less strong Ce-O bond lengths, when the cerium atoms are reduced.

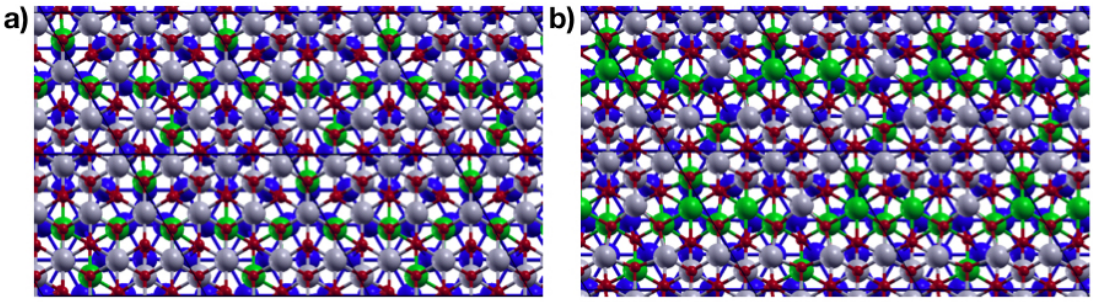

FIGURE B.3: a) 2MLs CeO_2/Ag, b) 2MLs CeO_{2-x}/Ag where a surface oxygen has been removed. The color code is the same as in Fig. B.2.

B.4 Conclusions

We have found that, because of the presence of the Ag support, or, as a consequence of oxygen removal, the reduction configurations of the cerium atoms in CeO_2/Ag form ordered long range superstructures as also found experimentally for the case of Cu support [209].

Bibliography

[1] Jacques C. Védrine. "Metal Oxides in Heterogeneous Oxidation Catalysis: State of the Art and Challenges for a More Sustainable World". In: *ChemSusChem* 12.3 (2019), pp. 577–588. DOI: 10.1002/cssc.201802248. URL: https://onlinelibrary.wiley.com/doi/abs/10.1002/cssc.201802248.

[2] Jacques C. Védrine. "Heterogeneous Catalysis on Metal Oxides". In: *Catalysts* 7.11 (2017). ISSN: 2073-4344. DOI: 10.3390/catal7110341. URL: https://www.mdpi.com/2073-4344/7/11/341.

[3] W. Ostwald. In: *Nature* 65 (1902), p. 502.

[4] Aiqin Wang, Jun Li, and Tao Zhang. "Heterogeneous single-atom catalysis". In: *Nature Reviews Chemistry* (2018), p. 1. DOI: 10.1038/s41570-018-0010-1. URL: https://doi.org/10.1038/s41570-018-0010-1.

[5] Antonio Ruiz Puigdollers et al. "Increasing Oxide Reducibility: The Role of Metal/Oxide Interfaces in the Formation of Oxygen Vacancies". In: *ACS Catalysis* 7.10 (2017), pp. 6493–6513. DOI: 10.1021/acscatal.7b01913. URL: https://doi.org/10.1021/acscatal.7b01913.

[6] Jingyue Liu. "Catalysis by supported single metal atoms". In: *Acs Catalysis* 7.1 (2016), pp. 34–59. DOI: 10.1021/acscatal.6b01534. URL: https://doi.org/10.1021/acscatal.6b01534.

[7] Xinjiang Cui et al. "Bridging homogeneous and heterogeneous catalysis by heterogeneous single-metal-site catalysts". In: *Nature Catalysis* 1.6 (June 2018), pp. 385–397. ISSN: 2520-1158. DOI: 10.1038/s41929-018-0090-9. URL: https://doi.org/10.1038/s41929-018-0090-9.

[8] K. Asakura et al. "Structure and catalytic combustion activity of atomically dispersed Pt species at MgO surface". In: *Applied Catalysis A: General* 188.1 (1999), pp. 313 –324. ISSN: 0926-860X. DOI: https://doi.org/10.1016/S0926-860X(99)00247-1. URL: http://www.sciencedirect.com/science/article/pii/S0926860X99002471.

[9] Qi Fu, Howard Saltsburg, and Maria Flytzani-Stephanopoulos. "Active Nonmetallic Au and Pt Species on Ceria-Based Water-Gas Shift Catalysts". In: *Science* 301.5635 (2003), pp. 935–938. ISSN: 0036-8075. DOI: 10.1126/science.1085721. URL: https://science.sciencemag.org/content/301/5635/935.

[10] Xin Zhang, Hui Shi, and Bo-Qing Xu. "Catalysis by Gold: Isolated Surface Au3+ Ions are Active Sites for Selective Hydrogenation of 1,3-Butadiene over Au/ZrO2 Catalysts". In: *Angewandte Chemie International Edition* 44.43 (2005), pp. 7132–7135. DOI: 10.1002/anie.200502101. URL: https://onlinelibrary.wiley.com/doi/abs/10.1002/anie.200502101.

[11] Simon F. J. Hackett et al. "High-Activity, Single-Site Mesoporous Pd/Al2O3 Catalysts for Selective Aerobic Oxidation of Allylic Alcohols". In: *Angewandte Chemie International Edition* 46.45 (2007), pp. 8593–8596. DOI: 10.1002/anie.200702534. URL: https://onlinelibrary.wiley.com/doi/abs/10.1002/anie.200702534.

[12] Botao Qiao et al. "Single-atom catalysis of CO oxidation using Pt1/FeOx". In: *Nature Chemistry* 3 (July 2011), p. 634. URL: https://doi.org/10.1038/nchem.1095.

[13] Botao Qiao et al. "Ultrastable single-atom gold catalysts with strong covalent metal-support interaction (CMSI)". In: *Nano Research* 8.9 (Sept. 2015), pp. 2913–2924. ISSN: 1998-0000. DOI: 10.1007/s12274-015-0796-9. URL: https://doi.org/10.1007/s12274-015-0796-9.

[14] Wei Tang et al. "Methane complete and partial oxidation catalyzed by Pt-doped CeO2". In: *Journal of Catalysis* 273.2 (2010), pp. 125 –137. ISSN: 0021-9517. DOI: https://doi.org/10.1016/j.jcat.2010.05.005. URL: http://www.sciencedirect.com/science/article/pii/S0021951710001648.

[15] Changbin Zhang et al. "Alkali-Metal-Promoted Pt/TiO2 Opens a More Efficient Pathway to Formaldehyde Oxidation at Ambient Temperatures". In: *Angewandte Chemie International Edition* 51.38 (2012), pp. 9628–9632. DOI: 10.1002/anie.201202034. URL: https://onlinelibrary.wiley.com/doi/abs/10.1002/anie.201202034.

[16] Haisheng Wei et al. "FeOx-supported platinum single-atom and pseudo-single-atom catalysts for chemoselective hydrogenation of functionalized nitroarenes". In: *Nature Communications* 5 (Dec. 2014), p. 5634. URL: https://doi.org/10.1038/ncomms6634.

[17] Georgios Kyriakou et al. "Isolated Metal Atom Geometries as a Strategy for Selective Heterogeneous Hydrogenations". In: *Science* 335.6073 (2012), pp. 1209–1212. ISSN: 0036-8075. DOI: 10.1126/science.1215864. URL: https://science.sciencemag.org/content/335/6073/1209.

[18] Ming Yang, Lawrence F. Allard, and Maria Flytzani-Stephanopoulos. "Atomically Dispersed Au–(OH)x Species Bound on Titania Catalyze the Low-Temperature Water-Gas Shift Reaction". In: *Journal of the American Chemical Society* 135.10 (Mar. 2013), pp. 3768–3771. ISSN: 0002-7863. DOI: 10.1021/ja312646d. URL: https://doi.org/10.1021/ja312646d.

[19] Nan Yi et al. "Active gold species on cerium oxide nanoshapes for methanol steam reforming and the water gas shift reactions". In: *Energy Environ. Sci.* 3.6 (2010), pp. 831–837. DOI: 10.1039/B924051A. URL: http://dx.doi.org/10.1039/B924051A.

[20] Xiang-Kui Gu et al. "Supported Single Pt1/Au1 Atoms for Methanol Steam Reforming". In: *ACS Catalysis* 4.11 (Nov. 2014), pp. 3886–3890. DOI: 10.1021/cs500740u. URL: https://doi.org/10.1021/cs500740u.

[21] Chengzhou Zhu et al. "Single-Atom Electrocatalysts". In: *Angewandte Chemie International Edition* 56.45 (2017), pp. 13944–13960. DOI: 10.1002/anie.201703864. URL: https://onlinelibrary.wiley.com/doi/abs/10.1002/anie.201703864.

[22] Jiwhan Kim, Hee-Eun Kim, and Hyunjoo Lee. "Single-Atom Catalysts of Precious Metals for Electrochemical Reactions". In: *ChemSusChem* 11.1 (2018), pp. 104–113. DOI: 10.1002/cssc.201701306. URL: https://onlinelibrary.wiley.com/doi/abs/10.1002/cssc.201701306.

[23] Steeve Chrétien and Horia Metiu. "Density Functional Study of the CO Oxidation on a Doped Rutile TiO2(110): Effect of Ionic Au in Catalysis". In: *Catalysis Letters* 107.3 (Mar. 2006), pp. 143–147. ISSN: 1572-879X. DOI: 10.1007/s10562-005-0014-6. URL: https://doi.org/10.1007/s10562-005-0014-6.

[24] P. Mars and D. W. van Krevelen. "Oxidations carried out by means of vanadium oxide catalysts". In: *Chemical Engineering Science* 3 (1954), pp. 41 –59. ISSN: 0009-2509. DOI: https://doi.org/10.1016/S0009-2509(54)80005-4. URL: http://www.sciencedirect.com/science/article/pii/S0009250954800054.

[25] Tiziano Montini et al. "Fundamentals and Catalytic Applications of CeO2-Based Materials". In: *Chemical Reviews* 116.10 (2016), pp. 5987–6041. DOI: 10.1021/acs.chemrev.5b00603. URL: https://doi.org/10.1021/acs.chemrev.5b00603.

[26] Gareth S Parkinson. "Iron oxide surfaces". In: *Surface Science Reports* 71.1 (2016), pp. 272–365. DOI: https://doi.org/10.1016/j.surfrep.2016.02.001. URL: http://www.sciencedirect.com/science/article/pii/S0167572916000054.

[27] Botao Qiao et al. "Highly efficient catalysis of preferential oxidation of CO in H2-rich stream by gold single-atom catalysts". In: *ACS Catalysis* 5.11 (2015), pp. 6249–6254. DOI: 10.1021/acscatal.5b01114. URL: ttps://doi.org/10.1021/acscatal.5b01114.

[28] Pengfei Xie et al. "Nanoceria-Supported Single-Atom Platinum Catalysts for Direct Methane Conversion". In: *ACS Catalysis* 8.5 (2018), pp. 4044–4048. DOI: 10.1021/acscatal.8b00004. URL: https://doi.org/10.1021/acscatal.8b00004.

[29] Filip Dvořák et al. "Creating single-atom Pt-ceria catalysts by surface step decoration". In: *Nature Communications* 7 (Feb. 2016), p. 10801. URL: https://doi.org/10.1038/ncomms10801.

[30] Nguyen-Dung Tran, Matteo Farnesi Camellone, and Stefano Fabris. "Probing the Reactivity of Pt/Ceria Nanocatalysts toward Methanol Oxidation: From Ionic Single-Atom Sites to Metallic Nanoparticles". In: *The Journal of Physical Chemistry C* 122.31 (2018), pp. 17917–17927. DOI: 10.1021/acs.jpcc.8b05735. URL: https://doi.org/10.1021/acs.jpcc.8b05735.

[31] Matthias Meier et al. "Probing the geometry of copper and silver adatoms on magnetite: quantitative experiment versus theory". In: *Nanoscale* 10.5 (2018), pp. 2226–2230. DOI: 10.1039/C7NR07319D. URL: http://dx.doi.org/10.1039/C7NR07319D.

[32] R. Bliem et al. "Subsurface cation vacancy stabilization of the magnetite (001) surface". In: *Science* 346.6214 (2014), pp. 1215–1218. ISSN: 0036-8075. DOI: 10.1126/science.1260556. URL: http://science.sciencemag.org/content/346/6214/1215.

[33] P. Hohenberg and W. Kohn. "Inhomogeneous Electron Gas". In: *Phys. Rev.* 136.3B (Nov. 1964), B864–B871. DOI: 10.1103/PhysRev.136.B864. URL: https://link.aps.org/doi/10.1103/PhysRev.136.B864.

[34] W. Kohn and L. J. Sham. "Self-Consistent Equations Including Exchange and Correlation Effects". In: *Phys. Rev.* 140.4A (Nov. 1965), A1133–A1138. DOI: 10.1103/PhysRev.140.A1133. URL: https://link.aps.org/doi/10.1103/PhysRev.140.A1133.

[35] John P. Perdew, Kieron Burke, and Matthias Ernzerhof. "Generalized Gradient Approximation Made Simple [Phys. Rev. Lett. 77, 3865 (1996)]". In: *Phys. Rev. Lett.* 78.7 (Feb. 1997), pp. 1396–1396. DOI: 10.1103/PhysRevLett.78.1396. URL: https://link.aps.org/doi/10.1103/PhysRevLett.78.1396.

[36] Peter Jan Hendrik Denteneer. "The pseudopotential density functional method applied to semiconducting crystals". PhD Thesis. Technische Hogeschool, Eindhoven (Netherlands)., Dec. 1987.

[37] David Vanderbilt. "Soft self-consistent pseudopotentials in a generalized eigenvalue formalism". In: *Phys. Rev. B* 41 (11 1990), pp. 7892–7895. DOI: 10.1103/PhysRevB.41.7892. URL: https://link.aps.org/doi/10.1103/PhysRevB.41.7892.

[38] Vladimir I. Anisimov, Jan Zaanen, and Ole K. Andersen. "Band theory and Mott insulators: Hubbard U instead of Stoner I". In: *Phys. Rev. B* 44.3 (July 1991), pp. 943–954. DOI: 10.1103/PhysRevB.44.943. URL: https://link.aps.org/doi/10.1103/PhysRevB.44.943.

[39] V. I. Anisimov et al. "Density-functional theory and NiO photoemission spectra". In: *Phys. Rev. B* 48.23 (Dec. 1993), pp. 16929–16934. DOI: 10.1103/PhysRevB.48.16929. URL: https://link.aps.org/doi/10.1103/PhysRevB.48.16929.

[40] I. V. Solovyev, P. H. Dederichs, and V. I. Anisimov. "Corrected atomic limit in the local-density approximation and the electronic structure of d impurities in Rb". In: *Phys. Rev. B* 50.23 (Dec. 1994), pp. 16861–16871. DOI: 10.1103/PhysRevB.50.16861. URL: https://link.aps.org/doi/10.1103/PhysRevB.50.16861.

[41] A. I. Liechtenstein, V. I. Anisimov, and J. Zaanen. "Density-functional theory and strong interactions: Orbital ordering in Mott-Hubbard insulators". In: *Phys. Rev. B* 52.8 (Aug. 1995), R5467–R5470. DOI: 10.1103/PhysRevB.52.R5467. URL: https://link.aps.org/doi/10.1103/PhysRevB.52.R5467.

[42] Vladimir I. Anisimov, F. Aryasetiawan, and A. I. Lichtenstein. "First-principles calculations of the electronic structure and spectra of strongly correlated systems: theLDA+Umethod". In: *Journal of Physics: Condensed Matter* 9.4 (Jan. 1997), pp. 767–808. DOI: 10.1088/0953-8984/9/4/002. URL: https://doi.org/10.1088%2F0953-8984%2F9%2F4%2F002.

[43] Matteo Cococcioni and Stefano de Gironcoli. "Linear response approach to the calculation of the effective interaction parameters in the LDA+U method". In: *Phys. Rev. B* 71.3 (Jan. 2005), p. 035105. DOI: 10.1103/PhysRevB.71.035105. URL: https://link.aps.org/doi/10.1103/PhysRevB.71.035105.

[44] H. Jonsson, G. Mills, and K. W. Jacobsen. "FRONT MATTER". In: *Classical and Quantum Dynamics in Condensed Phase Simulations*, pp. i–l. DOI: 10.1142/9789812839664_fmatter. URL: https://www.worldscientific.com/doi/abs/10.1142/9789812839664_fmatter.

[45] Graeme Henkelman, Blas P. Uberuaga, and Hannes Jónsson. "A climbing image nudged elastic band method for finding saddle points and minimum energy paths". In: *The Journal of Chemical Physics* 113.22 (2000), pp. 9901–9904. DOI: 10.1063/1.1329672. URL: https://doi.org/10.1063/1.1329672.

[46] Graeme Henkelman and Hannes Jónsson. "Improved tangent estimate in the nudged elastic band method for finding minimum energy paths and saddle points". In: *The Journal of Chemical Physics* 113.22 (2000), pp. 9978–9985. DOI: 10.1063/1.1323224. URL: https://doi.org/10.1063/1.1323224.

[47] Carlo Sbraccia. "Computer simulation of thermally activated processes". In: *SISSA (PhD Thesis), Trieste, Italy* (2005).

[48] Giulia Righi, Anna Franchini, and Rita Magri. "Attractive interactions between like-oriented surface steps from an ab initio perspective: Role of the elastic and electrostatic contributions". In: *Phys. Rev. B* 99.7 (Feb. 2019), p. 075311. DOI: 10.1103/PhysRevB.99.075311. URL: https://link.aps.org/doi/10.1103/PhysRevB.99.075311.

[49] Can Xu et al. "Nanoceria-Triggered Synergetic Drug Release Based on CeO2-Capped Mesoporous Silica Host–Guest Interactions and Switchable Enzymatic Activity and Cellular Effects of CeO2". In: *Advanced Healthcare Materials* 2.12 (2013), pp. 1591–1599. DOI: 10.1002/adhm.201200464. URL: https://onlinelibrary.wiley.com/doi/abs/10.1002/adhm.201200464.

[50] Alessandro Trovarelli et al. "The utilization of ceria in industrial catalysis". In: *Catalysis Today* 50.2 (1999), pp. 353 –367. ISSN: 0920-5861. DOI: https://doi.org/10.1016/S0920-5861(98)00515-X. URL: http://www.sciencedirect.com/science/article/pii/S092058619800515X.

[51] T. Bunluesin, R. J. Gorte, and G. W. Graham. "Studies of the water-gas-shift reaction on ceria-supported Pt, Pd, and Rh: Implications for oxygen-storage properties". In: *Applied Catalysis B: Environmental* 15.1 (1998), pp. 107 –114. ISSN: 0926-3373. DOI: https://doi.org/10.1016/S0926-3373(97)00040-4. URL: http://www.sciencedirect.com/science/article/pii/S0926337397000404.

[52] T. Shido and Y. Iwasawa. "Reactant-Promoted Reaction Mechanism for Water-Gas Shift Reaction on Rh-Doped CeO2". In: *Journal of Catalysis* 141.1 (1993), pp. 71 –81. ISSN: 0021-9517. DOI: https://doi.org/10.1006/jcat.1993.1119. URL: http://www.sciencedirect.com/science/article/pii/S002195178371119X.

[53] Yue Li, Qi Fu, and Maria Flytzani-Stephanopoulos. "Low-temperature water-gas shift reaction over Cu- and Ni-loaded cerium oxide catalysts". In: *Applied Catalysis B: Environmental* 27.3 (2000), pp. 179 –191. ISSN: 0926-3373. DOI: https://doi.org/10.1016/S0926-3373(00)00147-8. URL: http://www.sciencedirect.com/science/article/pii/S0926337300001478.

[54] Matteo Cargnello et al. "Control of Metal Nanocrystal Size Reveals Metal-Support Interface Role for Ceria Catalysts". In: *Science* 341.6147 (2013), pp. 771–773. ISSN: 0036-8075. DOI: 10.1126/science.1240148. URL: https://science.sciencemag.org/content/341/6147/771.

[55] D. Gamarra et al. "Preferential oxidation of CO in excess H2 over CuO/CeO2 catalysts: Characterization and performance as a function of the exposed face present in the CeO2 support". In: *Applied Catalysis B: Environmental* 130-131 (2013), pp. 224 –238. ISSN: 0926-3373. DOI: https://doi.org/10.1016/j.apcatb.2012.11.008. URL: http://www.sciencedirect.com/science/article/pii/S0926337312005206.

[56] Shuang LIU et al. "Ceria-based catalysts for soot oxidation: a review". In: *Journal of Rare Earths* 33.6 (2015), pp. 567 –590. ISSN: 1002-0721. DOI: https://doi.org/10.1016/S1002-0721(14)60457-9. URL: http://www.sciencedirect.com/science/article/pii/S1002072114604579.

[57] A. Bueno-López. "Diesel soot combustion ceria catalysts". In: *Applied Catalysis B: Environmental* 146 (2014), pp. 1 –11. ISSN: 0926-3373. DOI: https://doi.org/10.1016/j.apcatb.2013.02.033. URL: http://www.sciencedirect.com/science/article/pii/S0926337313001227.

[58] P. G. Lustemberg, L. Feria, and M. V. Ganduglia-Pirovano. "Single Ni Sites Supported on CeO2(111) Reveal Cooperative Effects in the Water–Gas Shift Reaction". In: *The Journal of Physical Chemistry C* (Sept. 2018). ISSN: 1932-7447. DOI: 10.1021/acs.jpcc.8b06231. URL: https://doi.org/10.1021/acs.jpcc.8b06231.

[59] Mogens Mogensen et al. "Physical properties of mixed conductor solid oxide fuel cell anodes of doped CeO2". In: *Journal of the Electrochemical Society* 141.8 (1994), pp. 2122–2128. DOI: 10.1149/1.2055072.

[60] Olga A. Marina et al. "A solid oxide fuel cell with a gadolinia-doped ceria anode: preparation and performance". In: *Solid State Ionics* 123.1 (1999), pp. 199 –208. ISSN: 0167-2738. DOI: https://doi.org/10.1016/S0167-2738(99)00111-3. URL: http://www.sciencedirect.com/science/article/pii/S0167273899001113.

[61] Anca Faur Ghenciu. "Review of fuel processing catalysts for hydrogen production in PEM fuel cell systems". In: *Current Opinion in Solid State and Materials Science* 6.5 (2002), pp. 389 –399. ISSN: 1359-0286. DOI: https://doi.org/10.1016/S1359-0286(02)00108-0. URL: http://www.sciencedirect.com/science/article/pii/S1359028602001080.

[62] Valentina Bambagioni et al. "Energy Efficiency Enhancement of Ethanol Electrooxidation on Pd–CeO2/C in Passive and Active Polymer Electrolyte-Membrane Fuel Cells". In: *ChemSusChem* 5.7 (2012), pp. 1266–1273. DOI: 10.1002/cssc.201100738. URL: https://onlinelibrary.wiley.com/doi/abs/10.1002/cssc.201100738.

[63] Fabio R Negreiros, Matteo Farnesi Camellone, and Stefano Fabris. "Effects of thermal fluctuations on the hydroxylation and reduction of ceria surfaces by molecular H2". In: *The Journal of Physical Chemistry C* 119.37 (2015), pp. 21567–21573. DOI: 10.1021/acs.jpcc.5b07030. URL: https://doi.org/10.1021/acs.jpcc.5b07030.

[64] A. Mastalir et al. "Steam reforming of methanol over Cu/ZrO2/CeO2 catalysts: a kinetic study". In: *Journal of Catalysis* 230.2 (2005), pp. 464 –475. ISSN: 0021-9517. DOI: https://doi.org/10.1016/j.jcat.2004.12.020. URL: http://www.sciencedirect.com/science/article/pii/S0021951704006098.

[65] Hisayuki Oguchi et al. "Steam reforming of methanol over Cu/CeO2/ZrO2 catalysts". In: *Applied Catalysis A: General* 281.1 (2005), pp. 69 –73. ISSN: 0926-860X. DOI: https://doi.org/10.1016/j.apcata.2004.11.014. URL: http://www.sciencedirect.com/science/article/pii/S0926860X04009184.

[66] Yanyong Liu et al. "Highly active copper/ceria catalysts for steam reforming of methanol". In: *Applied Catalysis A: General* 223.1 (2002), pp. 137 –145. ISSN: 0926-860X. DOI: https://doi.org/10.1016/S0926-860X(01)00733-5. URL: http://www.sciencedirect.com/science/article/pii/S0926860X01007335.

[67] Adam D. Mayernick and Michael J. Janik. "Methane Activation and Oxygen Vacancy Formation over CeO2 and Zr, Pd Substituted CeO2 Surfaces". In: *The Journal of Physical Chemistry C* 112.38 (2008), pp. 14955–14964. DOI: 10.1021/jp805134s. URL: https://doi.org/10.1021/jp805134s.

[68] Yaxin Chen et al. "Fabrication, characterization, and stability of supported single-atom catalysts". In: *Catal. Sci. Technol.* 7.19 (2017), pp. 4250–4258. DOI: 10.1039/C7CY00723J. URL: http://dx.doi.org/10.1039/C7CY00723J.

[69] Edvin Fako, Zbigniew Lodziana, and Núria López. "Comparative single atom heterogeneous catalysts (SAHCs) on different platforms: a theoretical approach". In: *Catalysis Science & Technology* 7.19 (2017), pp. 4285–4293. DOI: 10.1039/C7CY01136A. URL: http://dx.doi.org/10.1039/C7CY01136A.

[70] N V Skorodumova, Micael Baudin, and Kersti Hermansson. "Surface properties of CeO 2 from first principles". In: *Physical Review B* 69.7 (2004), p. 75401. DOI: 10.1103/PhysRevB.69.075401. URL: https://link.aps.org/doi/10.1103/PhysRevB.69.075401.

[71] Stefano Fabris et al. "Electronic and atomistic structures of clean and reduced ceria surfaces". In: *The Journal of Physical Chemistry B* 109.48 (2005), pp. 22860–22867. DOI: 10.1021/jp0511698. URL: https://doi.org/10.1021/jp0511698.

[72] D R Mullins, S H Overbury, and D R Huntley. "Electron spectroscopy of single crystal and polycrystalline cerium oxide surfaces". In: *Surface Science* 409.2 (1998), pp. 307–319. DOI: https://doi.org/10.1016/S0039-6028(98)00257-X. URL: http://www.sciencedirect.com/science/article/pii/S003960289800257X.

[73] David A Siegel et al. "Determination of the surface structure of CeO2 (111) by low-energy electron diffraction". In: *The Journal of chemical physics* 139.11 (2013), p. 114703. DOI: 10.1063/1.4820826. URL: https://doi.org/10.1063/1.4820826.

[74] Yaroslava Lykhach et al. "Oxide-based nanomaterials for fuel cell catalysis: the interplay between supported single Pt atoms and particles". In: *Catalysis Science & Technology* 7.19 (2017), pp. 4315–4345. DOI: 10.1039/C7CY00710H. URL: http://dx.doi.org/10.1039/C7CY00710H.

[75] David A Andersson et al. "Modeling of CeO_2, Ce_2O_3, and CeO_{2-x} in the LDA+ U formalism". In: *Physical Review B* 75.3 (2007), p. 35109. DOI: 10.1103/PhysRevB.75.035109. URL: https://link.aps.org/doi/10.1103/PhysRevB.75.035109.

[76] Joachim Paier, Christopher Penschke, and Joachim Sauer. "Oxygen Defects and Surface Chemistry of Ceria: Quantum Chemical Studies Compared to Experiment". In: *Chemical Reviews* 113.6 (2013), pp. 3949–3985. DOI: 10.1021/cr3004949. URL: https://doi.org/10.1021/cr3004949.

[77] Ekaterina V Tsipis and Vladislav V Kharton. "Electrode materials and reaction mechanisms in solid oxide fuel cells: a brief review". In: *Journal of Solid State Electrochemistry* 12.11 (2008), pp. 1367–1391. DOI: 10.1007/s10008-008-0611-6. URL: https://doi.org/10.1007/s10008-008-0611-6.

[78] Eric W McFarland and Horia Metiu. "Catalysis by doped oxides". In: *Chemical reviews* 113.6 (2013), pp. 4391–4427. DOI: 10.1021/cr300418s. URL: https://doi.org/10.1021/cr300418s.

[79] Shuang Wang et al. "Synergistic effects towards H2 oxidation on the Cu-CeO2 electrode: a combination study with DFT calculations and experiments". In: *J. Mater. Chem. A* 4.15 (2016), pp. 5745–5754. DOI: 10.1039/C6TA00732E. URL: http://dx.doi.org/10.1039/C6TA00732E.

[80] Bingyun Ao, Ruizhi Qiu, and Shu-Xian Hu. "First-Principles Insights into the Oxidation States and Electronic Structures of Ceria-Based Binary, Ternary, and Quaternary Oxides". In: *The Journal of Physical Chemistry C* 123.1 (2019), pp. 175–184. DOI: 10.1021/acs.jpcc.8b09852. URL: https://doi.org/10.1021/acs.jpcc.8b09852.

[81] Aron Walsh et al. "Oxidation states and ionicity". In: *Nature Materials* 17.11 (Nov. 2018), pp. 958–964. ISSN: 1476-4660. DOI: 10.1038/s41563-018-0165-7. URL: https://doi.org/10.1038/s41563-018-0165-7.

[82] Paolo Giannozzi et al. "QUANTUM ESPRESSO: a modular and open-source software project for quantum simulations of materials". In: *Journal of physics: Condensed matter* 21.39 (2009), p. 395502. DOI: 10.1088/0953-8984/21/39/395502. URL: https://doi.org/10.1088\%2F0953-8984\%2F21\%2F39\%2F395502.

[83] P. Giannozzi et al. "Advanced capabilities for materials modelling with QUANTUM ESPRESSO". In: *Journal of Physics: Condensed Matter* 29.46 (2017), p. 465901. URL: http://stacks.iop.org/0953-8984/29/i=46/a=465901.

[84] Hendrik J Monkhorst and James D Pack. "Special points for Brillouin-zone integrations". In: *Phys. Rev. B* 13.12 (June 1976), pp. 5188–5192. DOI: 10.1103/PhysRevB.13.5188. URL: https://link.aps.org/doi/10.1103/PhysRevB.13.5188.

[85] LeRoy Eyring. "Chapter 27 The binary rare earth oxides". In: *Non-metallic Compounds - I*. Vol. 3. Handbook on the Physics and Chemistry of Rare Earths. Elsevier, 1979, pp. 337 –399. DOI: 10.1016/S0168-1273(79)03010-5. URL: http://www.sciencedirect.com/science/article/pii/S0168127379030105.

[86] Graeme Henkelman, Blas P Uberuaga, and Hannes Jónsson. "A climbing image nudged elastic band method for finding saddle points and minimum energy paths". In: *The Journal of chemical physics* 113.22 (2000), pp. 9901–9904. DOI: 10.1063/1.1329672. URL: https://doi.org/10.1063/1.1329672.

[87] Richard FW Bader. *Atoms in molecules*. Wiley Online Library, 1990.

[88] *Introduction to Solid State Physics, 8th Edition*. Wiley, author = Kittel, C. , year = 2004.

[89] Yuanhao Tang et al. "Electronic states of metal (Cu, Ag, Au) atom on CeO2 (1 1 1) surface: The role of local structural distortion". In: *Journal of Power Sources* 197 (2012), pp. 28–37. ISSN: 0378-7753. DOI: https://doi.org/10.1016/j.jpowsour.2011.09.026. URL: http://www.sciencedirect.com/science/article/pii/S0378775311017320.

[90] M Jansen and P Fischer. "Eine neue darstellungsmethode für monoklines silber (I, III) oxid (AgO), einkristallzüchtung und röntgenstrukturanalyse". In: *Journal of the Less Common Metals* 137.1-2 (1988), pp. 123–131. DOI: https://doi.org/10.1016/0022-5088(88)90080-X. URL: http://www.sciencedirect.com/science/article/pii/002250888890080X.

[91] B K Meyer et al. "Binary copper oxide semiconductors: From materials towards devices". In: *physica status solidi (b)* 249.8 (2012), pp. 1487–1509. DOI: 10.1002/pssb.201248128. URL: https://onlinelibrary.wiley.com/doi/abs/10.1002/pssb.201248128.

[92] Matteo Farnesi Camellone and Stefano Fabris. "Reaction mechanisms for the CO oxidation on Au/CeO2 catalysts: Activity of substitutional Au3+/Au+ cations and deactivation of supported Au+ adatoms". In: *Journal of the American Chemical Society* 131.30 (2009), pp. 10473–10483. DOI: 10.1021/ja902109k. URL: https://doi.org/10.1021/ja902109k.

[93] María Marta Branda et al. "On the difficulties of present theoretical models to predict the oxidation state of atomic Au adsorbed on regular sites of CeO2(111)". In: *The Journal of Chemical Physics* 131.9 (2009), p. 094702. DOI: 10.1063/1.3216102. eprint: https://aip.scitation.org/doi/pdf/10.1063/1.3216102. URL: https://aip.scitation.org/doi/abs/10.1063/1.3216102.

[94] Burkhard Standke and Martin Jansen. "Ag2O3, a novel binary silver oxide". In: *Angewandte Chemie International Edition in English* 24.2 (1985), pp. 118–119. DOI: 10.1002/anie.198501181. URL: https://onlinelibrary.wiley.com/doi/abs/10.1002/anie.198501181.

[95] Changjun Zhang et al. "Structure of gold atoms on stoichiometric and defective ceria surfaces". In: *The Journal of chemical physics* 129.19 (2008), p. 194708. DOI: 10.1063/1.3009629. URL: https://doi.org/10.1063/1.3009629.

[96] PETER G Jones et al. "Gold (III) chloride oxide". In: *Acta Crystallographica Section B: Structural Crystallography and Crystal Chemistry* 35.10 (1979), pp. 2380–2381.

[97] Zongxian Yang et al. "Physisorbed, Chemisorbed, and Oxidized CO on Highly Active Cu- CeO_2 (111)". In: *The Journal of Physical Chemistry C* 114.10 (2010), pp. 4486–4494. DOI: 10.1021/jp909174u. URL: https://doi.org/10.1021/jp909174u.

[98] Vladimir Shapovalov and Horia Metiu. "Catalysis by doped oxides: CO oxidation by AuxCe1- xO2". In: *Journal of Catalysis* 245.1 (2007), pp. 205–214. DOI: https://doi.org/10.1016/j.jcat.2006.10.009. URL: http://www.sciencedirect.com/science/article/pii/S0021951706003526.

[99] M Veronica Ganduglia-Pirovano, Juarez L F Da Silva, and Joachim Sauer. "Density-functional calculations of the structure of near-surface oxygen vacancies and electron localization on CeO 2 (111)". In: *Physical review letters* 102.2 (2009), p. 26101. DOI: 10.1103/PhysRevLett.102.026101. URL: https://link.aps.org/doi/10.1103/PhysRevLett.102.026101.

[100] Lucie Szabová et al. "Thermodynamic, electronic and structural properties of Cu/CeO 2 surfaces and interfaces from first-principles DFT+ U calculations". In: *The Journal of Chemical Physics* 133.23 (2010), p. 234705. DOI: 10.1063/1.3515424. URL: https://doi.org/10.1063/1.3515424.

[101] Hyun You Kim and Graeme Henkelman. "CO oxidation at the interface between doped CeO2 and supported Au nanoclusters". In: *The journal of physical chemistry letters* 3.16 (2012), pp. 2194–2199. DOI: 10.1021/jz300631f. URL: https://doi.org/10.1021/jz300631f.

[102] Max García-Melchor and Núria López. "Homolytic products from heterolytic paths in H2 dissociation on metal oxides: the example of CeO2". In: *The Journal of Physical Chemistry C* 118.20 (2014), pp. 10921–10926. DOI: 10.1021/jp502309r. URL: https://doi.org/10.1021/jp502309r.

[103] Delia Fernández-Torre et al. "Hydrogen activation, diffusion, and clustering on CeO2 (111): A DFT+ U study". In: *The Journal of chemical physics* 141.1 (2014), p. 14703. DOI: 10.1063/1.4885546. URL: https://doi.org/10.1063/1.4885546.

[104] Mar¸al Capdevila-Cortada, Zbigniew Łodziana, and Núria López. "Performance of DFT+U Approaches in the Study of Catalytic Materials". In: *ACS Catalysis* 6.12 (2016), pp. 8370–8379. DOI: 10.1021/acscatal.6b01907. URL: https://doi.org/10.1021/acscatal.6b01907.

[105] Raquel Juarez et al. "Heterolytic and heterotopic dissociation of hydrogen on ceria-supported gold nanoparticles. Combined inelastic neutron scattering and FT-IR spectroscopic study on the nature and reactivity of surface hydrogen species". In: *Chemical Science* 1.6 (2010), pp. 731–738. DOI: 10.1039/C0SC00336K. URL: http://dx.doi.org/10.1039/C0SC00336K.

[106] R. A. Olsen, G. J. Kroes, and E. J. Baerends. "Atomic and molecular hydrogen interacting with Pt(111)". In: *The Journal of Chemical Physics* 111.24 (1999), pp. 11155–11163. DOI: 10.1063/1.480473. eprint: https://doi.org/10.1063/1.480473. URL: https://doi.org/10.1063/1.480473.

[107] M.Y. Wang et al. "Interaction of H2 with transition metal homonuclear dimers Cu2, Ag2, Au2 and heteronuclear dimers PdCu, PdAg and PdAu". In: *Journal of Molecular Structure: THEOCHEM* 804.1 (2007), pp. 47 –55. ISSN: 0166-1280. DOI: https://doi.org/10.1016/j.theochem.2006.10.007. URL: http://www.sciencedirect.com/science/article/pii/S0166128006006877.

[108] Yaroslava Lykhach et al. "Reactivity of atomically dispersed Pt2+ species towards H2: model Pt-CeO2 fuel cell catalyst". In: *Physical Chemistry Chemical Physics* 18.11 (2016), pp. 7672–7679. ISSN: 1463-9076. DOI: 10.1039/C6CP00627B. URL: http://dx.doi.org/10.1039/C6CP00627B.

[109] Giulia Righi, Rita Magri, and Annabella Selloni. "H2 Dissociation on Noble Metal Single Atom Catalysts Adsorbed on and Doped into CeO2 (111)". In: *The Journal of Physical Chemistry C* 123.15 (Apr. 2019), pp. 9875–9883. ISSN: 1932-7447. DOI: 10.1021/acs.jpcc.9b00609. URL: https://doi.org/10.1021/acs.jpcc.9b00609.

[110] Gianvito Vilé et al. "Ceria in Hydrogenation Catalysis: High Selectivity in the Conversion of Alkynes to Olefins". In: *Angewandte Chemie International Edition* 51.34 (2012), pp. 8620–8623. DOI: 10.1002/anie.201203675. URL: https://onlinelibrary.wiley.com/doi/abs/10.1002/anie.201203675.

[111] Gianvito Vilé et al. "Opposite Face Sensitivity of CeO2 in Hydrogenation and Oxidation Catalysis". In: *Angewandte Chemie International Edition* 53.45 (2014), pp. 12069–12072. DOI: 10.1002/anie.201406637. URL: https://onlinelibrary.wiley.com/doi/abs/10.1002/anie.201406637.

[112] Delia Fernandez-Torre et al. "Insight into the adsorption of water on the clean CeO2 (111) surface with van der Waals and hybrid density functionals". In: *The Journal of Physical Chemistry C* 116.25 (2012), pp. 13584–13593.

[113] Canan Karakaya and Robert J. Kee. "Progress in the direct catalytic conversion of methane to fuels and chemicals". In: *Progress in Energy and Combustion Science* 55 (2016), pp. 60 –97. ISSN: 0360-1285. DOI: https://doi.org/10.1016/j.pecs.2016.04.003. URL: http://www.sciencedirect.com/science/article/pii/S0360128515300642.

[114] Pierre Schwach, Xiulian Pan, and Xinhe Bao. "Direct Conversion of Methane to Value-Added Chemicals over Heterogeneous Catalysts: Challenges and Prospects". In: *Chemical Reviews* 117.13 (2017), pp. 8497–8520. DOI: 10.1021/acs.chemrev.6b00715. URL: https://doi.org/10.1021/acs.chemrev.6b00715.

[115] Nicolas Abatzoglou and Steve Boivin. "A review of biogas purification processes". In: *Biofuels, Bioproducts and Biorefining* 3.1 (2009), pp. 42–71. DOI: 10.1002/bbb.117. URL: https://onlinelibrary.wiley.com/doi/abs/10.1002/bbb.117.

[116] Neil R. Foster. "Direct catalytic oxidation of methane to methanol — a review". In: *Applied Catalysis* 19.1 (1985), pp. 1 –11. ISSN: 0166-9834. DOI: https://doi.org/10.1016/S0166-9834(00)82665-2. URL: http://www.sciencedirect.com/science/article/pii/S0166983400826652.

[117] Hassan Aljama, Jens K. Nørskov, and Frank Abild-Pedersen. "Theoretical Insights into Methane C–H Bond Activation on Alkaline Metal Oxides". In: *The Journal of Physical Chemistry C* 121.30 (2017), pp. 16440–16446. DOI: 10.1021/acs.jpcc.7b05838. URL: https://doi.org/10.1021/acs.jpcc.7b05838.

[118] Raimund Horn and Robert Schlögl. "Methane Activation by Heterogeneous Catalysis". In: *Catalysis Letters* 145.1 (Jan. 2015), pp. 23–39. ISSN: 1572-879X. DOI: 10.1007/s10562-014-1417-z. URL: https://doi.org/10.1007/s10562-014-1417-z.

[119] Patrick Tomkins, Marco Ranocchiari, and Jeroen A. van Bokhoven. "Direct Conversion of Methane to Methanol under Mild Conditions over Cu-Zeolites and beyond". In: *Accounts of Chemical Research* 50.2 (2017), pp. 418–425. DOI: 10.1021/acs.accounts.6b00534. URL: https://doi.org/10.1021/acs.accounts.6b00534.

[120] Junmei Wei and Enrique Iglesia. "Mechanism and Site Requirements for Activation and Chemical Conversion of Methane on Supported Pt Clusters and Turnover Rate Comparisons among Noble Metals". In: *The Journal of Physical Chemistry B* 108.13 (Apr. 2004), pp. 4094–4103. ISSN: 1520-6106. DOI: 10.1021/jp036985z. URL: https://doi.org/10.1021/jp036985z.

[121] Fanglin Che, Su Ha, and Jean-Sabin McEwen. "Catalytic Reaction Rates Controlled by Metal Oxidation State: CH Bond Cleavage in Methane over Nickel-Based Catalysts". In: *Angewandte Chemie International Edition* 56.13 (2017), pp. 3557–3561. DOI: 10.1002/anie.201611796. URL: https://onlinelibrary.wiley.com/doi/abs/10.1002/anie.201611796.

[122] Ernst D. German and Moshe Sheintuch. "Methane steam reforming rates over Pt, Rh and Ni(111) accounting for H tunneling and for metal lattice vibrations". In: *Surface Science* 656 (2017), pp. 126 –139. ISSN: 0039-6028. DOI: https://doi.org/10.1016/j.susc.2016.03.024. URL: http://www.sciencedirect.com/science/article/pii/S0039602816300358.

[123] Ya-Qiong Su et al. "Stable Pd-Doped Ceria Structures for CH4 Activation and CO Oxidation". In: *ACS Catalysis* 8.1 (2018), pp. 75–80. DOI: 10.1021/acscatal.7b03295. URL: https://doi.org/10.1021/acscatal.7b03295.

[124] Hyun You Kim, Hyuck Mo Lee, and Graeme Henkelman. "CO Oxidation Mechanism on CeO2-Supported Au Nanoparticles". In: *Journal of the American Chemical Society* 134.3 (2012), pp. 1560–1570. DOI: 10.1021/ja207510v. URL: https://doi.org/10.1021/ja207510v.

[125] Pablo G. Lustemberg et al. "Room-Temperature Activation of Methane and Dry Re-forming with CO2 on Ni-CeO2(111) Surfaces: Effect of Ce3+ Sites and Metal–Support Interactions on C–H Bond Cleavage". In: *ACS Catalysis* 6.12 (2016), pp. 8184–8191. DOI: 10.1021/acscatal.6b02360. URL: https://doi.org/10.1021/acscatal.6b02360.

[126] Kiyoshi Otsuka and Masaharu Hatano. "The catalysts for the synthesis of formaldehyde by partial oxidation of methane". In: *Journal of Catalysis* 108.1 (1987), pp. 252 –255. ISSN: 0021-9517. DOI: https://doi.org/10.1016/0021-9517(87)90172-2. URL: http://www.sciencedirect.com/science/article/pii/0021951787901722.

[127] M. Verónica Ganduglia-Pirovano. "The non-innocent role of cerium oxide in heterogeneous catalysis: A theoretical perspective". In: *Catalysis Today* 253 (2015), pp. 20 –32. ISSN: 0920-5861. DOI: https://doi.org/10.1016/j.cattod.2015.01.049. URL: http://www.sciencedirect.com/science/article/pii/S0920586115001364.

[128] Alessandro Trovarelli and Jordi Llorca. "Ceria Catalysts at Nanoscale: How Do Crystal Shapes Shape Catalysis?" In: *ACS Catalysis* 7.7 (2017), pp. 4716–4735. DOI: 10.1021/acscatal.7b01246. URL: https://doi.org/10.1021/acscatal.7b01246.

[129] Kebin Zhou et al. "Enhanced catalytic activity of ceria nanorods from well-defined reactive crystal planes". In: *Journal of Catalysis* 229.1 (2005), pp. 206 –212. ISSN: 0021-9517. DOI: https://doi.org/10.1016/j.jcat.2004.11.004. URL: http://www.sciencedirect.com/science/article/pii/S0021951704005366.

[130] Evan W. Zhao et al. "Shaped Ceria Nanocrystals Catalyze Efficient and Selective Para-Hydrogen-Enhanced Polarization". In: *Angewandte Chemie International Edition* 54.48 (2015), pp. 14270–14275. DOI: 10.1002/anie.201506045. URL: https://onlinelibrary.wiley.com/doi/abs/10.1002/anie.201506045.

[131] Marçal Capdevila-Cortada, Max García-Melchor, and Núria López. "Unraveling the structure sensitivity in methanol conversion on CeO2: A DFT+U study". In: *Journal of Catalysis* 327 (2015), pp. 58 –64. ISSN: 0021-9517. DOI: https://doi.org/10.1016/j.jcat.2015.04.016. URL: http://www.sciencedirect.com/science/article/pii/S0021951715001104.

[132] Zongyuan Liu et al. "In Situ Investigation of Methane Dry Reforming on Metal/Ceria(111) Surfaces: Metal–Support Interactions and C-H Bond Activation at Low Temperature". In: *Angewandte Chemie International Edition* 56.42 (2017), pp. 13041–13046. DOI: 10.1002/anie.201707538. URL: https://onlinelibrary.wiley.com/doi/abs/10.1002/anie.201707538.

[133] Ya-Qiong Su et al. "Highly Active and Stable CH4 Oxidation by Substitution of Ce4+ by Two Pd2+ Ions in CeO2(111)". In: *ACS Catalysis* 8.7 (July 2018), pp. 6552–6559. DOI: 10.1021/acscatal.8b01477. URL: https://doi.org/10.1021/acscatal.8b01477.

[134] Matthew D. Krcha, Adam D. Mayernick, and Michael J. Janik. "Periodic trends of oxygen vacancy formation and C–H bond activation over transition metal-doped CeO2 (111) surfaces". In: *Journal of Catalysis* 293 (2012), pp. 103 –115. ISSN: 0021-9517. DOI: https://doi.org/10.1016/j.jcat.2012.06.010. URL: http://www.sciencedirect.com/science/article/pii/S0021951712001820.

[135] Priyank Khirsariya and Raju K. Mewada. "Single Step Oxidation of Methane to Methanol–Towards Better Understanding". In: *Procedia Engineering* 51 (2013), pp. 409 –415. ISSN: 1877-7058. DOI: https://doi.org/10.1016/j.proeng.2013.01.057. URL: http://www.sciencedirect.com/science/article/pii/S1877705813000581.

[136] Pablo G. Lustemberg et al. "Direct Conversion of Methane to Methanol on Ni-Ceria Surfaces: Metal–Support Interactions and Water-Enabled Catalytic Conversion by Site Blocking". In: *Journal of the American Chemical Society* 140.24 (2018), pp. 7681–7687. DOI: 10.1021/jacs.8b03809. URL: https://doi.org/10.1021/jacs.8b03809.

[137] Vitaly L. Sushkevich et al. "Selective anaerobic oxidation of methane enables direct synthesis of methanol". In: *Science* 356.6337 (2017), pp. 523–527. ISSN: 0036-8075. DOI: 10.1126/science.aam9035. URL: http://science.sciencemag.org/content/356/6337/523.

[138] Karthik Narsimhan et al. "Catalytic Oxidation of Methane into Methanol over Copper-Exchanged Zeolites with Oxygen at Low Temperature". In: *ACS Central Science* 2.6 (June 2016), pp. 424–429. ISSN: 2374-7943. DOI: 10.1021/acscentsci.6b00139. URL: https://doi.org/10.1021/acscentsci.6b00139.

[139] Daniel Knapp and Tom Ziegler. "Methane Dissociation on the Ceria (111) Surface". In: *The Journal of Physical Chemistry C* 112.44 (2008), pp. 17311–17318. DOI: 10.1021/jp8039862. URL: https://doi.org/10.1021/jp8039862.

[140] Stefan Grimme. "Semiempirical GGA-type density functional constructed with a long-range dispersion correction". In: *Journal of Computational Chemistry* 27.15 (2006), pp. 1787–1799. DOI: 10.1002/jcc.20495. URL: https://onlinelibrary.wiley.com/doi/abs/10.1002/jcc.20495.

[141] Steven J. Duclos et al. "High-pressure x-ray diffraction study of CeO_2 to 70 GPa and pressure-induced phase transformation from the fluorite structure". In: *Phys. Rev. B* 38.11 (Oct. 1988), pp. 7755–7758. DOI: 10.1103/PhysRevB.38.7755. URL: https://link.aps.org/doi/10.1103/PhysRevB.38.7755.

[142] L. Gerward and J. Staun Olsen. "Powder diffraction analysis of cerium dioxide at high pressure". In: *Powder Diffraction* 8.2 (1993), pp. 127–129. DOI: 10.1017/S0885715600017966.

[143] Ya-Qiong Su et al. "Stable Pd-Doped Ceria Structures for CH4 Activation and CO Oxidation". In: *ACS Catalysis* 8.1 (Jan. 2018), pp. 75–80. DOI: 10.1021/acscatal.7b03295. URL: https://doi.org/10.1021/acscatal.7b03295.

[144] Michael Nolan et al. "Density functional theory studies of the structure and electronic structure of pure and defective low index surfaces of ceria". In: *Surface Science* 576.1 (2005), pp. 217 –229. ISSN: 0039-6028. DOI: https://doi.org/10.1016/j.susc.2004.12.016. URL: http://www.sciencedirect.com/science/article/pii/S0039602804015651.

[145] John J. Carey and Michael Nolan. "Dissociative adsorption of methane on the Cu and Zn doped (111) surface of CeO2". In: *Applied Catalysis B: Environmental* 197 (2016), pp. 324 –336. ISSN: 0926-3373. DOI: https://doi.org/10.1016/j.apcatb.2016.04.004. URL: http://www.sciencedirect.com/science/article/pii/S0926337316302612.

[146] Rochelle M Cornell and Udo Schwertmann. *The iron oxides: structure, properties, reactions, occurrences and uses*. John Wiley & Sons, 2003.

[147] Macarena Munoz et al. "Preparation of magnetite-based catalysts and their application in heterogeneous Fenton oxidation - A review". In: *Applied Catalysis B: Environmental* 176-177 (2015), pp. 249 –265. ISSN: 0926-3373. DOI: https://doi.org/10.1016/j.apcatb.2015.04.003. URL: http://www.sciencedirect.com/science/article/pii/S0926337315001848.

[148] Pedro Tartaj et al. "The iron oxides strike back: from biomedical applications to energy storage devices and photoelectrochemical water splitting". In: *Advanced Materials* 23.44 (2011), pp. 5243–5249. DOI: 10.1002/adma.201101368. URL: https://onlinelibrary.wiley.com/doi/abs/10.1002/adma.201101368.

[149] Kunfeng Zhao et al. "High activity of Au/γ-Fe_2O_3 for CO oxidation: effect of support crystal phase in catalyst design". In: *ACS Catalysis* 5.6 (2015), pp. 3528–3539. DOI: 10.1021/cs5020496. URL: https://doi.org/10.1021/cs5020496.

[150] D. Widmann and R. J. Behm. "Activation of Molecular Oxygen and the Nature of the Active Oxygen Species for CO Oxidation on Oxide Supported Au Catalysts". In: *Accounts of Chemical Research* 47.3 (Mar. 2014), pp. 740–749. ISSN: 0001-4842. DOI: 10.1021/ar400203e. URL: https://doi.org/10.1021/ar400203e.

[151] Sharif Najafishirtari et al. "Metal-support interaction in catalysis: The influence of the morphology of a nano-oxide domain on catalytic activity". In: *Applied Catalysis B: Environmental* 237 (2018), pp. 753 –762. ISSN: 0926-3373. DOI: https://doi.org/10.1016/j.apcatb.2018.06.033. URL: http://www.sciencedirect.com/science/article/pii/S0926337318305678.

[152] P. Tartaj et al. "Advances in magnetic nanoparticles for biotechnology applications". In: *Journal of Magnetism and Magnetic Materials* 290-291 (2005), pp. 28 –34. ISSN: 0304-8853. DOI: https://doi.org/10.1016/j.jmmm.2004.11.155. URL: http://www.sciencedirect.com/science/article/pii/S0304885304013952.

[153] Wei Zhou et al. "Amorphous Iron Oxide Decorated 3D Heterostructured Electrode for Highly Efficient Oxygen Reduction". In: *Chemistry of Materials* 23.18 (2011), pp. 4193–4198. DOI: 10.1021/cm201439d. URL: https://doi.org/10.1021/cm201439d.

[154] Kaipei Qiu et al. "Highly efficient oxygen reduction catalysts by rational synthesis of nanoconfined maghemite in a nitrogen-doped graphene framework". In: *ACS Catalysis* 6.6 (2016), pp. 3558–3568. DOI: 10.1021/acscatal.6b00531. URL: https://doi.org/10.1021/acscatal.6b00531.

[155] Junjie Wang et al. "Three-dimensionally mesostructured Fe2O3 electrodes with good rate performance and reduced voltage hysteresis". In: *Chemistry of Materials* 27.8 (2015), pp. 2803–2811. DOI: 10.1021/cm504365s. URL: https://doi.org/10.1021/cm504365s.

[156] H. Shokrollahi. "A review of the magnetic properties, synthesis methods and applications of maghemite". In: *Journal of Magnetism and Magnetic Materials* 426 (2017), pp. 74 –81. ISSN: 0304-8853. DOI: https://doi.org/10.1016/j.jmmm.2016.11.033. URL: http://www.sciencedirect.com/science/article/pii/S0304885316313397.

[157] Aaron M Jubb and Heather C Allen. "Vibrational spectroscopic characterization of hematite, maghemite, and magnetite thin films produced by vapor deposition". In: *ACS Applied Materials & Interfaces* 2.10 (2010), pp. 2804–2812. DOI: 10.1021/am1004943. URL: https://doi.org/10.1021/am1004943.

[158] Ricardo Grau-Crespo et al. "Vacancy ordering and electronic structure of γ-Fe2O3 (maghemite): a theoretical investigation". In: *Journal of Physics: Condensed Matter* 22.25 (2010), p. 255401. DOI: 10.1088/0953-8984/22/25/255401. URL: https://doi.org/10.1088\%2F0953-8984\%2F22\%2F25\%2F255401.

[159] G. A. Waychunas. "Crystal chemistry of oxides and oxyhydroxides". In: *Rev.Mineral.Geochem* 2511 (1991).

[160] GW Van Oosterhout and CJM Rooijmans. "A new superstructure in gamma-ferric oxide". In: *Nature* 181.4601 (1958), p. 44.

[161] C Greaves. "A powder neutron diffraction investigation of vacancy ordering and covalence in γ-Fe2O3". In: *Journal of Solid State Chemistry* 49.3 (1983), pp. 325–333. ISSN: 0022-4596. DOI: https://doi.org/10.1016/S0022-4596(83)80010-3. URL: http://www.sciencedirect.com/science/article/pii/S0360128515300496.

[162] AN Shmakov et al. "Vacancy Ordering in γ-Fe2O3: Synchrotron X-ray Powder Diffraction and High-Resolution Electron Microscopy Studies". In: *Journal of Applied Crystallography* 28.2 (1995), pp. 141–145. DOI: 10.1107/S0021889894010113. URL: https://doi.org/10.1107/S0021889894010113.

[163] Jens-Erik Jørgensen et al. "Formation of γ-Fe2O3 nanoparticles and vacancy ordering: An in situ X-ray powder diffraction study". In: *Journal of Solid State Chemistry* 180.1 (2007), pp. 180–185. DOI: https://doi.org/10.1016/j.jssc.2006.09.033. URL: http://www.sciencedirect.com/science/article/pii/S0022459606005342.

[164] Rossitza Pentcheva et al. "Jahn-Teller stabilization of a polar metal oxide surface: Fe_3O_4 (001)". In: *Physical review letters* 94.12 (2005), p. 126101. DOI: 10.1103/PhysRevLett.94.126101. URL: https://link.aps.org/doi/10.1103/PhysRevLett.94.126101.

[165] Roger C Baetzold and Hong Yang. "Computational study on surface structure and crystal morphology of γ-Fe2O3: Toward deterministic synthesis of nanocrystals". In: *The Journal of Physical Chemistry B* 107.51 (2003), pp. 14357–14364. DOI: 10.1021/jp035785k. URL: https://doi.org/10.1021/jp035785k.

[166] Pan Guo, Xin Guo, and Chuguang Zheng. "Roles of γ-Fe2O3 in fly ash for mercury removal: Results of density functional theory study". In: *Applied Surface Science* 256.23 (2010), pp. 6991–6996. DOI: https://doi.org/10.1016/j.apsusc.2010.05.013. URL: http://www.sciencedirect.com/science/article/pii/S0169433210006781.

[167] Hendrik J. Monkhorst and James D. Pack. "Special points for Brillouin-zone integrations". In: *Phys. Rev. B* 13.12 (June 1976), pp. 5188–5192. DOI: 10.1103/PhysRevB.13.5188. URL: https://link.aps.org/doi/10.1103/PhysRevB.13.5188.

[168] Matteo Cococcioni and Stefano de Gironcoli. "Linear response approach to the calculation of the effective interaction parameters in the $\backslashmathrm{LDA}+\backslashmathrm{U}$ method". In: *Phys. Rev. B* 71.3 (Jan. 2005), p. 35105. DOI: 10.1103/PhysRevB.71.035105. URL: https://link.aps.org/doi/10.1103/PhysRevB.71.035105.

[169] R. Dronskowski. "The Little Maghemite Story: A Classic Functional Material". In: *Advanced Functional Materials* 11.1 (2001), pp. 27–29. DOI: 10.1002/1616-3028(200102)11:1<27::AID-ADFM27>3.0.CO;2-X. URL: https://onlinelibrary.wiley.com/doi/abs/10.1002/1616-3028%28200102%2911%3A1%3C27%3A%3AAID-ADFM27%3E3.0.CO%3B2-X.

[170] Per-Olov Löwdin. "On the Non-Orthogonality Problem Connected with the Use of Atomic Wave Functions in the Theory of Molecules and Crystals". In: *The Journal of Chemical Physics* 18.3 (1950), pp. 365–375. DOI: 10.1063/1.1747632. URL: https://doi.org/10.1063/1.1747632.

[171] Per-Olov Löwdin. "On the Nonorthogonality Problem**The work reported in this paper has been sponsored in part by the Swedish Natural Science Research Council, in part by the Air Force Office of Scientific Research (OSR) through the European Office of Aerospace Research (OAR), U.S. Air Force under Grant AF-EOAR 67-50 with Uppsala University, and in part by the National Science Foundation under Grant GP-5419 with the University of Florida." In: ed. by Per-Olov Löwdin. Vol. 5. Advances in Quantum Chemistry. Academic Press, 1970, pp. 185 –199. DOI: 10.1016/S0065-3276(08)60339-1. URL: http://www.sciencedirect.com/science/article/pii/S0065327608603391.

[172] Karsten Reuter and Matthias Scheffler. "Composition, structure, and stability of RuO_2 (110) as a function of oxygen pressure". In: *Phys. Rev. B* 65.3 (Dec. 2001), p. 035406. DOI: 10.1103/PhysRevB.65.035406. URL: https://link.aps.org/doi/10.1103/PhysRevB.65.035406.

[173] Karsten Reuter and Matthias Scheffler. "Composition and structure of the RuO_2 (110) surface in an O_2 and CO environment: Implications for the catalytic formation of CO_2". In: *Physical Review B* 68.4 (2003), p. 045407. DOI: 10.1103/PhysRevB.68.045407. URL: https://link.aps.org/doi/10.1103/PhysRevB.68.045407.

[174] Ricardo Grau-Crespo, C. Richard A. Catlow, and Nora H. de Leeuw. "A computer modeling study of redox processes on the FeSbO4 (100) surface". In: *Journal of Catalysis* 248.1 (2007), pp. 77 –88. ISSN: 0021-9517. DOI: https://doi.org/10.1016/j.jcat.2007.02.015. URL: http://www.sciencedirect.com/science/article/pii/S0021951707000668.

[175] M. W. Chase. *NIST-JANAF thermochemical tables*. Washington, D.C.: American Chemical Society ; Woodbury, N.Y. : American Institute of Physics for the National Institute of Standards and Technology, 1998.

[176] R. Pentcheva et al. "A combined DFT/LEED-approach for complex oxide surface structure determination: Fe_3O_4(001)". In: *Surface Science* 602.7 (2008), pp. 1299 –1305. ISSN: 0039-6028. DOI: https://doi.org/10.1016/j.susc.2008.01.006. URL: http://www.sciencedirect.com/science/article/pii/S0039602808000113.

[177] M. Fonin et al. "Formation of magnetic domains and domain walls in epitaxial Fe3O4(100) elements (invited)". In: *Journal of Applied Physics* 109.7 (2011), p. 07D315. DOI: 10.1063/1.3540678. URL: https://doi.org/10.1063/1.3540678.

[178] Zbigniew Lodziana. "Surface Verwey Transition in Magnetite". In: *Phys. Rev. Lett.* 99.20 (Nov. 2007), p. 206402. DOI: 10.1103/PhysRevLett.99.206402. URL: https://link.aps.org/doi/10.1103/PhysRevLett.99.206402.

[179] Xiaohu Yu et al. "Adsorption of Au_n (n= 1-4) clusters on Fe_3O_4 (001) B-termination". In: *RSC Advances* 5.56 (2015), pp. 45446–45453. DOI: 10.1039/C5RA06294B. URL: http://dx.doi.org/10.1039/C5RA06294B.

[180] Narasimham Mulakaluri, Rossitza Pentcheva, and Matthias Scheffler. "Coverage-Dependent Adsorption Mode of Water on Fe3O4(001): Insights from First Principles Calculations". In: *The Journal of Physical Chemistry C* 114.25 (2010), pp. 11148–11156. DOI: 10.1021/jp100344n. URL: https://doi.org/10.1021/jp100344n.

[181] Juan Rubio-Zuazo et al. "Electronic structure of FeO, γ- Fe2O3, and Fe3O4 epitaxial films using high-energy spectroscopies". In: *Physical Review B* 97.23 (2018), p. 235148. DOI: 10.1103/PhysRevB.97.235148. URL: https://link.aps.org/doi/10.1103/PhysRevB.97.235148.

[182] Maíra dos Santos Pires et al. "Experimental and theoretical study on the reactivity of maghemite doped with Cu2+ in oxidation reactions: structural and thermodynamic properties towards a Fenton catalyst". In: *RSC Advances* 6.84 (2016), pp. 80830–80839. DOI: 10.1039/C6RA11032K. URL: http://dx.doi.org/10.1039/C6RA11032K.

[183] Zbyněk Novotný et al. "Ordered Array of Single Adatoms with Remarkable Thermal Stability: $Au/Fe_3O_4(001)$$". In: *Phys. Rev. Lett.* 108.21 (May 2012), p. 216103. DOI: 10.1103/PhysRevLett.108.216103. URL: https://link.aps.org/doi/10.1103/PhysRevLett.108.216103.

[184] Roland Bliem et al. "Cluster Nucleation and Growth from a Highly Supersaturated Adatom Phase: Silver on Magnetite". In: *ACS Nano* 8.7 (July 2014), pp. 7531–7537. ISSN: 1936-0851. DOI: 10.1021/nn502895s. URL: https://doi.org/10.1021/nn502895s.

[185] Gareth S. Parkinson et al. "Carbon monoxide-induced adatom sintering in a Pd/Fe3O4 model catalyst". In: *Nature Materials* 12 (June 2013), p. 724. URL: https://doi.org/10.1038/nmat3667.

[186] Jeremy P. Allen, David O. Scanlon, and Graeme W. Watson. "Electronic structures of silver oxides". In: *Phys. Rev. B* 84.11 (Sept. 2011), p. 115141. DOI: 10.1103/PhysRevB.84.115141. URL: https://link.aps.org/doi/10.1103/PhysRevB.84.115141.

[187] Hongqing Shi, Ryoji Asahi, and Catherine Stampfl. "Properties of the gold oxides Au_2O_3 and Au_2O: First-principles investigation". In: *Phys. Rev. B* 75.20 (May 2007), p. 205125. DOI: 10.1103/PhysRevB.75.205125. URL: https://link.aps.org/doi/10.1103/PhysRevB.75.205125.

[188] Giulia Righi and Rita Magri. "Reduction and Oxidation of Maghemite (001) Surfaces: The Role of Iron Vacancies". In: *The Journal of Physical Chemistry C* 123.25 (June 2019), pp. 15648–15658. ISSN: 1932-7447. DOI: 10.1021/acs.jpcc.9b03657. URL: https://doi.org/10.1021/acs.jpcc.9b03657.

[189] Juan Adanez et al. “Progress in Chemical-Looping Combustion and Reforming technologies”. In: *Progress in Energy and Combustion Science* 38.2 (2012), pp. 215 –282. ISSN: 0360-1285. DOI: https://doi.org/10.1016/j.pecs.2011.09.001. URL: http://www.sciencedirect.com/science/article/pii/S0360128511000505.

[190] Turgut M. Gür. “Comprehensive review of methane conversion in solid oxide fuel cells: Prospects for efficient electricity generation from natural gas”. In: *Progress in Energy and Combustion Science* 54 (May 2016), pp. 1–64. ISSN: 0360-1285. DOI: 10.1016/j.pecs.2015.10.004. URL: http://www.sciencedirect.com/science/article/pii/S0360128515300496.

[191] L. Gerward et al. “Bulk modulus of CeO2 and PrO2—An experimental and theoretical study”. In: *Journal of Alloys and Compounds* 400.1 (2005), pp. 56 – 61. ISSN: 0925-8388. DOI: https://doi.org/10.1016/j.jallcom.2005.04.008. URL: http://www.sciencedirect.com/science/article/pii/S0925838805003403.

[192] A. Nakajima, A. Yoshihara, and M. Ishigame. “Defect-induced Raman spectra in doped CeO_2”. In: *Phys. Rev. B* 50.18 (Nov. 1994), pp. 13297–13307. DOI: 10.1103/PhysRevB.50.13297. URL: https://link.aps.org/doi/10.1103/PhysRevB.50.13297.

[193] Christoph Loschen et al. “First-principles LDA+U and GGA+U study of cerium oxides: Dependence on the effective U parameter”. In: *Phys. Rev. B* 75.3 (Jan. 2007), p. 035115. DOI: 10.1103/PhysRevB.75.035115. URL: https://link.aps.org/doi/10.1103/PhysRevB.75.035115.

[194] Stefano Fabris et al. “Taming multiple valency with density functionals: A case study of defective ceria”. In: *Phys. Rev. B* 71.4 (Jan. 2005), p. 041102. DOI: 10.1103/PhysRevB.71.041102. URL: https://link.aps.org/doi/10.1103/PhysRevB.71.041102.

[195] N. V. Skorodumova et al. “Electronic, bonding, and optical properties of CeO_2 and Ce_2O_3 from first principles”. In: *Phys. Rev. B* 64.11 (Aug. 2001), p. 115108. DOI: 10.1103/PhysRevB.64.115108. URL: https://link.aps.org/doi/10.1103/PhysRevB.64.115108.

[196] C. Sevik and Çağin T. “Mechanical and electronic properties of CeO_2, ThO_2, and (Ce, Th)O_2 alloys”. In: *Phys. Rev. B* 80.1 (July 2009), p. 014108. DOI: 10.1103/PhysRevB.80.014108. URL: https://link.aps.org/doi/10.1103/PhysRevB.80.014108.

[197] Juarez L. F. Da Silva et al. “Hybrid functionals applied to rare-earth oxides: The example of ceria”. In: *Phys. Rev. B* 75.4 (Jan. 2007), p. 045121. DOI: 10.1103/PhysRevB.75.045121. URL: https://link.aps.org/doi/10.1103/PhysRevB.75.045121.

[198] Jesús Graciani et al. “Comparative Study on the Performance of Hybrid DFT Functionals in Highly Correlated Oxides: The Case of CeO2 and Ce2O3”. In: *Journal of Chemical Theory and Computation* 7.1 (Jan. 2011), pp. 56–65. ISSN: 1549-9618. DOI: 10.1021/ct100430q. URL: https://doi.org/10.1021/ct100430q.

[199] P. Jeffrey Hay et al. “Theoretical study of CeO2 and Ce2O3 using a screened hybrid density functional”. In: *The Journal of Chemical Physics* 125.3 (July 2006), p. 034712. ISSN: 0021-9606. DOI: 10.1063/1.2206184. URL: https://doi.org/10.1063/1.2206184 (visited on 09/16/2019).

[200] E. Wuilloud et al. "Spectroscopic Evidence for Localized and Extended f-Symmetry States in CeO_2". In: *Phys. Rev. Lett.* 53.2 (July 1984), pp. 202–205. DOI: 10.1103/PhysRevLett.53.202. URL: https://link.aps.org/doi/10.1103/PhysRevLett.53.202.

[201] H. Pinto et al. "Neutron diffraction study of Ce2O3". In: *Physics Letters A* 88.2 (Feb. 1982), pp. 81–83. ISSN: 0375-9601. DOI: 10.1016/0375-9601(82)90596-5. URL: http://www.sciencedirect.com/science/article/pii/0375960182905965.

[202] Zhen-Wei Niu et al. "Elastic and electronic properties of Ce2O3 from first principles". In: *Journal of Alloys and Compounds* 551 (Feb. 2013), pp. 672–676. ISSN: 0925-8388. DOI: 10.1016/j.jallcom.2012.10.136. URL: http://www.sciencedirect.com/science/article/pii/S0925838812019159.

[203] Stefano Fabris, Stefano de Gironcoli, and Stefano Baroni. "Electron localization in pure and defective ceria by a unified LDA+ U approach". In: *arXiv preprint cond-mat/0312601* (2003).

[204] A.V. Prokofiev, A.I. Shelykh, and B.T. Melekh. "Periodicity in the band gap variation of Ln2X3 (X = O, S, Se) in the lanthanide series". In: *Journal of Alloys and Compounds* 242.1 (Sept. 1996), pp. 41–44. ISSN: 0925-8388. DOI: 10.1016/0925-8388(96)02293-1. URL: http://www.sciencedirect.com/science/article/pii/0925838896022931.

[205] D.R. Mullins, P.V. Radulovic, and S.H. Overbury. "Ordered cerium oxide thin films grown on Ru(0001) and Ni(111)". In: *Surface Science* 429.1 (June 1999), pp. 186–198. ISSN: 0039-6028. DOI: 10.1016/S0039-6028(99)00369-6. URL: http://www.sciencedirect.com/science/article/pii/S0039602899003696.

[206] Hong Jiang et al. "Localized and Itinerant States in Lanthanide Oxides United by GW@LDA+U". In: *Phys. Rev. Lett.* 102.12 (Mar. 2009), p. 126403. DOI: 10.1103/PhysRevLett.102.126403. URL: https://link.aps.org/doi/10.1103/PhysRevLett.102.126403.

[207] José A Rodriguez et al. "Water-Gas Shift Reaction on a Highly Active Inverse CeOx/Cu(111) Catalyst: Unique Role of Ceria Nanoparticles". In: *Angewandte Chemie International Edition* 48.43 (2009), pp. 8047–8050. DOI: 10.1002/anie.200903918. URL: https://onlinelibrary.wiley.com/doi/abs/10.1002/anie.200903918.

[208] Fan Yang et al. "CO Oxidation on Inverse CeOx/Cu(111) Catalysts: High Catalytic Activity and Ceria-Promoted Dissociation of O2". In: *Journal of the American Chemical Society* 133.10 (2011), pp. 3444–3451. ISSN: 0002-7863. DOI: 10.1021/ja1087979. URL: https://doi.org/10.1021/ja1087979.

[209] Lucie Szabová et al. "Distinct Physicochemical Properties of the First Ceria Monolayer on Cu(111)". In: *The Journal of Physical Chemistry C* 116.11 (2012), pp. 6677–6684. ISSN: 1932-7447. DOI: 10.1021/jp211955v. URL: https://doi.org/10.1021/jp211955v.

[210] Jesús Graciani et al. "Unraveling the Nature of the Oxide–Metal Interaction in Ceria-Based Noble Metal Inverse Catalysts". In: *The Journal of Physical Chemistry C* 118.46 (2014), pp. 26931–26938. ISSN: 1932-7447. DOI: 10.1021/jp509947t. URL: https://doi.org/10.1021/jp509947t.